Toward a novel vibronic model for hierarchical conjugated hydrocarbons

Emmeline Ho

THÈSE POUR OBTENIR LE GRADE DE DOCTEUR DE L'UNIVERSITÉ DE MONTPELLIER

En Chimie et Physico-chimie des Matériaux

École doctorale Sciences chimiques Balard – ED 459

Unité de recherche Institut Charles Gerhardt de Montpellier

Vers un modèle vibronique innovant pour les hydrocarbures conjugués

Présentée par Emmeline HO
Le 6 juillet 2018

Sous la direction de Benjamin LASORNE

Devant le jury composé de

Jean-Sébastien FILHOL, Professeur, Université de Montpellier	Président du jury
Valérie BRENNER, Directrice de recherche, CEA Saclay	Rapporteur
Graham A. WORTH, Professeur, University College London	Rapporteur
Isabelle DEMACHY, Professeur, Université Paris-Saclay	Membre du jury
Stéphane HUMBEL, Professeur, Université d'Aix-Marseille	Membre du jury
Benjamin LASORNE, Chargé de recherche, CNRS Montpellier	Directeur de thèse

UNIVERSITÉ DE MONTPELLIER

"*If you have a problem, just rotate*" G. A. Worth

"*A vaincre sans péril, on triomphe sans gloire*"

Remerciements

Avant tout, je tiens à remercier mon directeur de thèse, pour la qualité de son encadrement, sa disponibilité, ses conseils (scientifiques, mais aussi administratifs et diplomatiques), pour sa grande patience et toute l'écoute dont il a fait preuve au cours de ces trois années.

Je remercie également les membres du jury qui ont accepté d'évaluer mon travail, en particulier les rapporteurs Graham A. Worth et Valérie Brenner.

Merci à l'équipe CTMM au sein de laquelle j'ai pu effectuer ma thèse dans des conditions agréables; en particulier à Marie pour ses discussions toujours très instructives, ainsi que Christophe et Jean-Seb pour leurs avis éclairés sur l'après-thèse. Une pensée aussi à Fabrice et Françoise pour leur compétence et leur disponibilité.

Merci à tous ceux qui ont équilibré ma vie pendant la thèse : la salsa family, en particulier les coachs Jérémy&Olaia, et mes rayons de soleil (et de folie) Omar et Marina; le club de kungfu, en particulier Aziz pour sa bienveillance à la hauteur de toutes mes courbatures, et le profond respect qu'il a pour son art.

Un grand merci aux amis qui m'ont toujours soutenue : Rosana, Sophie, Rokhi, Tristan J., Doriane, Gaëtan, Yoann; en particulier, Clémence et Muriel, qui ont toujours cru en moi plus que moi-même, et mes amis les plus fous : Eric et Manon. Et un merci tout particulier à ceux qui m'ont le plus supportée (et pas juste soutenue) [1] *: Aurelie, ma grande soeur spirituelle, Benjamin G. mon grand frère de thèse adoptif, Mélissa et Mathieu, Stéphane.*

Comme les remerciements c'est important, merci à Tristan, Adeline et Leïla. Je tiens d'ailleurs à bénir les concepteurs de Latex, et le Chef Bernard pour ses pâtisseries (surtout les tartes au chocolat).

Je remercie bien sûr ma famille, surtout mon père qui a été le premier à m'apprendre à réfléchir et à me donner le goût des sciences et du travail bien fait, et ma grand-mère sur qui je peux toujours compter.

[1] Cette catégorie inclut également de personnes mentionnées plus haut.

Une pensée enfin pour l'équipe Théosim du LCP d'Orsay, dont la plupart des membres ont contribué à ma formation de physico-chimiste. En particulier, je remercie Michèle pour la qualité de ses cours de mécanique quantique, et Isabelle pour sa bienveillance en tant qu'enseignante et encadrante, et qui m'a tout simplement donné envie de faire une thèse.

Contents

Notations

Constants

$\hbar$	reduced constant of Planck $h/2\pi$
ε_0	vacuum permittivity
e	elementary charge
m_e	electron mass

Definitions

$\hat{O}$	operator associated to observable O
$\hat{O}^\dagger$	adjoint operator of $\hat{O}$
δ_{ij}	Kronecker constant $\begin{cases} 1 & \text{if } i = j \\ 0 & \text{if } i \neq j \end{cases}$
$\mathbf{1}_n$	unity matrix of rank n (adapted to the context when n is omitted)
$\boldsymbol{O}$	matrix representation of $\hat{O}$ in a basis
$\boldsymbol{O}^t$	transposed matrix of $\boldsymbol{O}$
$\boldsymbol{O}^\dagger$	adjoint matrix of $\boldsymbol{O}$
O_{ij}	elements of indices i, j of the matrix $\boldsymbol{O}$
$\lvert \dots \rangle$	state vector, element of an Hilbert space
$\langle r \rvert$	dual of $\lvert r \rangle$
$\boldsymbol{r}$	representation of $\vec{r}$ as a column vector in a basis
r_i	element of index i of $\boldsymbol{r}$

Indices i, j, k, l, m, n are integers except when explicitely mentionned otherwise.

We will not use tensor notations, so $a^{(n)}$ represents an object a numbered n and a^i is an object a to power i.

For a position vector in the euclidian space, we denote $r_{(i,a)}$ the element of coordinate

a of atom i with $a \in x, y, z$ and $\boldsymbol{r}[(i)]$ the vector

$$\boldsymbol{r}[(i)] = \begin{pmatrix} r_{(i,x)} \\ r_{(i,y)} \\ r_{(i,z)} \end{pmatrix}$$

Part I

Introduction

0.1 Light harvesting and energy transfer

Organic semiconductors are photo- and electroactive materials that are able to transduct an energy flux *via* their π-system, and can also be used for the production and conduction of an electric current generated from light absorption (or conduction and release of energy through light emission) [1–7]. They are designed as new generations of electronic and optoelectronic devices with applications in photovoltaics, electroluminescence, and artificial photosynthesis: organic solar cells [7], organic transistors [8], organic light-emitting diodes (OLEDs) [9], and biomimetic light-harvesting antennae [10–14]. Within this perspective, the Nobel Prize in Chemistry 2000 was awarded for the discovery and development of conductive polymers [15–18].

In this context, understanding the mechanisms involved in energy transfer is crucial for the synthesis of compounds showing such properties. To do so, the so-called nanostar happens to be a system of choice, which exhibits a particularly efficient (around 98%) and fast (about a few picoseconds according to the literature) energy transfer (see below) [19, 20].

The nanostar is a dendritic polyphenylene ethynylene (PPE) macromolecule terminated by a perylene, see figure 0.1, initially designed to mimic natural photosythesis, and first synthesized by J. S. Moore and *al.* in 1994 [21], thus often viewed as a biomimetic, photosynthetic "nanoleaf" or "nanotree".

PPEs are complex, yet hierarchical, π-conjugated organic macromolecules that present a huge potential in the context of organic nano-optoelectronics [8, 13]. Among them (see examples in figure 0.2), the dendritic ones are often classified between the compact and the extended dendrimers, both exhibiting a tree-branched architecture that makes them remarkably efficient synthetic light-harvesting antennae, able to collect photons from several peripheral points [22].
Compact dendrimers are constituted of same length *para*-building blocks, so part of the energy transfers are due to entropic reasons [11, 23–26]. On the other hand, extended dendrimers (such as the nanostar) are constituted of building blocks of increasing lengths from the periphery to the core, which yields an energy gradient at the origin of the efficient energy transfer [19, 27, 28].

The present thesis is focused on the study of energy transfer within photoexcited

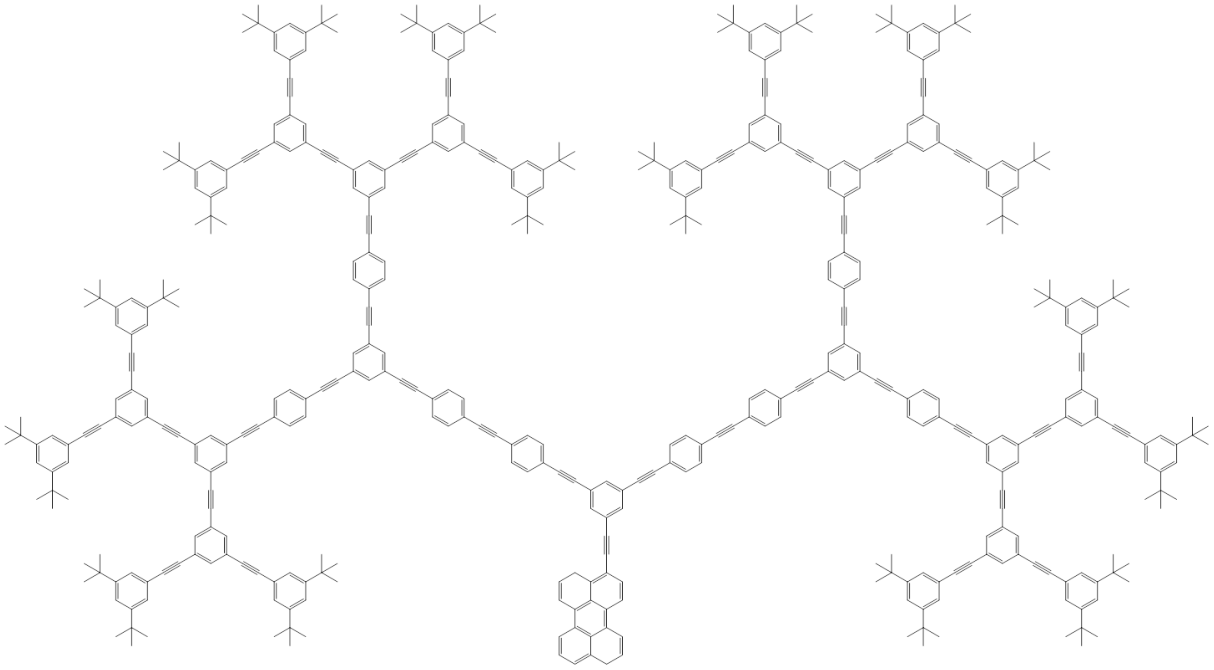

Figure 0.1: The "nanostar".

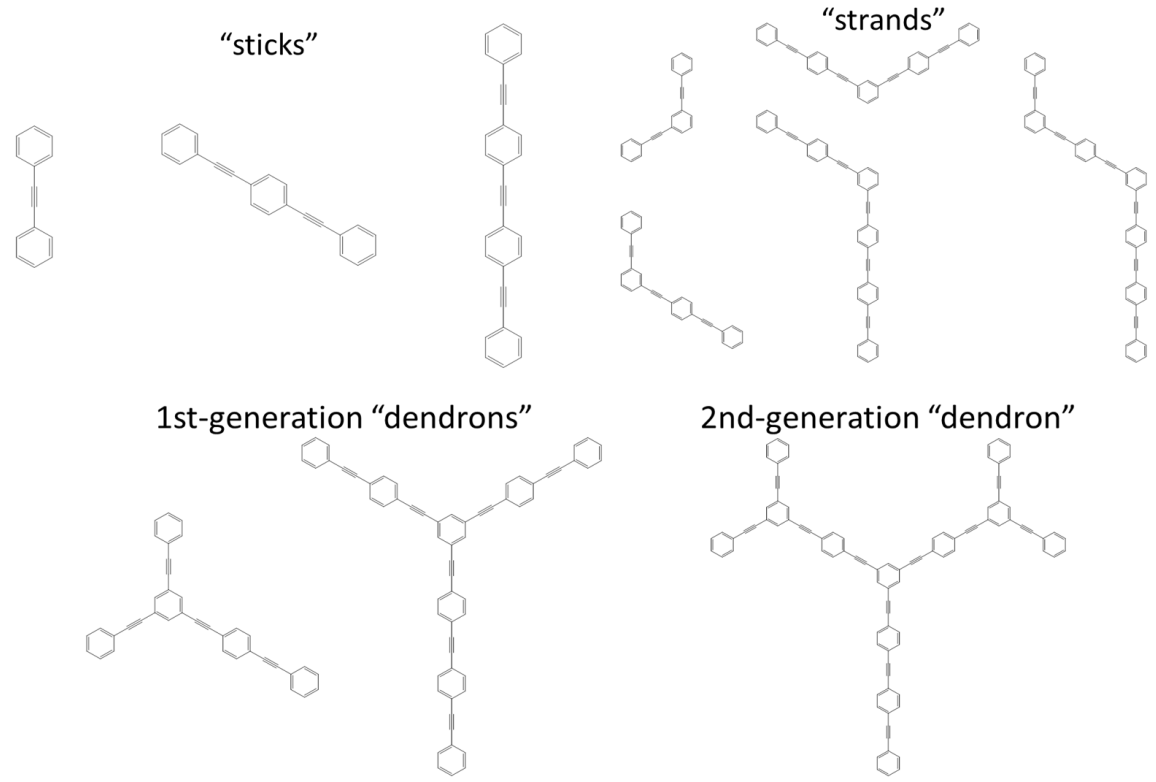

Figure 0.2: Various PPEs.

PPEs, so as to understand, rationalize, and simulate the mechanisms involved in this process, in relationship with the properties of their constitutive units.

0.2 State of the art and general objectives

Lots of efforts were made these last thirty years, and are still made currently, to unravel the mechanisms governing the behavior of PPEs at the microscopic and molecular levels. Yet, identifying systematic and transferable relations between the structure and properties of such macromolecules from those of their subunits still raises a number of open issues for both experiments and theory, as recently stated [29].

Such a description requires to correctly account for various effects acting on various length, time, and energy scales, which appears challenging at first sight.

We summarize in the following the elements of answers raised in the literature along with the current open issues and technical barriers to be lifted.

Historically, the first insight into the electronic structure of PPEs came from steady-state spectroscopy experiments [27, 30]. The authors highlighted that the absorption spectrum of the nanostar is almost additive and dominated by individual contributions of $\pi \rightarrow \pi^*$ locally excited (LE) electronic states on "sticks". This was later confirmed by other experimental [20, 28, 31–33] and theoretical studies [34–42] on other types of *meta*-PPEs. Thus, quantitative descriptions are required to rationalize the structure-property relations, in particular the fact that *meta*-substitution partially disrupts π-conjugation in PPEs [34, 43–45].

The occurence of dark charge-transfer states and their possible effect on the energy transfer is still an open question, since their description is sensitive to the level of theory used in calculations [46]. Such states are likely to trap the excitation, thus quenching the transfer and should thus be studied with special care [47].

From a dynamic point of view, the energy transfer in the nanostar is actually an ultra-fast and unidirectional excitation transfer occuring *via* a cascade of internal conversions among "sticks" of increasing lengths within the dendritic structures [19, 27, 30, 41, 42, 48–53]. Peripheral chromophores absorb light at high energies so the excitation is transducted

from a chromophore to the adjacent one along the energy gradient created by the different lengths of the chromophores (*shishiodoshi* effect) [42]. For now, it is assumed that this ideal mechanism involves conical intersections which remain to be fully characterized, experimentally and computationally, along with the effect of non-adiabatic couplings.

Approximate calculations (mixed quantum-classical dynamics with semiempirical potential energies) on linear *meta*-PPEs indicated that the energy is vibronically mediated through in-plane high-frequency skeletal C≡C modes [42, 48, 49, 51–53]. To evaluate the contribution of these nuclear modes and others in the relaxation through conical intersections, it is crucial to have access to the evolution of electronic state populations and coherences with respect to time. This still awaits for higher-level simulations and confrontation to experiments involving ultrafast femtosecond and two-dimensional (2D) spectroscopy.

Finally, specific issues may arise from the macromolecular structure of PPEs such as the nanostar. First, even though through-bond interactions (intramolecular regime) are assumed to dominate in the excitation transfer process, through-space interactions (intermolecular regime) among not-covalently-bonded *para*-fragments may also contribute [40, 44]. The competition between these two effects can only be rationalized confronting 2D spectroscopy with multiscale/multimethod simulations based on system-bath models [29, 54, 55].

Then, ramified *meta*-junctions are points of meeting for excitations arriving from different *para*-fragments, which may cause local exciton blockades [56]. Such situations require to be addressed with simulations and transport models adapted to multibranched networks [25].

In large-enough dendrimers, conformational disorder is also to be taken into account. In particular, torsions and soft vibrational modes extending over the whole range of the macromolecules may be crucial upon modulating oscillator strengths and inducing line broadening in samples at room temperature [41, 57, 58]. Torsions do not disrupt the π-conjugation as dramatically as for double bonds (due to the cylindric topology of the triple bond), and may tune optical-path lengths [59], thus preventing exciton blockade. Rationalizing the effect of torsions upon optical-path lengths is then of particular interest for the global description of the excitation transfer [60, 61].

0.3 Objectives of the thesis

The present thesis manuscript starts with a general presentation of the relevant formalisms, methods, and concepts. Results and discussion are essentially divided into two parts; the first one is dedicated to the electronic structure of PPEs, whilst the second one proposes a first step toward the construction of a quasidiabatic model of "coupled" potential-energy surfaces, aimed at being generalizable to any PPE dendrimer.

The electronic structure of *meta*-PPEs is rationalized with respect to the electronic structure of their constitutive *para*-fragments. Both are characterized with DFT or TDDFT calculations performed at the ground state and relevant first few excited states with the Gaussian package [62].

The reliability of the level of theory we used (DFT and TDDFT; CAM-B3LYP/6-31+G*) is assessed in the first place [63]. Our work confirms the additivity in the absorbtion spectra of *meta*-PPEs already raised in the literature, along with the local character of the excited states. More precisely, we show that the first relevant excited states are each dominated by a single transition between near frontier orbitals (HOMO, LUMO, HOMO-1, LUMO+1,...) and that all the properties we studied show the same additive behavior as the absorption spectra, in particular at the orbital level.

From these results, a clear hierarchy appears in the electronic structure of PPEs, and we define pseudo-fragments, which carry molecular orbitals of molecular "fragments" sharing common atoms within *meta*-substituted benzene rings.

Accessible conical intersections are identified in the case of a symmetric *meta*-PPE, giving credit to the ideal mechanism proposed in the literature. The implication of the C≡C bonds in the internal conversion process is also confirmed, and other modes are identified as coordinates of the branching spaces. Tightly avoided crossings proving the proximity of conical intersections and the possibility of internal conversion processes are also identified for a more complex system.

Considering the hierarchy highlightened in the study of the electronic structure, a multiscale model is proposed to express the energies of the electronic states of *meta*-PPEs in terms of relevant local nuclear coordinates. Intermediate energies are considered: electronic energies of *para*-PPEs, frontier-orbital energies of *para*-PPEs, orbital energies

of basic units, which define the different steps of the model. The interactions to account for at each step of the model are described upon considering concepts inspired from tight-binding formalisms.

An effective model is proposed to express the energies of the frontier orbitals of *para*-PPEs in terms of effective Hückel-type parameters of benzene and acetylene, and validation of the underlying approximations is performed. Preliminary work to express the dependence of the energy in terms of local nuclear coordinates is performed.

Part II

Conceptual development

The present thesis has two objectives. The first one is to rationalize the exciton transfer in *meta*-PPEs and also serves the second objective, which is to construct a novel diabatic representation for the electronic energies of PPEs with respect to the nuclear coordinates.

With such a diabatic representation, two points are addressed. First, diabatic states ease the chemical interpretation of the variation of the electronic energies between two different geometries. Then, it provides potential energy surfaces that can be used to perform dynamics simulations beyond the Born-Oppenheimer approximation. A diabatic representation for the electronic energies with respect to the nuclear coordinates can also be termed a vibronic (Hamiltonian) model.

The usual method for building a vibronic model is based on a second-order Taylor expansion along the $3N-6$ vibrational modes (N is the number of atoms) and requires to evaluate Hessian matrices. The nanostar counts around 500 atoms, which yield around 1500 nuclear modes, and thus more than a million elements of Hessian matrix to determine[2]. The task is even more formidable considering that there is no way to fully automatize the diabatization procedure.

This is where the interest of our model resides. We identified diabatic states that we describe as resulting from simple interactions between local frontier orbitals thanks to the strong hierarchy existing in PPEs. The hierarchy leads to a simple expression of the total energies (electronic Hamiltonian matrix elements) in terms of the frontier orbitals of the basic units. On the other hand, the locality of the frontier orbitals yields a simplified dependence with respect to a reduced number of local nuclear coordinates.

All together, this enable us to express the total electronic energy (more specifically, each element of the vibronic Hamiltonian matrix) in an unusual and simple way, in the form of a functional of only a few functions, themselves depending on a limited type of nuclear coordinates, see figure 0.3.

[2]The Hessian matrix is symmetric, so $\frac{M(M+1)}{2}$ parameters are required to determine a Hessian matrix of rank M.

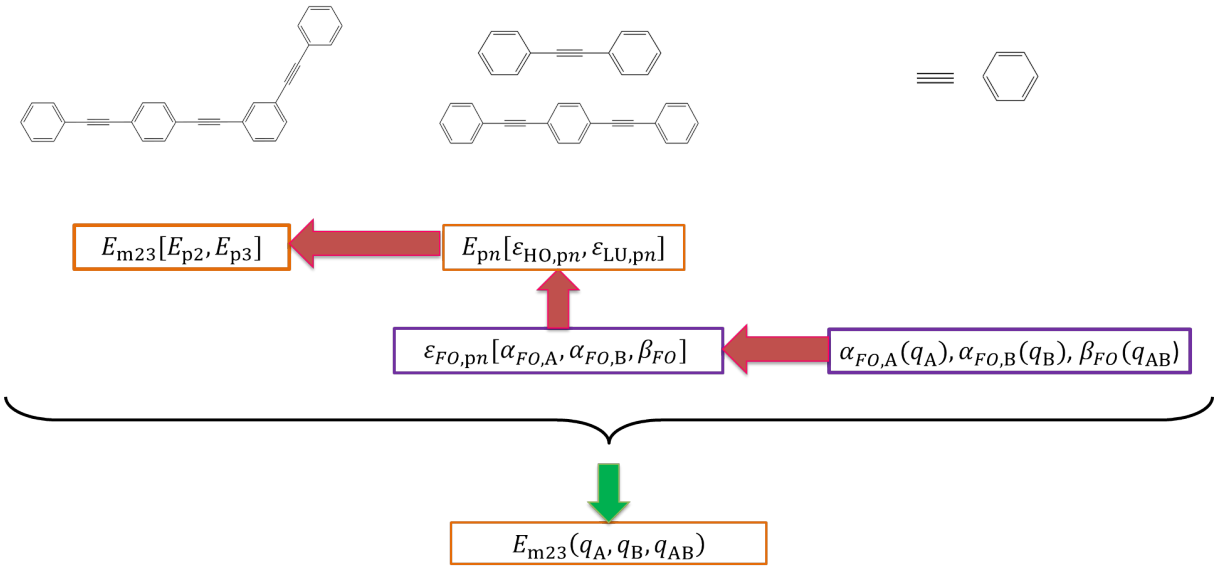

Figure 0.3: Structure of the vibronic model; a reduced number of parameters.

Nomenclature of PPEs

For all aspects presented in this manuscript, we used the following notations for the PPEs.

n-ring *para*-PPE ("*para*" may be omitted) will be named p*n*, where *n* is the number of rings.

We define the building blocks of *meta*-PPEs as the ensembles of rings and acetylenes connected in *para*. The simplest *meta*-PPEs are constituted of two building blocks. For reasons that will be justified later on, a *meta*-phenylene is considered as part of each of two building blocks. As an example, the *meta*-PPE presented in figure 0.4 is constituted of two building blocks, of two and three rings respectively. This will be denoted (2,3)-*meta*-PPE, or m23 for a more compact notation. *Meta*-PPEs constituted of building blocks with different numbers of rings may be termed as "mixed".

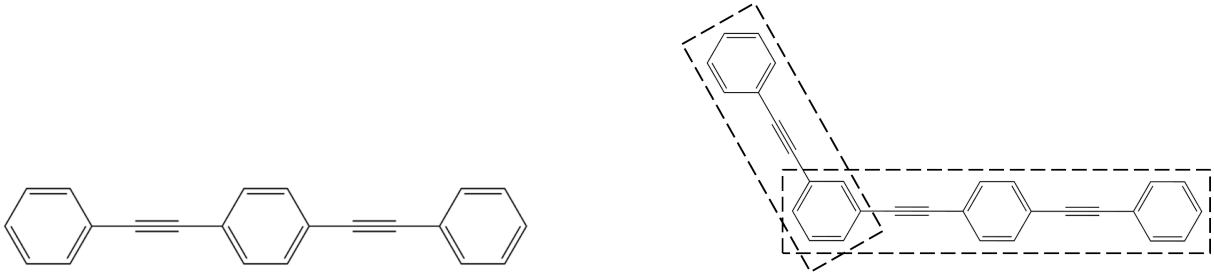

Figure 0.4: 3-ring *para*-PPE named p3 (left) and (2,3)-*meta*-PPE named m23 (right).

If the PPE presents several *meta*-junctions (figure 0.5, the notation still accounts for the number of rings of each building block. It starts from the terminal building block with

the smallest number of rings and goes on along the *meta*-connections. The *meta*-PPE constituted of the succession of 2-,3-, and 4-ring building blocks is thus named (2,3,4)-*meta*-PPE (which is different from (3,2,4)-*meta*-PPE), or m234 in compact notation.

In the case where three building blocks share a common *meta*-phenylene, the "*star*" (or "s") label is used instead of "*meta*" (or "m"); example given: (2,2,2)-*star*-PPE, also named s222.

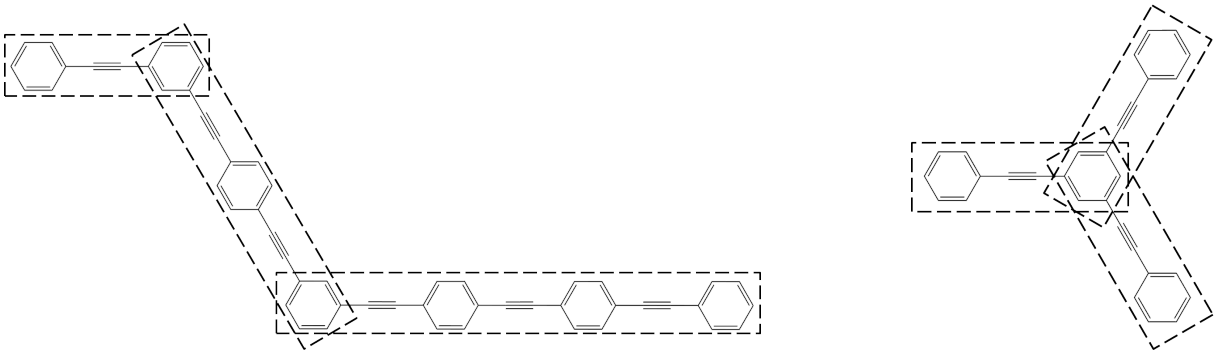

Figure 0.5: (2,3,4)-*meta*-PPE also named m234 (left), and (2,2,2)-*star*- PPE also named s222 (right).

Building blocs sharing a *meta*-phenylene will also be termed *meta*-building blocks.

0.4 A hierarchical system

We prove in Part IV that the electronic structure of the PPEs is highly hierarchical, see figure 0.6. Indeed, the frontier orbitals of the building blocks of a *meta*-PPE correspond to a small pertubation of the frontier orbitals of the corresponding *para*-PPEs. In other words, the interactions between two building blocks coupled in *meta* are perturbative with respect to the interactions inside each building block.

This also stands for the interactions between the rings and the acetylenes inside a building block (a *para*-PPE): the frontier orbitals of benzene and acetylene clearly stand out in the frontier orbital of *para*-PPEs, see figure 0.7 (and thus in the ones of building blocks), meaning that the interactions defining the rings and the acetylenes dominate over the interactions between them.

We rely on this hierarchy to set up a model for expressing electronic energies for the PPEs from the energies of the frontier orbitals of benzene and acetylene. Within this model, we aim to combine the accuracy of TDDFT calculations with the physical interpretation of extended-Hückel (XH) calculations into a new model, providing high-quality energies that can be interpreted in terms of hierarchical interactions.

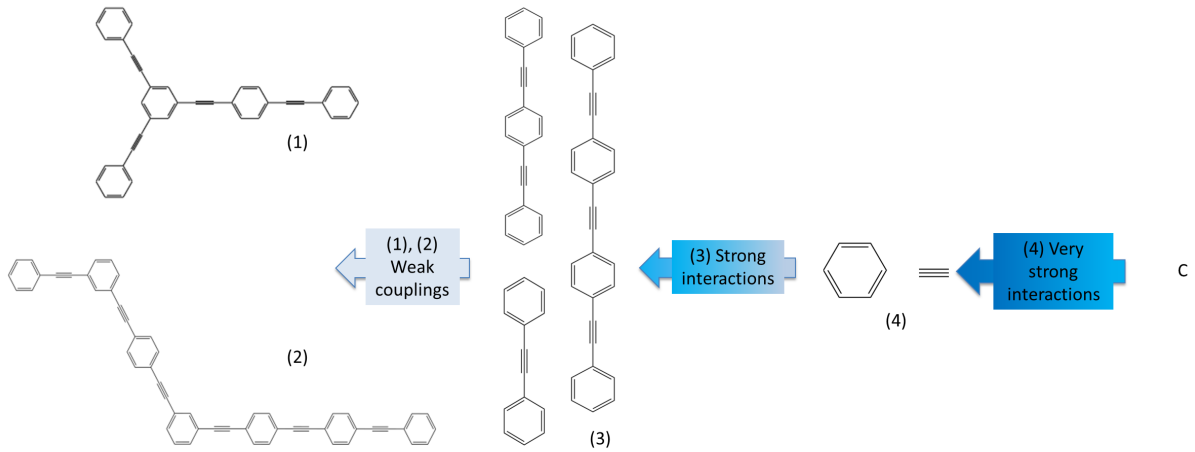

Figure 0.6: Hierarchy in the electronic interactions in *meta*-PPEs.

Figure 0.7: HOMO of tolane (left) and LUMO of tolane (right).

0.5 Multiscale approach

Within this perspective, we build a multiscale vibronic model, the structure of which is inspired by the Hubbard approach, see figure 0.8. We illustrate our approach on the example of m23. In a first step, we do not consider the energy E_0 of the ground state and focus on the description of transition energies ΔE between the ground state and the excited states.

The construction of the model (and of any other model) relies on two different tasks. One consists in chosing the framework within which interactions will be described, that is actual modeling (vertical steps in figure 0.8). The other one consists in ensuring that the model "works" and provides suitable results with respect to a reference, that is fitting (horizontal steps).

The hierarchy in the electronic structure of PPEs is the key that allows the bottom-up construction of the electronic energies based on perturbative interactions. Thanks to this, the description of each interaction can be done separately.

We start by exposing the modeling strategy, which is presented in figure 0.8.

As proved in Part IV, the electronic states of p2 and p3 can be seen as quasi-diabatic

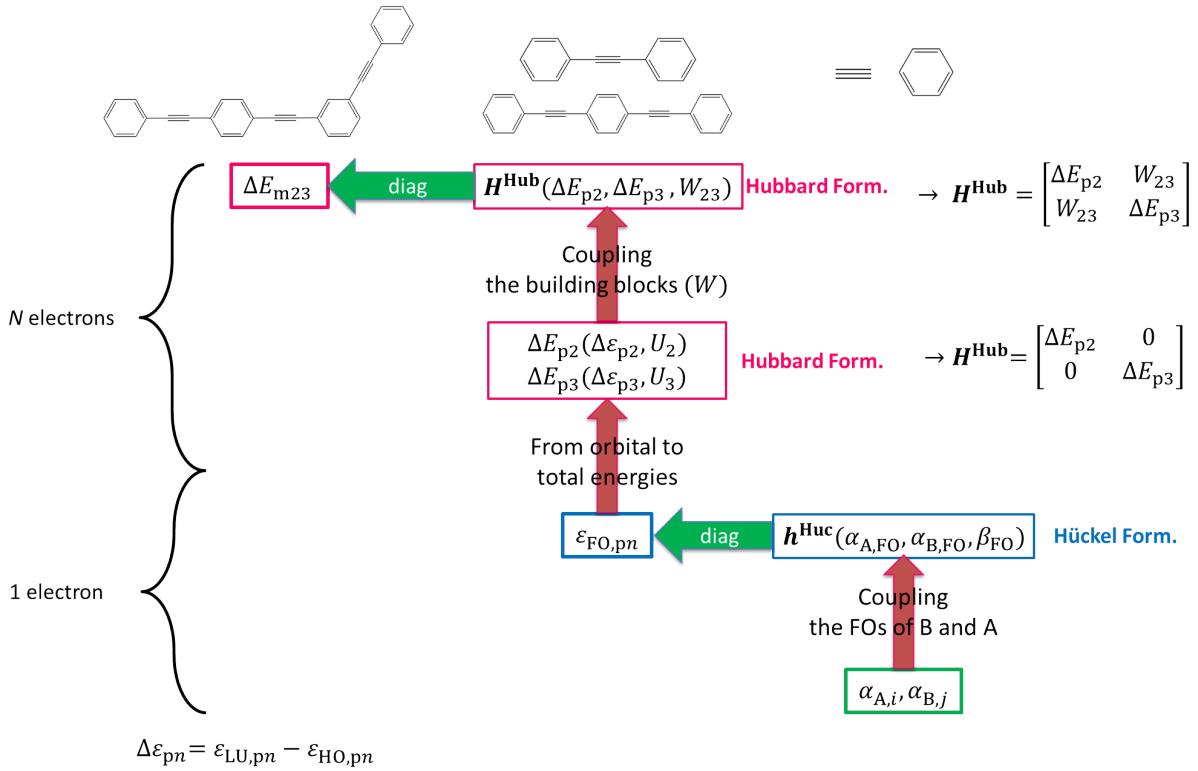

Figure 0.8: Structure of the vibronic model. Decomposition of the transition energy. FO = HO of LU.

states of m23. For this reason, the electronic energies in m23 will be considered as the result of a weak coupling W between the S_1 state of p2 ($|S_1(p_2)\rangle$) and the S_1 state of p3 ($|S_1(p_3)\rangle$).

Thus, the corresponding Hubbard matrix $\boldsymbol{H}^{\mathrm{Hub}}(\boldsymbol{Q})$ in terms of the nuclear coordinates (see figure 0.11) is the representation of the electronic Hamiltonian $\boldsymbol{H}^{\mathrm{el}}(\boldsymbol{Q})$ in the localized basis ($|S_1(p_3)\rangle$,$|S_1(p_2)\rangle$). The latter constitutes a quasi-diabatic basis for m23, while it is the adiabatic basis for p2 and p3 when they do not interact.

The potential coupling W between them has a somewhat similar meaning to the resonance integral β of the Hückel model and to the hopping integral t of the Hubbard model.

Expressing ΔE in terms of $\Delta\varepsilon$ is not trivial at all. Indeed, this step is the bridge between the one-electron problem and the many-electron one, which is basically the central problem of all quantum chemistry methods. To make this bridge, we could brutally set up a mapping from orbital energies to state energies. Doing so, we would basically create another parametrization to get the energy from a given geometry, that is a new semi-empirical method. Yet, this is not what we aim for.

TDDFT energies are assumed to be quantitative (at least in our case, see refer-

ence [63]). On the other hand, in XH methods (and other methods derived from the Hückel theory), the electronic energy is calculated by considering the weak intramolecular interactions arising from the layout of the system. Then, even if the results are not quantitative, they account for the physics of this type of system.

As a matter of fact, we have observed that the energy gap between the frontier orbitals (XH calculations) correlates linearly with the $S_0 - S_1$ transition energy (TDDFT calculations) for various geometries and numbers of rings, see figure 0.9.

This linear correspondance between TDDFT and XH results can thus be interpreted in two ways. First, the evolution of the TDDFT results follows the evolution of the physics of the PPEs, so the TDDFT results do have a physical meaning in our case. Then, it shows that the $S_0 - S_1$ transition energy can be qualitatively (quantitatively up to a mapping) reduced to the gap between the two frontier orbitals provided by XH calculations.

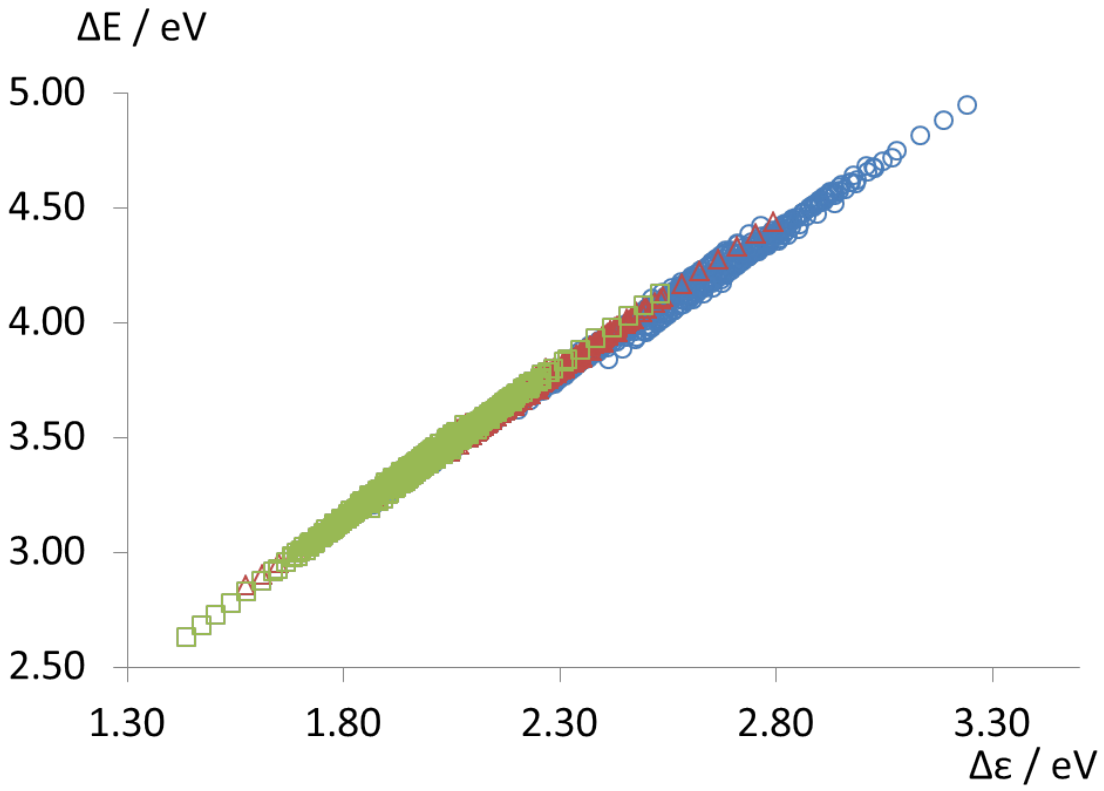

Figure 0.9: Transition energy ΔE (TDDFT) between S_0 and S_1 as a function of the gap $\Delta\varepsilon$ (XH) between the frontier orbitals of the 2- (blue), 3- (red), and 4- (green) ring *para*-PPEs.

Now, the transitions between the frontier orbitals of *para*-PPEs are representative of the S_0–S_1 transition, so we express the transition energy between the electronic states ΔE in terms of the energy required to promote one electron from the HO to the LU, see

figure 0.10. In the frame of the Hubbard model, the energies of the ground state and first excited state read

$$E_0 = 2\varepsilon_{\mathrm{HO}} + U \tag{1}$$

$$E_1 = \varepsilon_{\mathrm{HO}} + \varepsilon_{\mathrm{LU}} \tag{2}$$

where $U > 0$ is the electronic repulsion between two electrons in the HOMO. Then the transition energy reads

$$\Delta E = \Delta\varepsilon - U \tag{3}$$

where $\Delta\varepsilon = \varepsilon_{LU} - \varepsilon_{HO}$ is the energy difference between the frontier orbitals.

We only consider the repulsion between two eletrons in the same orbital and neglect the

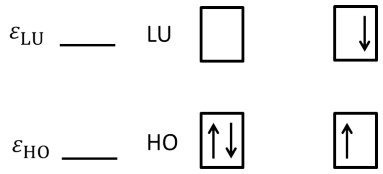

Figure 0.10: Representation of the electronic configurations associated with the ground state (left) and first excited state (right) from an excitonic point of view.

one between two electrons in different orbitals.

Finally, the energies $\varepsilon_{FO,\mathrm{p}n}$ (FO = HO, LU) of the frontier orbitals of the *para*-PPEs are expressed in terms of effective energies of the frontier orbitals of benzene and acetylene ($\alpha_{FO,\mathrm{B}}$ and $\alpha_{FO,\mathrm{A}}$) within the framework of a Hückel-type model with fragment sites. This will be fully exposed in the next chapter. We consider the energies of the orbitals of benzene (B) and acetylene (A) provided by extended-Hückel calculations.

To ensure the validity of the model, reference energy values are used along the bottom-up construction. We start the actual construction of the model with the molecular orbitals of benzene and acetylene, whose energies are calculated at the extended-Hückel level and constitute our reference. The model energies $\varepsilon_{FO,\mathrm{p}n}$ (FO = HO, LU) of the frontier orbitals of the *para*-PPEs are fitted to extended-Hückel values $\varepsilon^{\mathrm{ref}}_{FO,\mathrm{p}n}$. The model transition energies for the electronic excited states $\Delta E_{\mathrm{p}n}$ are fitted using TDDFT values as targets $\Delta E^{\mathrm{ref}}_{\mathrm{p}n}$ (figure 0.11).

This strategy can be applied to any *meta*-PPE considering the relevant building blocks, as will be derived in the last part of the manuscript.

In principle, such a strategy should be relevant for any photoactive supramolecule built from the repetition of basic units.

0.6 Methodological relevance

0.6.1 A smart decomposition of the energy

In quantum chemistry, the Coulomb potentials are fully defined for a set of charged particles at given positions.

In contrast, the practical difficulty of quantum dynamics is that the effective potential acting on the nuclei depends on the system and is unknown. Then, for a given system, fitting is the only way to access the PES without computing the energy at each useful point, which is neither possible, nor wanted, especially for large systems[3]. Yet, fitting is a formidable task on its own, which was not our objective here.

This drawback is tremendously reduced in molecular dynamics thanks to the use of force fields (most often based on molecular mechanics) that are supposed to be transferable. The universality of force fields comes from the fact that they decompose the energy into individual and universal contributions (spring forces, interactions between charges, dipole moments, etc.), which are eventually summed up according to the geometry of the system to be studied.

The key-points of our model are that, (i) as a function of the nuclear position that interpolates the energy, the PES can also be interpreted as an internal potential field, (ii) PPEs are quite similar to conjugated polyenes, so the same physical principles should apply to both. Then, Hückel-type models provide us with the tools to decompose the electronic energy into universal contributions, thus enabling the model we propose to be transferable, at least in principle.

Finally, this novel vibronic model is a smart decomposition of the electronic energy in terms of orbital energies, orbital occupations, and repulsion terms, which can thus be

[3]This is even worse considering non-adiabatic or diabatic representations since they cannot be accessed straightfowardly.

physically interpreted, as opposed to the commonly used Taylor expansions. Each fitted parametrization performed can be rationalized according to those terms.

0.6.2 A simplified expression for the electronic energy

Let us now analyze how this decomposition allows to simplify the expression of the total energy in terms of the nuclear coordinates. A schematic representation is presented in figure 0.11.

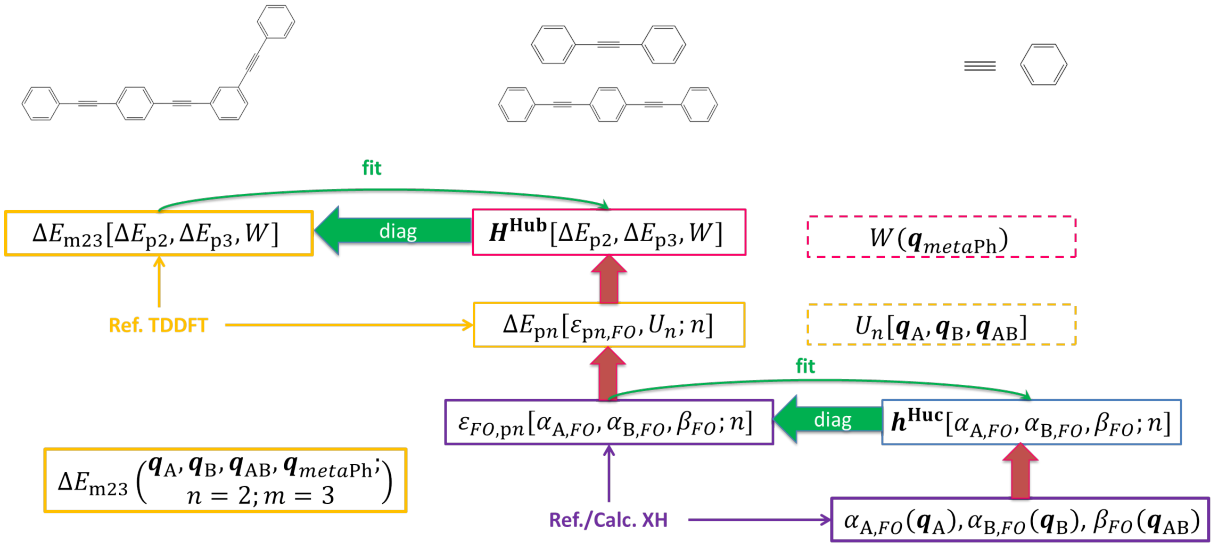

Figure 0.11: Structure of our vibronic model. Dependence with the nuclear coordinates.

The energies of the frontier orbitals $\varepsilon_{FO,n}$ (FO = HO or LU) of the *para*-PPEs are considered as functionals of the energies α of the frontier orbitals of benzene and acetylene, and the resonance integral β; it also depends parametrically on the number of rings n: $\varepsilon_{FO}\left[\alpha_{\mathrm{B},FO}, \alpha_{\mathrm{A},FO}, \beta_{FO}; n\right]$. Those parameters depend in turn on the nuclear coordinates of benzene ($\alpha_{\mathrm{B},FO}(\boldsymbol{q}_{\mathrm{B}})$), acetylene ($\alpha_{\mathrm{A},FO}(\boldsymbol{q}_{\mathrm{A}})$), and on the distance between adjacent benzene and acetylene ($\beta_{FO}(\boldsymbol{q}_{\mathrm{AB}})$), respectively. We ignore the out-of-plane motions in this work. Hence

$$\varepsilon_{FO,n}\left[\alpha_{\mathrm{B},FO}(\boldsymbol{q}_{\mathrm{B}}), \alpha_{\mathrm{A},FO}(\boldsymbol{q}_{\mathrm{A}}), \beta_{FO}(\boldsymbol{q}_{\mathrm{AB}}); n\right] = \varepsilon_{FO}\left(\boldsymbol{q}_{\mathrm{B}}, \boldsymbol{q}_{\mathrm{A}}, \boldsymbol{q}_{\mathrm{AB}}; n\right) \tag{4}$$

and

$$\Delta\varepsilon_{n}\left[\alpha_{\mathrm{B},FO}(\boldsymbol{q}_{\mathrm{B}}), \alpha_{\mathrm{A},FO}(\boldsymbol{q}_{\mathrm{A}}), \beta_{FO}(\boldsymbol{q}_{\mathrm{AB}}); n\right] = \Delta\varepsilon_{n}\left(\boldsymbol{q}_{\mathrm{B}}, \boldsymbol{q}_{\mathrm{A}}, \boldsymbol{q}_{\mathrm{AB}}; n\right) \ . \tag{5}$$

The expression of U is not trivial and will be discussed in the last part of this manuscript. For now, it may depend on any of the local nuclear coodinates $\boldsymbol{q}_{\mathrm{B}}$, $\boldsymbol{q}_{\mathrm{A}}$, and $\boldsymbol{q}_{\mathrm{AB}}$, and parametrically on n: $U = U_n(\boldsymbol{q}_{\mathrm{B}}, \boldsymbol{q}_{\mathrm{A}}, \boldsymbol{q}_{\mathrm{AB}})$.

We express the transition energy $\Delta E_{\mathrm{p}n}$ in pn in terms of $\Delta\varepsilon$ and U. Thus, they are also functionals of the parameters $\alpha_{\mathrm{B},FO}(\boldsymbol{q}_{\mathrm{B}})$, $\alpha_{\mathrm{A},FO}(\boldsymbol{q}_{\mathrm{A}})$ and $\beta_{FO}(\boldsymbol{q}_{\mathrm{AB}})$. Considering equation 5, this leads to

$$\Delta E_{\mathrm{p}n}\left[\Delta\varepsilon_n, U_n\right] = \Delta E_{\mathrm{p}n}\left[\alpha_{\mathrm{B},FO}(\boldsymbol{q}_{\mathrm{B}}), \alpha_{\mathrm{A},FO}(\boldsymbol{q}_{\mathrm{A}}), \beta_{FO}(\boldsymbol{q}_{\mathrm{AB}}); n\right] \tag{6}$$

$$= \Delta E_{\mathrm{p}n}\left(\boldsymbol{q}_{\mathrm{B}}, \boldsymbol{q}_{\mathrm{A}}, \boldsymbol{q}_{\mathrm{AB}}; n\right) \tag{7}$$

Finally, we express the energies of S_1 and S_2 in the *meta*-PPE mkl ($k \neq l$) in terms of the energies of S_1 in pk and pl and the coupling W between the building blocks. Considering the local character of S_1 and S_2, their energies only depend on nuclear coordinates associated to the l- ($\boldsymbol{q}_{\mathrm{p}l}$) and k- ($\boldsymbol{q}_{\mathrm{p}k}$) ring building blocks, respectively. Also, we consider that the coupling between S_1 and S_2 is mediated through the *meta*-phenylene, so the coupling W depends on its internal nuclear coordinates $\boldsymbol{q}_{meta\text{-}\mathrm{Ph}}$, hence

$$\Delta E_{\mathrm{m}kl} = \Delta E_{\mathrm{m}kl}\left[\Delta E_{\mathrm{p}k}(\boldsymbol{q}_{\mathrm{p}k}), \Delta E_{\mathrm{p}l}(\boldsymbol{q}_{\mathrm{p}l}), W(\boldsymbol{q}_{meta\mathrm{Ph}})\right] \ . \tag{8}$$

Combining equations 7 and 8 reveals the possibility to express the electronic energy in terms of a few type of local nuclear coordinates.

$$\Delta E_{\mathrm{m}kl} = \Delta E_{\mathrm{m}kl}\left(\{\boldsymbol{q}_{\mathrm{B}}, \boldsymbol{q}_{\mathrm{A}}, \boldsymbol{q}_{\mathrm{AB}}; k\}_k, \{\boldsymbol{q}_{\mathrm{B}}, \boldsymbol{q}_{\mathrm{A}}, \boldsymbol{q}_{\mathrm{AB}}; l\}_l, \boldsymbol{q}_{meta\mathrm{Ph}}\right) \tag{9}$$

$$= \Delta E_{\mathrm{m}kl}\left(\boldsymbol{q}^k_{\mathrm{B}}, \boldsymbol{q}^k_{\mathrm{A}}, \boldsymbol{q}^k_{\mathrm{AB}}, \boldsymbol{q}^l_{\mathrm{B}}, \boldsymbol{q}^l_{\mathrm{A}}, \boldsymbol{q}^l_{\mathrm{AB}}, \boldsymbol{q}_{meta\mathrm{Ph}}; k; l\right) \tag{10}$$

This equation highlights the fact that our vibronic models can provide an expression for the electronic energy involving only the local nuclear coordinates and two indices, for any *meta*-PPE constituted of two building blocks.

It is important to note that within this framework, the expression of $\Delta E_{\mathrm{m}kl}$ depends on all the local nuclear coordinates, that is $4n - 3$ modes on each n-ring building block plus $\boldsymbol{q}_{meta\mathrm{Ph}}$. This is a first simplification with respect to considering all the nuclear modes of the molecule. By providing expressions of the Hückel parameters in terms of the local coordinates $\alpha_i(\boldsymbol{q}_i)$, we do not reduce the number of variables $\boldsymbol{q}_i$ or their accessible values. But since $\alpha_i(\boldsymbol{q}_i)$ is determined and can be repeated as many times as necessary, we reduce the actual number of parameters on which the models depends. This constitutes a tremendous simplification compared with the usual Taylor expansions.

In principle, only one parameter j and one set of local coordinates $\left\{\boldsymbol{q}^{j}_{\mathrm{B}}, \boldsymbol{q}^{j}_{\mathrm{A}}, \boldsymbol{q}^{j}_{\mathrm{AB}}, \boldsymbol{q}^{lj}_{meta\mathrm{Ph}}\right\}$ must be added for each extra *meta*-junction PPEs, that correspond to the number of rings of the extra building block and the collective nuclear mode over its common *meta*-phenylene, see figure 0.12.

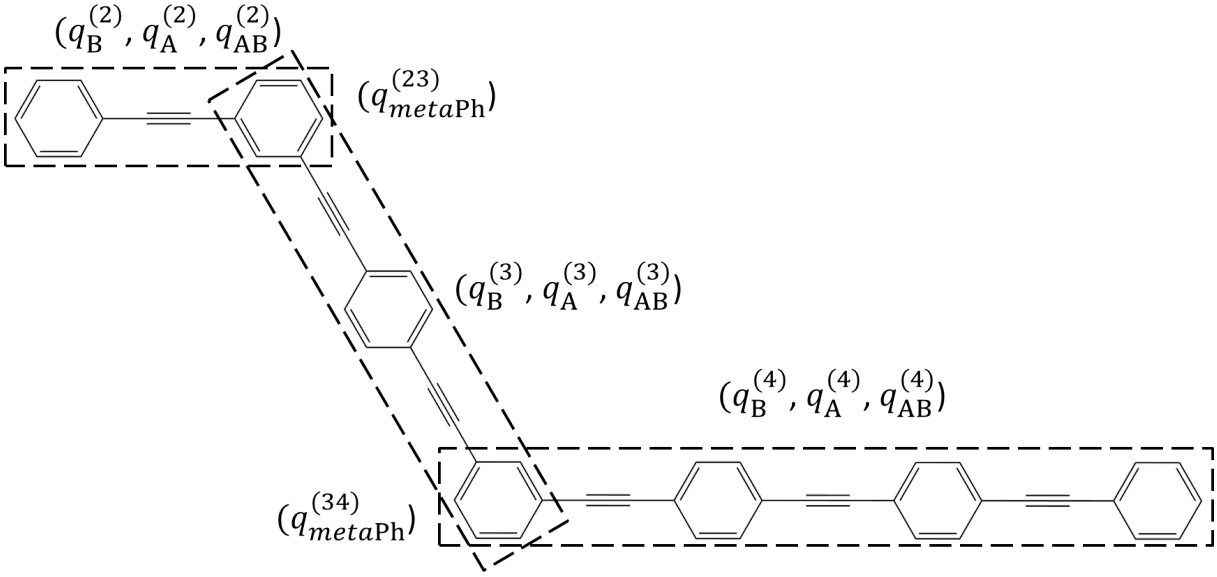

Figure 0.12: Sets of local nuclear coordinates to consider for m234 in the vibronic model.

0.7 Conclusion

In this thesis manuscript, we present the work that was achieved to characterize the PPEs (Part IV), and which justifies the energetical decomposition of *meta*-PPEs at several levels. The data collected during this characterization have then been used for the construction of the vibronic model (Part V).

The construction of some steps of the model is still in progress, but the results presented here are promising.

Part III

Theory

The essential concepts (first two chapters) and methods (last three chapters) that were used along this thesis are recalled in the present part.

One of the two objectives of this project is the description of the electronic excitation transfers in PPEs. According to the literature [42, 49], such processes correspond to a sequence of internal conversions mediated through conical intersections (see chapter 2).

Conical intersections are specific points of contact between potential energy surfaces. Their effect on the molecular dynamics cannot be described correctly within the frame of the adiabatic approximation. Indeed, in the vicinity of conical intersections, the couplings between the electronic and nuclear motions (non-adiabatic couplings) are too strong to be neglected, which yields non-adiabatic processes.

Chapter 1 introduces the general formalism associated with the description of non-adiabatic processes, and recalls the essential concepts and possible approximations. Chapter 2 is dedicated to the representation of conical intersections.

The electronic structure (ground state and first few excited states) and vibrations of PPEs containing up to 54 carbon atoms were studied in detail. To do so, DFT and TDDFT calculations were performed, as the best compromise between accuracy and computational cost for such large systems. Generalities about those computational methods are presented in chapters 3 and 4.

The second objective of this project is the construction of a vibronic model for the electronic energies of PPEs. Along this construction, and because PPEs present a conjugated π-system, the interactions we must account for (correlation, exchange, Coulomb) are essentially governed by π-orbital overlap. Thus, effective orbital-based models derived from the Hückel formalism are expected to be relevant. We recall the formalisms on which our model will rely in chapter 5.

Chapter 1

General formalism

The essential references for this chapter are: [64–70].

The wavefunctions that are the solutions of the molecular Schrödinger equation depend on both the electronic and nuclear coordinates. In most cases, the typical energy and time scales of electrons (light particles) and nuclei (heavy particles) differ by a few orders of magnitude. It is thus often valid to consider that the electronic states adjust instantaneoulsy to the nuclear motion, which is the adiabatic approximation.

The full problem is then treated in two steps: first, the resolution of the electronic Schrödinger equation with fixed nuclei (quantum chemistry); second, the resolution of the Schrödinger equation for the nuclei in the mean field of the electrons (quantum dynamics), which may be achieved within the framework of the (adiabatic) Born-Oppenheimer approximation. Beyond the adiabatic approximation, the nuclear motion actually induces non-adiabatic couplings (also called vibronic couplings) between the electronic states. The two-step resolution must then be generalized upon taking those non-adiabatic couplings into account. Thereafter, we focus on singlet electronic states, except when explicitly mentioned.

1.1 The molecular Hamiltonian

The investigations carried out within the present thesis exclude relativistic effects. We define $\boldsymbol{R} = (\boldsymbol{R}_1, ..., \boldsymbol{R}_N)$ and $\boldsymbol{r} = (\boldsymbol{r}_1, ..., \boldsymbol{r}_n)$, the nuclear coordinates of the N nuclei and n electrons within a molecular system, respectively. The corresponding molecular

Hamiltonian is defined as

$$\hat{H}^{\mathrm{mol}}(\boldsymbol{r},\boldsymbol{R}) = \hat{T}^{\mathrm{n}}(\boldsymbol{R}) + \hat{T}^{\mathrm{el}}(\boldsymbol{r}) + \hat{V}^{\mathrm{nn}}(\boldsymbol{R}) + \hat{V}^{\mathrm{ee}}(\boldsymbol{r}) + \hat{V}^{\mathrm{ne}}(\boldsymbol{r},\boldsymbol{R}) \tag{1.1}$$

with

$\hat{T}^{\mathrm{n}}(\boldsymbol{R})$: the nuclear kinetic energy operator;

$\hat{T}^{\mathrm{el}}(\boldsymbol{r})$: the electronic kinetic energy operator;

$\hat{V}^{\mathrm{nn}}(\boldsymbol{R})$: the electrostatic potential between the nuclei;

$\hat{V}^{\mathrm{ee}}(\boldsymbol{r})$: the electrostatic potential between the electrons;

$\hat{V}^{\mathrm{ne}}(\boldsymbol{R},\boldsymbol{r})$: the electrostatic potential between the nuclei and the electrons.

The corresponding time-independent Schrödinger equation reads

$$\hat{H}^{\mathrm{mol}}(\boldsymbol{r},\boldsymbol{R})\Psi_i^{\mathrm{mol}}(\boldsymbol{r},\boldsymbol{R}) = E_i^{\mathrm{mol}}\Psi_i^{\mathrm{mol}}(\boldsymbol{r},\boldsymbol{R}) \tag{1.2}$$

where the eigenvalue E_i^{mol} is the energy associated with the i^{th} eigenvector Ψ_i^{mol}. The couples (Ψ_i^{mol},E_i^{mol}) are the stationary solutions of the following time-dependent Schrödinger equation:

$$\hat{H}^{\mathrm{mol}}(\boldsymbol{r},\boldsymbol{R},t)\Psi^{\mathrm{mol}}(\boldsymbol{r},\boldsymbol{R},t) = \mathrm{i}\hbar\frac{\partial}{\partial t}\Psi^{\mathrm{mol}}(\boldsymbol{r},\boldsymbol{R},t) \tag{1.3}$$

The non-stationary solutions can be decomposed over the basis of the stationary eigenvectors:

$$\Psi^{\mathrm{mol}}(\boldsymbol{r},\boldsymbol{R},t) = \sum_i c_i(t)\Psi_i^{\mathrm{mol}}(\boldsymbol{r},\boldsymbol{R}) \tag{1.4}$$

where the time-dependence is contained in the expansion coefficients.

1.2 Separation of the molecular Hamiltonian

1.2.1 The electronic problem

The resolution of the full Schrödinger equation 1.2, for many-body systems can only be achieved numerically.

In most situations, it is legitimate to consider that the electrons move much faster than the nuclei (due to the ratio of their masses). This leads to the following approximate

picture: (i) The electrons can be viewed as evolving in the field created by the fixed nuclei; (ii) Should the nuclei move, the electrons would respond/relax instantly, that is that the electronic structure adiabatically follows the nuclear motion. This is called the adiabatic or Born-Oppenheimer approximation (discussed later on). We will show first that such a description still provides a convenient starting point for a more general description, even beyond the adiabatic approximation.

As mentioned in the introduction, the first step to solve the time-independent equation 1.2 consists in dealing with the electronic part, independently of the nuclear motion. The electronic Hamiltonian $\hat{H}^{\mathrm{el}}$ is thus defined by removing the nuclear kinetic energy $\hat{T}^{\mathrm{n}}$:

$$\hat{H}^{\mathrm{el}}(\boldsymbol{r};\boldsymbol{R}) = \hat{T}^{\mathrm{el}}(\boldsymbol{r}) + \hat{V}^{\mathrm{nn}}(\boldsymbol{R}) + \hat{V}^{\mathrm{ee}}(\boldsymbol{r}) + \hat{V}^{\mathrm{ne}}(\boldsymbol{r},\boldsymbol{R}) \tag{1.5}$$

$$\hat{H}^{\mathrm{mol}}(\boldsymbol{r},\boldsymbol{R}) = \hat{T}^{\mathrm{n}}(\boldsymbol{R}) + \hat{H}^{\mathrm{el}}(\boldsymbol{r};\boldsymbol{R}) \tag{1.6}$$

and the corresponding electronic time-independent Schrödinger equation reads[1]

$$\hat{H}^{\mathrm{el}}(\boldsymbol{r};\boldsymbol{R})\phi_\alpha^{\mathrm{el}}(\boldsymbol{r};\boldsymbol{R}) = E_\alpha^{\mathrm{el}}(\boldsymbol{R})\phi_\alpha^{\mathrm{el}}(\boldsymbol{r};\boldsymbol{R}) \ . \tag{1.7}$$

The eigenvectors $\phi_\alpha^{\mathrm{el}}(\boldsymbol{r};\boldsymbol{R})$ are the adiabatic electronic states of the system. As well as the electronic Hamiltonian, they characterize the electronic structure at a given nuclear geometry $\boldsymbol{R}$ (often termed "fixed nuclei" Hamiltonian). Thus, the Hamiltonian and the eigenvectors depend explicitly on the electronic coordinates $\boldsymbol{r}$ and parametrically on the nuclear coordinates $\boldsymbol{R}$. One can note that the energy $E_\alpha^{\mathrm{el}}(\boldsymbol{R})$ (or eigenvalue) associated with an electronic state also depends parametrically on the nuclear coordinates.

As they are solutions of an eigenvalue problem, the adiabatic states form a complete orthonormal basis set $\left\{\phi_\alpha^{\mathrm{el}}(\boldsymbol{r};\boldsymbol{R})\right\}_\alpha$ (see equation 1.8).

$$\forall \boldsymbol{R}, \qquad \begin{aligned} \langle \phi_\alpha^{\mathrm{el}};\boldsymbol{R}|\phi_\beta^{\mathrm{el}};\boldsymbol{R}\rangle &= \delta_{\alpha\beta} \\ \sum_\alpha |\phi_\alpha^{\mathrm{el}};\boldsymbol{R}\rangle\langle\phi_\beta^{\mathrm{el}};\boldsymbol{R}| &= \hat{1} \end{aligned} \tag{1.8}$$

Quantum chemistry methods are designed to solve the electronic Schrödinger equation 1.7 (with further approximations), and thus to compute the electronic states and their energies (along with other properties) for a chosen geometry of the system. This procedure has to be repeated for each geometry that has to be considered.

[1] In this notation, the operator and its eigenvectors depend parametrically on the variables written after the symbol ";" (here the nuclear coordinates $\boldsymbol{R}$).

1.2.2 The adiabatic expansion

To solve the time-dependent Schrödinger equation, the total wavefunction Ψ_{mol} can be conveniently expanded over the basis of the adiabatic states, which are now assumed to be known

$$\forall \boldsymbol{R}, \begin{cases} \Psi^{\text{mol}}(\boldsymbol{r}, \boldsymbol{R}, t) = \sum_\alpha \chi^{\text{n}}_\alpha(\boldsymbol{R}, t)\phi^{\text{el}}_\alpha(\boldsymbol{r}; \boldsymbol{R}) \\ \chi^{\text{n}}_\alpha(\boldsymbol{R}, t) = \left\langle \phi^{\text{el}}_\alpha; \boldsymbol{R} | \Psi^{\text{mol}}(\boldsymbol{R}, t) \right\rangle \end{cases} \tag{1.9}$$

where we use Dirac's bracket notation for the electronic coordinates $\boldsymbol{r}$ only.

This constitutes the Born or adiabatic expansion. One of the interests of this formulation is that the total wavefunction is expanded on a set of well-defined stationary functions (electronic part), and the time-dependence only appears in the expansion coefficients, which constitute the nuclear part.

Considering the basis of the adiabatic states, the electronic degrees of freedom are attached to α, which is discrete, instead of $\boldsymbol{r}$, which is continuous. In contrast, the nuclear degrees of freedom are attached to the continuous coordinate $\boldsymbol{R}$ in this representation.

The expansion 1.9 provides an ansatz for solving the full Schrödinger equation 1.3 (see below). It is exact as long as the $\left\{\phi^{\text{el}}_\alpha(\boldsymbol{r}; \boldsymbol{R})\right\}_\alpha$ basis set is complete, but becomes an approximation as soon as the basis is truncated. In particular, under the Born-Oppenheimer approximation the basis is reduced to only one electronic state (usually the ground-state); for descriptions beyond the Born-Oppenheimer approximation, the basis set is usually limited to a subset of strongly interacting electronic states (this is sometimes referred to as the bloc- or group-Born-Oppenheimer approximation).

1.2.3 Non-adiabatic couplings (NACs)

As mentioned in introduction, the nuclear motion may induce couplings between electronic states. Such couplings cause the involved electronic states to influence each other response to the nuclear motion. Since one can no longer consider that a single electronic state follows adiabatically the nuclear motion, these couplings are termed "non-adiabatic".

Let $\Psi^{\text{mol}}(\boldsymbol{r}, \boldsymbol{R}, t)$ describe a solution of equation 1.3. Separating the molecular Hamil-

tonian (equation 1.1) and using the Born expansion 1.9, equation 1.3 becomes

$$\left[\hat{T}^{\mathrm{n}}(\boldsymbol{R}) + \hat{H}^{\mathrm{el}}(\boldsymbol{R})\right] \sum_{\beta} \chi^{\mathrm{n}}_{\beta}(\boldsymbol{R}, t)|\phi^{\mathrm{el}}_{\beta}; \boldsymbol{R}\rangle = \mathrm{i}\hbar \frac{\partial}{\partial t} \sum_{\beta} \chi^{\mathrm{n}}_{\beta}(\boldsymbol{R}, t)|\phi^{\mathrm{el}}_{\beta}; (\boldsymbol{R})\rangle$$

where the dependence of $\hat{H}^{\mathrm{el}}(\boldsymbol{R})$ with $\boldsymbol{r}$ is now implicit according to the ket representation for the electronic part.

We consider the expression 3.10 for the nuclear kinetic energy operator[2].

$$\hat{T}^{\mathrm{n}}(\boldsymbol{R}) = -\frac{\hbar^2}{2} \sum_{K} \frac{1}{M_K} \Delta_K \tag{1.10}$$

After projection on an adiabatic state $\phi^{\mathrm{el}}_{\alpha}(\boldsymbol{r}; \boldsymbol{R})$ and integration over the electronic coordinates $\boldsymbol{r}$, the previous equation can be recast as

$$\sum_{\beta} \left[\delta_{\alpha\beta} \left(\hat{T}^{\mathrm{n}}(\boldsymbol{R}) + E^{\mathrm{el}}_{\alpha}(\boldsymbol{R})\right) + \hbar^2 \hat{\Lambda}_{\alpha\beta}(\boldsymbol{R})\right] \chi^{\mathrm{n}}_{\beta}(\boldsymbol{R}, t) = \mathrm{i}\hbar \frac{\partial}{\partial t} \chi^{\mathrm{n}}_{\alpha}(\boldsymbol{R}, t) \tag{1.11}$$

By definition, the non-adiabatic coupling operators $\hat{\Lambda}_{\alpha\beta}(\boldsymbol{R})$ result from the action of the kinetic energy operator of the nuclei on the adiabatic electronic states. With respect to the gradient operator $\boldsymbol{\nabla}_K$, this action leads to first order terms, also called "derivative couplings", and of second order terms, also called "scalar couplings".

$$\hat{\Lambda}_{\alpha\beta}(\boldsymbol{R}) = -\sum_{K} \left(\frac{1}{M_K} \boldsymbol{D}^K_{\alpha\beta}(\boldsymbol{R}) \cdot \boldsymbol{\nabla}_K + \frac{1}{2M_K} C^K_{\alpha\beta}(\boldsymbol{R})\right) \tag{1.12}$$

where the derivative couplings read

$$\boldsymbol{D}^K_{\alpha\beta}(\boldsymbol{R}) = \langle \phi^{\mathrm{el}}_{\alpha}; \boldsymbol{R} | \boldsymbol{\nabla}_K \phi^{\mathrm{el}}_{\beta}; \boldsymbol{R}\rangle \tag{1.13}$$

and the scalar couplings read

$$C^K_{\alpha\beta}(\boldsymbol{R}) = \langle \phi^{\mathrm{el}}_{\alpha}; \boldsymbol{R} | \Delta_K \phi^{\mathrm{el}}_{\beta}; \boldsymbol{R}\rangle \ . \tag{1.14}$$

Inserting the closure relationship into the divergence of the derivative couplings allows to express the scalar couplings in terms of the derivative ones

$$C^K_{\alpha\beta}(\boldsymbol{R}) = \boldsymbol{\nabla}_K \cdot \boldsymbol{D}^K_{\alpha\beta}(\boldsymbol{R}) + \sum_{\gamma} \boldsymbol{D}^K_{\alpha\gamma}(\boldsymbol{R}) \cdot \boldsymbol{D}^K_{\gamma\beta}(\boldsymbol{R}) \ . \tag{1.15}$$

[2]We use simplified notations for the differentiation operators: $\Delta_K \equiv \Delta_{\boldsymbol{R}_K}$ and $\boldsymbol{\nabla}_K \equiv \boldsymbol{\nabla}_{\boldsymbol{R}_K}$, where $\boldsymbol{R}_K$ is the K^{th} component of the collective nuclear coordinate $\boldsymbol{R}$. M_K denote the corresponding nuclear mass.

When two electronic states are near degenerate, the corresponding nuclear wavefunctions obey coupled equations and are no longer independent, which corresponds to large values of the NACs. This appears formally in the off-diagonal Hellmann-Feynman theorem [71, 72], which gives another expression for the derivative couplings

$$\boldsymbol{D}^K_{\alpha\beta}(\boldsymbol{R}) = \frac{\langle \phi^{\mathrm{el}}_\alpha; \boldsymbol{R} | \boldsymbol{\nabla}_K \hat{H}^{\mathrm{el}}(\boldsymbol{R}) | \phi^{\mathrm{el}}_\beta; \boldsymbol{R} \rangle}{E^{\mathrm{el}}_\beta(\boldsymbol{R}) - E^{\mathrm{el}}_\alpha(\boldsymbol{R})} \ . \tag{1.16}$$

The amplitude of the non-adiabatic couplings (NACs) increases as the energy difference decreases, until they diverge when the electronic states are degenerate, namely at conical intersections. Those strong couplings around conical intersections reflect a strong interdependence between the electronic and vibrational motions. Thanks to these, electronic excitation energy may be transfered through vibrational modes, allowing the system to change its electronic state without light emission, on timescales usually less than a picosecond.

1.3 Born-Oppenheimer approximation

The Born-Oppenheimer approximation is equivalent as neglecting the non-adiabatic couplings $\hat{\Lambda}_{\alpha\beta}$ in the molecular Hamiltonian. Since their amplitude is inversely proportional to the masses of the nuclei (see above), which are heavy particles, the approximation is reasonable in most cases.

Doing so, equation 1.11 reveals the Schrödinger equation for the nuclei and the nuclear Hamiltonian $\hat{H}^{\mathrm{n}}_\alpha(\boldsymbol{R})$ for each electronic state

$$\hat{H}^{\mathrm{n}}_\alpha(\boldsymbol{R}) \chi^{\mathrm{n}}_\alpha(\boldsymbol{R}, t) = \mathrm{i}\hbar \frac{\partial}{\partial t} \chi^{\mathrm{n}}_\alpha(\boldsymbol{R}, t) \tag{1.17}$$

$$\hat{H}^{\mathrm{n}}_\alpha(\boldsymbol{R}) = \hat{T}^{\mathrm{n}}(\boldsymbol{R}) + E^{\mathrm{el}}_\alpha(\boldsymbol{R}) \tag{1.18}$$

The nuclear wavefunctions (vibrational states) are determined by the potential part of the Hamiltonian, which is actually the energy of the corresponding adiabatic states. Then, nuclear wavefunctions on different electronic states are not coupled, and we are back to electrons adjusting instantaneously to the nuclear motion while the nuclei move in the adiabatic potential created by a single electronic state (principle of the PESs).

This is reasonable only as long as the electronic states involved in the study are energetically different enough, which is usually the case for ground-state reactivity. Unfortunately, the approximation is no longer valid when the electronic states get close in energy, which is the case around conical intersections, as already pointed out. Thus, the description of conical intersections is a typical beyond-Born-Oppenheimer problem.

1.4 One-electron approximation

Let us come back to the electronic problem. We now consider the "fixed nuclei" Hamiltonian and present the so-called one-electron approximation, which is the fondation of most methods in quantum chemistry, from the semi-empirical ones (derived from the Hückel model) to *ab initio* wavefunction and DFT methods.

As mentioned above, the electronic Schrödinger equation can be solved exactly only for one electron and one nucleus, which yields the so-called hydrogenoid orbitals. The orbitals of a polyelectronic atom or of a molecule are derived from the one-electron (or mean-field) approximation. In a system with N electrons, this assumes that each electron evolves in a mean potential accounting for the average repulsion of the other $N-1$ electrons. Consequently, the polyelectronic hamiltonian $\hat{H}$ (dropping the label "el" here for simplicity) can, first, be approximated as the separated sum of N effective one-electron Hamiltonians $\hat{h}(e_i)$, sharing identical expressions (indistinguishable particles), and that depending only on the position of the electron e_i (Hückel, Fock, or Kohn-Sham operators).

Usually, molecular orbitals φ_i are expressed using the so-called linear combination of atomic orbitals (LCAO) expansion over a basis set of N atomic orbitals χ_μ.

$$\varphi_i = \sum_{\mu}^{N} c_{i\mu}\chi_\mu \tag{1.19}$$

The LCAO expansion would be exact provided that the basis set of atomic orbitals were complete. In practice, the summation runs over extended bases for calculations, or is limited to the valence atomic orbitals for qualitative descriptions.

The product of a one-electron space function $\phi_i(\boldsymbol{r}_k)$ and a one-electron spin function $\xi_i(\sigma_k)$, $\psi_i(\boldsymbol{r}_k, \sigma_k) = \phi_i(\boldsymbol{r}_k)\xi_i(\sigma_k)$, is called a spin-orbital. Since electrons are fermions, the Pauli exclusion principle requires the total wavefunction $\Psi(\boldsymbol{r}, \boldsymbol{\sigma})$ describing the N-electron system ($N > 1$) to be antisymmetric with respect to the exchange of any two electrons.

To ensure this property, the simplest type of ansatz for an N-electron wavefunction is a linear combination of $N!$ identical Hartree products of N spin-orbitals, built to be antisymmetric with respect to the $N!$ possible exchanges among the N electrons, namely a Slater determinant. In the case of a two-electron system, this reads

$$\Psi(\boldsymbol{r}_1, \sigma_1, \boldsymbol{r}_2, \sigma_2) = \frac{\psi_1(\boldsymbol{r}_1, \sigma_1)\psi_2(\boldsymbol{r}_2, \sigma_2) - \psi_1(\boldsymbol{r}_2, \sigma_2)\psi_2(\boldsymbol{r}_1, \sigma_1)}{\sqrt{2}} \tag{1.20}$$

$$= \frac{1}{\sqrt{2}} \begin{vmatrix} \psi_1(\boldsymbol{r}_1, \sigma_1) & \psi_2(\boldsymbol{r}_1, \sigma_1) \\ \psi_1(\boldsymbol{r}_2, \sigma_2) & \psi_2(\boldsymbol{r}_2, \sigma_2) \end{vmatrix} \tag{1.21}$$

$$= |\psi_1 \psi_2| \tag{1.22}$$

Each molecular orbital φ_i is characterized by the LCAO coefficients of equation 1.19, and is associated with the energy ε_i. They are determined by solving the following equation

$$\hat{h}\varphi_i = \varepsilon_i \varphi_i \tag{1.23}$$

The projection of the equation on the atomic orbitals χ_μ (where $\mu = 1, ..., N$) and the expansion of φ in the LCAO approach lead to the secular equations

$$\sum_{\nu=1}^{N} (h_{\mu\nu} - \varepsilon S_{\mu\nu}) c_\nu = 0 \tag{1.24}$$

where $h_{\mu\nu} = \langle \chi_\mu | \hat{h} | \chi_\nu \rangle$ ($\hat{h}$ is the one-electron Hamiltonian operator, for example the Fock operator in the Hartree-Fock method) and $S_{\mu\nu} = \langle \chi_\mu | \chi_\nu \rangle$. The secular equations are N coupled equations, linear with respect to the coefficients c_ν, and characterized by the secular determinant:

$$\left| \boldsymbol{h} - \varepsilon \boldsymbol{S} \right| \tag{1.25}$$

where $\boldsymbol{h}$ and $\boldsymbol{S}$ are the Hamiltonian and idendity matrix representations in the basis of the atomic orbitals $\{\chi_\nu\}_{\nu=1,...,N}$. $\boldsymbol{S}$ is also called the overlap matrix.

The set of coefficients c_ν that is solution of the secular equations only defines a molecular orbital if the secular determinant vanishes (otherwise $c_\nu = 0$).

$$\left| \boldsymbol{h} - \varepsilon \boldsymbol{S} \right| = 0 \tag{1.26}$$

The ε that are solutions of this linear system are the N values of the orbital energies ε_l, each one of them corresponding to a molecular orbital φ_l.

Within this approach, the total wavefunction is expressed as a single determinant. To improve the description of the system, the post-Hartree-Fock wavefunction can be expanded over several Slater determinants, which leads to the so-called configuration interaction or multiconfiguration methods.

Chapter 2

Representation of conical intersections

The conceptual bases for this chapter can be found in references [67, 68, 73, 74].

The formalism relative to non-adiabatic couplings was presented, highlighting the divergence of the kinetic couplings at points of degeneracy, which correspond to an infinite probability of changing from an electronic state to another. This reveals that this representation of the electronic states is not adapted to describe the electronic structure around such points of degeneracy.

The adiabatic representation is based on electronic states that are solutions of the electronic Schrödinger equation. In this representation, the adiabatic electronic states are labelled according to their relative energies. For interpreting thermal reactivity, chemists must study the ground state (lowest adiabatic state, most often a singlet, denoted S_0). For an elementary act, the reaction pathway directly connects the reactants and products through the transition state, which is the highest energy point along the pathway.

On the other hand, in photochemistry the reactant is excited upon light absorption to one of its excited state S_n ($n > 0$), and relaxes along the S_n PES until it eventually fluoresces back to S_0 in the region of the product or undergoes radiationless decay processes such as internal conversion.

When a photochemical process is thermally forbidden, the potential energy surface of the adiabatic ground state shows a significant transition barrier between the reactant and the product. This transition barrier actually corresponds to the amount of energy that

is required for adjusting the electronic states of the reactant to the ones of the product. One may notice that in the framework of Marcus theory for electrochemical processes, this barrier is very aptly named "rearrangement energy" [75, 76].

Provided this, it is obvious that the electronic states of the reactant are different from the electronic states of the product (chemical bonds and lone pairs, hence the electronic cloud, have been rearranged and do not concern the same nuclei). In the adiabatic representation, the electronic states relax along the reaction coordinate in order to compensate for the perturbation due to the nuclear motion (further details are given in section 2.2). This alteration of the nature of the adiabatic states is not explicit though, due the way the electronic states are labelled.

Along the same line, Walsh diagrams [77–86] enable us to make a correlation between the electronic states of the reactant and product following their respective natures (figure 2.1), which is usually justified in textbooks from symmetry considerations [87]. This representation is implicitely based on diabatic states, labelled according to their electronic nature, and is formally defined as the representation in which non-adiabatic couplings vanish. In this representation, the nature of each electronic state is conserved from the excited reactant to the product, so the PES is regular and the energy gradient is always defined.

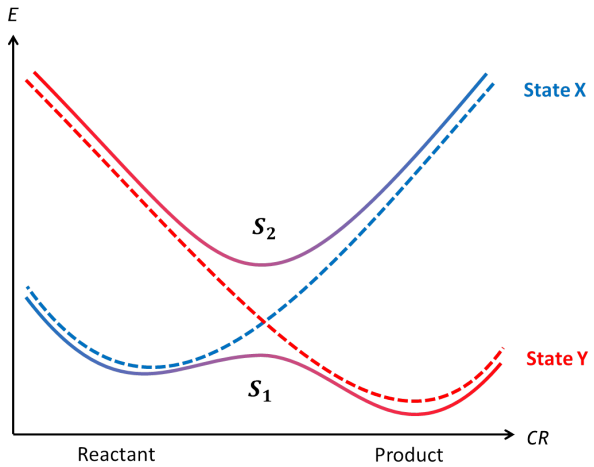

Figure 2.1: Avoided crossing. In dashed lines, diabatic states; in full lines, adiabatic states.

2.1 Two-state electronic Hamiltonian matrix

The essence of conical intersections can be understood within a two-state model. Let $|\Phi_1^{\mathrm{ad}}; \boldsymbol{R}\rangle$ and $|\Phi_2^{\mathrm{ad}}; \boldsymbol{R}\rangle$ be two electronic adiabatic states, with energies $E_1(\boldsymbol{R})$ and $E_2(\boldsymbol{R})$. The matrix representing the electronic Hamiltonian is diagonal in this basis of eigenstates

$$\boldsymbol{H}^{\mathrm{ad}}(\boldsymbol{R}) = \begin{bmatrix} E_1(\boldsymbol{R}) & 0 \\ 0 & E_2(\boldsymbol{R}) \end{bmatrix} \tag{2.1}$$

Let us assume another arbitrary orthonormal basis $\{|\Phi_1; \boldsymbol{R}\rangle, |\Phi_2; \boldsymbol{R}\rangle\}$ spaning the same Hilbert space as the adiabatic states $|\Phi_1^{\mathrm{ad}}; \boldsymbol{R}\rangle$ and $|\Phi_2^{\mathrm{ad}}; \boldsymbol{R}\rangle$. The two bases can be related by a rotation characterized by the so-called mixing angle $\theta(\boldsymbol{R})$ that statisfies:

$$\begin{cases} |\Phi_1^{\mathrm{ad}}; \boldsymbol{R}\rangle = \cos\theta(\boldsymbol{R})|\Phi_1; \boldsymbol{R}\rangle + \sin\theta(\boldsymbol{R})|\Phi_2; \boldsymbol{R}\rangle \\ |\Phi_2^{\mathrm{ad}}; \boldsymbol{R}\rangle = -\sin\theta(\boldsymbol{R})|\Phi_1; \boldsymbol{R}\rangle + \cos\theta(\boldsymbol{R})|\Phi_2; \boldsymbol{R}\rangle \end{cases} \tag{2.2}$$

In the arbitrary basis, the electronic Hamiltonian matrix is not necessarily diagonal. For real-valued states, the matrix is real and symmetric and reads

$$\boldsymbol{H}(\boldsymbol{R}) = \begin{bmatrix} H_{11}(\boldsymbol{R}) & H_{12}(\boldsymbol{R}) \\ H_{21}(\boldsymbol{R}) & H_{22}(\boldsymbol{R}) \end{bmatrix} = S(\boldsymbol{R})\mathbf{1} + \begin{bmatrix} -D(\boldsymbol{R}) & W(\boldsymbol{R}) \\ W(\boldsymbol{R}) & D(\boldsymbol{R}) \end{bmatrix} \tag{2.3}$$

with

$$H_{ij}(\boldsymbol{R}) = \langle \Phi_i; \boldsymbol{R}|\hat{H}^{\mathrm{el}}(\boldsymbol{R})|\Phi_j; \boldsymbol{R}\rangle \tag{2.4}$$

where we introduced

$$S(\boldsymbol{R}) = \frac{H_{11}(\boldsymbol{R}) + H_{22}(\boldsymbol{R})}{2} = \frac{E_1(\boldsymbol{R}) + E_2(\boldsymbol{R})}{2} \tag{2.5}$$

$$D(\boldsymbol{R}) = \frac{H_{22}(\boldsymbol{R}) - H_{11}(\boldsymbol{R})}{2} \tag{2.6}$$

$$W(\boldsymbol{R}) = H_{12}(\boldsymbol{R}) = H_{21}(\boldsymbol{R}) \tag{2.7}$$

The decomposition 2.3 of the Hamiltonian matrix brings out a diagonal part and a residual symmetric matrix with vanishing trace and opposite eigenvalues. The Hamiltonian matrices expressed in the arbitrary and adiabatic bases are related through a similarity transformation involving the same rotation matrix $\boldsymbol{U}(\boldsymbol{R})$ that characterizes the rotation 2.2 between the corresponding states:

$$\boldsymbol{U}(\boldsymbol{R}) = \begin{bmatrix} \cos\theta(\boldsymbol{R}) & -\sin\theta(\boldsymbol{R}) \\ \sin\theta(\boldsymbol{R}) & \cos\theta(\boldsymbol{R}) \end{bmatrix} \tag{2.8}$$

$$\boldsymbol{H}^{\mathrm{ad}}(\boldsymbol{R}) = \boldsymbol{U}^{\dagger}(\boldsymbol{R})\boldsymbol{H}(\boldsymbol{R})\boldsymbol{U}(\boldsymbol{R}) \tag{2.9}$$

Diagonalizing the residual matrix using the rotation $\boldsymbol{U}(\boldsymbol{R})$ allows us to define explicitely the mixing angle

$$\tan 2\theta(\boldsymbol{R}) = -\frac{W(\boldsymbol{R})}{D(\boldsymbol{R})} \tag{2.10}$$

Finally, the adiabatic energies can be recast as:

$$\begin{aligned} E_{1,2}(\boldsymbol{R}) &= S(\boldsymbol{R}) \mp \Delta(\boldsymbol{R}) \\ \Delta(\boldsymbol{R}) &= \sqrt{D^2(\boldsymbol{R}) + W^2(\boldsymbol{R})} \end{aligned} \tag{2.11}$$

2.2 Conical intersections

Conical intersections are points of degeneracy between two (or more [88–90]) adiabatic states. They may be accidental or due to symmetry. Let us first express the conditions for a conical intersection.

Let $\boldsymbol{R}_0$ be the locus of a conical intersection between two adiabatic states, then

$$E_1(\boldsymbol{R}_0) = E_2(\boldsymbol{R}_0) = S(\boldsymbol{R}_0) \tag{2.12}$$

and

$$D(\boldsymbol{R}_0) = W(\boldsymbol{R}_0) = 0 \tag{2.13}$$

The degeneracy requires both $D(\boldsymbol{R}_0)$ and $W(\boldsymbol{R}_0)$ to vanish. Reciprocally, the directions associated with the greatest increase of $D(\boldsymbol{R})$ and $W(\boldsymbol{R})$, namely their gradients, are the most efficient for lifting the degeneracy at the first order from a conical intersection (see figure 2.2). The plane defined by those gradients is the so-called branching space. Then, in the space of the $3N-6$ internal degrees of freedom for the nuclei (N being the

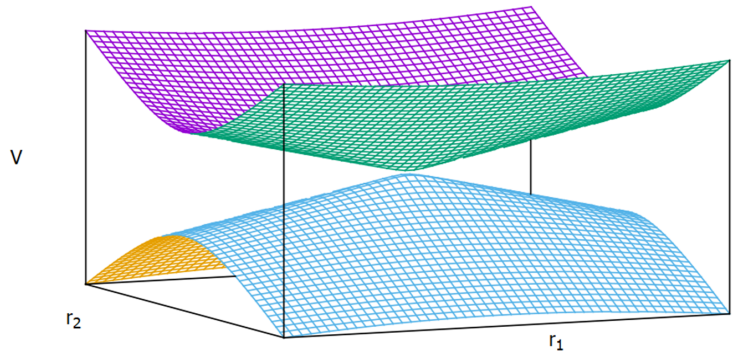

Figure 2.2: Degeneracy lifting from a conical intersection.

number of atoms of the system), a conical intersection between two same-spin states lives in a space of $3N - 8$ degrees of freedom, called "the seam".

The PESs of the two adiabatic states are not regular because of the square-root function (equation 2.11). In particular, they touch at the conical intersection (of coordinates $\boldsymbol{R}_0$) which is the locus of a singular point for the surface. This singularity comes with a discontinuity for the energy gradients 2.11 and a divergence of the non-adiabatic couplings, which also appear in equation 1.16.

These are pathological for the theoretical description for two reasons. First, a singular point is always a huge complication for the fitting of analytical surfaces. Then, the energy gradients and couplings are required, and thus are expected to be determined, to evaluate the transfer of population between the two states around the conical intersection.

2.3 Diabatic basis

To tackle the issues in describing the area around conical intersections, a suitable set of electronic states is needed, which evolve smoothly with the geometry.

The so-called diabatic states are defined such that the corresponding NACs vanish. Since this condition is actually rarely fulfilled, in practice we call "diabatic states" the states minimizing the amplitude of the NACs. They correspond to electronic states that are labelled according to their chemical nature (which sometimes turns out to be their symmetry) by opposition to the adiabatic states which are labelled with respect to their energy. One may recognize in this the same considerations involved in the construction of Walsh diagrams used to demonstrate the Woodward-Hoffman rules for pericyclic reactions [91–97]. Consequently, diabatic states generally provide a suitable support for chemical

interpretation.

The direct consequence of this definition is that the diabatic states are regular and do not change much with the geometry, even in the vicinity of conical intersections. Then, contrarily to the adiabatic energies, the diabatic ones actually cross while moving through a conical intersection[1].

Provided that the diabatic and adiabatic states form complete bases of the same Hilbert space, they are similar up to a geometry-dependent rotation. Unfortunately, there is no way to access the diabatic states straightfowardly, making it very difficult to automatize the transformation from the adiabatic ones (known) to the diabatic basis (unknown).

2.4 Branching space

Both vectors of the branching space can be derived from first-order degenerate perturbation theory in the crude adiabatic representation. We denote $\boldsymbol{x}^{\mathrm{ad},(1)}$ and $\boldsymbol{x}^{\mathrm{ad},(2)}$ the tuning (or half gradient of the energy difference) and the (derivative) coupling vectors, respectively. Their components satisfy[2]

$$\begin{aligned} x_j^{\mathrm{ad},(1)} &= \frac{\langle \Phi_2^{\mathrm{ad}};\boldsymbol{R}_0|\partial_j \hat{H}^{\mathrm{el}}(\boldsymbol{R}_0)|\Phi_2^{\mathrm{ad}};\boldsymbol{R}_0\rangle - \langle \Phi_1^{\mathrm{ad}};\boldsymbol{R}_0|\partial_j \hat{H}^{\mathrm{el}}(\boldsymbol{R}_0)|\Phi_1^{\mathrm{ad}};\boldsymbol{R}_0\rangle}{2} \\ x_j^{\mathrm{ad},(2)} &= \langle \Phi_1^{\mathrm{ad}};\boldsymbol{R}_0|\partial_j \hat{H}^{\mathrm{el}}(\boldsymbol{R}_0)|\Phi_2^{\mathrm{ad}};\boldsymbol{R}_0\rangle \end{aligned} \tag{2.14}$$

where $\boldsymbol{R}_0$ is the locus of a conical intersection. It is worth to notice that this set of vectors is attached to the choice made for the degenerate adiabatic states. Indeed, let us consider another set of degenerate electronic states $|\Phi_1;\boldsymbol{R}_0\rangle$ and $|\Phi_2;\boldsymbol{R}_0\rangle$ related to the original states through the mixing angle $\theta(\boldsymbol{R}_0)$. Inserting equation 2.2 into 2.14, the branching space vectors associated to $|\Phi_1;\boldsymbol{R}_0\rangle$ and $|\Phi_2;\boldsymbol{R}_0\rangle$ satisfy

$$\begin{aligned} x_j^{(1)} &= \cos 2\theta(\boldsymbol{R}_0) x_j^{\mathrm{ad},(1)} - \sin 2\theta(\boldsymbol{R}_0) x_j^{\mathrm{ad},(2)} \\ x_j^{(2)} &= \sin 2\theta(\boldsymbol{R}_0) x_j^{\mathrm{ad},(1)} - \cos 2\theta(\boldsymbol{R}_0) x_j^{\mathrm{ad},(2)} \end{aligned} , \tag{2.15}$$

which proves that even though they span the same branching space, the definition of the vectors is attached to the two states specifically chosen within the twice-degenerate subspace.

[1] Since the adiabatic states are labelled according to their relative energies, their labels are preserved from one side to the other of a conical intersection, so the adiabatic energies actually touch and do not cross.

[2] Details of the derivation can be found in reference [67].

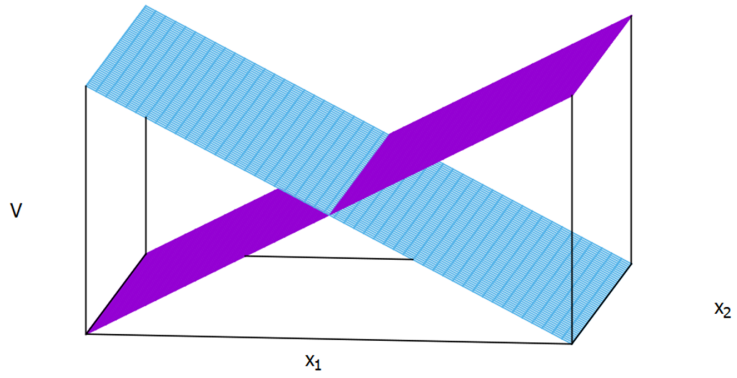

Figure 2.3: Diabatic potential energy surfaces.

As can be noted, the vectors rotate twice as fast as the states, considering a given set of electronic states (here the adiabatic states) as a reference. A direct consequence is that for a mixing angle $\theta(\boldsymbol{R}_0) = \pi/4$, the role of the gradient of the energy difference and of the coupling directions are inverted.

This point is illustrated more vividly when considering diabatic states in the form of so-called crude adiabatic states. Let $|\Phi_\alpha^{\text{dia}}; \boldsymbol{R}\rangle$ and $|\Phi_\beta^{\text{dia}}; \boldsymbol{R}\rangle$ be two diabatic states assumed to be degenerate eigenstates at $\boldsymbol{R}_0$. They are associated with $\boldsymbol{x}^{(1)}$ and $\boldsymbol{x}^{(2)}$ as the tuning and coupling modes, respectively, see figures 2.3 and 2.6.

We recall that the electronic Hamiltonian matrix is no longer diagonal (except at $\boldsymbol{R}_0$) in this basis, and the corresponding couplings between the diabatic states read

$$H_{\alpha\beta}^{\text{dia}}(\boldsymbol{R}) = \langle \Phi_\alpha^{\text{dia}}; \boldsymbol{R} | \hat{H}^{\text{el}}(\boldsymbol{R}) | \Phi_\beta^{\text{dia}}; \boldsymbol{R} \rangle \ . \tag{2.16}$$

Those are called "potential couplings", by opposition to the kinetic couplings arising in the adiabatic representation, and vanish at the conical intersection (at $\boldsymbol{R} = \boldsymbol{R}_0$). For a displacement from $\boldsymbol{R}_0$ along the coupling mode $\boldsymbol{x}^{(2)}$, the value of the coupling is related to the amplitude of the degeneracy lifting of the conical intersection, that is the splitting of adiabatic states at an avoided crossing[3].

In the example of cyclobutadiene, the ground state (adiabatic) presents two wells corresponding to the two equivalent deformations (horizontal and vertical) of the square, which is the minimum of the second excited state, see figure 2.5. The diabatic potentials

[3]The difference between the eigenvalues of the electronic Hamiltonian matrix in the diabatic basis reads $\Delta V = 2\sqrt{\left(\frac{H_{\beta\beta} - H_{\alpha\alpha}}{2}\right)^2 + (H_{\alpha\beta})^2}$

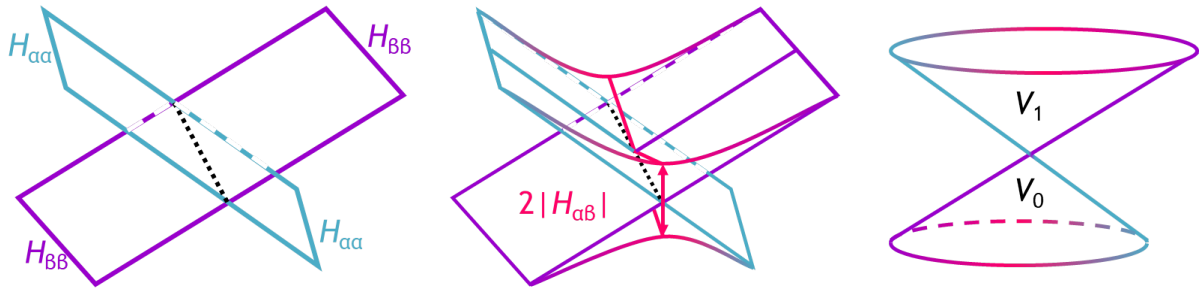

Figure 2.4: Diabatic potentials (left), diabatic potentials and the potential couplings (middle), and adiabatic potentials (right) around a conical intersection.

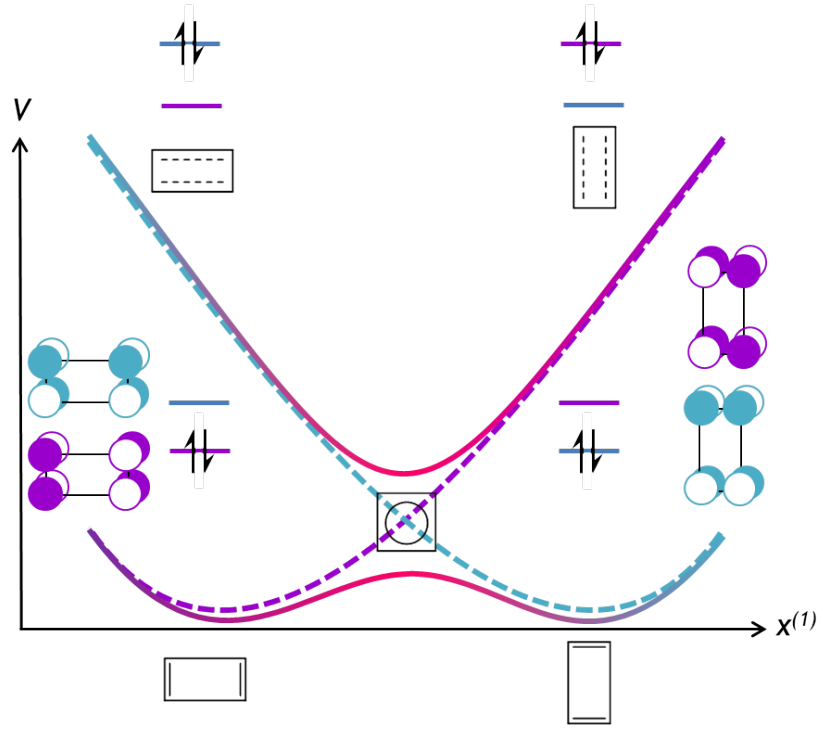

Figure 2.5: Avoided crossing in cyclobutadiene.

follow the evolution of the molecular orbitals corresponding to each deformation, while the adiabatic potentials switch from one to another across the avoided crossing.

Remembering that the choice of diabatic states is not unique, we perform a $\pi/4$-rotation yielding a set of diabatic states $|\Phi_+^{\mathrm{dia}}; \boldsymbol{R}\rangle$ and $|\Phi_-^{\mathrm{dia}}; \boldsymbol{R}\rangle$ that are the normalized sum and difference of the diabatic states $|\Phi_\alpha^{\mathrm{dia}}; \boldsymbol{R}\rangle$ and $|\Phi_\beta^{\mathrm{dia}}; \boldsymbol{R}\rangle$. As mentioned above, the tuning and coupling modes are exchanged between these two sets of states, so $\boldsymbol{x}_+^{(1)} = \boldsymbol{x}^{(2)}$ and $\boldsymbol{x}_-^{(2)} = -\boldsymbol{x}^{(1)}$.

In the example of cyclobutadiene, the new states correspond to symmetrized combinations of the diabatic states associated with the deformations. Then, in the direction discriminating the deformations (tuning), the coupling between the symmetrized states

evolves and the corresponding diagonal potentials stay parallel, see figure 2.6.

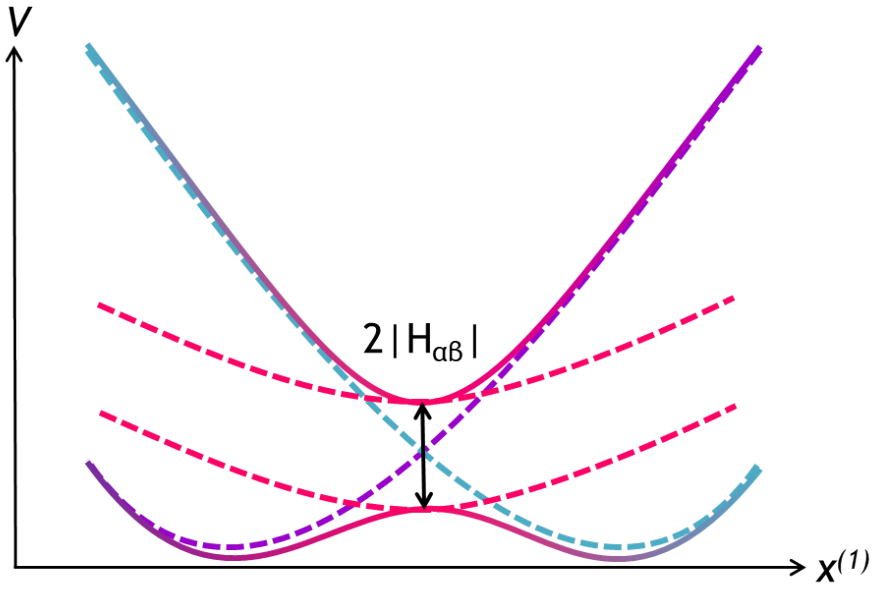

Figure 2.6: Electronic potentials along the mode $\boldsymbol{x}^{(1)}$ at a point displaced from the conical intersection along $\boldsymbol{x}^{(2)}$ (avoided crossing). Adiabatic potentials are in full line, diabatic potentials are in dashed line. $\boldsymbol{x}^{(1)}$ ($\boldsymbol{x}^{(2)}$) is the tuning (coupling) mode for the diabatic states $|\Phi_\alpha^{\text{dia}}; \boldsymbol{R}\rangle$ and $|\Phi_\beta^{\text{dia}}; \boldsymbol{R}\rangle$ that tend asymptotically to the adiabatic states. At the avoided crossing, the adiabatic states are identical to the $\pi/4$-rotated diabatic states $|\Phi_+^{\text{dia}}; \boldsymbol{R}\rangle$ and $|\Phi_-^{\text{dia}}; \boldsymbol{R}\rangle$ (pink dashed lines).

Chapter 3

Density functional theory (DFT)

This chapter is based on the following references: [98–100]

Density functional theory (DFT) encompasses a family of quantum mechanics methods among the most used when it comes to the electronic structure of the ground state, would it be in physics, chemistry, material sciences, etc.

Contrarily to wavefunction methods, which rely on the $3N$-variable wavefunction, DFT makes use of the one-electron density, which is only a 3-variable object. The scaling of DFT (in N) is thus more advantageous than the one of wavefunction methods (in powers of N or $N!$). In addition, the accuracy of DFT methods is comparable to the accuracy of post-Hartree-Fock methods, which, along with the scaling, causes its popularity.

The original idea is due to Thomas and Fermi, who realized in the 1920s that the electron distribution in an atom could be approximated by the electron density, using a statistical model. The formalism of DFT we use nowadays was established later by Hohenberg, Kohn, and Sham.

3.1 A density method

The objective is to determine the ground-state energy of the electronic Hamiltonian $\hat{H}^{\text{el}}$, considering a N-electron system without relativistic effects.

Removing the labels "el" in equations 1.7 and 1.5 for simpler notations, the electronic Schrödinger equation reads[1]

$$\hat{H}|\Psi\rangle = E|\Psi\rangle \tag{3.1}$$

$$\hat{H} = \hat{T} + \hat{V}_{\text{ee}} + \hat{V}_{\text{ne}} \ . \tag{3.2}$$

The basis of density functional theory (DFT) is to use the one-electron density $n(\boldsymbol{r})$ instead of the N-electron wavefunction $\Psi_N(\boldsymbol{r}_1, \cdots, \boldsymbol{r}_N)$ to solve the electronic problem. Doing so, one solves the electronic problem considering the 3-variable density instead of the $3N$-variable wavefunction. In addition, the density is an observable that can be measured experimentally, contrarily to the wavefunction. In the present paragraph, we introduce the basic quantities used in density theory that will be required later on.

The density matrix $\boldsymbol{\gamma}_N$ in the space of the space-spin coordinates $\boldsymbol{x}_i = (\boldsymbol{r}_i, \sigma_i)$ for N particles reads

$$\boldsymbol{\gamma}_N(\boldsymbol{x}_1, ..., \boldsymbol{x}_N, \boldsymbol{x}'_1, ..., \boldsymbol{x}'_N) = \Psi_N(\boldsymbol{x}_1, ..., \boldsymbol{x}_N)\Psi^*_N(\boldsymbol{x}'_1, ..., \boldsymbol{x}'_N) \ . \tag{3.3}$$

Reduced densities and density matrices give access to the expectation values of operators upon considering explicitly some among N electrons and integrating over the others. Non-local operators require density matrices while densities are sufficient for local operators. The order corresponds to the number of bodies that interact together.

In particular, the one-electron (or 1^{st}-order) reduced density matrix $\boldsymbol{\gamma}_1(\boldsymbol{r}_1, \boldsymbol{r}'_1)$ characterizes one among N electrons of arbitrary spin, irrespectively of the other $N-1$ electrons.

$$\boldsymbol{\gamma}_1(\boldsymbol{r}_1, \boldsymbol{r}'_1) = N \int \Psi_N(\boldsymbol{x}_1, ..., \boldsymbol{x}_N)\Psi^*_N(\boldsymbol{x}'_1, ..., \boldsymbol{x}'_N) d\sigma_1 d\boldsymbol{x}_2, ..., d\boldsymbol{x}_N \tag{3.4}$$

This quantity is required to evaluate the effect of non-local one-electron operators (for example, the electron kinetic energy).

[1] One may note that the electronic Hamiltonian presented in chapter 1 also contained the Coulomb interaction between the nuclei. Since the electronic Hamiltonian is considered for fixed nuclei, the Coulomb interaction between the nuclei is a constant and does not affect the electronic eigenstates. It can be added afterwards to the electronic eigenvalues as an energy shift.

For local one-electron operators (for example, the electron-nucleus potential energy), the one-electron density at one point, $n(\boldsymbol{r}_1) = \boldsymbol{\gamma}_1(\boldsymbol{r}_1, \boldsymbol{r}_1)$, is enough. It is the diagonal of $\boldsymbol{\gamma}_1(\boldsymbol{r}_1, \boldsymbol{r}'_1)$ and corresponds to the density of probability of finding one electron at position $\boldsymbol{r}_1$ with an arbitrary spin σ_1, independently of the positions and spins of the other electrons. It can be obtained from the N-electron wavefunction $\Psi_N(\boldsymbol{x}_1, \cdots, \boldsymbol{x}_N)$ as

$$n(\boldsymbol{r_1}) = N \int \cdots \int |\Psi_N(\boldsymbol{x}_1, \boldsymbol{x}_2, ..., \boldsymbol{x}_N)|^2 d\sigma_1 d\boldsymbol{x}_2, ..., d\boldsymbol{x}_N \tag{3.5}$$

and it is normalized to the number of electrons: $\int n(\boldsymbol{r}) d\boldsymbol{r} = N$.

Consistently with the one-electron reduced density matrix $\boldsymbol{\gamma}_1(\boldsymbol{r}_1, \boldsymbol{r}'_1)$, the electron-pair reduced density matrix $\boldsymbol{\gamma}_2(\boldsymbol{r}_1, \boldsymbol{r}_2, \boldsymbol{r}'_1, \boldsymbol{r}'_2)$ is defined as

$$\boldsymbol{\gamma}_2(\boldsymbol{r}_1, \boldsymbol{r}_2, \boldsymbol{r}'_1, \boldsymbol{r}'_2) = \frac{N(N-1)}{2} \int \Psi_N(\boldsymbol{x}_1, \boldsymbol{x}_2, ..., \boldsymbol{x}_N) \Psi^*_N(\boldsymbol{x}'_1, \boldsymbol{x}'_2 ..., \boldsymbol{x}'_N) d\sigma_1 d\sigma_2 d\boldsymbol{x}_3, ..., d\boldsymbol{x}_N \ . \tag{3.6}$$

The diagonal of $\boldsymbol{\gamma}_2(\boldsymbol{r}_1, \boldsymbol{r}_2, \boldsymbol{r}_1, \boldsymbol{r}_2)$ corresponds to the electron-pair density $n_2(\boldsymbol{r}_1, \boldsymbol{r}_2)$, that is the density of probability of finding any two electrons at positions $\boldsymbol{r}_1$ and $\boldsymbol{r}_2$ with arbitrary spins σ_1 and σ_2. It can be obtained from the N-electron wavefunction as

$$n_2(\boldsymbol{r}_1, \boldsymbol{r}_2) = \frac{N(N-1)}{2} \int \cdots \int |\Psi_N(\boldsymbol{x}_1, \boldsymbol{x}_2, ..., \boldsymbol{x}_N)|^2 d\sigma_1 d\sigma_2 d\boldsymbol{x}_3, ..., d\boldsymbol{x}_N \tag{3.7}$$

and integrates to the number of distinct unordered pairs within N electrons:
$\int \int n_2(\boldsymbol{r}_1, \boldsymbol{r}_2) d\boldsymbol{r}_1 d\boldsymbol{r}_2 = \frac{N(N-1)}{2}$. This quantity is required to evaluate the effect of local two-electron operators (for example, the electron-electron potential energy).

3.2 Hohenberg-Kohn theorems

The Hohenberg and Kohn theorems prove that all the ground-state properties of a system can be obtained from the knowledge of its ground-state density [101].

For a given number of electrons, the actual nature of the system is determined by the so-called external potential $v_{\text{ne}}(\boldsymbol{r})$, which corresponds to the attraction that the nuclei (at given positions) exert on any electron. It thus determines the ground-state density $n_0(\boldsymbol{r})$. The corresponding energy $V_{\text{ne}}[n]$ reads

$$V_{\text{ne}}[n] = \int n(\boldsymbol{r}) v_{\text{ne}}(\boldsymbol{r}) d\boldsymbol{r} \tag{3.8}$$

The first theorem states that the ground-state density also determines the external potential (up to a constant)[2] , which ensures the existence of a one-to-one mapping between both quantities, and the existence of a universal density functional $F_{\mathrm{HK}}[n]$ such that

$$E_{v_{\mathrm{ne}}}[n] = \int n(\boldsymbol{r}) v_{\mathrm{ne}}(\boldsymbol{r}) d\boldsymbol{r} + F_{\mathrm{HK}}[n] \tag{3.9}$$

where $F_{\mathrm{HK}}[n] = T[n] + V_{\mathrm{ee}}[n]$ and

$$T[n] = \langle \Psi_N[n] | \hat{T} | \Psi_N[n] \rangle \tag{3.10}$$

$$V_{\mathrm{ee}}[n] = \langle \Psi_N[n] | \hat{V}_{\mathrm{ee}} | \Psi_N[n] \rangle \tag{3.11}$$

The second part of the theorem allows the calculation of the ground-state energy variationally with respect to the density[3].

$$E_{0,v_{\mathrm{ne}}} = \min_n E[n] = \min_n \left\{ \int n(\boldsymbol{r}) v_{\mathrm{ne}}(\boldsymbol{r}) d\boldsymbol{r} + F_{\mathrm{HK}}[n] \right\} \tag{3.12}$$

where the minimization runs over the N-electron densities that are ground-state densities associated to an external potential. The energy of the ground-state is reached for the density n_0 associated to the external potential of the system.

Applying the variational principal requires a functional expression of the universal density functional $F_{\mathrm{HK}}[n]$ in terms of the density. This can be obtained using the one-electron density matrix and the electron-pair density introduced above (equations 3.4 and 3.7, respectively), here in atomic units:

$$T[n] = -\frac{1}{2} \int \left[\nabla^2 \gamma_1(\boldsymbol{r}_1, \boldsymbol{r}_1') \right]_{\boldsymbol{r}_1' = \boldsymbol{r}_1} d\boldsymbol{r}_1 \tag{3.13}$$

$$V_{\mathrm{ee}}[n] = \frac{1}{2} \int \int \frac{n_2(\boldsymbol{r}_1, \boldsymbol{r}_2)}{|\boldsymbol{r}_1 - \boldsymbol{r}_2|} d\boldsymbol{r}_1 d\boldsymbol{r}_2 \tag{3.14}$$

Yet, $\gamma_1(\boldsymbol{r}_1, \boldsymbol{r}_1')$ and $n_2(\boldsymbol{r}_1, \boldsymbol{r}_2)$ are unknown for the correlated system, so $T[n]$ and $V_{\mathrm{ee}}[n]$ are also unknown.

3.3 Kohn-Sham equations

With the Kohn-Sham equations, one solves a simpler auxiliary problem involving N non-interacting electrons instead of the real N-interacting electron problem [102]. This is

[2] "The external potential $v_{\mathrm{ne}}(\boldsymbol{r})$, and hence the total energy, is a unique functional of the electron density $n(\boldsymbol{r})$."

[3] "The electron density that minimizes the energy of the overall functional is the true electron density corresponding to the full solution of the Schrödinger equation."

relevent only if the Kohn-Sham orbitals yield a density $n_S(\boldsymbol{r})$ identical to the exact ground-state density $n_0(\boldsymbol{r})$ of the real system, which is ensured thanks to the Kohn-Sham potential $v^{\mathrm{KS}}(\boldsymbol{r})$.

Within this perspective, the auxiliary wavefunction $\Psi_S(\boldsymbol{x}_1, \boldsymbol{x}_2, ..., \boldsymbol{x}_N)$ is defined as a single Slater determinant $\Psi_S(\boldsymbol{x}_1, \boldsymbol{x}_2, ..., \boldsymbol{x}_N) = |\phi_1 \phi_2 \cdots \phi_N|$ yielding the density

$$n_S(r) = \sum_{i=1}^{N} |\phi_i(\boldsymbol{r})|^2 \tag{3.15}$$

The functions $\phi_i(\boldsymbol{r})$ that yield the ground-state density of the system are termed Kohn-Sham spin-orbitals. The kinetic energy of the auxiliary system is exact and reads

$$T_S[n] = \sum_{i=1}^{N} \langle \phi_i | -\frac{1}{2}\nabla_i^2 | \phi_i \rangle \tag{3.16}$$

In addition, the bielectronic contribution $V_{\mathrm{ee}}[n]$ can be expressed as

$$V_{\mathrm{ee}}[n] = \frac{1}{2} \int \int \frac{n(\boldsymbol{r}_1)\tilde{n}(\boldsymbol{r}_2^{r_1})}{|\boldsymbol{r}_1 - \boldsymbol{r}_2|} d\boldsymbol{r}_1 d\boldsymbol{r}_2 \tag{3.17}$$

where $\tilde{n}(\boldsymbol{r}_2^{r_1})$ is the conditional probability to find an electron at position $\boldsymbol{r}_2$ considering another electron occupies the position $\boldsymbol{r}_1$.
The conditional probability accounts for the fact that the existence of a first electron "prevents" the second one to be at any position in space. This is equivalent to considering that the first electron creates a hole around itself that the second electron must avoid (exchange-correlation hole), and leads to

$$n(\boldsymbol{r}_1)\tilde{n}(\boldsymbol{r}_2^{r_1}) = n(\boldsymbol{r}_1)\left[n(\boldsymbol{r}_2) + n^{\mathrm{hole}}(\boldsymbol{r}_1, \boldsymbol{r}_2)\right] \ . \tag{3.18}$$

The bielectronic energy $V_{\mathrm{ee}}[n]$ can thus be recast as

$$V_{\mathrm{ee}}[n] = J[n] + \epsilon_{\mathrm{xc}}^{\mathrm{hole}}[n] \tag{3.19}$$

where

$$J[n] = \frac{1}{2} \int \int \frac{n(\boldsymbol{r}_1)n(\boldsymbol{r}_2)}{|\boldsymbol{r}_1 - \boldsymbol{r}_2|} d\boldsymbol{r}_1 d\boldsymbol{r}_2 \tag{3.20}$$

and

$$\epsilon_{\mathrm{xc}}^{\mathrm{hole}}[n] = \frac{1}{2} \int \int \frac{n(\boldsymbol{r}_1)n^{\mathrm{hole}}(\boldsymbol{r}_1, \boldsymbol{r}_2)}{|\boldsymbol{r}_1 - \boldsymbol{r}_2|} d\boldsymbol{r}_1 d\boldsymbol{r}_2 \tag{3.21}$$

Finally, the energy can be expressed in terms of the density as follows

$$E[n] = T_S[n] + J[n] + \int n(\boldsymbol{r}) v_{\text{ne}}(\boldsymbol{r}) d\boldsymbol{r} + E_{\text{xc}}[n] \tag{3.22}$$

where $E_{\text{xc}}[n] = T[n] - T_S[n] + \epsilon_{\text{xc}}^{\text{hole}}[n]$ is the exchange-correlation energy.
Thus, within the Kohn-Sham decomposition, only the exchange-correlation energy is left to approximate for calculating the total electronic energy functional.

After some derivation, the minimization using the method of Lagrange multipliers yields the Kohn-Sham equations.

$$\left\{ -\frac{1}{2}\nabla^2 + v^{\text{KS}}(\boldsymbol{r}) \right\} \phi_i(\boldsymbol{r}) = \varepsilon_i \phi_i(\boldsymbol{r}) \tag{3.23}$$

We define the Kohn-Sham one-electron Hamiltonian $\hat{h}^{\text{KS}}$ and the Kohn-Sham potential $v^{\text{KS}}(\boldsymbol{r})$ such as

$$\begin{aligned} \hat{h}^{\text{KS}}(\boldsymbol{r}) &= -\frac{1}{2}\nabla^2 + v^{\text{KS}}(\boldsymbol{r}) \\ v^{\text{KS}}(\boldsymbol{r}) &= v_{\text{H}}(\boldsymbol{r}) + v_{\text{ne}}(\boldsymbol{r}) + v_{\text{xc}}(\boldsymbol{r}) \end{aligned} . \tag{3.24}$$

where $v_{\text{xc}}(\boldsymbol{r}) = \dfrac{\delta E_{\text{xc}}[n]}{\delta n(\boldsymbol{r})}$ is the exchange-correlation potential and $v_{\text{H}}(\boldsymbol{r}) = \int \dfrac{n(\boldsymbol{r}')}{|\boldsymbol{r} - \boldsymbol{r}'|} d\boldsymbol{r}'$ is the Hartree potential.

The local potential $v_{\text{xc}}(\boldsymbol{r})$ is a functional of the density defined as the functional derivative of the Hartree-exchange-correlation energy[4]. Since $v_{\text{xc}}(\boldsymbol{r})$ depends on the density, the one-electron Kohn-Sham equations form a set of N coupled self-consistent equations.

$v_{\text{xc}}(\boldsymbol{r})$ can be seen as the most important term of the expansion since it contains the corrections to the kinetic energy and Coulomb interaction, yet we can only approximate it. Provided that $v_{\text{xc}}(\boldsymbol{r})$ is known exactly, the minimization leads to the exact density and energy for the ground state.

[4]The functional derivative, also called kernel, corresponds to the quantity that has to be integrated to recover a variation of the functional. In this case, the energy E_{xc} is a functional of the density n, and $\delta E_{\text{xc}}[n] = \int d\boldsymbol{r} \dfrac{\delta E_{\text{xc}}[n]}{\delta n(\boldsymbol{r})} \delta n(\boldsymbol{r})$

Chapter 4

Time-dependent density functional theory (TDDFT)

This chapter uses the following references: [68, 103–107].

In principle, the wavefunctions for the excited states can be obtained combining the variational principle together with orthonormalization with respect to the lower states, which is precisely the drawback of the procedure: the calculation of the n lower states is required prior to the calculation of state S_n. State-average methods enable to obtain a set of states by optimizing them altogether. This may be quite efficient in the case of states that are close enough in energy. Yet, common DFT methods remain quite limited to access the excited states straightfowardly.

To circumvent this limitation, DFT can be extended to a time-dependent version. In time-dependent density functional theory, the system undergoes a time-dependent perturbation likely to cause a transition from the ground state to an excited state. The time-dependent Schrödinger equation takes the non-stationary character of the perturbation into account, and the "reaction" of the system is described with the so-called "response theory".

Several kinds of time-dependent density functional theory (TDDFT) methods exist and are discriminated according to the approximations they rely on. In this thesis, we focus on the method we used for our own calculations, which is the most common linear-response TDDFT.

4.1 Time-dependent Kohn-Sham equations

The principle of TDDFT is to access the energies of the excited states of an N-interacting electron system, initially in its ground state, by analyzing its reaction and relaxation to a perturbation (excitation) $\hat{W}(t)$. This can be achieved upon studying the linear response of the ground state to the time-dependent perturbation $\hat{W}(t)$. A general derivation of linear-response theory is presented in Appendix B, which will be the guide line to the present derivation. Using the previous notations, the Schrödinger equation reads

$$\mathrm{i}\hbar\frac{d}{dt}|\Psi(t)\rangle = \left[\hat{T} + \hat{V}_{\mathrm{ee}} + \hat{V}_{\mathrm{ne}} + \hat{W}(t)\right]|\Psi(t)\rangle$$

The transitions induced by an ideal monochromatic LASER result from the interaction between the system and a sinusoidal electric field such that

$$\boldsymbol{E}(t) = \epsilon\cos\omega t\boldsymbol{e}_z \tag{4.1}$$

For the sake of simplicity, we choose to align the electric field with the z-axis of a frame attached to the molecular system.

The perturbation of the system is the corresponding electric potential,

$$\hat{W}(t) = \epsilon z\cos\omega t = \epsilon\hat{W}\cos\omega t \tag{4.2}$$

As presented in chapter 3, the Kohn-Sham equations for DFT rely on the Hohenberg and Kohn theorem and the Kohn-Sham decomposition for the universal density functional. In a time-dependent context, the Kohn-Sham decomposition is still valid but the proof of the Hohenberg and Kohn theorem must be adjusted.

The Runge-Gross theorem [108] is the transposition of the Hohenberg theorem to the time-dependent case. It ensures the mapping from the density to the external potential and the existence of the three-variable universal density functional, all of them being time-dependent. As a consequence, the time-dependent Kohn-Sham potential is time-dependent in two ways: (i) directly, because it contains the time-dependent perturbation, (ii) indirectly, through the evolution of the exchange-correlation term which is a functional of the time-dependent density.

We thus consider a time-dependent system, characterized by time-dependent KS orbitals and a time-dependent KS potential. Consequently, the time-dependent Kohn-Sham equations read

$$\frac{d}{dt}\varphi_i(\boldsymbol{r},t) = \left[-\frac{1}{2}\nabla^2 + v^{\mathrm{KS}}[n](\boldsymbol{r},t)\right]\varphi_i(\boldsymbol{r},t) \tag{4.3}$$

where $v^{\mathrm{KS}}[n](\boldsymbol{r},t) = v_{\mathrm{ne}}[n](\boldsymbol{r}) + \hat{W}(\boldsymbol{r},t) + v_{\mathrm{xc}}[n](\boldsymbol{r},t)$.

It is worth to note that the external and Hartree potentials only depend on time through the density, contrarily to the exchange-correlation potential, which is unknown and may depend on time both directly and through the density.

Considering equation 3.24, the time-dependent KS equations can be recast as

$$\frac{d}{dt}\varphi_i(\boldsymbol{r},t) = \left[\hat{h}^{\mathrm{KS}}(\boldsymbol{r}) + \hat{W}(\boldsymbol{r},t) + \delta v_{\mathrm{xc}}[n](\boldsymbol{r},t)\right]\varphi_i(\boldsymbol{r},t) \tag{4.4}$$

where $\delta v_{\mathrm{xc}}[n](\boldsymbol{r},t) = v_{\mathrm{xc}}[n](\boldsymbol{r},t) - v_{\mathrm{xc}}[n](\boldsymbol{r})$ is the variation of the potential $v_{\mathrm{xc}}[n](\boldsymbol{r},t)$ with time. As mentioned in note 4, $\delta v_{\mathrm{xc}}[n](\boldsymbol{r},t)$ is related to the functional derivative of v_{xc} with respect to the density n.

The eigenfunctions $\varphi_i(\boldsymbol{r},t)$ are the time-dependent Kohn-Sham orbitals. The Kohn-Sham wavefunction $\Phi(\boldsymbol{r}_1,...,\boldsymbol{r}_N,t)$ is a N-electron time-dependent Slater determinant built from the N time-dependent Kohn-Sham orbitals and is expected to reproduce the exact time-dependent electron density $n(\boldsymbol{r},t)$ of the system. Thus, the excitation poles of the Kohn-Sham densities should also be poles for the real density of the molecule and give its exact excitation energies.

By analogy with response theory (section B.3), a time-dependent Kohn-Sham orbital $\varphi(\boldsymbol{r},t)$ is expanded over the basis of the stationary orbitals $\varphi_{i=0,1,2...}(\boldsymbol{r})$, associated to the energies $\varepsilon_{i=0,1,2...}$.

$$\varphi(\boldsymbol{r},t) = \sum_i e^{-\mathrm{i}\omega_i t} c_i(t)\varphi_i(\boldsymbol{r}) \tag{4.5}$$

with $\omega_i = \varepsilon_i/\hbar$.

All it takes to describe the evolution of the Kohn-Sham system is the knowledge of the linear coefficients $c_i(t)$. This requires to express the perturbation of the Kohn-Sham system, at any time t. In particular, the variation of the exchange-correlation potential

$\delta v_{\mathrm{xc}}[n](\boldsymbol{r},t)$ is *a priori* dependent on time explicitely but also through the time-dependent density. The exact formulation of its variation from time $t=0$ is then pretty complicated, and shows a dependence with the frequency ω.

4.2 Adiabatic approximation

Here, the adiabatic approximation consists in the instantaneous adjustement of the density to time. In this framework, the exchange-correlation potential is approximated to the ground-state potential evaluated at the time-dependent density $n(\boldsymbol{r},t)$,

$$v_{\mathrm{xc}}[n](\boldsymbol{r},t) \simeq v_{\mathrm{xc}}[n(t)](\boldsymbol{r})$$

this is also valid for their variations

$$\delta v_{\mathrm{xc}}[n](\boldsymbol{r},t) \simeq \delta v_{\mathrm{xc}}[n(t)](\boldsymbol{r}) \ . \tag{4.6}$$

Considering equation 3.23, the functional derivative of $v_{\mathrm{xc}}[n(t)](\boldsymbol{r})$ with respect to the density reads

$$\delta v_{\mathrm{xc}}[n(t)](\boldsymbol{r}) = \int d\boldsymbol{r'} f_{\mathrm{xc}}(\boldsymbol{r},\boldsymbol{r'})\delta n(\boldsymbol{r'},t) \tag{4.7}$$

where $f_{\mathrm{xc}}(\boldsymbol{r},\boldsymbol{r'}) = \dfrac{\delta^2 E_{\mathrm{xc}}[n(t)]}{\delta n(\boldsymbol{r},t)\delta n(\boldsymbol{r'},t)}$.

One may notice that the kernel $f_{\mathrm{xc}}(\boldsymbol{r},\boldsymbol{r'})$ is local in time [1] so no memory effects are taken into account. In addition, the Fourier transform becomes frequency-independent, which is the reason why TDDFT can only describe mono-excited electronic states (see below).

[1] In the general case, $\delta v_{\mathrm{xc}}[n](\boldsymbol{r},t) = \int d\boldsymbol{r'} \int dt' \dfrac{\delta^2 E_{\mathrm{xc}}[n(t)]}{\delta n(\boldsymbol{r},t)\delta n(\boldsymbol{r'},t')}\delta n(\boldsymbol{r'},t')$. If n adjusts instantaneously to t, the time-dependent kernel $f_{\mathrm{xc}}(\boldsymbol{r},\boldsymbol{r'},t,t')$ is approximated to $f_{\mathrm{xc}}(\boldsymbol{r},\boldsymbol{r'},t,t') \simeq \delta(t-t')\dfrac{\delta^2 E_{xc}[n(t)]}{\delta n(\boldsymbol{r'},t')\delta n(\boldsymbol{r},t)}$.

4.3 Casida equations

By analogy with linear response theory, the linear response coefficients for TDDFT satisfy:

$$\begin{aligned}\frac{d}{dt}c_n(t) = &-\frac{\mathrm{i}W_{n0}}{2\hbar}\left[e^{\mathrm{i}(\Delta\omega_n+\omega)t} + e^{-\mathrm{i}(\omega-\Delta\omega_n)t}\right] \\ &- \frac{N\mathrm{i}}{\hbar}\sum_{m>0} e^{-\mathrm{i}(\Delta\omega_m-\Delta\omega_n)t}c_m^{(1)}(t)\langle n0|f_{xc}|0m\rangle \\ &- \frac{N\mathrm{i}}{\hbar}\sum_{m>0} e^{-\mathrm{i}(\Delta\omega_m+\Delta\omega_n)t}c_m^{(1)*}(t)\langle nm|f_{xc}|00\rangle\end{aligned} \tag{4.8}$$

where $\langle ij|f_{\mathrm{xc}}|kl\rangle = \int d\boldsymbol{r}\int d\boldsymbol{r'}\varphi_i^*(\boldsymbol{r})\varphi_j^*(\boldsymbol{r'})f_{\mathrm{xc}}(\boldsymbol{r},\boldsymbol{r'})\varphi_k(\boldsymbol{r})\varphi_l(\boldsymbol{r'})$. N is the number of electrons. Since the Kohn-Sham orbitals are real, the notation of the kernel term may be simplified as follows:

$$\langle n0|f_{\mathrm{xc}}|0m\rangle = \langle nm|f_{\mathrm{xc}}|00\rangle = f_{\mathrm{xc}}^{nm} \tag{4.9}$$

By analogy with linear response theory again, we impose that integration provides the linear response coefficients under the form

$$c_n(t) = \tilde{X}_n(\omega)e^{\mathrm{i}(\Delta\omega_n+\omega)t} + \tilde{X}_n(-\omega)e^{-\mathrm{i}(\omega-\Delta\omega_n)t} \tag{4.10}$$

where $\tilde{X}_n(\omega)$ and $\tilde{X}_n(-\omega)$ are to be determined.

Inserting the decomposition 13.9 into the time-dependent KS equation 4.4, identification of terms for $m > 0$ gives the equations of Casida

$$\begin{aligned}(\Delta\omega_n-\omega)\,\tilde{X}_n(-\omega) &= -\frac{W_{n0}}{2\hbar} - N\sum_{m>0} f_{\mathrm{xc}}^{nm}\left(\tilde{X}_m(-\omega)+\tilde{X}_m^*(\omega)\right) \\ (\Delta\omega_n+\omega)\,\tilde{X}_m^*(\omega) &= -\frac{W_{n0}^*}{2\hbar} - N\sum_{m>0} f_{\mathrm{xc}}^{nm}\left(\tilde{X}_m(-\omega)+\tilde{X}_m^*(\omega)\right)\end{aligned} \tag{4.11}$$

which can be summarized under matrix form [109]

$$\left(\begin{bmatrix}\boldsymbol{A} & \boldsymbol{B}\\ \boldsymbol{B}^* & \boldsymbol{A}^*\end{bmatrix} - \omega\begin{bmatrix}\mathbf{1} & \mathbf{0}\\ \mathbf{0} & -\mathbf{1}\end{bmatrix}\right)\begin{bmatrix}\tilde{\boldsymbol{X}}(-\omega)\\ \tilde{\boldsymbol{X}}^*(\omega)\end{bmatrix} = -\begin{bmatrix}\boldsymbol{\mathcal{V}}\\ \boldsymbol{\mathcal{V}}^*\end{bmatrix} \tag{4.12}$$

where $\boldsymbol{\mathcal{V}}_j = \dfrac{W_{j0}}{2\hbar}$, $\boldsymbol{A}_{ij} = \delta_{ij}\Delta\omega_i + Nf_{\mathrm{xc}}^{ij}$ and $\boldsymbol{B}_{ij} = Nf_{\mathrm{xc}}^{ij} \neq 0$.

This represents a system of non-linear coupled equations which are to be solved iteratively. The number of eigensolutions admitted by the Hessian matrix operator of the left-hand side is maximized by the dimension of the matrix, which prevents from describing more than single excitations. In contrast, beyond the adiabatic approximation, the kernel f_{xc}^{ij} and thus the Hessian matrix are frequency-dependent, which allows to explore a larger space of eigensolutions, in particular multiexcitations.

4.3.1 Tamm-Dancoff approximation (TDA)

A common approximation is the so-called Tamm-Dancoff approximation (TDA). In this approximation, excitations and de-excitations are turned independent by setting $\boldsymbol{B} = \boldsymbol{0}$ [110]. The equation 4.12 reduces to the system

$$\begin{cases} (\boldsymbol{A} - \omega)\, \tilde{\boldsymbol{X}}(-\omega) = \boldsymbol{\mathcal{V}} \\ (\boldsymbol{A}^* + \omega)\, \tilde{\boldsymbol{X}}^*(\omega) = \boldsymbol{\mathcal{V}}^* \end{cases} \tag{4.13}$$

The formalism is then equivalent to a configuration interaction singles (CIS) method.

4.4 Practical considerations

4.4.1 Expansion over a basis

In practice, the orbitals are expanded over a basis set of atomic functions $\{\chi_\mu(\boldsymbol{r})\}$ (see LCAO in section 1.4). Gaussian-type functions, localized on each atom μ, are often used for molecular studies due to their convenient integration properties.

$$\phi_i(\boldsymbol{r}) = \sum_{\mu=1}^{M} c_{\mu i} \chi_\mu(\boldsymbol{r}) \tag{4.14}$$

The whole resolution consists in calculating the expansion coefficients $c_{\mu i}$ of the Kohn-Sham orbitals $\phi_i(\boldsymbol{r})$ over the atomic functions with a self-consistent procedure. The expression of the Kohn-Sham orbitals is then injected into equation 3.23 to obtain the energy of the ground-state.

It is worth to notice that the Kohn-Sham determinants are single determinants that should not be assimilated to the Hartree-Fock single determinant. Indeed, the auxiliary and the Hartree-Fock problem are both expressed within the one-electron approximation and thus satisfy the equation 1.23 but the Hamiltonians involved are different. Consequently, the Kohn-Sham (KS) and HF orbitals are different, and so are the determinants that are built over them.

4.4.2 Functionals

Along the years, various functionals were parametrized to approximate the exchange and correlation energy. The functionals are classified according to the approximations they

rely on.

In the first generation of approximation, the density is assumed to be uniform (homogeneous electron gas) and is only computed locally, without considering the shape of the density around. This constitutes the local density approximation (LDA).

The first improvement was to consider a (more realistic) non-uniform electronic density, and to account for its variations using the gradient of the density. Such non-local approaches are termed generalized gradient approximations (GGA). The well-known Becke88 [111], PW (Perdrew-Wang) [112], and PBE (Perdew-Burke-Ernzerhof) [113] exchance functionals are built over this approximation.

Finally, hybrid exchange-correlation functionals are obtained by combining a part of GGA functionals for exchange and correlation and a part of (exact) HF exchange. Among these, the range-separated functionals combine different ratios between the GGA and HF contributions at short range and long range.

The formulation of B3LYP was proposed by Becke in 1993 [114] and has been one of the most-used functional for calculations on molecular system since then. It combines the B88 gradient-corrected functional for the exchange energy and the LYP [115] functional for the correlation energy.

The CAM-B3LYP functional was used for DFT and TDDFT calculations in this work. As a range-separated functional, CAM-B3LYP allows a better long-range description by distinguishing the expression of the exchange-energy kernel at short and long ranges, the two of them being connected by a parametrized error function. It was built from the famous hybrid functional B3LYP, augmented with the long-range correction for exchange of Tawada [116] .

The accuracy of CAM-B3LYP is equivalent to the one of B3LYP for atomic ionization energies and shows significant improvements for excitation energies, charge-transfer excitations, and oscillator strengths [117]. These improvements make CAM-B3LYP suitable for DFT and TDDFT calculations on molecular systems such as those studied in the present work, as mentioned in the literature [118, 119].

4.4.3 Vibronic spectra

In this paragraph, we briefly summarize the approach used for the calculations of vibrationally-resolved electronic spectra with the Gaussian package [62, 120].

The vibrationally-resolved electronic spectrum (transitions between vibronic states) can be computed analytically under the harmonic approximation. This is usually done in the framework of the Franck-Condon (FC) approximation, and requires the calculations of the associated FC factors [121]. In this thesis, we only focus on optical absorptions.

The following notations will be used thereafter

$'$: placed next to a letter/symbol, refers to the initial state

$''$: placed next to a letter/symbol, refers to the final state

N: represents the number of atoms in the molecule or system of interest

M: represents the number of normal modes in the molecule or system of interest

The intensity in optical absorption spectra is proportional to the rate of photon absorption per molecule and unit of radiant energy

$$I(\omega) \propto \sigma(\omega) = \frac{4\pi^2\omega}{3c} \sum_{'} \rho^{'} \sum_{''} |\langle \Psi^{'} | \boldsymbol{\mu} | \Psi^{''} \rangle|^2 \delta(E^{''} - E^{'} - \hbar\omega) \tag{4.15}$$

where $\rho^{'}$ is the Boltzmann population of an initial state, $\langle \Psi^{'} | \boldsymbol{\mu} | \Psi^{''} \rangle$ is the transient dipole moment between an initial state $|\Psi^{'}\rangle$ and a final one $|\Psi^{''}\rangle$ and ω is the radiation angular frequency.

For the values of ω corresponding to an energy of absorption, the intensity depends only on the population of the initial state and on the transition dipole moment associated with the transition.

Several approximations are made to get a convenient expression for the transition dipole moment. First, we work in the framework of the Born-Oppenheimer approximation, so the total wavefunction Ψ and dipole moment $\boldsymbol{\mu}$ may be decomposed into an electronic part and a nuclear one.

$$\langle \Psi^{'} | \boldsymbol{\mu} | \Psi^{''} \rangle = \langle \psi^{'}_{\mathrm{e}} \psi^{'}_{\mathrm{n}} | \boldsymbol{\mu}_{\mathrm{e}} | \psi^{''}_{\mathrm{e}} \psi^{''}_{\mathrm{n}} \rangle + \langle \psi^{'}_{\mathrm{e}} \psi^{'}_{\mathrm{n}} | \boldsymbol{\mu}_{\mathrm{n}} | \psi^{''}_{\mathrm{e}} \psi^{''}_{\mathrm{n}} \rangle \tag{4.16}$$

where the second term of the right-hand side vanishes due to orthogonal electronic states.

Then the rotation is separated from the vibration (Eckart condition [122, 123]) and we neglect the energetic contribution of the rotation with respect to the vibration. This will

appear in our notations by denoting the vibrational wavefunction $|\boldsymbol{v}\rangle = |\psi_v\rangle$ where the vector $\boldsymbol{v}$ contains the quantum numbers defined below. Considering all these approximations, the transition dipole moment reads

$$\langle \Psi^{'} | \boldsymbol{\mu} | \Psi^{"} \rangle \approx \langle \boldsymbol{v}^{'} | \boldsymbol{\mu}_{if} | \boldsymbol{v}^{"} \rangle \tag{4.17}$$

where $\boldsymbol{\mu}_{if} = \langle \psi_{\mathrm{e}}^{'} | \boldsymbol{\mu}_{\mathrm{e}} | \psi_{\mathrm{e}}^{"} \rangle$ is the electronic transition dipole moment.

Vibrations are assumed to be uncoupled under the harmonic approximation, which allows to write the total vibrational wavefunction as a product of monodimensional wavefunctions $\psi_{v_i}(Q_i)$ where Q_i is the normal coordinate describing the i^{th} vibration of the molecule. Under this approximation, the quantities v_i are good quantum numbers describing the vibrational state $|\boldsymbol{v}\rangle$.

$$|\boldsymbol{v}\rangle = |\prod_{i=1}^{M} \psi_{v_i}\rangle \tag{4.18}$$

Considering that the electronic transition is much faster than the nuclear motion, the electronic transition dipole moment can be Taylor-expanded around the equilibrium geometry of the final state. Finally, expanding up to the second order, the transition dipole moment reads

$$\begin{aligned} \langle \Psi^{'} | \boldsymbol{\mu} | \Psi^{"} \rangle \approx & \mu_{if}(\boldsymbol{Q}_0^{"}) \langle \boldsymbol{v}^{'} | \boldsymbol{v}^{"} \rangle \\ & + \sum_{k=1}^{M} \left(\frac{\partial \boldsymbol{\mu}_{if}}{\partial Q_k^{"}} \right)\Bigg|_{\boldsymbol{Q}_0} \langle \boldsymbol{v}^{'} | Q_k^{"} | \boldsymbol{v}^{"} \rangle \\ & + \sum_{k,l=1}^{M} \left(\frac{\partial^2 \boldsymbol{\mu}_{if}}{\partial Q_k^{"} \partial Q_l^{"}} \right)\Bigg|_{\boldsymbol{Q}_0} \langle \boldsymbol{v}^{'} | Q_k^{"} Q_l^{"} | \boldsymbol{v}^{"} \rangle \end{aligned} \tag{4.19}$$

The overlap integral $\langle \boldsymbol{v}^{'} | \boldsymbol{v}^{"} \rangle$ is usually called FC integral (or FC factor). Indeed, the zeroth-order term corresponds to a static electronic transition dipole, which is precisely the FC principle (the electron transition happens too fast for the nuclei to move). When transitions are allowed, $\boldsymbol{\mu}_{if}(\boldsymbol{Q}_0^{"}) \gg 0$ and this approximation provides very good results. Yet, in case of forbidden electronic transitions, it is required to consider the evolution of the transition dipole moment with nuclear coordinates to describe the vibrational progression properly. This would be done by the first-order term, and corresponds to the Herzberg-Teller (HT) approximation.

The transition dipole moment including the HT term can be expressed using only FC integrals between different vibronic states.

$$\begin{aligned}\langle \Psi^{'}|\boldsymbol{\mu}|\Psi^{"}\rangle \approx \mu_{if}(\boldsymbol{Q}_0^{"})\langle \boldsymbol{v}^{'}|\boldsymbol{v}^{"}\rangle \\ + \sum_{k=1}^{M}\left(\frac{\partial \boldsymbol{\mu}_{if}}{\partial Q_k^{"}}\right)\Bigg|_{\boldsymbol{Q}_0}\sqrt{\frac{\hbar}{2\omega_k^{"}}}\Big[\sqrt{\boldsymbol{v}_k^{"}}\langle \boldsymbol{v}^{'}|\boldsymbol{v}^{"}-1_k^{"}\rangle \\ + \sqrt{\boldsymbol{v}_k^{"}+1}\langle \boldsymbol{v}^{'}|\boldsymbol{v}^{"}+1_k^{"}\rangle\Big]\end{aligned} \tag{4.20}$$

where $|\boldsymbol{v}^{"}-1_k^{"}\rangle$ represents the same vibrational state as $|\boldsymbol{v}^{"}\rangle$ except for one quantum of energy in the i^{th} vibrational mode. In practice, the second-order term is not evaluated in the procedure implemented in G09. The first one is. We stopped at the FC order in this thesis, as we considered allowed transitions.

With G09, all the evaluated transitions start from the vibrational ground state of the initial electronic state. After some mathematical derivations, the FC integrals can be expressed as

$$\begin{aligned}\langle 0^{'}|\boldsymbol{v}^{"}\rangle =& \frac{1}{\sqrt{2v_i^{"}}}\Big[D_i\langle 0^{'}|\boldsymbol{v}^{"}-1_i^{"}\rangle + \sqrt{2(v_i^{"}-1)}C_{ii}\langle 0^{'}|\boldsymbol{v}^{"}-2_i^{"}\rangle \\ &+ \sum_{j=1,j\neq i}^{M}\sqrt{2v_j^{"}}C_{ij}\langle 0^{'}|\boldsymbol{v}^{"}-1_i^{"}-1_j^{"}\rangle\Big]\end{aligned} \tag{4.21}$$

The factors D_i and C_{ij} are elements of the following matrices:

$$\boldsymbol{C} = 2\boldsymbol{\Gamma}^{''1/2}(\boldsymbol{J}^T\boldsymbol{\Gamma}^{'}\boldsymbol{J}+\boldsymbol{\Gamma}^{''})^{-1}\boldsymbol{\Gamma}^{''1/2}-\boldsymbol{I}$$

$$\boldsymbol{D} = -2\boldsymbol{\Gamma}^{''1/2}(\boldsymbol{J}^T\boldsymbol{\Gamma}^{'}\boldsymbol{J}+\boldsymbol{\Gamma}^{''})^{-1}\boldsymbol{J}^T\boldsymbol{\Gamma}^{'}\boldsymbol{K}$$

where

$$\boldsymbol{J} = \boldsymbol{L}^{'-1}\boldsymbol{L}^{''}$$

$$\boldsymbol{K} = \boldsymbol{L}^{'-1}\boldsymbol{M}^{1/2}\boldsymbol{\Delta X}$$

$\boldsymbol{\Gamma}$ is the diagonal matrix of the reduced frequencies (one per electronic state)

$\boldsymbol{J}$ is the rotation matrix between the two sets of normal modes, also called Duschinsky matrix

$\boldsymbol{K}$ is the shift vector between the two minima

$\boldsymbol{L}$ is the transformation matrix from mass-weighted Cartesian coordinates to normal coordinates (one per electronic state)

$\boldsymbol{M}$ is the diagonal matrix of atomic masses

$\boldsymbol{\Delta X}$ is the vector representing the shift of the Cartesian coordinates of the nuclei between the two minima.

Finally these expressions show that the intensity of vibronic transitions, and thus the absorption spectrum, mainly depends on the shift between the electronic wells and on the mixing (rotation) of the vibrational modes during the transition.

Chapter 5

Effective orbital-based models for π-electrons

The references for this chapter are: [96, 97, 124–126].

We use the common shortcut "π- (or σ-) electrons" to denote the electrons that occupy π- (or σ-) orbitals, if the two systems are well separated.

In this chapter we recall the theoretical frameworks that will be used in the last part of this manuscript for constructing our vibronic model.

The systems we are interested in are conjugated hydrocarbons, so their photochemical properties are mainly governed by the frontier orbitals, which belong to the π-system (well separated from the σ-system). The final objective of our model will be to reproduce the photochemistry of *meta*-PPE (*e.g.* m23) that is divided in building blocks (*e.g.* p2 and p3). In particular, one must be able to account for the process of electronic excitation transfer that occurs from one block to another, using molecular orbitals of basic units (benzene and acetylene) as a starting point, see figure 5.1.

The construction of the model will thus be based on a multiscale approach, where each step will consist in accounting for a level of interaction within the system.

In a first step, we construct the frontier orbitals of the building blocks from the interaction between the frontier orbitals of the basic units. In such systems, the interaction between two orbitals is mainly proportional to the overlap, yielding relative energies that are correctly described through Hückel-type models. In addition, in the framework of those models, the correlation, Coulomb, and exchange interactions contribute as an offset

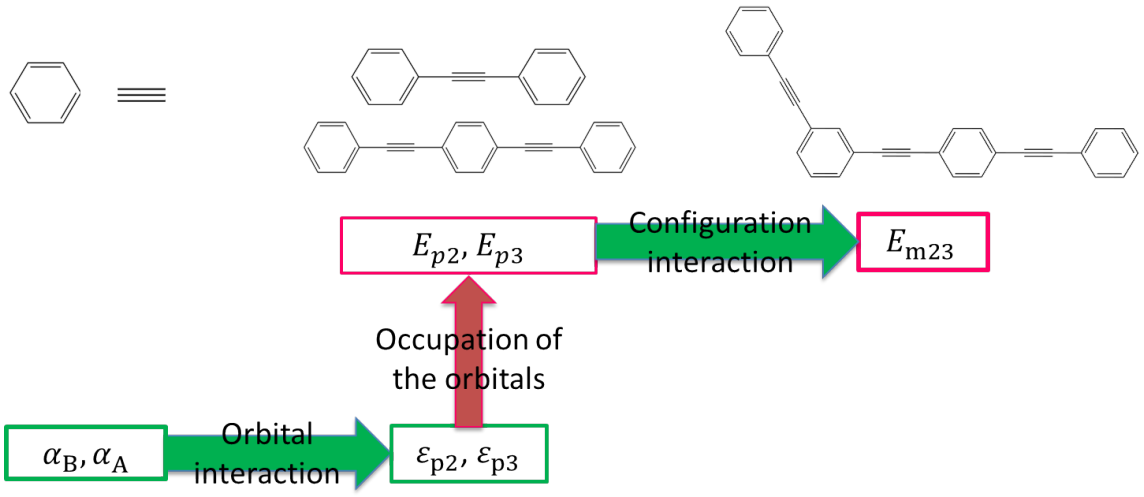

Figure 5.1: Scheme of the main steps of the vibronic model.

to the energy of the orbitals. This offset is almost equal for each orbital of the π-system, and thus does not affect the relative energies of the π-orbitals.

In a second step, we define the electronic states of the building blocks as configurations in terms of orbital occupations. The third step can be seen as an interaction between the configurations previously defined. Both will be considered within the framework of the Hubbard model.

5.1 Empirical models

In the the 1930s, Erich Hückel proposed several approximations aiming at studying the electronic structure of conjugated hydrocarbon molecules, which constitute the Hückel model [127]. Adapting some of the original approximations, Roald Hoffmann proposed an extension to the Hückel model in 1963 [128].

The interest of those models is that the interactions between the π-orbitals (and thus the corresponding energies of pertubation) are mainly proportional to their overlap S in the degenerate case or $\dfrac{S^2}{\Delta E}$ otherwise (ΔE being here the difference between the energies of the orbitals).

In these approaches, $\sigma-\pi$ separation is assumed, which is fair provided that π-electrons are more external and slower than σ electrons. Only the π-system, constituted of p atomic orbitals that are perpendicular to the molecular plane, is considered.

The one-electron approximation is applied, so the system is characterized by the sec-

ular determinant introduced in chapter 1, see equation 1.25. The treatment of the off-diagonal terms of $\boldsymbol{h}$ and $\boldsymbol{S}$ discriminates the Hückel and extended-Hückel models.

Within the Hückel model, the interaction through the one-electron Hamiltonian is neglected between non-adjacent atomic orbitals and the overlap between orbitals of different atoms are neglected. This reads

$$h_{ii} = \alpha_i \tag{5.1}$$

$$h_{ij} = \beta_{ij} \begin{cases} = 0 \text{ if } \varphi_i \text{ and } \varphi_j \text{ are not adjacent} \\ \neq 0 \text{ if they are} \end{cases} \tag{5.2}$$

$$S_{ij} = \delta_{ij} \tag{5.3}$$

where α_i corresponds to the ionization potential of the orbital χ_i (in a first approximation)
β_{ij} is the resonance integral between the electrons of atoms i and j
S_{ij} is the overlap integral between the atomic orbitals χ_i and χ_j.

The approximation of non-overlap 5.3 comes from the fact that the lateral overlap between π-orbitals is very small compared to the axial overlap between σ orbitals.

On the other hand, the overlap S_{ij} is considered between each atom pair (not only first neighbors) within the extended-Hückel model, and is used to define the interaction term between two atomic orbitals χ_i and χ_j through the Wolfsberg-Helmholtz approximation [129].

$$h_{ij} = K S_{ij} \frac{h_{ii} + h_{jj}}{2} \tag{5.4}$$

where $K = 1.75$ and is empirical.

In practice, the integrals α_i and β_{ij} used in Hückel calculations are not calculated but parametrized upstream. Thus, they have the same value for a given atom or pair of atoms separated by the distance r.

On the contrary, the Wolfsberg-Helmholtz approximation allows an empirical approximation of the bielectronic integrals, which is a step afore the Hückel method. The overlaps are calculated and vary with internuclear distances.

The validity of the results from the Hückel model is actually qualitatively comparable to the accuracy of self-consistent calculations for fully conjugated hydrocarbon molecules.

In particular, the Hückel models yield simple analytical results that reflect the main physical phenomena at the origin of the chemical properties of the system. Consequently, extended-Hückel calculations will also be presented later on as guides for the construction of the vibronic model.

Yet, such models can only provide energies of orbitals, which differ from the energies of the electronic states by the electronic correlation, see figure 5.2. To account for this contribution, we will introduce in our model a penalty similar to the on-site repulsion U of the Hubbard model (see Part V).

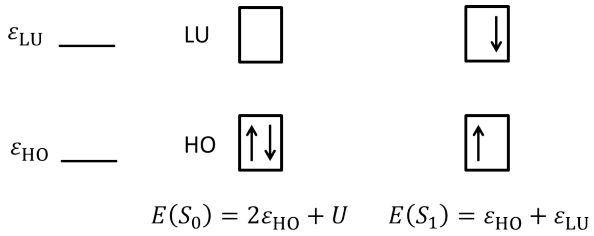

Figure 5.2: Representation of the electronic configurations associated with the ground state (left) and first excited state (right) from an excitonic point of view.

Part IV

Electronic structure of PPEs

Chapter 6

Introduction

To the best of our knowledge, the present part presents one of the most exhaustive theoretical characterization performed on the vibronic structure of various *para*- and *meta*-PPEs.

We start by assessing the validity of TDDFT for describing the electronic structure of the first excited states of PPEs. We show that, in this case, the calibration of computational methods requires to compare the calculated, vibrationally resolved, electronic absorption spectrum to the experimental one. The validity of the approximation that is commonly used in this context is discussed.

In chapter 8, we investigate the electronic structure of some *para*- and *meta*-PPEs, and put it in perspective with other typical molecular properties such as their equilibrium geometries, frontier orbitals, excitation energies, and the frequencies of specific vibrational modes. In particular, we enlighten that at the ground-state equilibrium geometry, typical bond lengths are almost identical within PPEs and from one PPE to another, irrespectively of the number of rings; this is less true at the equilibrium geometries of the first excited states, which are more likely to undergo boundary effects.

The excited states of *meta*-PPEs are localized on the building blocks including the common *meta*-phenylene, and the building blocks thus constitute chomophore units, similar to the *para*-PPEs. The common *meta*-phenylene is thus involved in two electronic states localized on each building block. In addition, the properties of the building blocks are equivalent to the ones of the corresponding *para*-PPEs. This stands in particular for the localization of the frontier orbitals, and leads to the introduction of the concept of

pseudo-fragment.

A full characterization of the electronic structure and properties of the (2,2)-*meta*-PPE (m22) is performed in chapter 9. Being the smallest *meta*-PPE, it is the simplest PPE that is likely to present conical intersections that couple the electronic states localized on different building blocks, and its symmetrical structure also imposes the symmetry of the geometry at such conical intersections, which facilitates their investigation. Several conical intersections are characterized, and components of the branching space are identified. An explanation to the unidirectional energy transfer in non-symmetrical *meta*-PPEs is proposed.

This analysis is in agreement with the literature [33, 42, 48–50, 52, 63], and supports the assumption according to which the excitation transfer along a non-symmetrical *meta*-PPE involves internal conversion *via* conical intersections between localized excited states.

The results of chapter 9 are used to investigate the unidirectional transfer in the non-symmetrical (2,3)-*meta*-PPE (m23) in the last chapter of this part. Its electronic structure along with typical properties are characterized at the equilibrium geometries of the first few electronic states. We insist on the nature of the excited states in terms of single transitions between molecular orbitals and on the topology (shape) of the latter. Weakly avoided crossings are identified with an energy difference of about 0.1 eV.

Stationary points were optimized and characterized with calculations performed at the CAM-B3LYP/6-31+G* level of theory, using the Gaussian09 package [62]. stationary points were characterized with corresponding frequency calculations.

Chapter 7

Validity of TDDFT approaches to study PPEs

Details about the present chapter were published [63] and the corresponding article is enclosed in Appendix A.

The vibrationally resolved absorption spectra of *para*-PPEs are computed with TDDFT (CAM-B3YP/6-31+G*) and compared to the experimental spectra [33,41] recorded at 77 K. The excellent agreement between both validates the adequacy of the TDDFT method to reproduce the electronic structure of PPEs. Our investigation lifts the disagreement raised in the literature [59,118,130] about the ability of TDDFT to describe the electronic structure of PPEs. In particular, we discuss the optimal conditions of the approximation that consists in comparing the calculated energy of the $0-0$ transition to the experimental absorption maxima to calibrate a theoretical method, which is known to fail in some cases. [118, 131, 132]

The vibrationally resolved absorption spectra thus computed are used for the assignment of the experimental absorption bands. Three main vibrational modes are thus identified as being involved in the $S_0 - S_1$ absorption process, and thus in the relaxation of S_1 after a Franck-Condon (FC) excitation. The most important one is the stretching of the acetylene bonds, which was already pointed out in the literature [49, 118].

Chapter 8

From *para*- to *meta*-PPEs

We investigate the electronic structure of the first few electronic states of some *para*- and *meta*-PPEs, and put it in perspective with other typical molecular properties such as their equilibrium geometries, frontier orbitals, excitation energies, and the frequencies of specific vibrational modes.

In particular, we identify that the ground-state equilibrium geometry is homogeneous in terms of bond lengths, both within a species and between different ones; this is less true at the equilibrium geometries of the first excited states due to boundary effects.

The localization of the first few excited states of *meta*-PPEs on constitutive building blocks including the common *meta*-phenylene is characterized from different perspectives. The similarity between the properties of the building blocks and the corresponding *para*-PPEs is highlightened.

From this, we introduce the concept of pseudo-fragments, whose molecular orbitals may interact within the framework of fragment decomposition, but which may share common atoms, here the common *meta*-phenylene.

8.1 *Para*-PPEs

8.1.1 Equilibrium geometries

The equilibrium geometries of the ground state, denoted $min\mathrm{S}_0$, and of the first excited state, denoted $min\mathrm{S}_1$, of p2 to p7 are pictured in figures 8.1 and 8.2, respectively. According to these, several qualitative observations can be made.

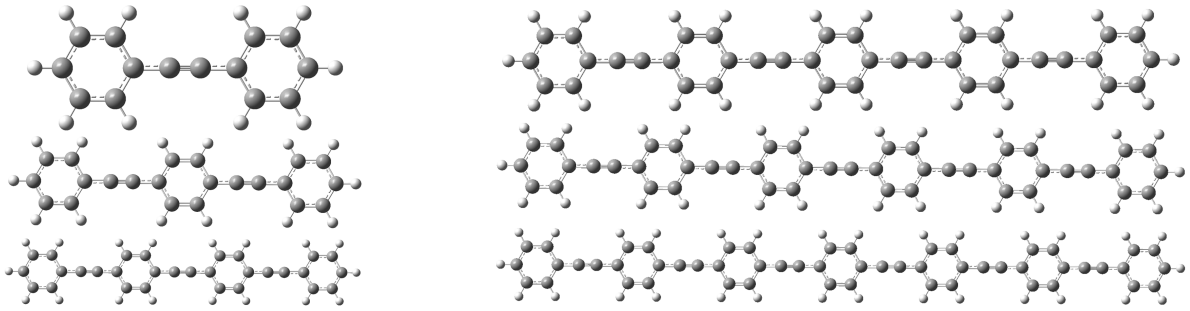

Figure 8.1: Optimized geometries of p2 to p7 in their respective ground states.

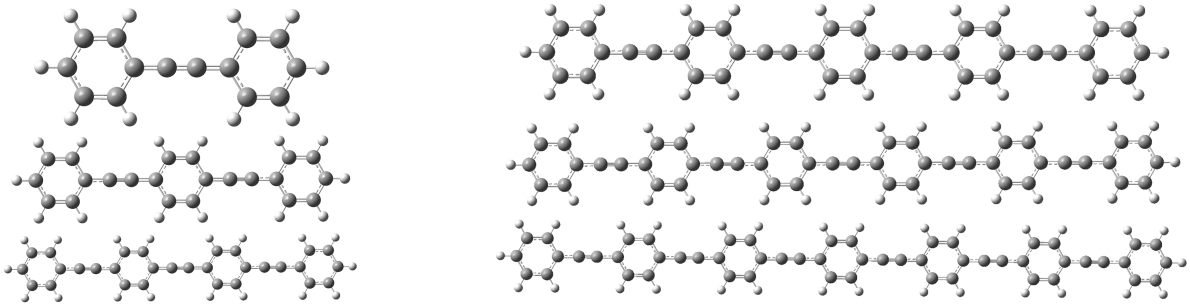

Figure 8.2: Optimized geometries of p2 to p7 in their respective first excited states.

First, a bonding scheme with an alternation of single-triple-simple bonds between aromatic rings seems to be typical of $min\mathrm{S}_0$ whilst cumulene-type bonds between quinoidal rings seem to be typical of $min\mathrm{S}_1$ (see representations of figure 8.4).

Then, the lengths of the acetylene bonds of a *para*-PPE are identical for $min\mathrm{S}_0$, but vary slightly at $min\mathrm{S}_1$. The same observation also stands for the lengths of the quinoidal bonds and the lengths of the internal bonds between a ring and an adjacent acetylene.

We confirm those observations by performing a quantitative analysis of the equilibrium geometries. Based on the previous observation, we identify three types of bond lengths that characterize the structure of PPEs. Those are the length of the quinoidal bonds (d_{quin}), the length of the acetylene bonds (d_{CC}), and the length of the internal bonds between a ring and an adjacent acetylene ($d_{\mathrm{C\text{-}Ph}}$), see figure 8.3.

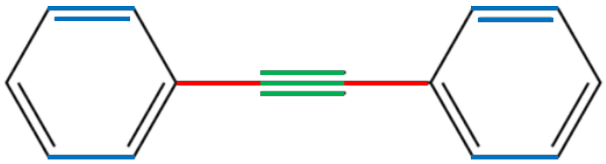

Figure 8.3: Acetylene (CC) bonds (green), quinoidal (quin) bonds (blue), and internal bonds bewteen acetylene and rings (C-Ph, in red).

Their variations can be quantified through the standard deviations to the mean values, which are reported for p2 to p7, in table 8.1 for $min\mathrm{S}_0$ and table 8.2 for $min\mathrm{S}_1$.

	mean $d_{\text{C-Ph}}$	$\sigma(d_{\text{C-Ph}})$	mean d_{CC}	$\sigma(d_{\text{CC}})$	mean d_{quin}	$\sigma(d_{\text{quin}})$
p2	1.431	0*	1.210	0*	1.389	0*
p3	1.429	0.001	1.210	0*	1.387	0.002
p4	1.429	0.001	1.210	0.000	1.387	0.002
p5	1.429	0.001	1.210	0.000	1.386	0.002
p6	1.428	0.001	1.210	0.000	1.386	0.002
p7	1.428	0.001	1.210	0.000	1.386	0.002
all *para*	1.429	0.001	1.210	0.000	1.386	0.002

Table 8.1: Lengths and standard deviations (in Å) of the characteristic bonds of *para*-PPEs in their ground state. * indicates a standard deviation that is zero for symmetry reasons.

	mean $d_{\text{C-Ph}}$	$\sigma(d_{\text{C-Ph}})$	mean d_{CC}	$\sigma(d_{\text{CC}})$	mean d_{quin}	$\sigma(d_{\text{quin}})$
p2	1.374	0*	1.255	0*	1.377	0*
p3	1.391	0.008	1.233	0*	1.374	0.009
p4	1.399	0.013	1.229	0.008	1.378	0.008
p5	1.404	0.013	1.223	0.007	1.377	0.008
p6	1.408	0.013	1.223	0.007	1.379	0.007
p7	1.410	0.012	1.219	0.006	1.379	0.007
all *para*	1.404	0.015	1.227	0.011	1.377	0.008

Table 8.2: Lengths and standard deviations (in Å) of the characteristic bonds of *para*-PPEs in their first excited state. * indicates a standard deviation that is zero for symmetry reasons.

At $min\mathrm{S}_0$, the bond lengths are very homogeneous in each molecule, that is that the values of $d_{\text{C-Ph}}$, d_{CC}, and d_{quin} are constant in the molecule. This is characterized by a weak standard deviation, here of 0.001 Å ($\sigma = 0$ correponds to a perfect homogeneity). The bonding scheme can thus be clearly identified as alternated single-triple-single bonds between aromatic rings over which the double bonds are fully delocalized.

In addition, from a *para*-PPE to another, the mean value of the bond length is constant up to 0.001 Å ($d_{\text{C-Ph}} = 1.43$ Å, $d_{\text{CC}} = 1.21$ Å, $d_{\text{quin}} = 1.39$ Å), with variations that are thus not significant. This property will be called transferability thereafter.

If finer tendancies were to be mentioned, we could notice that the mean value for internal and quinoidal bond lengths slightly decrease from the shortest PPEs to the largest ones.

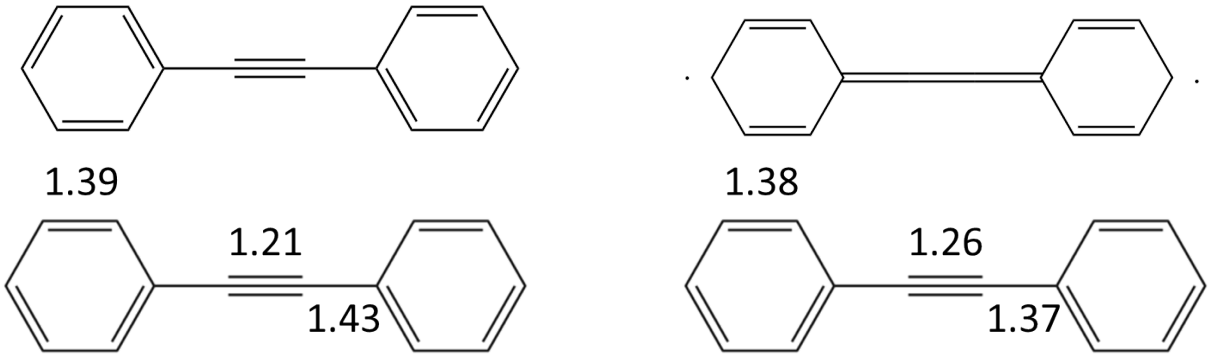

Figure 8.4: Bonding scheme in the ground state (left) and first excited state (right) of diphenylacetylene p2. Bond lengths are indicated in Å.

The bonding scheme at *min*S_1 involves shorter quinoidal and internal bonds than at *min*S_0, along with longer acetylene bonds. Compared to *min*S_0, this corresponds to stronger quinoidal and internal bonds and weaker acetylene bonds, which is consistent with the representation provided in figure 8.4.

Indeed, the strengthening of the quinoidal and internal bonds goes with an increase of their double-bond character, which comes from the localization of double bonds of the rings on the one hand, and the appearance of delocalization on the internal bonds on the other hand. Complementarily to this, the weakening of the acetylene bonds comes from a loss of electronic density on the triple bond that is no longer localized.

This can be understood reminding that the cumulenic bonding scheme in S_1 is in fact equivalent to a double-single-double bond alternation in the plane perpendicular to the molecule, see figure 8.5 (actual π-system).

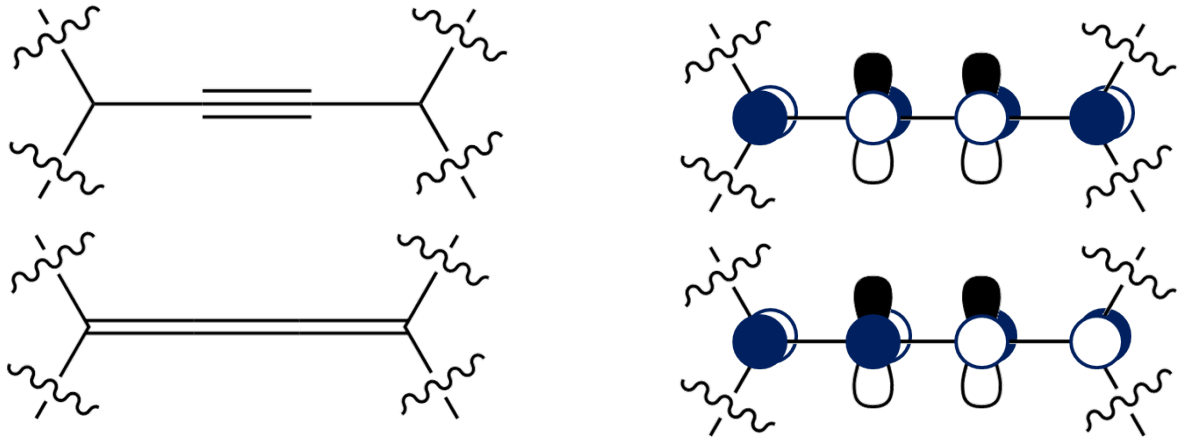

Figure 8.5: Orbital interaction of the alternated single-triple-single (top) and double-single-double (bottom) bonding schemes.

In addition, bond lengths are less homogeneous at *min*S_1 than at *min*S_0, which is

characterized by higher values for the standard deviation ($0.006 < \sigma < 0.013$ Å). More specifically, the quinoidal and internal bonds are longer at the extremities than at the center (the contrary for the acetylene bonds) in the same molecule, see figure 8.6. The inhomogeneity in the molecules can thus be interpreted as boundary effects.

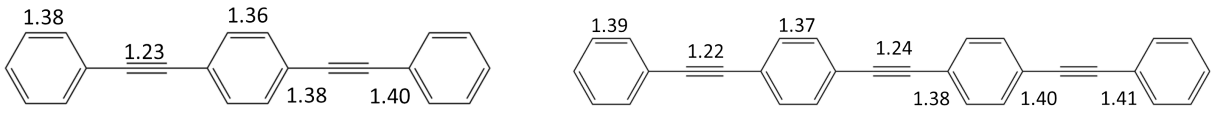

Figure 8.6: Main bond lengths at *min*S_1 for the 3- and 4-ring PPEs. Values are given in Å.

Those boundary effects are not specific to the first excited state but their impact is more important at *min*S_1 than at *min*S_0 due to their respective bonding schemes. Indeed, at *min*S_0, the rings and acetylenes are linked by single CC bonds. The π-system is thus localized on the rings and acetylene, which do not communicate much together, preventing the molecule from major deformations. On the contrary, *min*S_1 present an alternated double-single-double bonding scheme that carries the delocalization of the π-system all over the molecule. The expanse of this delocalization facilitates the reorganisation of the electronic density to adjust constraints such as border effects.

The transferability of the acetylene and internal bond lengths is also lost between *min*S_1 ($d_{\text{C-Ph}}$ goes from 1.37 Å to 1.41 Å, and d_{CC} goes from 1.26 Å to 1.22 Å) from p2 to p7.

One may note that the evolution of the quinoidal length is not monotonous; we are not able to rationalize this currently.

The configuration of the bonding scheme (up to boundary effects) is thus typical of either the ground state or the first excited state of *para*-PPEs.

8.1.2 Transition energies and frontier orbitals

Energies for the vertical (or Franck-Condon) and adiabatic transitions between S_0 and S_1 are reported in table 8.6. The adiabatic transition energies are the energy differences between the bottom wells of the two electronic potential energy surfaces.

The transition energies decrease as the number of rings increases, in agreement with the extension of the delocalization (organic chemistry approach) and the particule in a

Type of transition	p2	p3	p4
vertical	4.48	3.89	3.63
adiabatic	4.14	3.62	3.37

Table 8.3: Energies of the Franck-Condon (FC) and adiabatic $S_0 - S_1$ transitions in *para*-PPEs. Values are given in eV.

box (quantum chemistry approach).

In PPEs, excited states mainly result from single excitations[1] between the frontier orbitals ($\pi - \pi^*$ transitions) thereafter named HO and LU, respectively. The other significant contribution comes from the transition between the second frontier orbitals HO−1 and LU+1. From p2 to p7, this contribution gets more important to the expense of the HO–LU transition that still largely dominates, see table 8.4.

	f_{osc}	HO–LU	HO−1–LU+1
p2	0.9257	0.93	
p3	1.9208	0.91	0.05
p4	2.8965	0.86	0.09
p5	3.8637	0.80	012
p6	4.8299	0.74	0.15
p7	5.7926	0.68	0.17

Table 8.4: Contributions of the transitions between the pairs of frontier and second frontier orbitals to the first excited states of various PPEs at the minima of S_0, and the corresponding oscillator strengths, f_{osc}.

Since the main contributions to the first excited state are single transitions, there is no fundamental prescription against describing them with TDDFT (see also chapter 7).

From table 8.4, one can also note that the oscillator strengths associated with the first excited states regularly increase from p2 to p7, reflecting an increase in the overlap between the vibrational systems of the ground and first excited states in the matrix elements of the transition dipole.

[1] Coefficients c_i associated to each single excitation are given in the outputs of G09 energy calculations. Those coefficients are normalized over the transitions of α spins, which leads to $\sum_i c_i^2 = 1/2$. The total contributions (for α and β spins) correspond to twice the values of c_i^2 and sum up to one. In table 8.4, we only present the main contributions associated with $|c_i| > 0.10$ so the sum of the contributions is slightly less than one.

Since, at the minimum of the ground state, they largely dominate in the first excited state, we focus our analysis on the frontier orbitals of *para*-PPEs. The representation of the KS frontier orbitals is reported in figure 8.7 for p2 to p7.

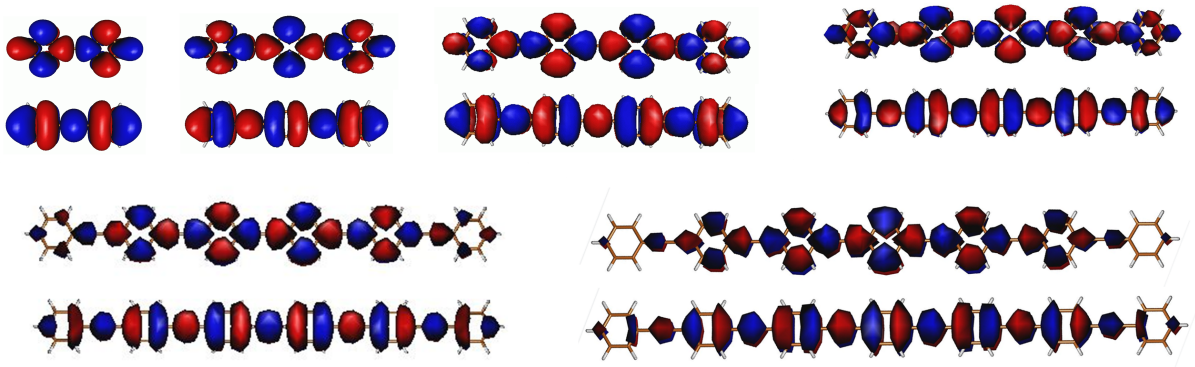

Figure 8.7: KS frontier orbitals of p2 to p7.

As expected for such conjugated molecules, the frontier orbitals belong to the π-system and are fully delocalized over the whole molecules (figure 8.7), except for boundary effects that arise with the increase of the number of rings.

It is worth to note that the frontier orbitals provided by extended-Hückel (XH) calculations (Caesar 2.0 software [133]) are similar to the KS ones from visual inspection, except for the boundary effects that are more pronounced on the XH orbitals.

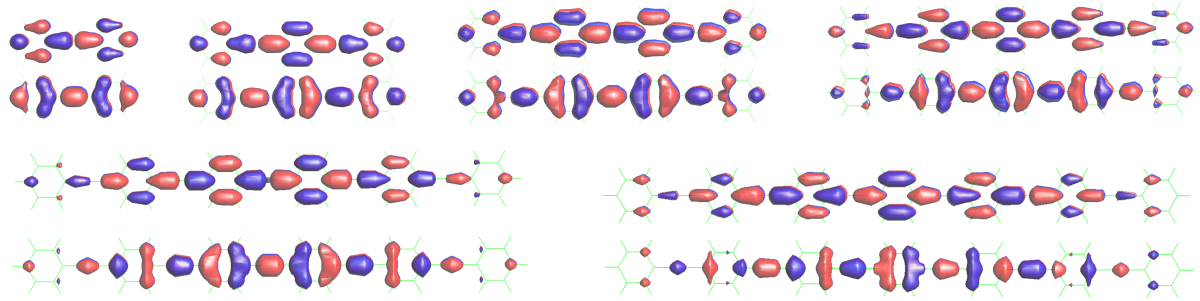

Figure 8.8: Frontier orbitals of p2 to p7 from extended-Hückel calculations performed with Caesar 2.0.

8.1.3 Vibrational frequencies

The minima are characterized with frequency calculations. As suggested in the literature [49, 118] and from our geometric analysis, the stretching mode of the acetylenes all in phase is characteristic of the electronic state.

In p2, p3 and p4, this mode is associated with values of the frequency at the equilibrium geometry of the ground state (around 2360 cm^{-1}) that are typical of the usual frequency

of the CC triple bond stretching, see table 8.8. The frequency associated to this mode at the equilibrium geometry of the first excited state is smaller (between 2185 and 2290 cm^{-1}), in agreement with the softening of the acetylene bonds.

8.2 Mixed *meta*-PPEs

We now present the results of the study of some *meta*-PPEs. Since one of the principal stakes of this thesis is to rationalize the unidirectional excitation transfer in PPEs, we start by considering only mixed *meta*-PPEs: m23, m34 and m234.

In the present section, we show that the first excited states of the *meta*-PPEs are localized on the constitutive building blocks, which mainly conserve the properties of the corresponding *para*-PPEs. In other words, the building blocks can be excited selectively.

Then, for each *meta*-PPE, we must consider at least as many excited states as building blocks. The electronic structure of a *meta*-PPE basically results from the addition of the electronic structures of its constitutive building blocks, which correspond to the electronic structures of the corresponding *para*-PPEs up to a perturbation.

We will present the manifestations of this in the orbital contributions, transition energies, geometric properties, and vibrational frequencies.

8.2.1 Frontier orbitals and pseudo-fragments

One of the most important aspects of the localization of the excited states is that is goes together with the localization of the frontier orbitals on the building blocks, and that the common *meta*-phenylene contributes to the orbitals localized on each building block [134]. In other words, *meta*-phenylenes must be considered as part and parcel of each building block, and they break the conjugation between them. This justifies our nomenclature for the *meta*-PPEs.

For a *meta*-PPE constituted of two building blocks, we consider the pair of frontier orbitals HO–LU and the pair of second frontier orbitals HO−1–LU+1, see figure 8.11. We use “near frontier orbitals” to term either the frontier or second frontier orbitals, or both.

The two orbitals within a given pair are mainly localized on the same building block, even if small contributions also exist on the rest of the molecule. These residual contributions actually ensure the orthogonality of the molecular orbitals and are not significant, so they are similar to the orthogonalization tails that are known in valence-bond theory.

Consequently, the near frontier orbitals are basically analogous (in shape and energy) to the frontier orbitals of the *para*-PPEs corresponding to the building block that on which they are localized, see figures 8.9 and 8.11.

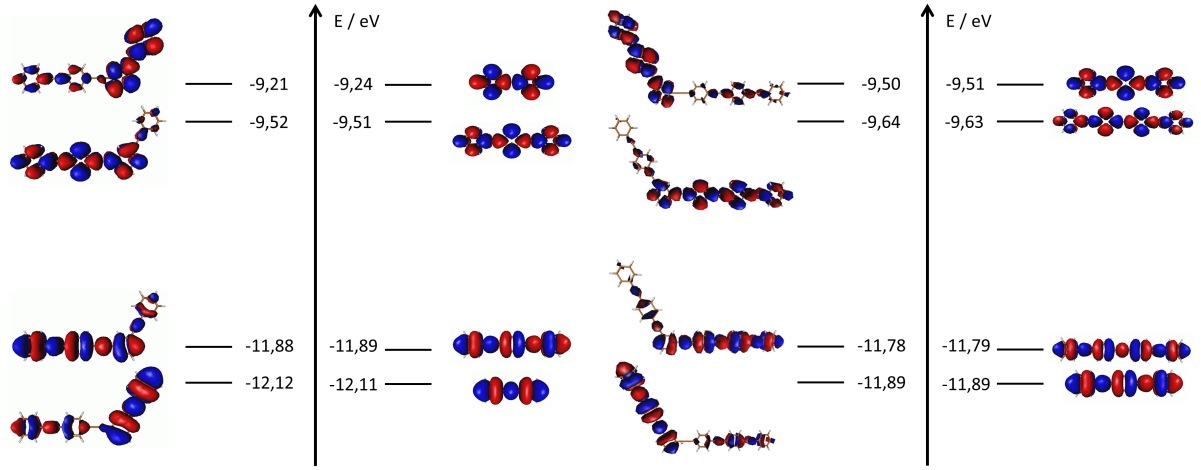

Figure 8.9: Frontier orbitals of m23 (left) and m34 (right), and schemes of principle of the additivity of the electronic structures of the building blocks in *meta*-PPEs.

More specifically, the near frontier orbitals of a *meta*-PPE can be interpreted as the result of the perturbative interaction between the frontier orbitals of *para*-PPEs localized on the corresponding building blocks, see figure 8.10. The frontier orbitals of the relevant *para*-PPEs can thus be seen as interacting as in the usual fragment method, except that the building blocks here share common atoms (namely the *meta*-phenylene).

Hence the notion of pseudo-fragment, that is a fragmentation of a complex molecular system according to orbital considerations. This fragmentation allows the pseudo-fragments to share a subfragment of common atoms when such a subfragment involves two orbitals together. In the present case, the pseudo-fragments of a *meta*-PPE are its constitutive building blocks, and the frontier orbitals of the pseudo-fragment are the frontier orbitals of the corresponding *para*-PPEs.

Of course, this also applies to *meta*-PPEs constituted of three (or more) building blocks, see figure 8.11. Then three pseudo-fragments must be taken into account and

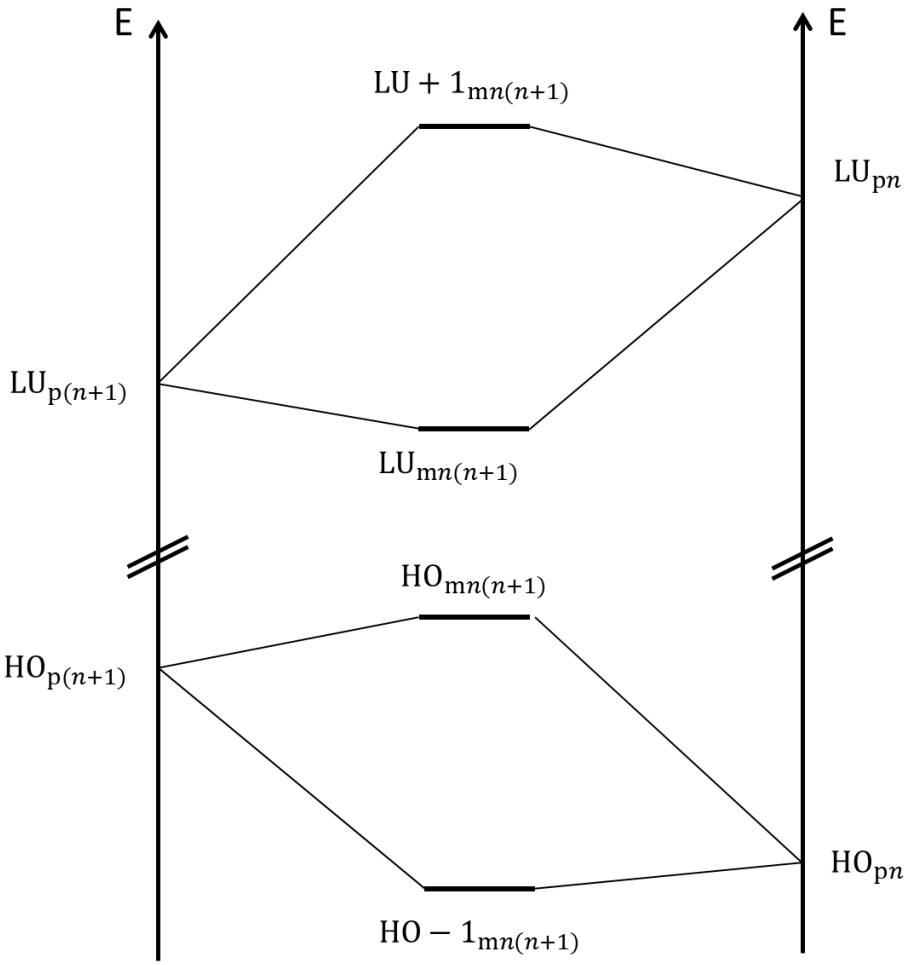

Figure 8.10: Scheme of principle of the perturbative interaction between the frontier orbitals of constitutive building blocks to form the near frontier orbitals of a *meta*-PPE.

yield three pairs of frontier orbitals. We term the pair HO−2,LU+2 the "third pair of frontier orbitals".

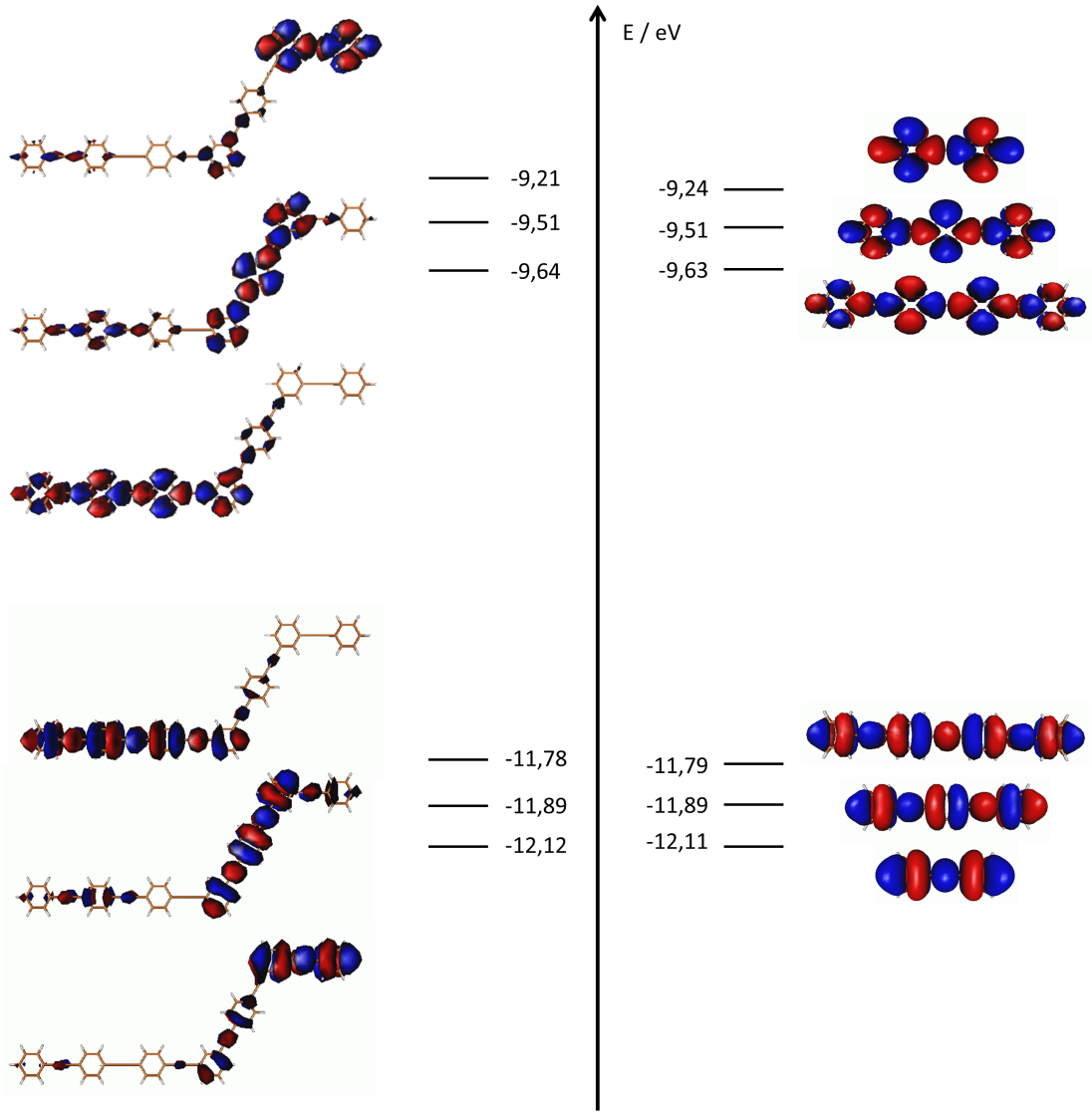

Figure 8.11: Frontier orbitals of m234 and scheme of principle of the additivity of the electronic structures of the building blocks in *meta*-PPEs.

8.2.2 Localized excitations and transition energies

Consistently with the definition of the pseudo-fragments, the first few excited states of a *meta*-PPE are dominated by single-electron transitions between pairs of near frontier orbitals ($S_1 \equiv$ HO–LU, $S_2 \equiv$ HO$-$1–LU+1, $S_3 \equiv$ HO$-$2–LU+2 if relevant), see table 8.5.

A given excited state is thus localized on a given pseudo-fragment (we may talk about "the excited state of a pseudo-fragment"), according to the location of the near frontier orbitals involved in the dominant transition, namely the location of the excitation is typical of the excited state. In particular, the excited states localized on the pseudo-fragments are ordered in the same way as the first excited state of each corresponding

para-PPE (the larger the number of rings, the lower the excited state). Each localized excited state can also be seen as a localized exciton, depicted as an excited electronic configuration involving the frontier orbitals of the pseudo-fragments, see figure 8.12.

For example, state S_1 mainly corresponds to the HO–LU transition, which is localized on the largest building block, that is the 3-ring for m23 (see gray line of table 8.5). The excitons associated to the first excited states of *meta*-PPEs are represented in figure 8.12.

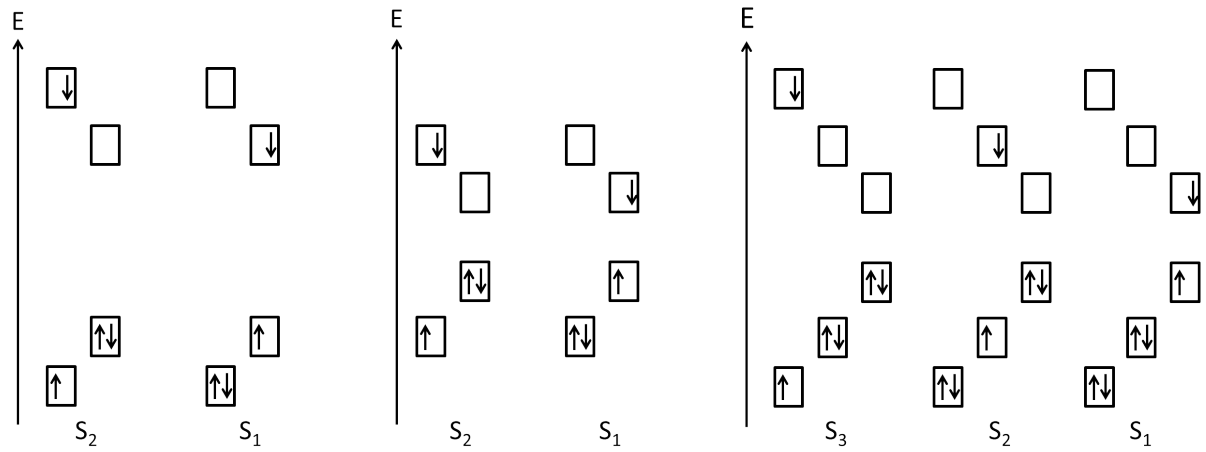

Figure 8.12: Representation of the excitons corresponding to the first excited states of m23 (left), m34 (middle), and m234 (right).

One may note that transitions occuring between orbitals located on different sites (HO−1–LU for example) also contribute to the excited states. Such transitions correspond to charge transfers[2], which are not well described with TDDFT calculations. If such small contributions are not critical for the description of the excited states, one should still keep an eye on them if they increase.

In addition, the oscillator strength associated to this excitation is $f_{\text{osc}} = 2.2183$, which is close in magnitude to the oscillator strength of the first excited state of the 3-ring *para*-PPE, $f_{\text{osc}} = 1.9208$ (see table 8.4), so the oscillator strengths also reproduce the local character of the excitation.

We will see in the the next chapters that this analysis may become more complicated at the minima of excited states.

In terms of energy, we verify that the transition energies of excited states of the pseudo-fragments are basically the same as the transition energies of S_1 in the corresponding

[2]The difference in the orbitals location can be examined through attachment and detachment matrices [135–137].

	Contributions to S_1				
	f_{osc}	HO–LU	HO−1–LU+1	HO−1–LU	HO–LU+1
d23	2.2183	0.82		0.04	0.04
d34	3.7141	0.65	0.03	0.09	0.08
d234	3.9857	0.64	0.03	0.07	0.10

	Contributions to S_2				
	f_{osc}	HO–LU	HO−1–LU+1	HO−1–LU	HO–LU+1
d23	0.8100	0.05	0.61	0.16	0.10
d34	1.3474	0.12	0.68	0.04	0.05
d234	1.4231	0.13	0.60	0.05	0.03

	Contributions to S_3					
	f_{osc}	HO1–LU1	HO2–LU2	HO2–LU1	HO1–LU2	HO2–LU3
d234	0.7968	0.05	0.55	0.05	0.11	0.04

Table 8.5: Contribution of the transitions between the near frontier orbitals to the first excited state of the PPEs at the minimum of S_0, and the corresponding oscillator strengths f_{osc}. Dominant contributions are reported in purple.

para-PPEs, which was already suggested in the literature [27,33,42,63]. This stands both at the electronic level with the vertical and adiabatic transition energies (calculated with the TDDFT method and reported in table 8.6), and at the molecular level with the gaps between the pairs of near frontier orbitals (calculated with the extended-Hückel method and reported on figures 8.9 and 8.11).

	FC transition energies					
	p2	m23	p3	m34	p4	m234
S_0–S_1	4.48	3.88	3.89	3.59	3.63	3.59
S_0–S_2		4.45		3.90		3.89
S_0–S_3						4.37

	Adiabatic transition energies					
	p2	m23	p3	m34	p4	m234
S_0–S_1	4.14	3.61	3.62	3.36	3.37	3.36
S_0–S_2		4.17		3.73		3.72
S_0–S_3						4.17

Table 8.6: FC and adiabatic transition energies in PPEs, and first excited states of *meta*-PPEs. The excitations are localized on 2-ring (blue), 3-ring (green) and 4-ring (red) building blocks, respectively. Values are given in eV.

8.2.3 Geometric properties

For m23 and m34, the equilibrium geometry of the ground state is homogeneous and presents the same bond lengths as in the *para*-PPEs (see figure 8.13 table 8.7).

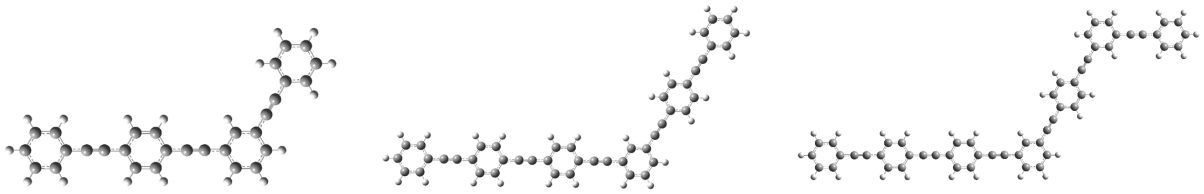

Figure 8.13: Optimized geometries of m23, m34, and m234 in their respective ground states.

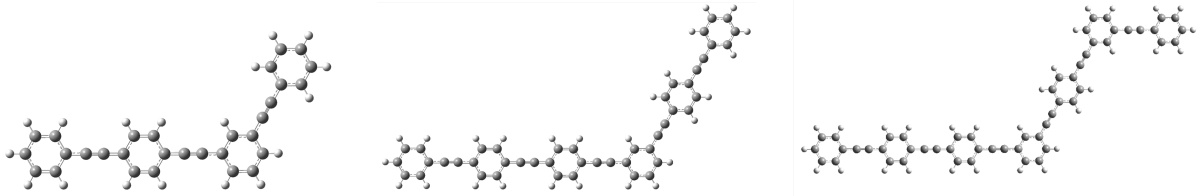

Figure 8.14: Optimized geometries of m23, m34, and m234 in their respective first excited states.

As for the relaxed excited states, the geometries of the building blocks are typical of a given electronic state in the same way as does the location of the pairs of near frontier orbitals (that is the larger the building block, the lower the excited state).

At the equilibrium geometry of S_1 in m23, the bond lengths of the 2-ring building block (the smallest one) are equal to the bond lengths of p2 at $min S_0$ (in particular for the alternated single-triple-single bonds between two rings), while the bond lengths of the 3-ring building block (the largest one) are equal to the bond lengths of p3 at $min S_1$ (in particular for the cumulene-type bonds between two rings).

This characterizes the location of the excitation on the 3-ring building block. This scheme is reversed at the equilibrium geometry of S_2 of m23, in agreement with the location of the excitation on the 2-ring building block. This point is schematically represented in figures 8.15, 8.16, and 8.17, and is valid for any *meta*-PPE.

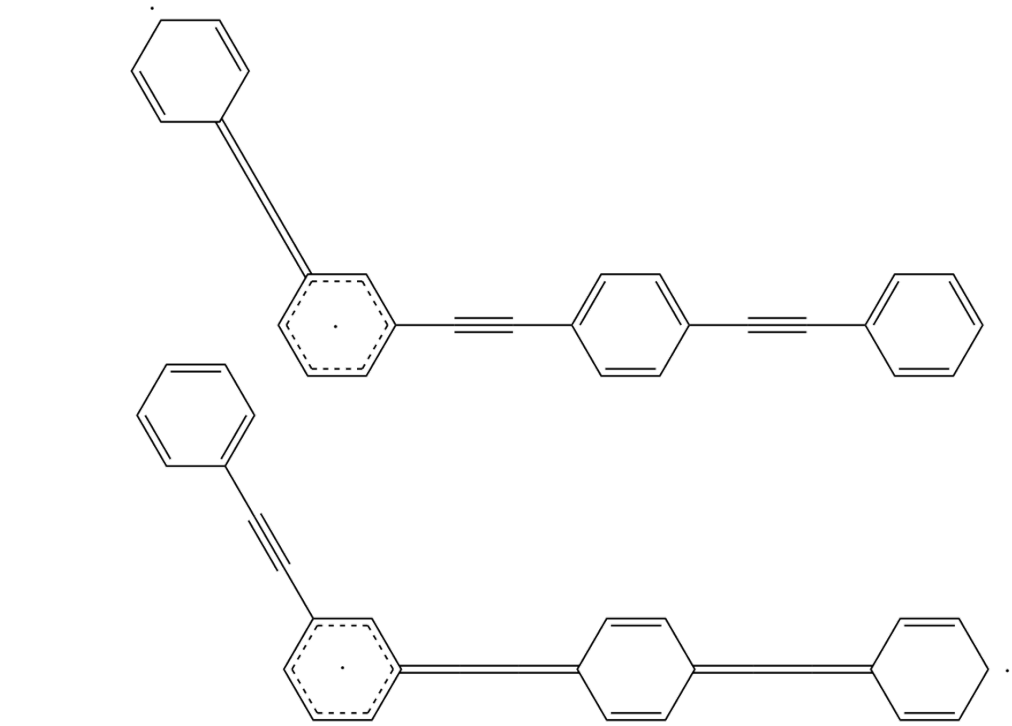

Figure 8.15: Representation of principle of the geometric localization of the excitation in m23.

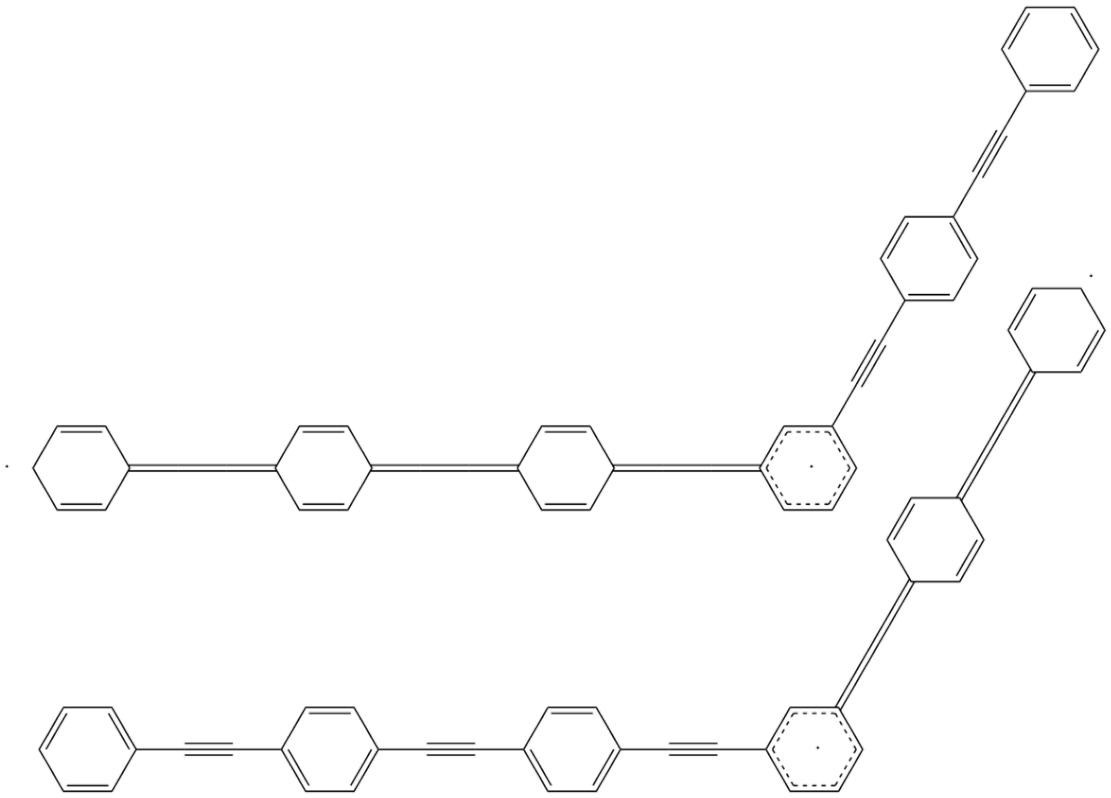

Figure 8.16: Representation of principle of the geometric localization of the excitation in m34.

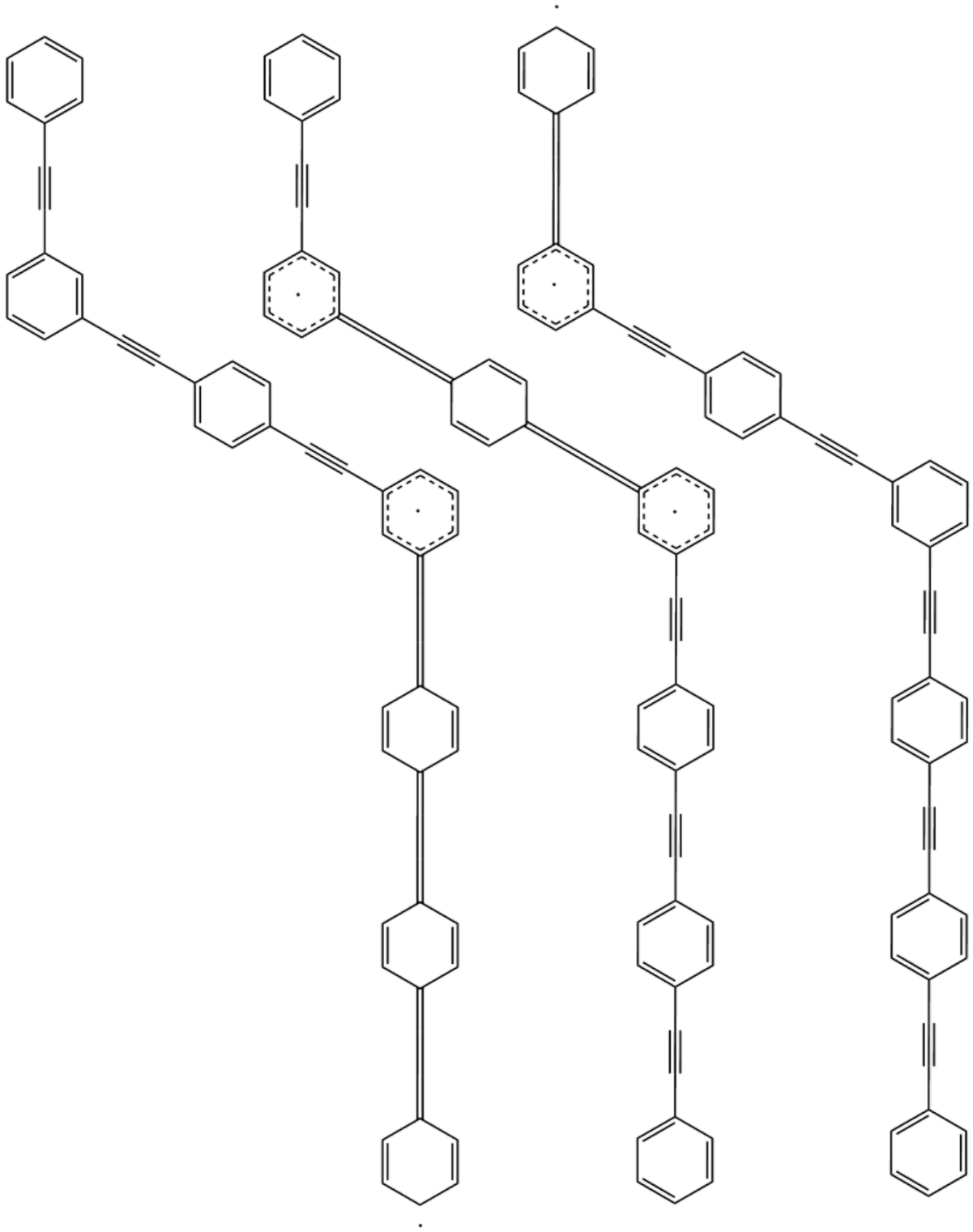

Figure 8.17: Representation of principle of the geometric localization of the excitation in m234.

2-ring building block

meta-PPE	eq. geom.	mean $d_{\text{C-Ph}}$	$\sigma(d_{\text{C-Ph}})$	mean d_{CC}	$\sigma(d_{\text{CC}})$	mean d_{quin}	$\sigma(d_{\text{quin}})$
m23	*min*S_0	1.431	0.000	1.210	0*	1.389	0.000
	minS_1	1.430	0.000	1.210	0*	1.391	0.003
	minS_2	1.384	0.001	1.245	0*	1.380	0.000
m234	*min*S_0	1.431	0.000	1.210	0*	1.389	0.000
	minS_1	1.431	0.000	1.210	0*	1.389	0.000
	minS_2	1.430	0.000	1.210	0*	1.391	0.002
	minS_3	1.385	0.001	1.245	0*	1.380	0.000

3-ring building block

meta-PPE	eq. geom.	mean $d_{\text{C-Ph}}$	$\sigma(d_{\text{C-Ph}})$	mean d_{CC}	$\sigma(d_{\text{CC}})$	mean d_{quin}	$\sigma(d_{\text{quin}})$
m23	*min*S_0	1.429	0.001	1.210	0.000	1.388	0.000
	minS_1	1.391	0.008	1.233	0.000	1.377	0.009
	minS_2	1.423	0.002	1.214	0.001	1.389	0.006
m34	*min*S_0	1.429	0.001	1.210	0.000	1.388	0.002
	minS_1	1.428	0.001	1.211	0.000	1.388	0.003
	minS_2	1.404	0.005	1.225	0.001	1.381	0.007
m234	*min*S_0	1.429	0.001	1.210	0.000	1.388	0.002
	minS_1	1.428	0.001	1.210	0.000	1.388	0.003
	minS_2	1.405	0.006	1.224	0.001	1.384	0.010
	minS_3	1.423	0.002	1.214	0.001	1.387	0.006

4-ring building block

meta-PPE	eq. geom.	mean $d_{\text{C-Ph}}$	$\sigma(d_{\text{C-Ph}})$	mean d_{CC}	$\sigma(d_{\text{CC}})$	mean d_{quin}	$\sigma(d_{\text{quin}})$
m34	*min*S_0	1.429	0.001	1.210	0.000	1.387	0.002
	minS_1	1.399	0.012	1.226	0.007	1.378	0.008
	minS_2	1.419	0.005	1.215	0.002	1.385	0.005
m234	*min*S_0	1.429	0.001	1.210	0.000	1.387	0.002
	minS_1	1.400	0.012	1.226	0.007	1.378	0.008
	minS_2	1.419	0.005	1.216	0.003	1.385	0.005
	minS_3	1.429	0.001	1.210	0.000	1.387	0.005

Table 8.7: Mean lengths and standard deviations (in Å) of the characteristic bonds at the equilibrium geometries of the first few electronic states, observed building block by building block, for different *meta*-PPEs. A gray line indicates that at the equilibrium geometry of state S_X, of the *meta*-PPE, the excitation is localized on the n-ring building block. * indicates a standard deviation that is zero for symmetry reasons.

8.2.4 Vibrational frequencies

Finally, the local character of the first few excited states of the *meta*-PPEs also appears in specific vibrational frequencies. More specifically, the frequency of a local vibration mode is essentially governed by the number of rings of the entity (building block or *para*-PPE)

and whether or not it is locally excited electronically.

The stretching modes of the acetylenes, denoted AA-modes, are the most representative for this. At *min*S_0, the first electronic states show several AA-modes localized on different building blocks, for which all the bonds stretch in phase.

The frequency of the AA-mode in pn is typical of n (within 1 cm^{-1} in S_0 or 10 cm^{-1} in S_1) and of the electronic state; it is preserved for the AA-mode localized on the n-ring building block of a *meta*-PPE, in the relevant electronic state. For example, $\bar{\nu}$ ranges from 2359 to 2361 cm^{-1} for any 3-ring entity in its local ground state.

Then, for a given excited state of a *meta*-PPE, the frequency of the AA-mode localized on the excited n-ring building block is similar to its frequency in S_1 of pn, whilst the frequencies of the AA-modes localized on the other building blocks are similar to their frequency in S_0 of the corresponding *para*-PPEs. For example, in m23, S_1 is localized on the 3-ring building block; the frequency of the AA-mode localized on that block is $\bar{\nu} = 2267 cm^{-1}$ (2268 in the first excited state of the 3-ring *para*-PPE), and the frequency of the AA-mode localized on the 2-ring building block is $\bar{\nu} = 2357 cm^{-1}$ (similar to the frequency in the ground state of the 2-ring *para*-PPE).

	At the ground-state minimum					
location	p2	m23	p3	m34	p4	m234
2-ring BB	2365	2367				2367
3-ring BB		2360	2359	2360		2361
4-ring BB				2356	2354	2356

	At the first-excited-state minimum					
location	p2	m23	p3	m34	p4	m234
2-ring BB	2185*	2357				2367
3-ring BB		2267*	2268*	2344		2344
4-ring BB				2285*	2290*	2285*

Table 8.8: Frequencies of the in-phase elongation of the acetylene bonds in the ground state of *para*-PPEs, and first excited states of *meta*-PPEs; the first column indicates the location of the normal mode. The excitations are localized on 2-ring (blue), 3-ring (green) and 4-ring (red) building blocks, respectively. Values are given in cm^{-1}. The exponent * indicates that the frequency is associated with a mode localized on a building block (or *para*-PPE) that is excited.

Chapter 9

Conical intersections in a symmetrical *meta*-PPE

The guideline of the present chapter is to identify and characterize conical intersections in *meta*-PPEs. To do so, we study the (2,2)-*meta*-PPE, denoted m22, being the smallest entity expected to present conical intersections between localized excited states. As will be shown below, the symmetry of m22 also helps in the search for conical intersections.

We start by a characterization of m22 at the equilibrium geometry of the first electronic state, S_1, which reveals a symmetrical double well (two lower-symmetry equivalent minima). Consistently with the previous part, those minima correspond to a localization of the excitation, either on one or the other building block, thus reflecting the properties previoulsy highlighted.

In addition, two transition states are characterized that are associated with electronic states of different irreducible representations within the high-symmetry group C_{2v}. Both connect the two S_1 equivalent minima and provide useful information to locate conical intersections.

Conical intersections are identified that are energetically accessible and components of the associated branching space are characterized below.

9.1 Localized excited states

We start by proving that *meta*-junctions hinder conjugation and thus are at the origin of the localized excited states, even in a symmetrical *meta*-PPE. The existence of such localized excited states, even in symmetrical *meta*-PPEs, confirms that pseudo-fragments can be used to interprete the electronic structure of any *meta*-PPE, which will be a key-point for the vibronic model we will present later on.

Pseudo-fragmentation is equivalent to dividing the total π-system of m22 into two local, superimposed π-subsystems on each building block. Thus, the evolution of the energy of the first excited state of p2 along the stretching of the acetylene bond is compared to the evolution of the first excited states of m22 along the stretching of one acetylene bond (the other one being frozen to the equilibrium distance at the ground state).

Along these cuts, it appears that the equilibrium geometry of the ground state yields an avoided crossing between $S_{1,meta}$ and $S_{2,meta}$ for m22. In addition, the first excited state $S_{1,para}$ of p2 follows $S_{2,meta}$ for a contracted acetylene bond and $S_{1,meta}$ for an elongated bond. Thus, $S_{1,para}$ (which is a pseudo-fragment excited state) represents a prototype of diabatic state for m22 that is localized on a building block.

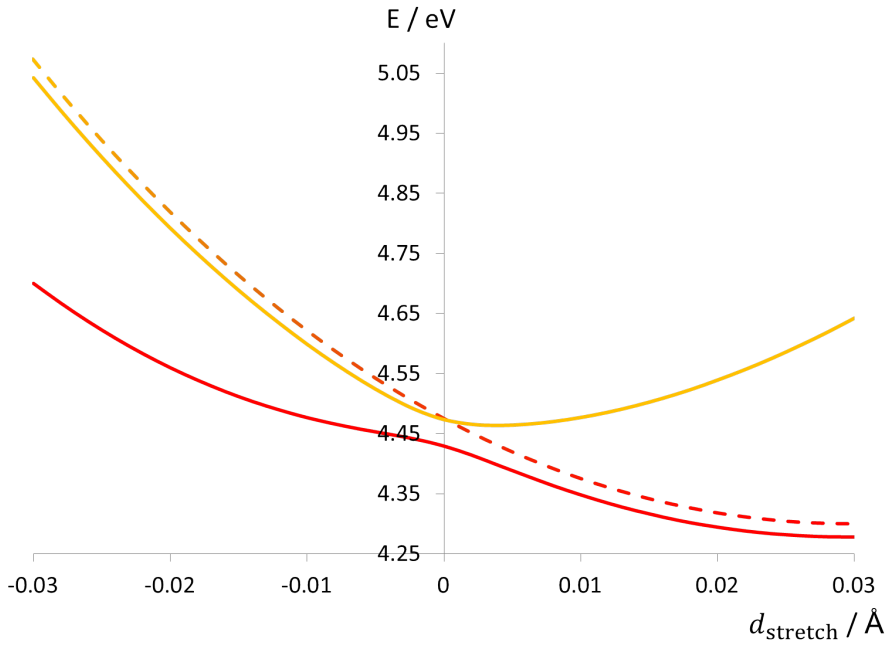

Figure 9.1: Evolution of the energies of the first two excited states along the elongation of one acetylene bond of m22 from its ground-state minimum (full lines). Evolution of the energy of the first excited state along the elongation of the acetylene bond of diphenylacetylene (dashed line). The bond lengths of both molecules are the same in the ground state up to 0.0001 Å.

9.2 Stationary points

The stationary points of m22 are now identified and characterized.

The study of the equilibrium geometries proves that all the properties of mixed *meta*-PPEs enlightened in the previous chapter also apply to the symmetrical m22, even though it is not obvious at first sight. In particular, the existence of localized excited states is assessed despite the higher symmetry of the molecule, considering the properties of the degenerate orbitals of benzene.

The analysis of the transition states, especially their geometries and vibrational frequencies, proves the role of the common *meta*-phenylene in lifting the degeneracy from conical intersections.

9.2.1 At the equilibrium geometries

The m22 species belongs to the C_{2v} point group of symmetry at the equilibrium geometry of the ground state $min\mathrm{S}_0$, see figure 9.2, which is consistent with standard chemical considerations. As expected from the analysis achieved in the previous chapter, the geometric characteristics of the building blocks are identical to the ones of the 2-ring PPE, see table 9.1. In particular, we easily recognize the alternation of single-triple-single CC bonds between two rings.

S_1 presents two equivalent equilibrium geometries $min\mathrm{S}_1$ and $min\mathrm{S}_1'$ that break the C_{2v} symmetry, see figure 9.2. Then, at $min\mathrm{S}_1$ and $min\mathrm{S}_1'$, m22 is similar to any of the mixed *meta*-PPEs we studied in the previous chapter, and shows all the characteristics of localized excitations. In terms of geometry, this appears with the alternation of single-triple-single CC bonds on one building block and the cumulenic bonding scheme on the other one, see table 9.1.

	$d_{\mathrm{CC,l}}$	$\mathrm{d_{C\text{-}Ph,l}}$	$d_{\mathrm{CC,r}}$	$d_{\mathrm{C\text{-}Ph,r}}$	d_{quin}	E_{S_0}	E_{S_1}	E_{S_2}	E_{S_3}
$\boldsymbol{min}\mathbf{S}_0$ (B_2)	1.210	1.431	1.210	1.431	1.402	0	4.43	4.47	4.61
$\boldsymbol{TS}_{B_2}$	1.233	1.401	1.233	1.401	1.419	0.18	4.25	4.33	4.52
$\boldsymbol{TS}_{A_1}$	1.230	1.398	1.230	1.398	1.447	0.19	4.29	4.30	4.53
$\boldsymbol{min}\mathbf{S}_1$ (C_s)	1.210	1.430	1.254	1.375	1.415	0.32	4.12	4.66	4.74

Table 9.1: Characteristic lengths (in Å) and energies (in eV) of the first electronic states of m22 at different stationary points. Indices "l" and "r" stand for "left hand side" and "right hand side", respctively.

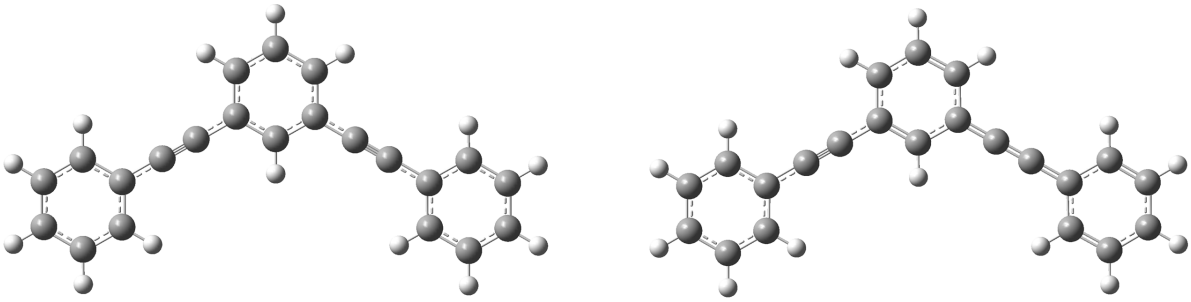

Figure 9.2: Optimized geometries at the minimum of the ground (left) and first excited (right) states.

Orbital analysis

We now show how the near frontier orbitals of the symmetrical m22 carry the same localization properties as the ones of mixed *meta*-PPEs. The near frontier orbitals were computed with both TDDFT and extended-Hückel methods, providing similar topologies. The energies we present come from the extended-Hückel calculations.

This analysis is not as trivial as expected at $min\mathrm{S}_0$, since the molecular orbitals are delocalized over the whole molecule for symmetry reasons. Again, we consider the two pairs of near frontier orbitals of m22; their shapes and the corresponding energies are reported in figure 9.3.

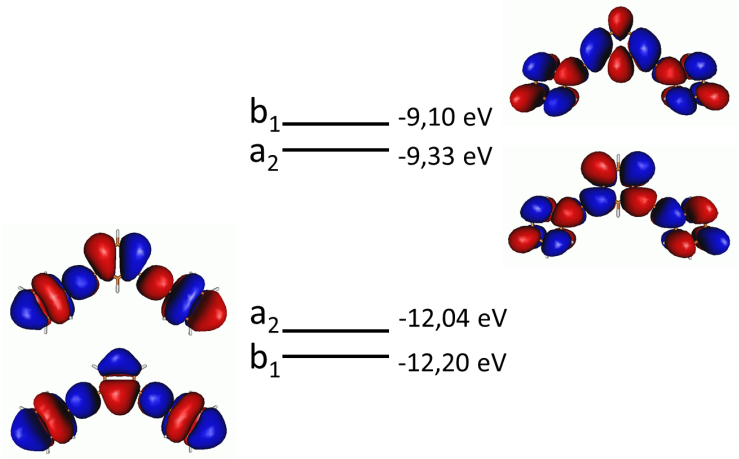

Figure 9.3: Pairs of molecular orbitals at the equilibrium geometry of the ground state. HO/HO−1 (left) and LU/LU+1 (right). Orbitals were calculated with TDDFT; the energies are provided by extended-Hückel calculations.

The shapes of the HO and HO−1 (LU and LU+1, respectively) is identical except on the central phenylene. The HO and LU are of symmetry a_2 whilst the HO−1 and LU+1 are of symmetry b_1 (in the C_{2v} point group), see figure 9.3.

For the occupied orbitals, the contribution on the central phenylene corresponds to the degenerate pair of HOs of benzene, sligthly deformed. Considering the properties of the degenerate orbitals of benzene, the contributions on the central phenylene can be seen as the sum and difference of two benzene HOs orientated along each building block, see figure 9.4.

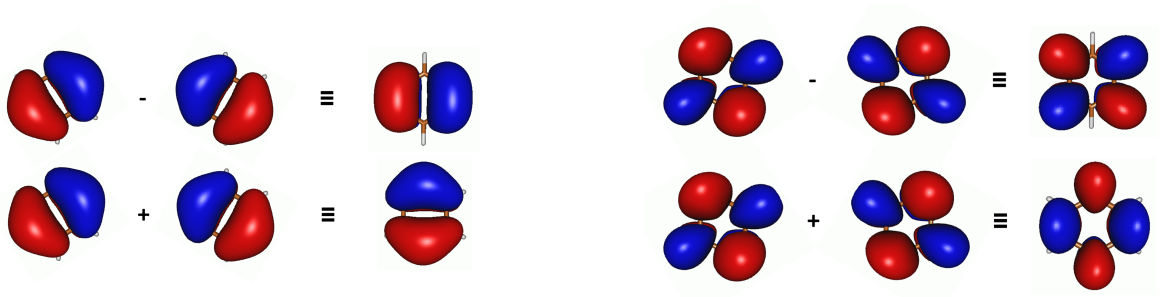

Figure 9.4: Rotation between two equivalent bases for the degenerate orbitals of benzene (occupied on the left, unoccupied on the right). The orbitals aligned with the building blocks form a non-orthogonal basis.

Consequently, one can also see the pair of HOs as the sum and difference of the HOs that are localized on the pseudo-fragments (figure 9.5), that is symmetrized orbitals. Contrarily to the pseudo-fragment orbitals, the symmetrized orbitals are not degenerate, so they are not eigenvectors. This lifting of degeneracy is due to (weak) through-space interactions in the orbitals, see figure 9.5. The orbital diagram illustrating this lifting of degeneracy is depicted in figure 9.6.

All this also stands for the unoccupied orbitals: the contribution on the central phenylene corresponds to the degenerate pair of LUs of benzene, sligthly deformed. Then, the contributions on the central phenylene can be seen as the sum and difference of two benzene LUs orientated along each building block, see figure 9.4.

At *min*S_1 and *min*$S_1^{'}$, the localization of the orbitals actually shows up. Indeed, *min*S_1 and *min*$S_1^{'}$ are non-symmetrical, so the two pseudo-fragments are not equivalent and the two pairs of near frontier orbitals are localized, as well as at the equilibrium geometries of mixed *meta*-PPEs, (see figure 9.7).

The energy order of the orbitals in a pair is consistent with their localization, see figure 9.8. Indeed, for the occupied orbitals, the interaction scheme on the CC bonds in terms

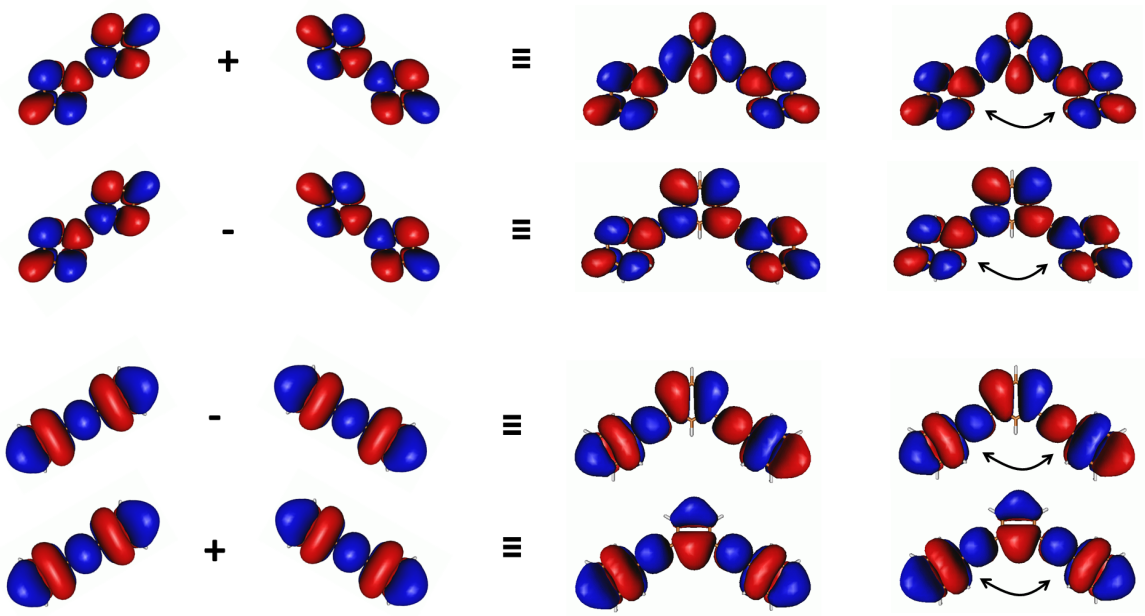

Figure 9.5: Decomposition of the near frontier orbitals (occupied on the bottom, unoccupied on the top) of m22 in terms of symmetrized orbitals coming from the sum and difference of orbitals localized on the building blocks. The orbitals aligned with the building blocks form a non-orthogonal basis. Secondary interactions are depicted on the right hand side.

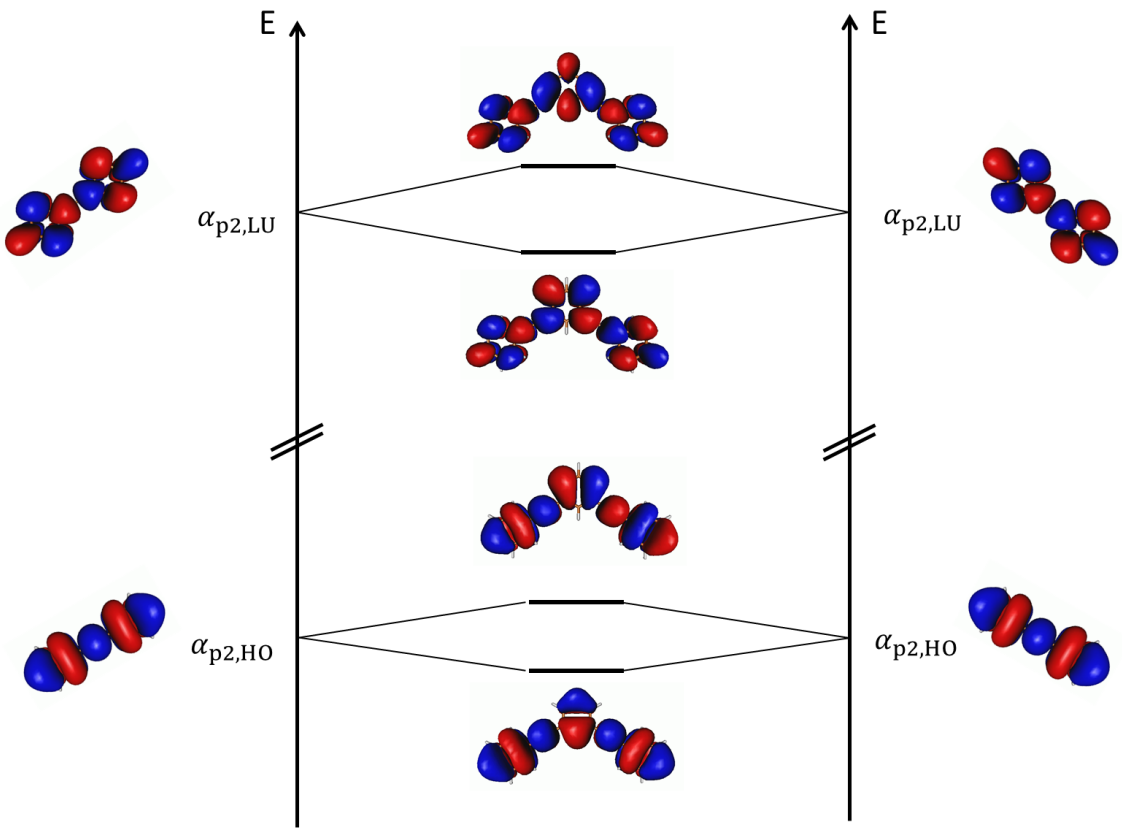

Figure 9.6: Composition diagram describing the interaction between the frontier orbitals of the pseudo-fragments of m22 by analogy with an orbital diagram.

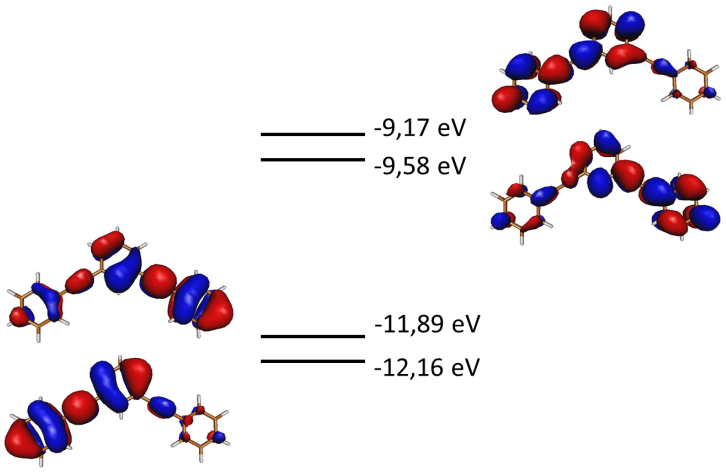

Figure 9.7: Pairs of molecular orbitals at the equilibrium geometry of the first excited state. HO/HO-1 (left) and LU/LU+1 (right). Orbitals were calculated with TDDFT; the energies are provided by extended-Hückel calculations.

of atomic orbitals between consecutive benzenes is: antibonding-bonding-antibonding. Considering that bonding interactions goes with shorter bonds and that antibonding interactions goes with larger bonds, this interaction scheme associated with the alternated bonding scheme yields lower energy.

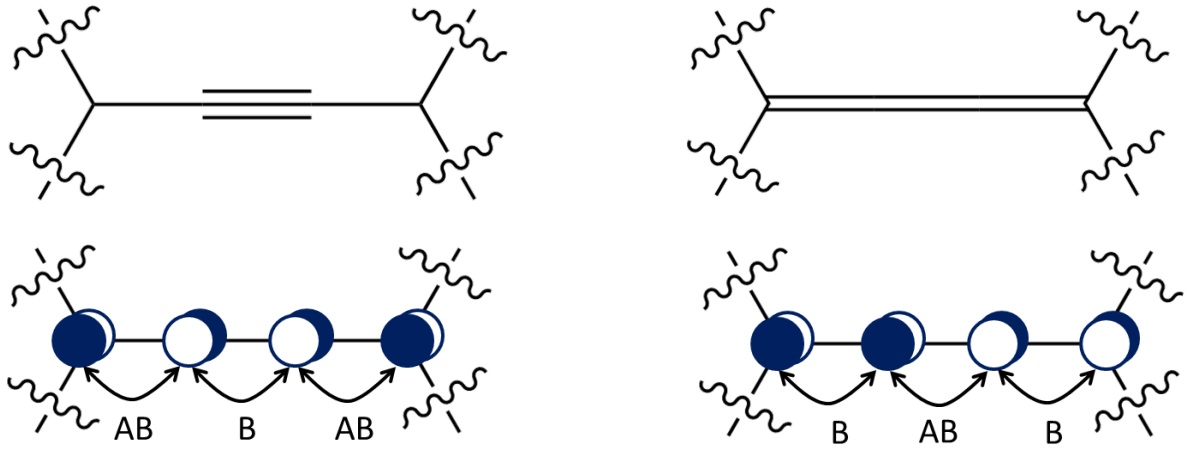

Figure 9.8: Bonding schemes and interpretation in terms of interaction between the orbitals; alternated bonding scheme (left), cumulenic-type bonding scheme (right). B stands for bonding interactions and AB stands for antibonding interactions.

On the contrary, the interaction scheme for the unoccupied orbitals is: bonding-antibonding-bonding and suits better with a cumulenic bonding scheme.

The energy difference between the two occupied (unoccupied) orbitals at $min\mathrm{S}_1$ is greater than the one at $min\mathrm{S}_0$ because the pseudo-fragment orbitals are no longer degenerate.

Transition analysis

At *min*S_0, the first two excited states result mainly from two transitions involving the four near frontier orbitals, see table 9.2.

The HO–LU transition can be considered as predominant in S_2 but two transitions contribute equivalently (and highly) to S_1, which was not expected in a first stage.

	At *min*S_0		At *min*S_1	
	Transition	Contribution	Transition	Contribution
S_1 (B_2 at *min*S_0)	HO−1 / LU	0.51	HO / LU	0.82
	HO / LU+1	0.43	HO−1 / LU	0.07
			HO / LU+1	0.05
S_2 (A_1 at *min*S_0)	HO / LU	0.76	HO−1 / LU	0.43
	HO−1 / LU+1	0.16	HO / LU+1	0.29

Table 9.2: Contributions of the main transitions to the first two excited states of m22 at *min*S_0 and *min*S_1.

This situation actually arises for symmetry reasons. Indeed, S_1 is of symmetry B_2, which discriminates the left from the right hand sides (provided the current orientation of our representations). Then, since this discrimination does not appear directly in the shape of the molecular orbitals (for symmetry reasons), it has to appear in the transitions involved and their contributions.

As an example, the simultaneous transitions HO-1→LU and HO→LU+1 with their respective contributions w_1 and w_2 are equivalent to a single transition between two mixed orbitals $\{w_1\text{HO-1} + w_2\text{LU}\}$ and $\{w_1\text{HO} + w_2\text{LU+1}\}$. In the case of equivalent contributions ($w_1 = w_2$), the mixed orbitals turn out to be the local orbitals, see figure 9.9.

In the present case, the contributions of these transitions to S_1 are not equal, yielding residual contributions analogous to orthogonalization tails.

This is the reverse situation to the one presented on figure 9.5, and thus proves that the two transitions contributing to S_1 are only due to symmetry, see figure 9.9.

At the minimum of S_1, no left-right symmetry constraints have to be fulfilled. Since both sides are not equivalent, it is important to notice that expansion of the transition orbitals is the larger on the side of the molecule presenting the alternated pattern.

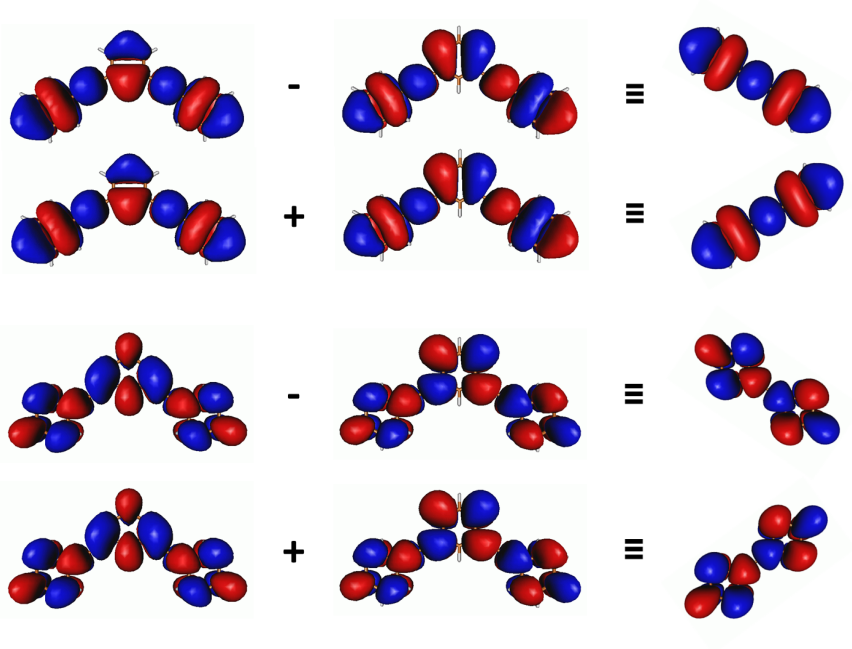

Figure 9.9: Combination of the symmetrized near frontier orbitals (occupied on the top, unoccupied on the bottom) of m22 into orbitals localized on the building blocks.

First, it is in agreement with the previous conclusion that the molecular orbitals are always localized on building blocks, the symmetrical structures being the only exceptions. This also stands for the corresponding transitions, provided that they imply orbitals located on the same building block.

Then, the HO–LU transition dominates in S_1 at its minimum (consistently with the observations made for mixed *meta*-PPEs), but no transition dominates in S_2 at this geometry (contrarily to what happens in mixed *meta*-PPEs), see table 9.2.

This simply comes from the fact that S_2 is not actually relevant as a "local excited state" of m22. Indeed, since the nature of the pseudo-fragments is the same, they yield similar transitions in terms of energy (typical of a 2-ring entity), see figure 9.6. In m23, S_1 and S_2 correspond to transitions in pseudo-fragments with different numbers of rings, which thus yield two non-symmetrical potentials (see figure 9.10). In m22, the two building blocks have the same number of rings so the excited states that are localized on them (allegedly S_1 and S_2) are associated with equivalent potentials. In other words, in m22, the two transitions that are localized on a building block are equivalent and thus lead to S_1.

It is worth to note that the transitions occuring between orbitals located on different

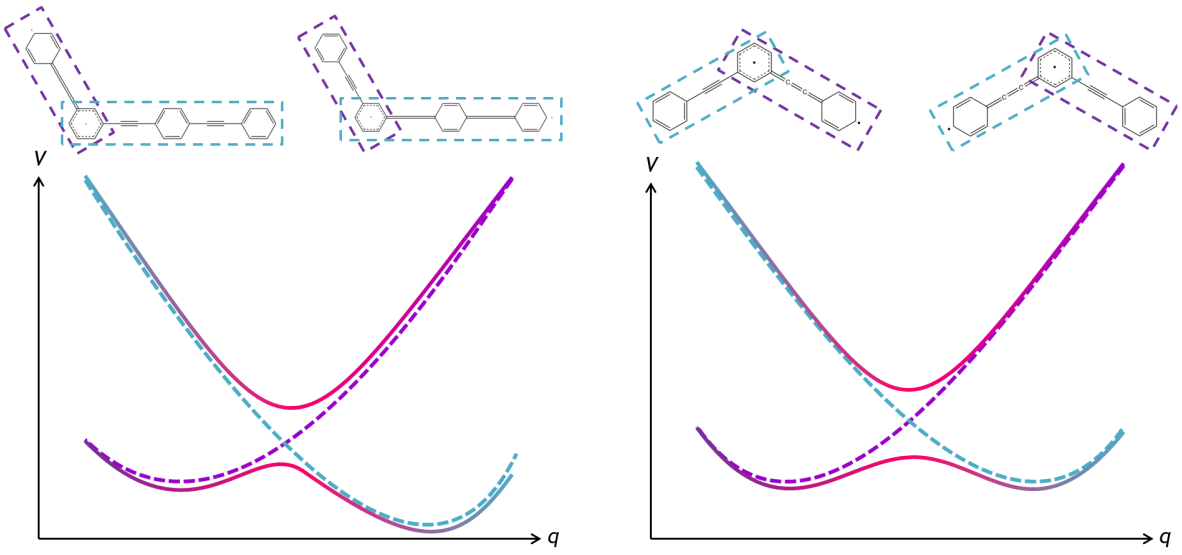

Figure 9.10: Scheme of the symmetrization of the first two localized excited states from m23 to m22. Full lines represent the adiabatic potentials of S_1 and S_2 whilst dashed lines represent the potential of localized excited states.

sites correspond to charge transfers[1], which are not well described with TDDFT calculations.

9.2.2 Transition states

Two transitions states are identified for S_1, that occur to be apparent minima within the C_{2v} symmetry point group. Both of them are directly connected to the two equivalent minima of S_1, along vibrational modes represented in figure 9.11. They are denoted TS_{B_2} and TS_{A_1}, respectively, according to the symmetry of S_1 at these geometries.

The transition frequency of TS_{A_1} is particularly intense: $\bar{\nu}(TS_{A_1}) = \mathrm{i}14875\mathrm{cm}^{-1}$. As we will show later on, this is due to the vicinity of a conical intersection.

Since they connect $min\mathrm{S}_1$ and $min\mathrm{S}_1'$, some of the geometric characteristics of TS_{B_2} and TS_{A_1} appear as a mix of the ones of $min\mathrm{S}_1$ and $min\mathrm{S}_1'$. In particular, the length of acetylene bonds in the transition states is the average of the lengths of each side of $min\mathrm{S}_1$ (or $min\mathrm{S}_1'$), see table 9.5.

The main difference between TS_{B_2} and TS_{A_1} resides in the *meta*-phenylene geometry, in particular the length of its quinoidal bonds, which is shorter for TS_{B_2}. They can be represented in terms of Lewis structure as a biradical quinoidal ring for TS_{B_2}, and a combination of two allyl-radicals in TS_{A_1}, see figure 9.12.

[1]The difference in the orbitals location can be examined through attachment and detachment matrices

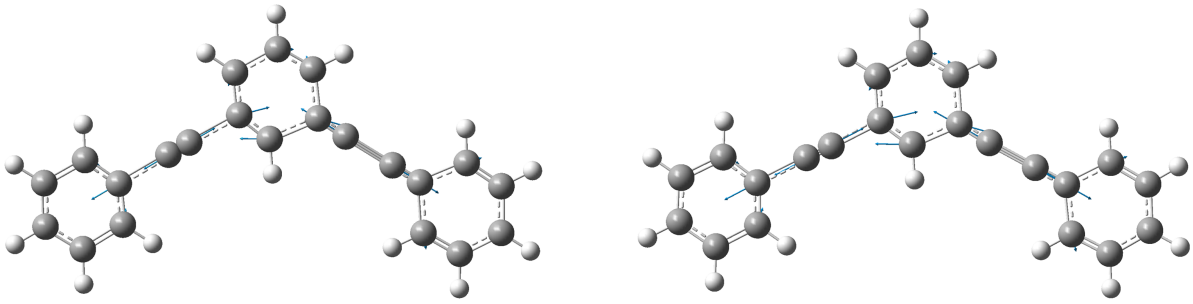

Figure 9.11: Transition mode of TS_{B_2} (left) and TS_{A_1} (right). The associated frequencies are $\bar{\nu}(TS_{\mathrm{B}_2}) = \mathrm{i}4892\mathrm{cm}^{-1}$ and $\bar{\nu}(TS_{\mathrm{A}_1}) = \mathrm{i}14875\mathrm{cm}^{-1}$.

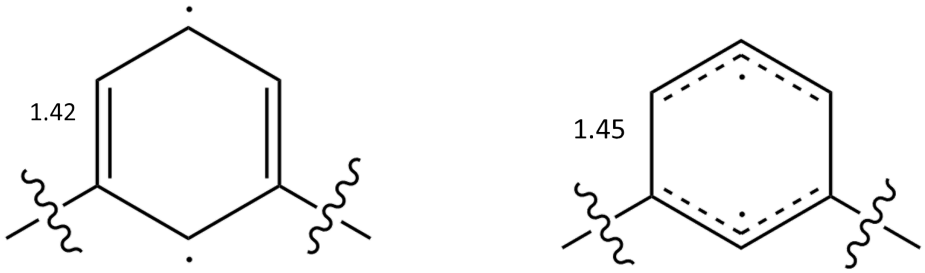

Figure 9.12: Lewis representations of the bonding schemes of the *meta*phenylenes of TS_{B_2} (left) and TS_{A_1} (right). Bond lengths are given in Å.

Then, it is expected (and confirmed right after) that the quinoidal bond play a crucial role in the vicinity of conical intersections.

One may note that such transitions states may have been studied as apparent minima in the C_{2v} subspace for their photochemical and physicochemical properties [44].

9.3 Exploration of the PES

Now, we explore the PES of m22 in search for conical intersections.

The potential energies of the relevant diabatic states cross between TS_{B_2} and TS_{A_1} by construction, which indicates that conical intersections energetically accessible can be found in the C_{2v}-space, especially between those two points. Thus, the first step is to explore the PES around the C_{2v} stationary points, following directions that preserve C_{2v} symmetry.

Other directions of the branching space are expected to break this symmetry, that is to particularize the sides of the molecule (see the discussion about symmetrized and localized orbitals). This is consistent with the fact that the minima of the first excited state were characterized within C_s symmetry.

[135–137].

To identify such components of the branching space, we rely on the literature [49, 63, 118] and the characterizations presented above to identify directions that could belong to the branching space.

9.3.1 Linear interpolations

Conical intersections

We know that a crossing has to happen between TS_{B_2} and TS_{A_1} so we start by exploring the PES between those two geometries, performing linear interpolations (and extrapolations).

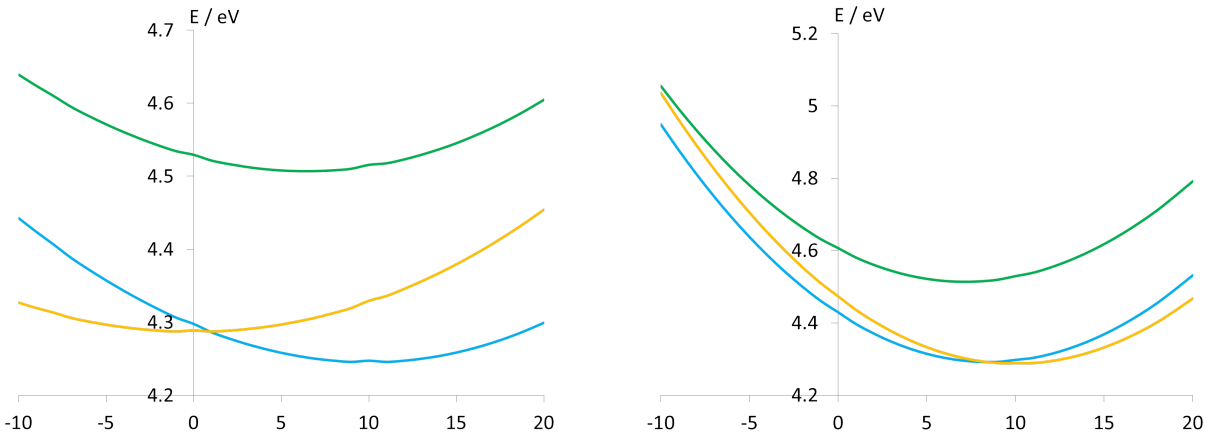

Figure 9.13: Evolution of the energies of the first three diabatic states of symmetry $1B_2$ (blue), $1A_1$ (yellow), $2B_2$ (green) along the linear interpolations between TS_{A_1} (point 0) and TS_{B_2} (point 10) on the left; between $min S_0$ (point 0) and TS_{A_1} (point 10) on the right.

The linear interpolation between the transition states shows that TS_{A_1} stands right next to a conical intersection (in terms of geometry) which confirms the previous assumption. A strong probability of population transfer is thus expected at this geometry.

Another conical intersection is met along the linear interpolation between $min S_0$ and TS_{A_1}.

Then, those two interpolation coordinates lift the degeneracy at a conical intersection. Consequently, their main components constitute valuable objects to qualitatively characterize the branching space.

Avoided crossings

Other linear interpolations from the transition states illustrate the fact that they correspond to avoided crossings between S_1 and S_2.

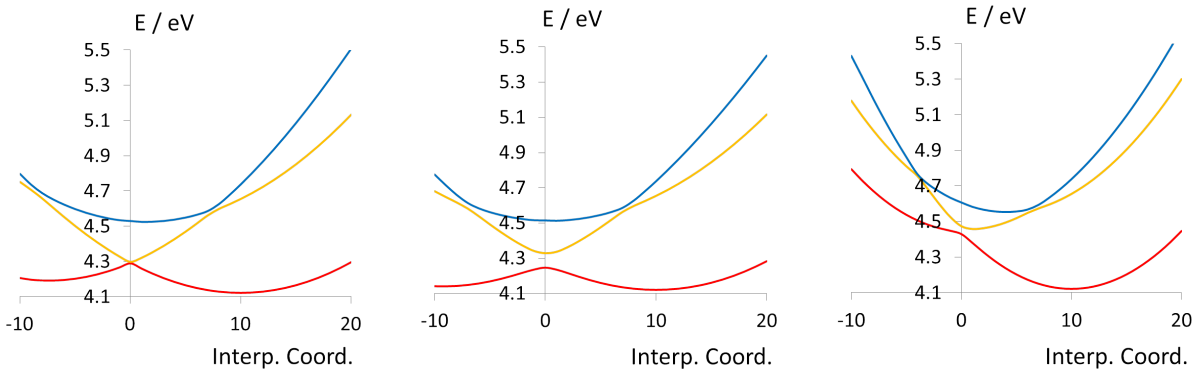

Figure 9.14: Evolution of the energies of the first three adiabatic states S_1 (red), S_2 (yellow), S_3 (blue) along the linear interpolations between TS_{A_1} (point 0) and $min S_1$ (point 10) on the left; between TS_{B_2} (point 0) $min S_1$ (point 10) in the center; between $min S_0$ (point 0) and $min S_1$ (point 10) on the right.

The geometries of the two transition states are quite similar, so their deformation, and thus the interpolation coordinate, is also similar when going to $min S_1$. Thus, the evolution of the energy of the electronic states is alike in those two cases.

On the other hand, the transition states are geometrically quite different from $min S_0$, which explains the topological differences along the path to $min S_1$.

9.3.2 A_1 components of the branching space

We search for conical intersections that belong to the C_{2v} symmetry. Spontaneously, we start by analyzing the influence of the elongation of the acetylene, for several reasons. First, because its importance was suggested in the literature [49, 118] and confirmed by our geometric study. Then because it is the main contribution to the transition modes of the transition states (figure 9.11). On the other hand, the length of the quinoidal bonds changes the most between those two geometries, which provides another direction to explore.

Scans along the symmetric elongation of the acetylene bonds, named mode 1, are performed from the C_{2v} stationary points (see figure 9.15); the other typical geometric parameters constitute the environment at each stationary point and are frozen along the scans.

Along this mode (and all the modes preserving the symmetry of the molecule), the electronic states can be refered either according to their energy (adiabatic perspective) or to their symmetry (diabatic perspective). Thus, for each point of the scan, the same value of the potential can be associated to a diabatic or adiabatic state, depending on the

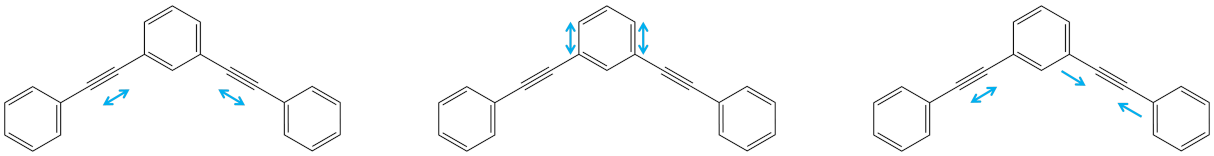

Figure 9.15: Mode 1: symmetric (a_1) elongation of the acetylene bonds (left); mode 2: symmetric (a_1) elongation of the quinoidal bonds (middle); mode 3: antisymmetric (b_2) elongation of the acetylene bonds (right).

purpose. In other words, each diabatic state is identical to an adiabatic state provided no crossing is met.

As mentionned in the characterization, the first three excited states are (very) close in energy around *min*S_0 (figure 9.16), TS_{B_2} (figure 9.17), and TS_{A_1} (figure 9.18), and even cross one with another along the mode. The diabatic state $1B_2$ corresponds to S_1 at *min*S_0 and TS_{B_2}, and to S_2 at TS_{A_1}; at these geometries, the diabatic state A_1 corresponds to S_2 and S_1 respectively, and the diabatic state $2B_2$ corresponds to S_3. In this study, the oscillators strengths will be used as a criterion for the characterization of the diabatic states (when it is possible).

Around *min*S_0, B_2 states are characterized by their oscillator strengths, so the states can easily be labelled according to their own symmetry. Zooms in the appropriate intervals show that $2B_2$ passes through $1B_2$ and $1A_1$, and that $1B_2$ and $1A_1$ cross each other at two points.

On the contrary, around the *TS* the oscillators strengths of the two diabatic states B_2 are inverted along the elongation mode, which is typical of a mixture between the two states. This does not happen in the FC environment, probably due to the different characteristics of the environment, that is the unchanged nuclear coordinates.

For each of the C_{2v} stationary points, crossings are met between the first three excited states, and particularly between the diabatic states $1B_2$ and $1A_1$. For reasons that will become more explicit in the following, we focus on the conical intersections between the diabatic states $1B_2$ and $1A_1$. The characteristics of the lowest conical intersection associated to each stationary point are gathered in table 9.3.

We will refer to those as the conical intersections "in the environment of *the corresponding stationary point*" to underline that their geometric structure is identical to the corresponding stationary point, except for the length of the acetylene bonds. Thus, the

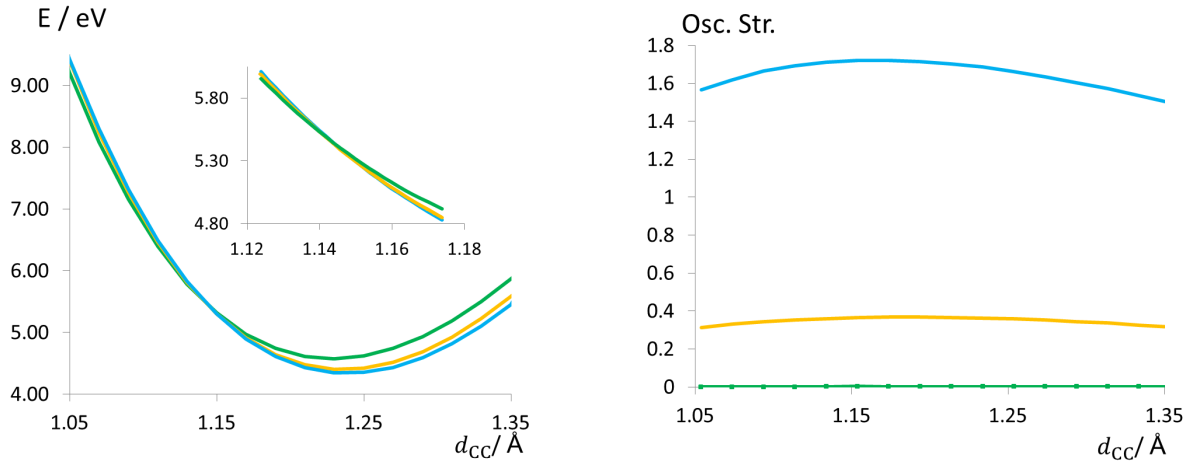

Figure 9.16: Evolution of the energies (left) and oscillator strengths (right) of the diabatic states of symmetry $1B_2$ (blue), $1A_1$ (yellow), $2B_2$ (green) around $min S_0$, along the symmetric (a_1) elongation of the acetylene bonds.

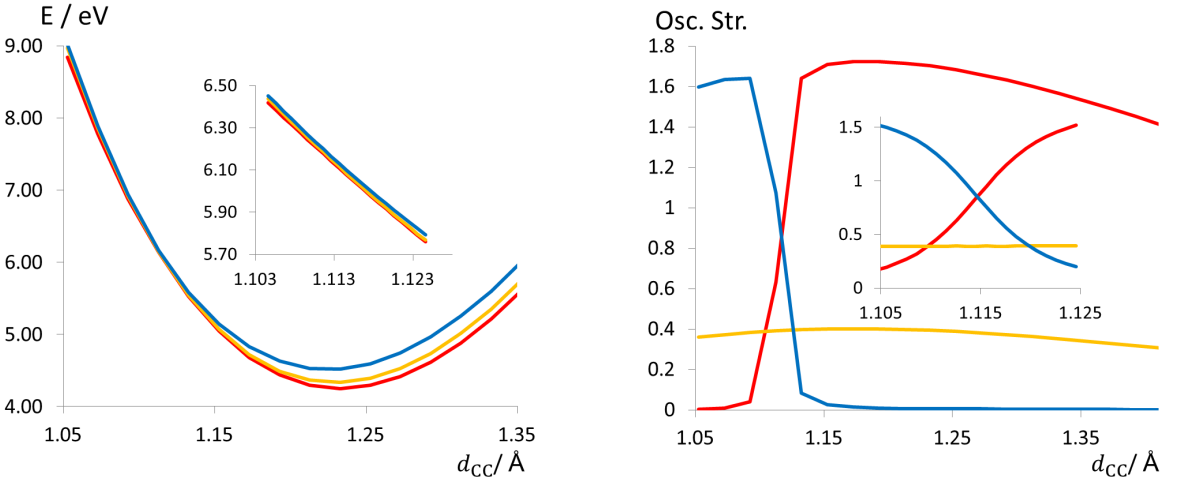

Figure 9.17: Evolution of the energies (left) and oscillator strengths (right) of the first three adiabatic states S_1 (red), S_2 (yellow), S_3 (blue) around TS_{B_2}, along the symmetric (a_1) elongation of the acetylene bonds.

symmetric elongation of the acetylene bonds is indeed a significant component of the branching space.

The conical intersections in the environments $min S_0$ and TS_{B_2} are almost three-state intersections. Since S_3 is B_2, it could *a priori* mix with S_1 and influence the evolution of the system at the conical intersection. This is particularly true in the environment of TS_{B_2}, in which oscillator strengths of S_1 and S_3 switch near this zone.

Yet, those intersections are about 1 eV above the lowest ones so they are not the most relevant intersections that could be found.

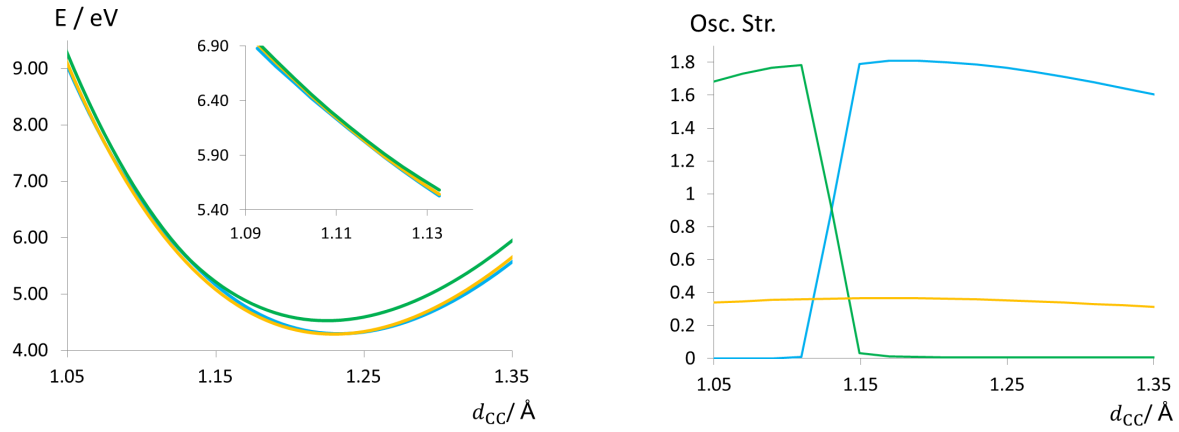

Figure 9.18: Evolution of the energies (left) and oscillator strengths (right) of the first three diabatic states of symmetry $1B_2$ (blue), $1A_1$ (yellow), $2B_2$ (green) around TS_{A_1}, along the symmetric (a_1) elongation of the acetylene bonds.

Environment	space explored	d_{CC} / Å	d_{quin} / Å	E_{S_0}	$E_{S_1} = E_{S_2}$	E_{S_3}
$min\mathrm{S}_0$	mode 1	1.1518	1.402	0.45	5.25	5.28
	C_{2v} seam	1.2358	1.4361	0.13	4.34	4.56
TS_{B_2}	mode 1	1.1186	1.419	1.17	5.95	5.97
	C_{2v} seam	1.2266	1.4615	0.27	4.32	4.56
TS_{A_1}	mode 1	1.2394	1.447	0.26	4.30	4.55
	C_{2v} seam	1.2294	1.4422	0.18	4.29	4.53

Table 9.3: Characterization of the lowest conical intersections of each environment. Energies are given in eV, with respect to the energy at the minimum of the ground state. Avoided crossings are considered as conical intersections for energy differences less than 0.001 eV.

On the other hand, the CC bond length at the conical intersection found right next to TS_{A_1} is typical of triple CC bonds. In addition, it is also very close to the minima of both S_1 and S_2 (see figure 9.18), which means that it is one of the lowest conical intersections of the whole C_{2v}-space. Finally, the energy barrier between the bottom wells and the intersection is reasonable (about 0.1 eV). Thus, this is a conical intersection of particular interest and will be denoted CI_{A_1} thereafter.

Mode 1 was expected to lift the degeneracy because of its typical role for going from $min\mathrm{S}_0$ to the TS and its contribution to the transition modes of the TSs. Now, considering the previous characterization, the main difference between those two structures is the length of the quinoidal bond. The scan along this mode, named mode 2, around CI_{A_1} is presented in figure 9.19. Not only is it indeed another component of the branching space, but it also appears to be more efficient than mode 1 to lift the degeneracy at the

conical intersection. One may note that along this mode, the diabatic state A_1 is the lowest energy one at the conical intersection.

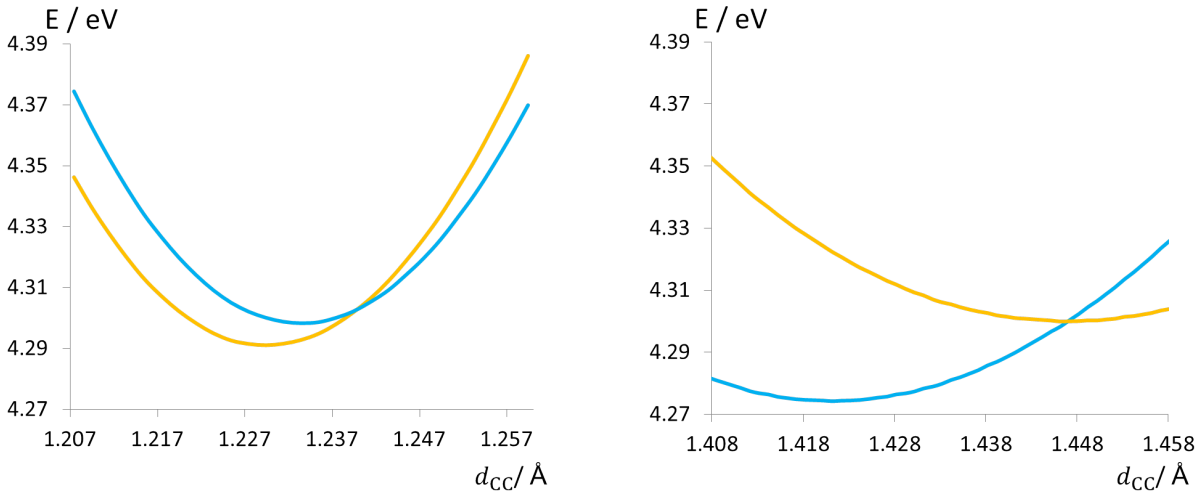

Figure 9.19: Evolution of the energies of the diabatic states $1B_2$ (blue) and $1A_1$ (yellow) along the symmetric elongation of the acetylene bond (left) and the quinoidal bond on the central benzene (right) in the environment TS_{A_1}. The figure on the left was resized to overcome scaling issues when being compared to the figure on the right.

9.3.3 B_2 components of the branching space

Now, we look for vectors of the branching space that will break the left-right symmetry of the molecule.

The first natural choice for this is the antisymmetric elongation mode of the acetylene, called mode 3, for several reasons. First, it has the right symmetry (b_2) and is the complementary mode to mode 1. In addition, this mode is one of the main modes involved in the nuclear coordinate connecting $min S_1$ and $min S_1'$.

Scans are performed along mode 3 from the lowest three conical intersections identified above.

As shown in figure 9.20, this mode is by far the most efficient to lift the degeneracy at the conical intersection. It yields double-well potential curves corresponding to two equivalent (local) minima, similar to $min S_1$ and $min S_1'$.

Similarly to cyclobutadiene (see section 2.4), diabatic states can be associated to the adiabatic potentials. Contrarily to the previous diabatic states that were based on sym-

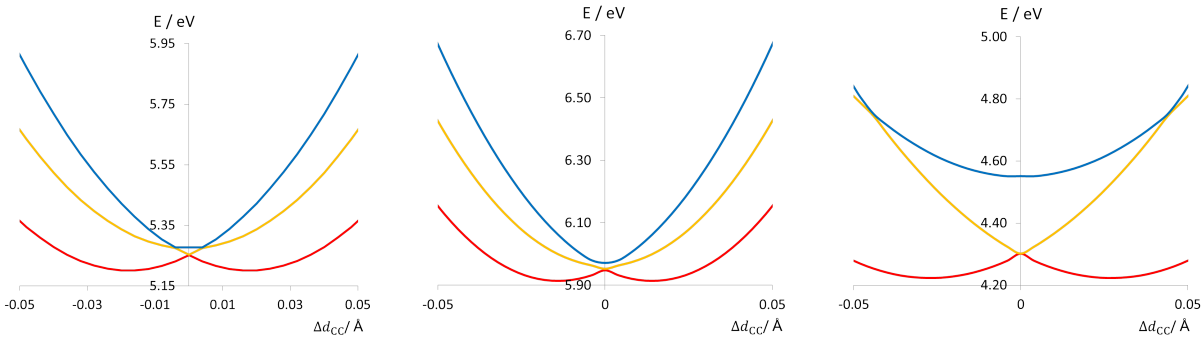

Figure 9.20: Evolution of the energies of the first three adiabatic states S_1 (red), S_2 (yellow), S_3 (blue) along the antisymmetric (b_2) mode of elongation of the acetylene around CI_{FC} (left), CI_{B_2} (middle), and CI_{A_1} (right).

metry, these ones are localized on each building block, so they are named "left" and "right" diabatic states, respectively, see figure 9.21.

Going through the conical intersection CI_{A_1} is the "favored" way to transfer the excitation from one side to another. Since m22 is symmetrical, the two wells are equivalent and the excitation can go back and forth through the conical intersection, provided an adequate amount of kinetic energy.

This interpretation in terms of diabatic states localized from either side of the *meta*-junction can be extrapoled to non-symmetrical structures, in particular to mixed *meta*-PPEs. We illustrate this point taking m23 as an example.

In m23, the wells are no longer equivalent. The well of S_2 (localized on the 2-ring building block) is higher in energy than the well of S_1 (localized on the 3-ring building block); see previous chapter. Then, the barrier to transfer the excitation from the 2-ring building block to the 3-ring building block is lower than the reverse barrier, see figure 9.21, thus explaining the unidirectional transfer mentioned in references [42, 49]. One may note that the three coordinates considered on figure 9.21, which lift degeneracy at different conical intersections, are necessarily different.

One may note that we do not try to predict the characteristics of the mode equivalent to mode 3 in m23. This will be addressed in the next chapter.

Since it is complementary to mode 2, the antisymmetric elongation of the quinoidal bonds is also expected to lift degeneracy at the conical intersection. We have not investigated this path yet, though.

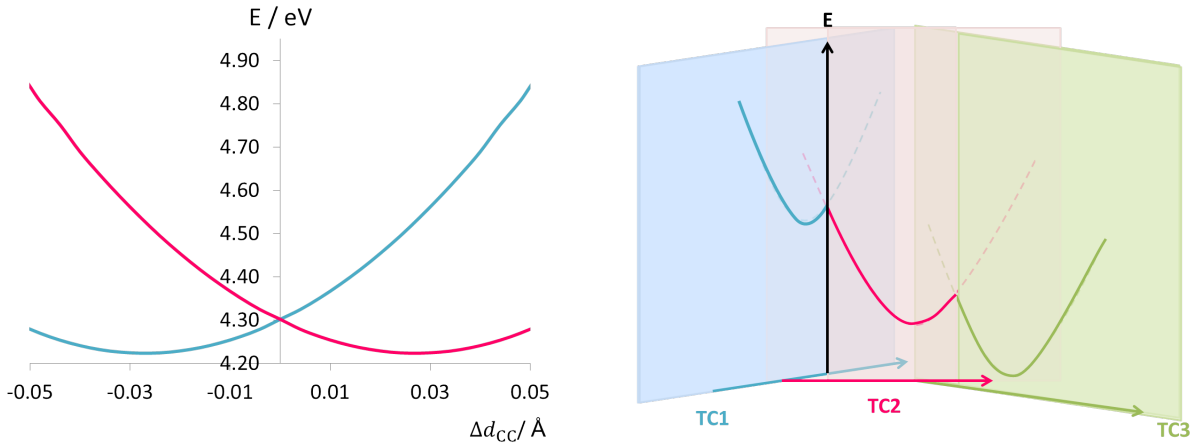

Figure 9.21: Evolution of the energies of the excited states along the antisymmetric mode of elongation of the acetylene bond in terms of left-right diabatic states (left) and extrapolation to a *shishiodoshi* (Japanese bamboo fountain) cascade (right).

9.3.4 Seams

We identified three modes lifting degeneracy at the conical intersection between the first two excited states of m22. In order to get a more global representation of the PES around the lowest conical intersections, we scanned simultaneously along modes 1, 2, and 3, two by two.

C_{2v} seam

We start by scanning the C_{2v} space along modes 1 and 2. It is important to note that the surfaces that are plotted here do not represent the whole seam. Indeed, provided C_{2v} symmetry, one vector of the branching space is supposed to be A_1 whilst the other one is supposed to be B_2. Here, we only analyze the evolution of the seam along two components of the A_1 vector.

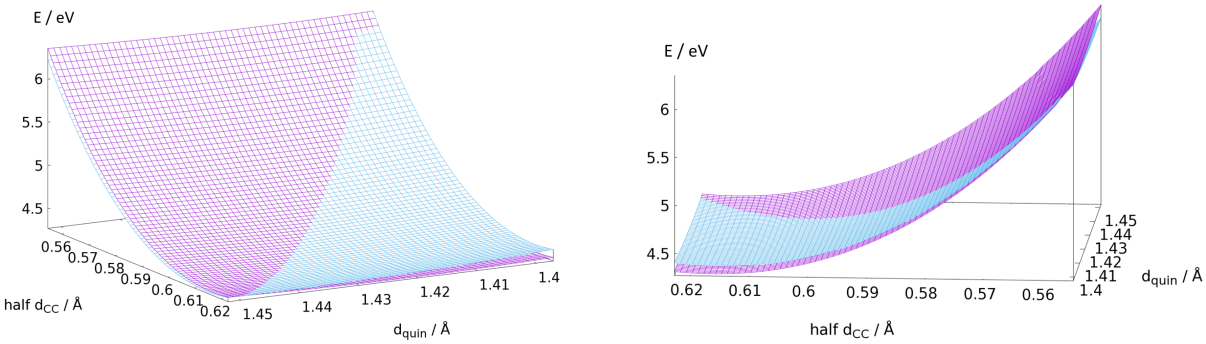

Figure 9.22: Evolution of the energies of the diabatic states $1B_2$ (purple) and $1A_1$ (blue) along the symmetric elongations of acetylene and quinoidal bonds of TS_{A_1}.

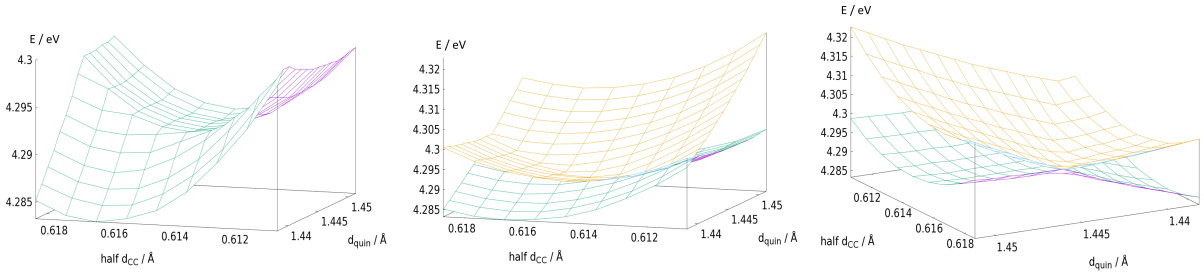

Figure 9.23: Evolution of the energies of the adiabatic states S_1 (green/purple) and S_2 (yellow/blue) around the lowest conical intersection along the symmetric elongations of acetylene and quinoidal bonds of TS_{A_1}.

A clear picture of the locus of conical intersections is provided by the representation of the diabatic states defined with respect to symmetry, see figure 9.22. Indeed, the two corresponding constrained PES in the C_{2v} space cross along the diagonal of the scanned space. The ensemble of the crossing points are conical intersections, so it defines a submanifold within the seam.

Owing to the scale of the figure, which corresponds to deformations that are energetically acceptable, the lifting of degeneracy is small with respect to the evolution of the energies across the surfaces. In the scanned space, the energy of the seam varies so a minimum can be located that corresponds to the lowest conical intersection within this space, see figure 9.23.

The same 2D-scan was also computed around the conical intersections in environments $min S_0$ and TS_{B_2}. The shape/behavior of the seam in these environments is similar to the one we just presented. The corresponding lowest conical intersections were identified, about 1 eV below the ones that were identified in the first place. This justifies *a posteriori* that we did not focus on them in the previous paragraph.

We identified that the two symmetric elongations of the acetylene bonds both belong to the branching space. Then it is expected that the independent evolution of the lengths of each bond also lifts the degeneracy at the conical intersection.

This choice of coordinates naturally brings out the two symmetrical diabatic states through the oscillator strengths. Indeed, the sudden inversion of the oscillator strengths going through TS_{A_1} along the seam is typical of the change in diabatic states that are coupled along a mode that preserves the symmetry (see the figures and discussion below). One may note that localized quasi-diabatic states stand out on the central view of figure 9.24.

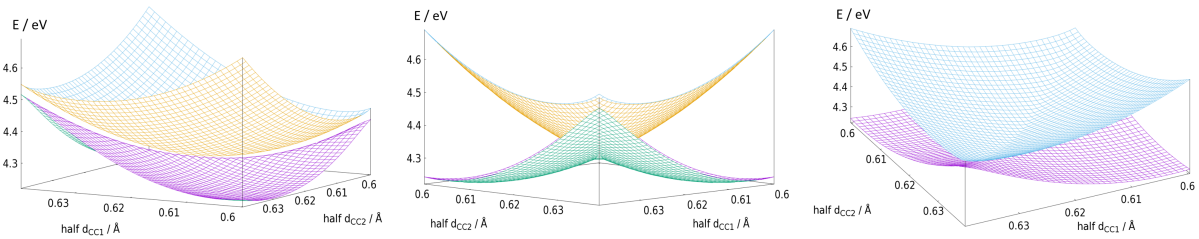

Figure 9.24: Evolution of the energies of the adiabatic states S_1 (green/purple) and S_2 (yellow/blue) along the independent elongations of the acetylene bonds of TS_{A_1}.

The 2D-plot allows to compare vividly the efficiency of the lifting of degeneracy along the two modes. In particular, we can see that it is almost too small to be seen along mode 1 whilst very marked along mode 3.

9.3.5 Comments about the branching space

The diagonal and antidiagonal of the graph correspond to the symmetric and antisymmetric modes of elongation, respectively. As previously mentioned, mode 1 lifts the degeneracy between the delocalized diabatic states determined with respect to symmetry (symmetric and antisymmetric combinations of local states), while mode 2 lifts the degeneracy between the localized diabatic states (left or right local excitations). Figure 9.24 provides a vivid example of the properties of the two complementary diabatic bases exposed in section 2.4.

Considering the localized states as the states of reference, mode 2 is the tuning mode along which the gradient of the energy difference is the largest. Along the perpendicular direction, that is mode 1, the localized diabatic states get coupled but stay degenerate in the corresponding diabatic representation.

Considering the delocalized states (labelled according to symmetry), they are tuned along mode 1 and coupled along mode 2. The direct consequence of this is the mixture of the oscillator strengths of the electronic states that basically tend to their mean value along mode 2, and the switch in the oscillator strengths of S_1 and S_2 along mode 1, see figure 9.25.

Finally, it is worth to mention that the modes identified so far do not span the entire branching space at CI_{A_1}, but are supposed to be qualitatively representative of it. The complete branching space at a given conical intersection has to be searched for automatically, through gradient techniques for example [138], which is currently under investiga-

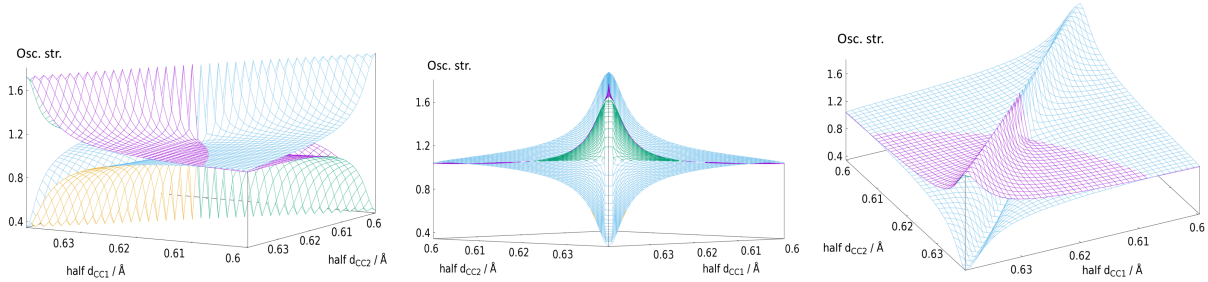

Figure 9.25: Evolution of the oscillator strengths of the adiabatic states S_1 (green/purple) and S_2 (yellow/blue) along the independent elongations of the acetylene bonds of TS_{A_1}.

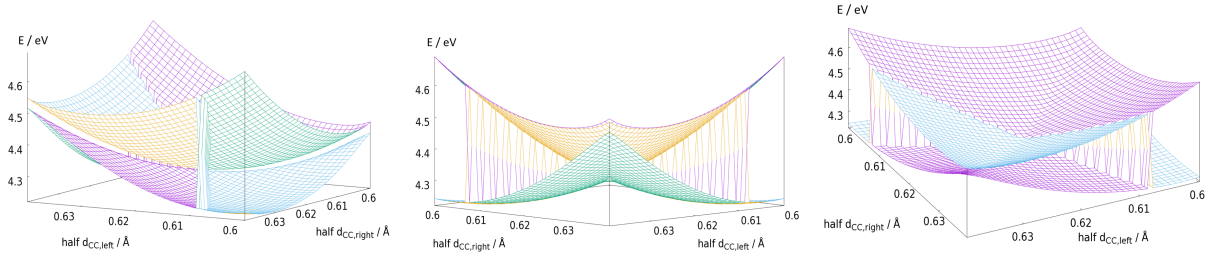

Figure 9.26: Evolution of the energies of the two first diabatic excited states along the independent elongations of the acetylene bonds of TS_{A_1}.

tion.

Chapter 10

Weakly avoided crossings in a non-symmetrical *meta*-PPE

The previous two chapters allowed the main properties of PPEs to be identified in terms of geometry, along with the characteristics of their first few electronic states. In particular, this interpretation provided an additional rationale justifying the unidirectionality of the excitation transfer in *meta*-PPEs, thus suggesting that the sequential process occurs *via* a sequence of conical intersections.

The aim of this chapter is to identify and characterize conical intersections in the (2,3)-*meta*-PPE (m23), which is the smallest PPE that is likely to exhibit non-symmetrical conical intersections mediating the excitation transfer between two unequivalent building blocks.

Stationary points were optimized and characterized with calculations performed at the CAM-B3LYP/6-31+G* level of theory with the Gaussian09 package [62].

10.1 Nature of the excited states at stationary points

Information about the typical lengths at the minima of the first three excited states are recalled in table 10.1, and the corresponding energies are given in table 10.2.

	eq.geom.	mean $d_{\text{C-Ph}}$	$\sigma(d_{\text{C-Ph}})$	mean d_{CC}	$\sigma(d_{\text{CC}})$	mean d_{quin}	$\sigma(d_{\text{quin}})$
2-ring	$min\text{S}_0$	1.431	0.000	1.210	0*	1.389	0.000
building	$min\text{S}_1$	1.430	0.000	1.210	0*	1.391	0.003
block	$min\text{S}_2$	1.384	0.001	1.245	0*	1.380	0.000
3-ring	$min\text{S}_0$	1.429	0.001	1.210	0.000	1.388	0.000
building	$min\text{S}_1$	1.391	0.008	1.233	0.000	1.377	0.009
block	$min\text{S}_2$	1.423	0.002	1.214	0.001	1.389	0.006

Table 10.1: Characteristic mean lengths (in Å) at the equilibrium geometries of the first three electronic states of m23.

	E_{S_0}	E_{S_1}	E_{S_2}	E_{S_3}
$\boldsymbol{min}\mathbf{S}_0$	0	3.88	4.45	4.56
$\boldsymbol{min}\mathbf{S}_1$	0.27	3.61	4.61	4.68
$\boldsymbol{min}\mathbf{S}_2$	0.23	3.99	4.17	4.52

Table 10.2: Energies (in eV) of the first electronic states at the minima in m23.

At the stationary points, S_2 is closer in energy from S_3 than from S_1. Thus, spanning the space of geometries, it is probable that conical intersections between S_2 and S_3 are met while searching for conical intersections between S_1 and S_2.

The stationary point are characterized by frequency calculations, also providing pieces of information about the localization of the excited states (see chapter 8). In addition, the minimum of S_2 appears to be almost a transition state for S_1, due to an intense vibration mode involving mainly acetylene stretchings, see figure 10.1. Then, the minimum of S_2 is a maximum for S_1 in the direction associated with this mode, resulting in an avoided crossing between S_1 and S_2.

The nature of the excited states can be characterized by the transitions between the molecular orbitals and the oscillator strengths.

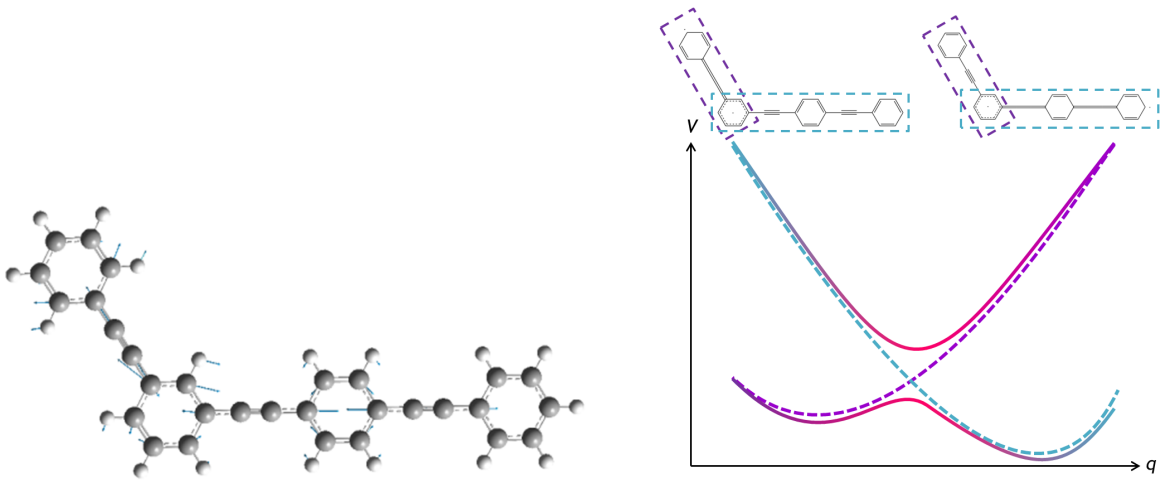

Figure 10.1: Vibration mode of S_1 at the minimum of S_2 associated to the frequency $\bar{\nu} = \mathrm{i}1489\mathrm{cm}^{-1}$ and scheme of principle of the avoided crossing at *min*S_2 along this mode.

Oscillator strengths may vary within 0.1 due to the mixture of different states. Thus, for orders of magnitude within 1.0 they can be used to discriminate states, but have to be manipulated carefully in case of smaller variations and values.

The magnitude of the oscillator strengths allows to discriminate the two diabatic states associated with S_1 and S_2 at the ground-state minimum, corresponding to $f_{\mathrm{osc}} > 2.0$ and $0.5 < f_{\mathrm{osc}} < 0.8$ (see table 10.3), and denoted D_1 and D_2, respectively (here, D stands for diabatic, not for doublet). The diabatic state D_1 corresponds to the adiabatic state S_1 at each minimum and D_2 corresponds to S_2 at all the minima but S_1. There, D_2 corresponds to S_3, which suggests that a crossing occurs between this minimum and the other ones.

The decomposition in terms of transitions suggests that the last diabatic state, denoted D_3 corresponds to S_3 at *min*S_0, *min*S_2, *min*S_3, and to S_2 at *min*S_1. Considering only the oscillator strengths, one may think that the diabatic state at *min*S_1 is different from the diabatic state at the other minima. To some extent, this is not totally wrong. Actually, the diabatic state D_3 has been affected by the presence of another diabatic state nearby (here D_2), and the mixture between both states results in opposite variations of their oscillator strengths.

Considering only those three states, D_3 will always be associated to the smallest oscillator strength.

Thus, diabatic state D_4 crosses with D_2 and D_3 along the coordinates connecting *min*S_1 to the other minima, and the adiabatic state S_2 changes its nature along those coordinates. Yet, it is worth to note that the nature of diabatic state D_2 is not the same

at all minima, which stands out particularly, considering the contribution of the HO−1–LU+1 transition. Pieces of answers can be provided by the analysis of the near frontier orbitals involved in D_2.

The near frontier orbitals are similar at *min*S_0, *min*S_1, and *min*S_3. At the minimum of S_2, the near frontier orbitals present unexpected delocalization and shapes, see figure 10.2. A linear interpolation and extrapolation is performed along the coordinate connecting *min*S_1 and *min*S_2 (presented later on). At the furthest point of extrapolation on the side of *min*S_2, denoted *extra*S_1S_2, the shape of the orbitals is similar to the one at the previous minima, except for the energy order. Considering this energy order, the adiabatic state S_1 (corresponding to the HO–LU transition) is localized on the 2-ring building block, and the adiabatic state S_2 (corresponding to the HO−1–LU+1 transition) is localized on the 3-ring building block.

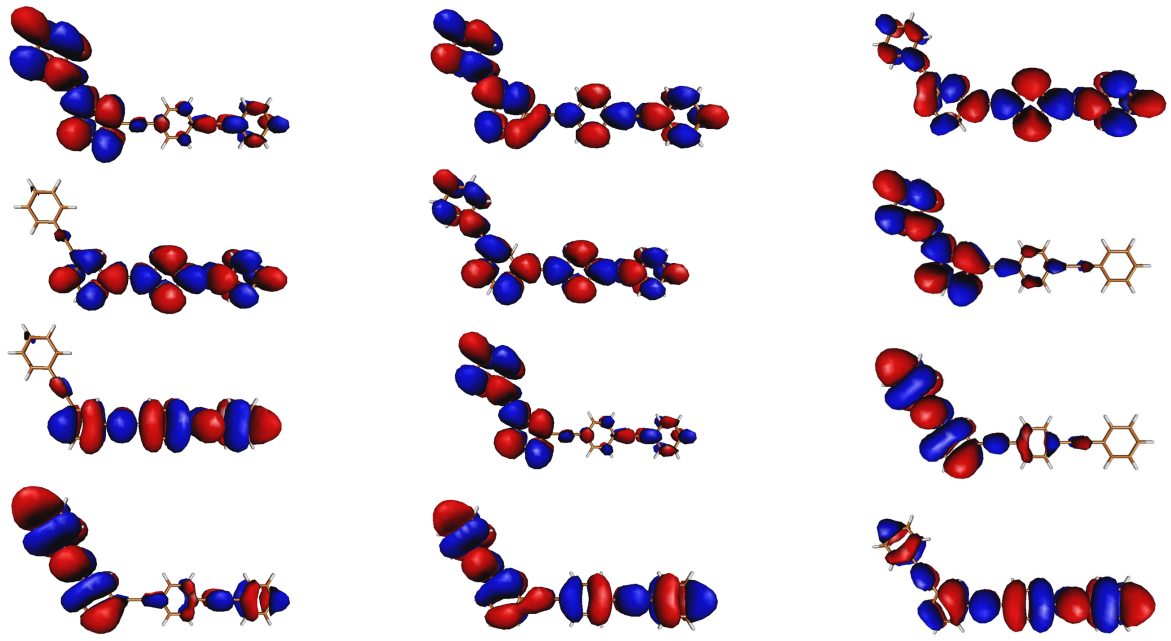

Figure 10.2: From bottom to top, HO−1, HO, LU, and LU+1 of the (2,3)-*meta*-PPE at the minimum of S_1 (left), minimum of S_2 (middle), last point (20) along the interpolation between both (right).

This can be interpreted qualitatively considering a diagram of correlation of the orbitals along the same line as Walsh diagrams, see figure 10.3. The localization of the near frontier orbitals switches from *min*S_1 to *extra*S_1S_2, along a coordinate that passes by *min*S_2, thus confirming that the diabatic states corresponding to S_1 at these geometries are different. As it happens, *min*S_2 is midway between *min*S_1 and *extra*S_1S_2 along the

path, see figure 10.4. Thus, its geometry is intermediate between both, as well as its orbitals, which explains their unexpected shapes.

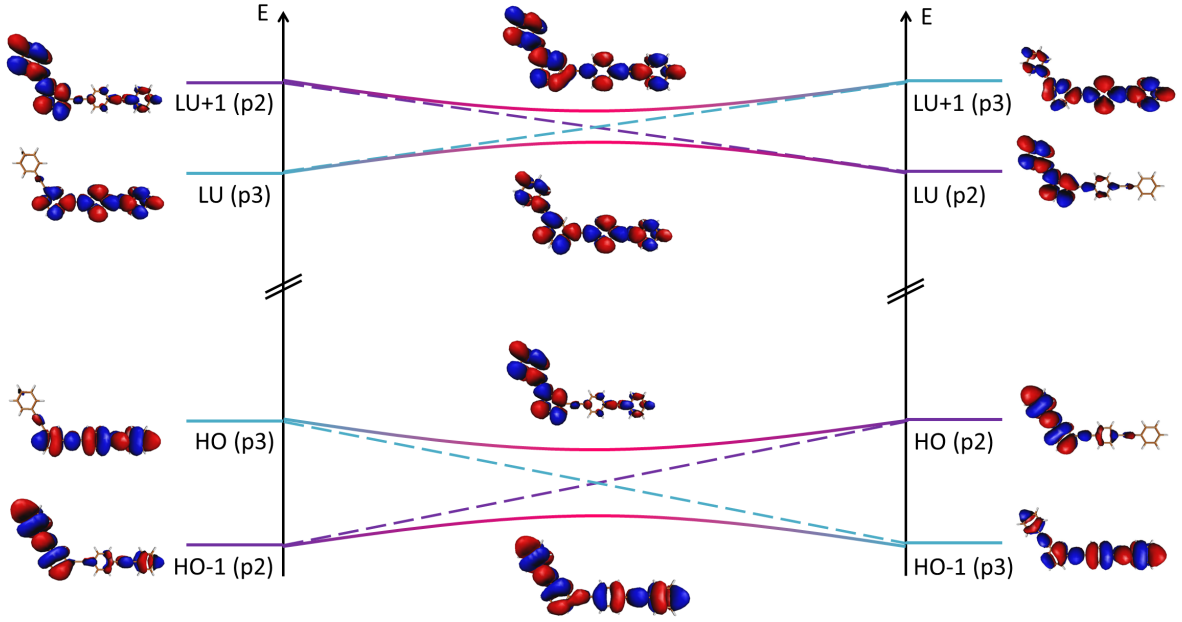

Figure 10.3: Correlation diagram between the near frontier orbitals of m23 from *min*S_1 to *extra*S_1S_2, passing through *min*S_2.

At the minimum of S_0

	S_1	S_2				S_3			
Oscillator strength	2.2183	0.8100				0.0081			
Transition	HO–LU	HO–LU	HO1–LU1	HO1–LU	HO–LU1	HO1–LU	HO–LU1	HO1–LU2	HO2–LU1
Contribution	0.82	0.05	0.61	0.16	0.10	0.22	0.25	0.12	0.10

At the minimum of S_1

	S_1	S_2				S_3	
Oscillator strength	2.2248	0.0498				0.6379	
Transition	HO–LU	HO1–LU	HO–LU1	HO1–LU2	HO2–LU1	HO1–LU1	HO–LU1
Contribution	0.91	0.43	0.14	0.08	0.09	0.48	0.29

At the minimum of S_2

	S_1			S_2				S_3	
Oscillator strength	2.5944			0.5281				0.0013	
Transition	HO–LU	HO1–LU	HO–LU1	HO–LU	HO1–LU1	HO1–LU	HO–LU1	HO1–LU	HO–LU1
Contribution	0.30	0.32	0.28	0.44	0.30	0.09	0.10	0.27	0.28

At the minimum of S_3

	S_1	S_2				S_3			
Oscillator strength	2.3075	0.7929				0.0066			
Transition	HO–LU	HO–LU	HO1–LU1	HO1–LU	HO–LU1	HO1–LU	HO–LU1	HO1–LU2	HO2–LU1
Contribution	0.78	0.08	0.54	0.19	0.12	0.26	0.30	0.08	0.09

Table 10.3: Energies (in eV) and oscillator strengths f_{osc} of the first electronic states at the minima of (2,3)-*meta*PPE.

10.2 Exploration of the PES

10.2.1 Linear interpolations

The assumptions proposed above can be verified upon analyzing the evolution of the adiabatic states along linear interpolations between the stationary points.

We start by analyzing what happens between the minima of S_1 and S_2, which are supposed to be involved in the excitation transfer.

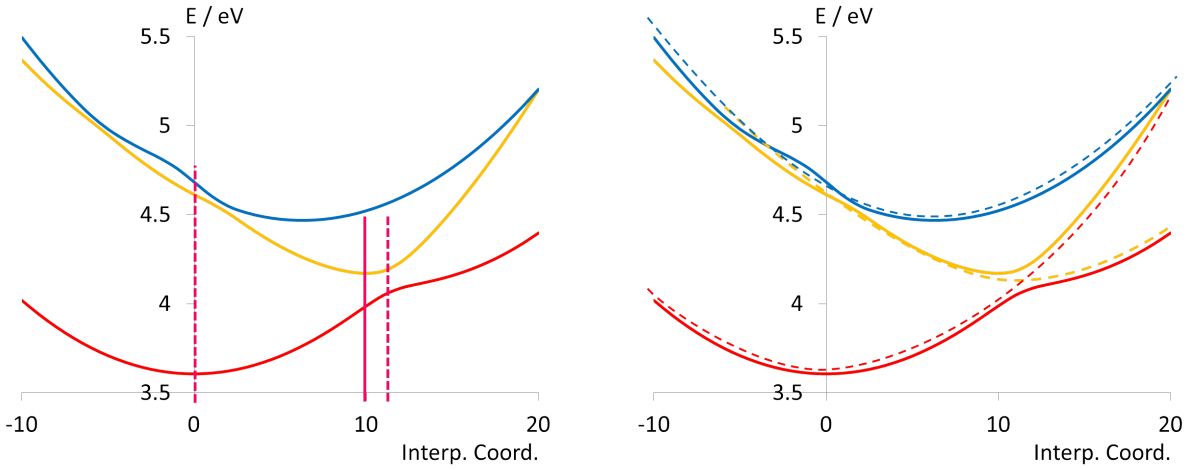

Figure 10.4: Evolution of the first three excited states along the linear interpolations and extrapolations from *min*S_1 to *min*S_2 (left), and representation of the corresponding diabatic states (right). Adiabatic states S_1 (red), S_2 (yellow), and S_3 (blue) are represented in full lines, diabatic states D_1 (red), D_2 (yellow) and D_3 (blue) are represented in dashed lines. The minimum of S_2 is projected along the bold pink line.

First, it appears that the minimum of S_2 is located right next to an avoided crossing with S_1, which explains the interaction between the electronic states and confirms the assumption about the unusual shapes of the frontier orbitals at *min*S_2.

As mentioned when analyzing the decomposition of the excited states, this avoided crossing is the locus of an actual crossing between the diabatic states D_1 and D_2, which are localized on the 3- and 2-ring building blocks, respectively. In addition, other avoided crossings occur around *min*S_1, this time between S_2 and S_3; we consider the one between the two minima. This avoided crossing makes D_2 cross with D_3, which is why D_2 corresponds to S_3 at *min*S_1.

Following the adiabatic states and their avoided crossings, one can represent the corresponding diabatic states (see figure 10.4). In particular, diabatic states D_1 and D_2 offer a first evidence in the sense of the *shishiodoshi* (Japanese bamboo fountain) excitation

transfer in non-symmetrical *meta*-PPEs [42, 48, 49, 51]. Indeed, keeping in mind that the interpolation coordinate is not the actual coordinate for the transfer, it still proves that the relaxation of D_2, that corresponds to an adiabatic S_n with $n > 1$, eventually leads to a crossing point with D_1 that corresponds to S_1.

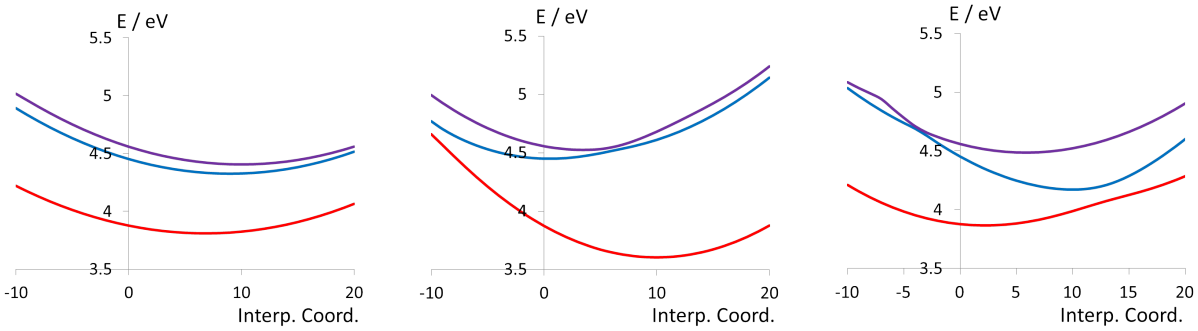

Figure 10.5: Evolution of S_1 (red), S_2 (blue), S_3 (purple) along the linear interpolations and extrapolations from *min*S_0 to *min*S_3 (left), *min*S_1 (middle), and *min*S_2 (right). Point 0 corresponds to *min*S_0, point 10 corresponds to *min*S_3, *min*S_1 and *min*S_2, respectively.

The oscillator strengths and contributing transitions for the first three excited states are very similar at *min*S_0 and *min*S_3, suggesting that the nature of the excited states is preserved between these two geometries. This is confirmed by the linear interpolation (figure 10.5), along which the evolution of the energies is very smooth and shows no (avoided) crossing point.

On the contrary, between *min*S_0 and *min*S_1, the nature of S_2 and S_3 clearly changes (oscillator strength and decomposition). S_2 and S_3 are indeed involved in a a weakly avoided crossing between the minima, leading to a sharp switch in the energy order and a mixture of the corresponding diabatic states, as assumed above.

Similarly, between *min*S_0 and *min*S_2, the oscillator strengths of S_1 and S_2 vary by about 0.3, and the contribution of the transitions change. The avoided crossing actually occurs after *min*S_2 (along the coordinate of linear interpolation), and before that, the states interact only weakly.

It is worth noting that the changes in the nature of the second excited state arise from different causes. First, S_2 is involved with S_3 on the first case and S_1 in the second case. Then, between *min*S_0 and *min*S_1, the diabatic states D_2 and D_3 do cross, so the two adiabatic states are associated with different diabatic states at the two different minima. Between *min*S_0 and *min*S_3, the diabatic states D_1 and D_2 do not cross but get close enough to interact strongly.

10.2.2 Local modes

In the previous chapter, we identified the stretching modes of acetylene and quinoidal bonds as being of particular interest to lift the degeneracy at conical intersections. Considering the normal modes at the stationary points, we define three modes combining the stretching of the acetylene bonds, see figure 10.6.

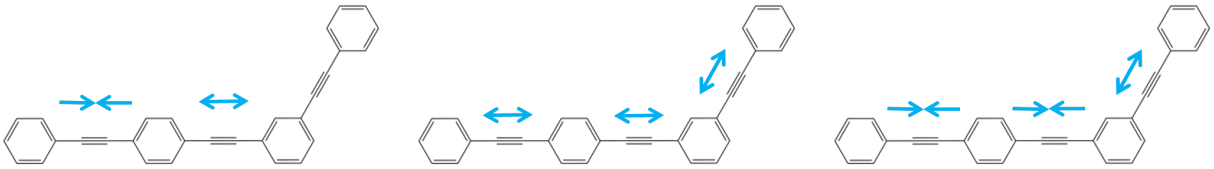

Figure 10.6: From left to right, the scanning vibration modes 1, 2, and 3 for the acetylene bonds.

Modes 1 and 2 affect the energy difference between S_2 and S_3 more than the energy difference between S_1 and S_2 (figures 10.9 and 10.10). In particular, S_1 and S_2 stay parallel along mode 1, which is not what we are interested in. Mode 2 actually decreases the energy difference between S_1 and S_2, suggesting that crossings may happen out of the scanning interval, at energies that are too high to be reasonable (more than 10 eV above the ground-state minimum).

On the contrary, mode 3 allows to get to avoided crossings between S_1 and S_2, meaning that it is a component lifting the degeneracy at the conical intersection. The minimal energy differences for the three environments are of about 0.1 eV, which is too large to talk about conical intersections. In order to find one, new scans are performed from the identified avoided crossing but no conical intersection could be found this way. The identification of "actual" conical intersections is an ongoing work, as well as the exploration along quinoidal modes of vibrations.

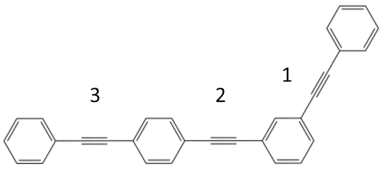

Figure 10.7: Definition of the scanning modes of vibration for the acetylene bonds.

	Bond 1	Bond 2	Bond 3	E_{S_1}	E_{S_2}
minS_0	1.210	1.210	1.210		
minS_1	1.210	1.233	1.233		
minS_2	1.245	1.215	1.213		
minS_0 AC	1.253	1.185	1.166	4.48	4.61
minS_1 AC	1.296	1.147	1.146	4.87	5.02
minS_2 AC	1.255	1.204	1.203	4.21	4.34

Figure 10.8: Characteristic lengths of the acetylene bonds (in Å) at the minima of the first electronic states of (2,3)-*meta*PPE and at the avoided crossings (AC) identified along mode 3 from the minima.

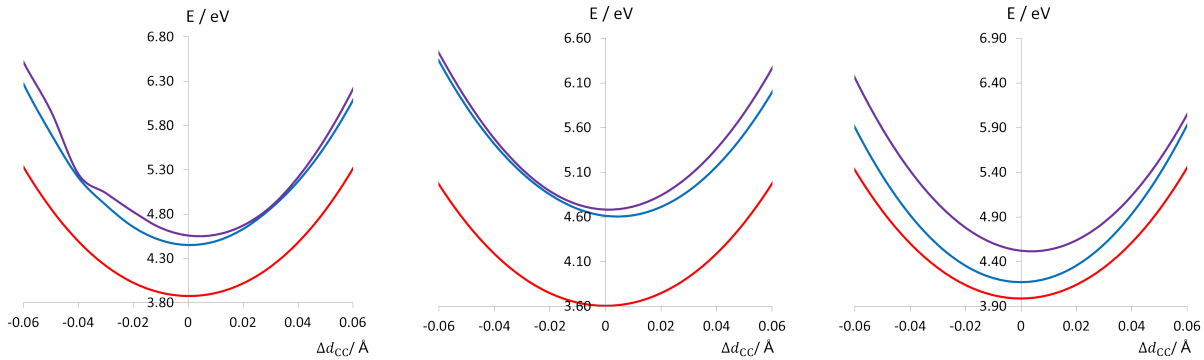

Figure 10.9: Evolution of the energy of S_1 (red), S_2 (blue), S_3 (purple) along mode 1 from *min*S_0 (left), *min*S_1 (middle), and *min*S_2 (right). The length difference is reported with respect to the length of bond 1 at the corresponding minimum.

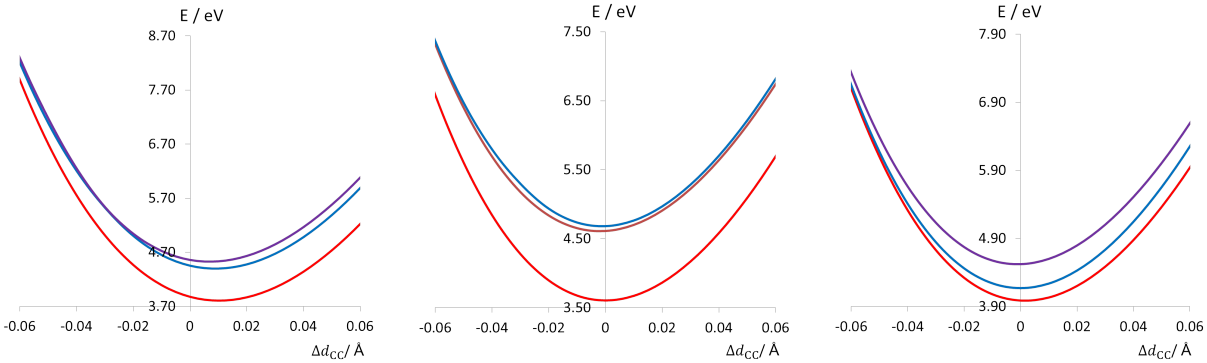

Figure 10.10: Evolution of the energy of S_1 (red), S_2 (blue), S_3 (purple) along mode 2 from *min*S_0 (left), *min*S_1 (middle), and *min*S_2 (right). The length difference is reported with respect to the length of bond 1 at the corresponding minimum.

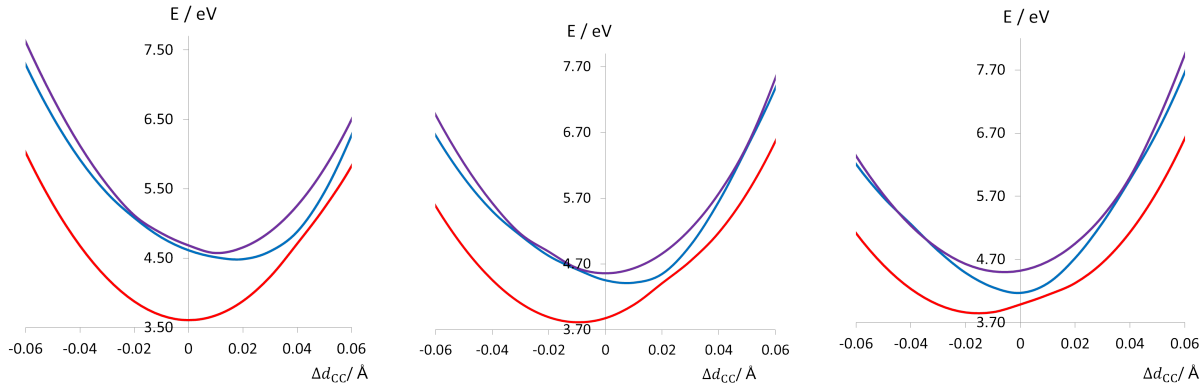

Figure 10.11: Evolution of the energy of S_1 (red), S_2 (blue), S_3 (purple) along mode 3 from *min*S_0 (left), *min*S_1 (middle), and *min*S_2 (right). The length difference is reported with respect to the length of bond 1 at the corresponding minimum.

Chapter 11

Conclusions and future prospects

The present part was dedicated to the static study of *para*- and first generation *meta*-PPEs.

The first chapter of this part assessed the validity of TDDFT as a method to compute the excited states of the PPEs. This was based on the ability of the method to reproduce the electronic absorption spectra along with the correct vibrational progression with respect to UV absorption experiments.

This point answered an open question raised in the literature [118, 130] due to the use of the usual approximation that consists in calibrating a computational method by comparing the calculated 0–0 transition energy with the experimental absorption maximum. The optimal conditions of validity of this approximation were discussed at this occasion.

The assignment of the vibrational contribution allowed to identify the nuclear coordinates that dominate along the relaxation of S_1 after an FC absorption.

A static characterization of the PPEs was performed at the ground state and first few excited states, from different points of view (geometric, energetic, orbital, vibrational). The characteristics of *meta*-PPEs have been put in perspective with the ones of the *para*-PPEs, which highlighted the possibility to see the *meta*-PPEs in terms of almost additive pseudo-fragments that can be excited selectively. This result was also verified for the symmetrical PPE m22.

Our results are in agreement with the literature, which states that the excitation transfer is mediated through the CC triple bond elongation. We also went further by

comparing the properties (geometries, energies, orbitals, vibrations) of a given PPE in different excitations states, and proved that they are typical of each electronic state.

This characterization will serve to study another point raised in the literature [20, 42, 48], that is that the excitation transfer occurs through a conical intersection. In particular, geometric characteristics at the equilibrium geometries of different excited states were used to search for conical intersections and identify their respective branching spaces.

The symmetrical *meta*-PPE m22 serves as the simplest prototype to identify and characterize conical intersections likely to mediate the excitation transfer in PPEs.

A full characterization of the electronic states as single transitions between pairs of near frontier orbitals allows to interprete the evolution of their energies in terms of localized diabatic states.

Several conical intersections were identified that are energetically accessible, in particular one that is close to a transition state for S_1. The lifting of degeneracy from a conical intersection was interpreted in terms of different sets of diabatic states according to the component followed. In particular, the coordinate that breaks the left-right symmetry of m22 particularizes the two pseudo-fragments, and is thus involved in the process of excitation transfer.

Exploration of the PES along relevant coordinates allows to identify a C_{2v} component of the seam, which supports a discussion about the branching space of one of the lowest conical intersections identified.

Coordinates of their respective branching spaces were identified thanks to the static study, that is the assignment of the absorption spectra (chapter 7) and the geometric characteristics of PPEs at the relaxed geometries of the electronic states (chapters 8 and 9). The interpretation of the lifting of the degeneracy along those coordinates in terms of localized diabatic states is in agreement with the *shishiodoshi* cascade proposed in the literature [42] to rationalize the excitation transfer in PPEs. The characterization of the exact branching space using an automated procedure is still in progress.

On the other hand, we focused on studying planar PPEs despite excited states may also relax along out-of–plane motions. In addition, we considered the linearity of the bonding scheme between the benzene rings, which is not ensured in principle. Indeed, it

was recently showed that accessible conical intersection occur along a path to the *trans* structure of the CC bonds connecting the rings of p2 [139].

Information collected for m22 were reinvested for the characterization of the electronic states of m23 and the research for conical intersections.

Avoided crossings were identified along coordinates that are likely to be involved in the excitation transfer. In particular, the equilibrium geometry of S_2 corresponds to a tight avoided crossing between S_1 and S_2. This suggests that after being excited, the relaxation of S_2 towards its minimum will efficiently cause a population transfer to S_1, with no risk for the wavepacket to get trapped.

Those are tight enough (about 0.15 eV) to yield population transfer between the excited states, though we did not succeed to identify real conical intersections yet. The search for actual conical intersections using a systematic algorithm following the gradient of the energy difference is in progress.

The information collected in the present part provides better understanding of the mechanism of the excitation transfer in PPEs. Such knowledge should serve as a basis for the elaboration of a vibronic model for the energy of the electronic states in terms of nuclear coordinates.

Part V

Construction of the vibronic model

Chapter 12

Introduction

DFT and TDDFT calculations are in principle capable of providing static insight into the electronic structure of PPEs. Yet, frequency calculations for example, applied to species with, say, seven rings, already require about a hundred days (cpu time), which constitutes a real, practical issue, especially because we aim to study larger PPEs in the future.

In addition, such large computational time may be perceived somewhat as a waste for systems that are not that complicated in terms of structure. Indeed, for any number of rings, a PPE merely is just a regular alternation of similar benzene and acetylene units, with only three possible local arrangements for benzene (either *ortho*-, which we did not consider in this work, *meta*-, or *para*-). For DFT and TDDFT calculations, this regularity cannnot be made useful directly, since the computation time depends eventually on the number and nature of nuclei and electrons, with no account of the repetition of identical fragments.

Along the same line, such calculations do not allow to rationalize the electronic energies with respect to the hierarchical architecture of the systems, hence the relevance of a novel approach exploiting it.

In the previous part, the electronic structure of PPEs has been investigated and characterized in detail. In particular, the multilevel hierarchy of *meta*-PPEs was highlighted, leading us to introduce the notion of pseudo-fragments, according to the localization of the π-molecular orbitals on the building blocks.

Based on this and other information collected in the previous part, a vibronic model could be constructed, following a multiscale approach allowed by the hierarchy of the

molecule and facilitated by the use of pseudo-fragments, see figure 12.1.

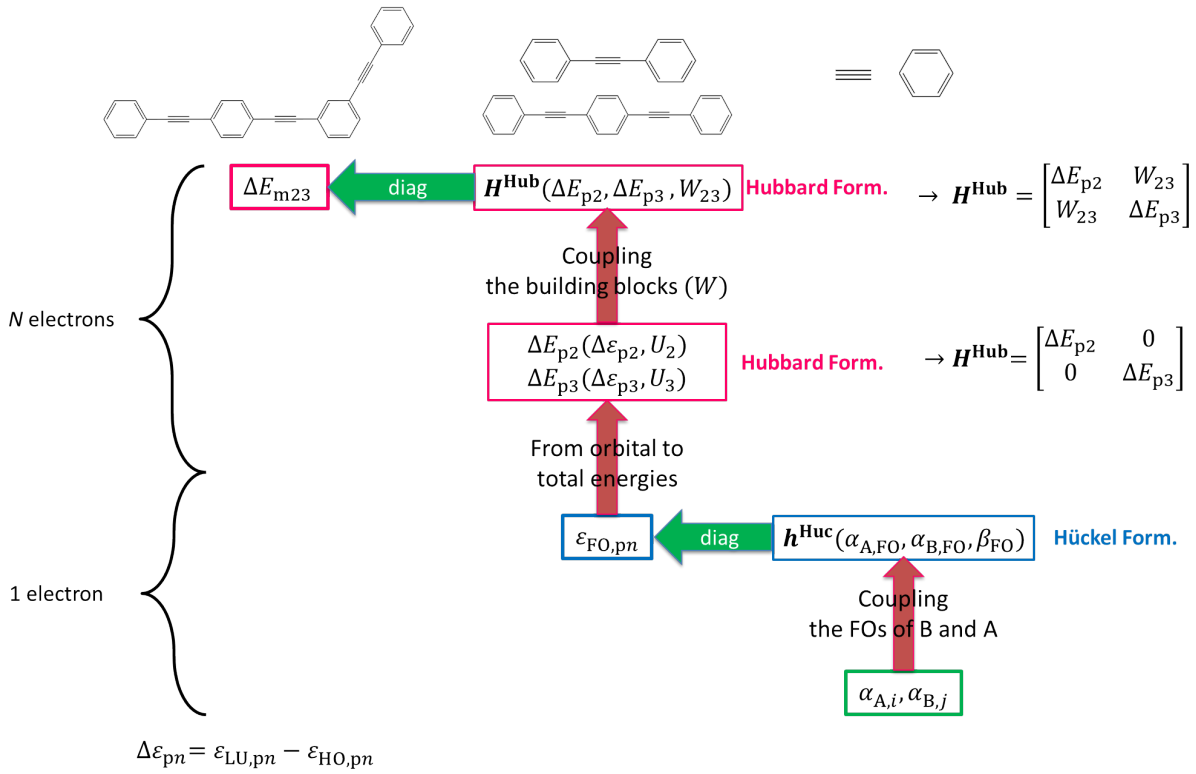

Figure 12.1: Structure of the vibronic model. Decomposition of the transition energy. FO = HO or LU.

We start upon proposing an effective Hückel-type model to describe the bottom part of our model, which corresponds to a one-electron system. This assumes, in particular, that the interaction between the frontier orbitals of benzene and acetylene, which are considered as basic fragments (fragment frontier orbitals), dominate in the frontier orbitals of *para*-PPEs. The interactions between the frontier orbitals are explicit whilst the other ones are only taken into account implicitely through the effectiveness of the model. This yields effective expressions for the energies of the frontier orbitals of *para*-PPEs in terms of the energies of the frontier orbitals of benzene and acetylene. The same methodology, with some adjustments, is also used to provide effective expressions for the energies of the frontier orbitas of *meta*-PPEs.

The validity of our approach is assessed according to two steps. First, for the *para*-PPEs, we compare the effective (optimized) values of the Hückel-type parameters to their non-effective (reference) values. Then, we inject these effective values into the effective expressions of the energies for the *meta*-PPEs, and compare them to the energies obtained

from direct calculations.

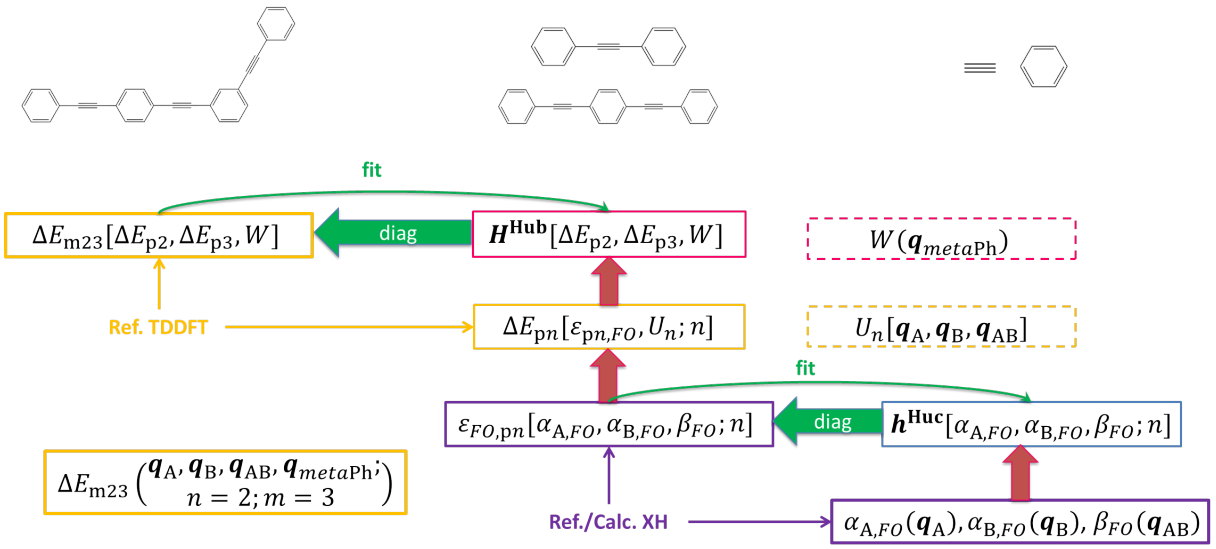

Figure 12.2: Structure of our vibronic model. Dependence with the nuclear coordinates.

On the other hand, we also address the dependence of the energy with the geometry, that is the parametrization of the model. To do so, we consider as local coordinates the deformations of benzene, acetylene, and the internal distance between both. We propose a functional (affine) expression of the electronic energies with respect to the orbital energies, and prove that the evolution of both the electronic and orbital energies with respect to local nuclear coordinates can be expressed as an affine equation.

The expression of the effective orbital energies (in the frame of the model described in chapter 13) in terms of effective Hückel-type parameters are then introduced in the parametrization. Thus, the effective electronic energies can be expressed in terms of the local nuclear coordinates of the orbital energies, themselves expressed in terms of effective parameters, each one being linearly dependent on the local coordinates, which leads to a final expression of the electronic energies in terms of the local nuclear coordinates.

Chapter 13

FFO model

We address the construction of the bottom part of our vibronic model.

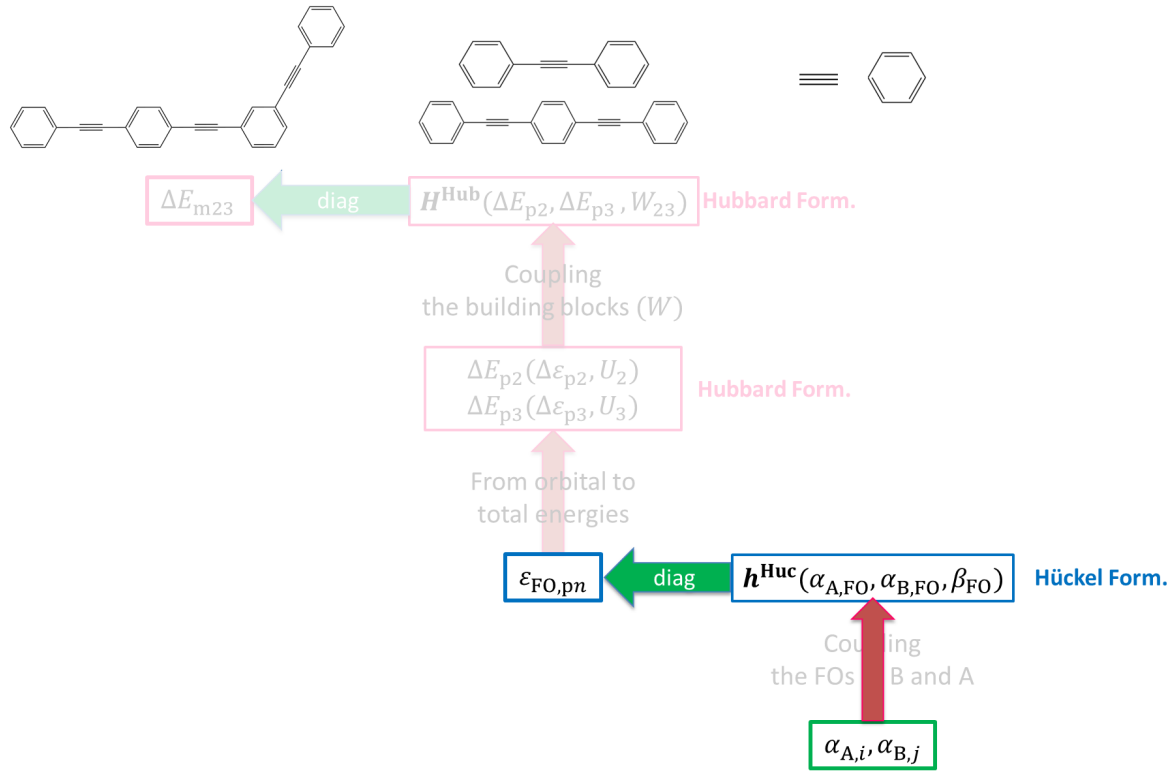

The objective is to build an effective Hückel-type matrix (first-neighbor approach) that reproduces the energies of the frontier orbitals of a *para*-PPE, using orbitals of molecular fragments (benzene and acetylene "superatomic" orbitals) as basic units instead of p_z carbon "atomic" orbitals. In addition, to reduce the number of parameters on which the model depends, we only take into account the frontier orbitals of benzene and acetylene explicitly, the remaining ones being taken into account implicitly.

This implies considering fragments constituted of frontier orbitals of benzene on the one hand and of acetylene on the other hand, the occupied and unoccupied systems being treated separately.

For constructing the model, we consider as a first approximation that the length of the acetylene bonds is the same both along a *para*-PPE and from a *para*-PPE to another (homogeneity and transferability at the equilibrium geometry of the ground state, see chapter 8). The same assumption is made for the geometry of benzene and the internal distance between adjacent benzene and acetylene.

13.1 Derivation on diphenylacetylene

We here present the part of the model connecting the energies of the frontier orbitals (FOs) of the sites (acetylene and benzene) to the energies of the FOs of the chromophores (*para*-PPEs; here, p2). To do so, we focus on the π-system and use the common notations α and β introduced in Part III; the sites A (acetylene) or B (benzene) will be indicated by the corresponding indices.

We build a Hückel-type matrix to express the energies of the frontier orbitals of p2 in terms of the interaction between the frontier orbitals of benzene and acetylene.

To do so, we use the approximations of the Hückel model in an unusual way: instead of considering the p_z orbitals of carbon atoms (atomic sites), we consider the frontier orbitals of molecular fragments (superatomic sites) that play the role of basic units (fragment sites), namely benzene and acetylene. In particular, the overlaps and resonance integrals between orbitals of non-ajdacent sites will be neglected. In practice, the distance between two non-adjacent sites is of about 5 Å, so this approximation is justified.

First, we consider the linear combinations of symmetry of the molecular orbitals of both benzene rings with respect to the center of inversion (see figure 13.1). Among the six π- and π^*- orbitals of each benzene ring, two can be ignored since they do not interact with the two π- and π^*-orbitals on acetylene for symmetry reasons. Those are the antisymmetric orbitals with respect to the plane that is perpendicular to the molecule and contains the main axis along the acetylene fragment.

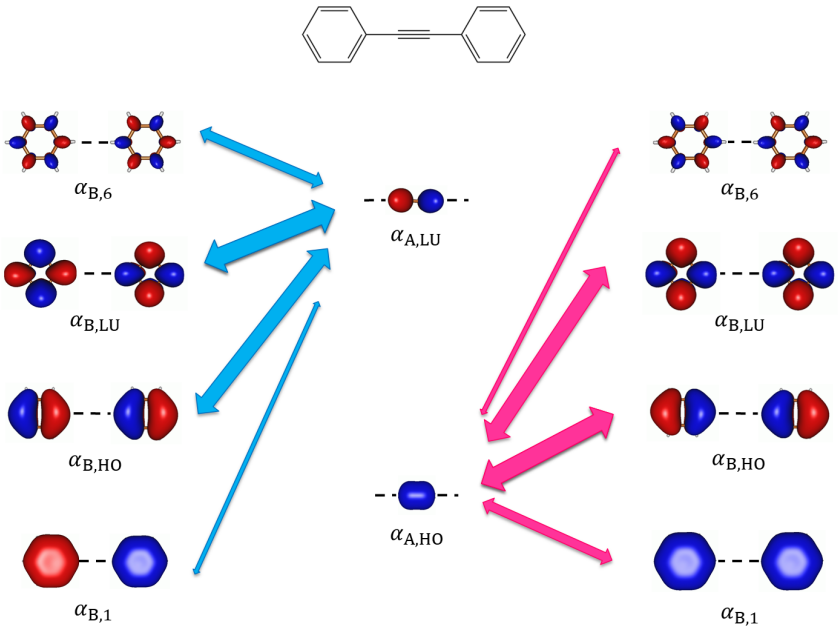

Figure 13.1: Qualitative representation of the interactions between the symmetrized π-orbitals of acetylene and benzene.

The complete Hückel-type matrix for p2 thus reads

$$\boldsymbol{H}_{\mathrm{p2}}^{\mathrm{Huck}} = \begin{pmatrix} \alpha_{B,1} & 0 & 0 & 0 & \beta^{g}_{\mathrm{p2},1} & & & & & \\ 0 & \alpha_{\mathrm{B},6} & 0 & 0 & \beta^{g}_{\mathrm{p2},6} & & & & & \\ 0 & 0 & \alpha_{\mathrm{B},HO} & 0 & \beta^{g}_{\mathrm{p2},HO} & & & 0 & & \\ 0 & 0 & 0 & \alpha_{\mathrm{B,LU}} & \beta^{g}_{\mathrm{p2,LU}} & & & & & \\ \beta^{g}_{\mathrm{p2},1} & \beta^{g}_{\mathrm{p2},6} & \beta^{g}_{\mathrm{p2,HO}} & \beta^{g}_{tol,LU} & \alpha_{\mathrm{A,LU}} & & & & & \\ & & & & & \alpha_{\mathrm{A,HO}} & \beta^{u}_{\mathrm{p2,HO}} & \beta^{u}_{\mathrm{p2},LU} & \beta^{u}_{1} & \beta^{u}_{6} \\ & & & & & \beta^{u}_{\mathrm{p2,HO}} & \alpha_{\mathrm{B,HO}} & 0 & 0 & 0 \\ & & 0 & & & \beta^{u}_{\mathrm{p2,LU}} & 0 & \alpha_{\mathrm{B,LU}} & 0 & 0 \\ & & & & & \beta^{u}_{\mathrm{p2},1} & 0 & 0 & \alpha_{\mathrm{B},1} & 0 \\ & & & & & \beta^{u}_{\mathrm{p2},6} & 0 & 0 & 0 & \alpha_{\mathrm{B},6} \end{pmatrix}. \tag{13.1}$$

One may note that, since we consider combinations of *two* orbitals of benzene interacting with the orbital of acetylene, $\beta^{\mathrm{sym}}_{\mathrm{p2,orb}} = \sqrt{2}\beta_{\mathrm{orb}}$ where β_{orb} corresponds to the interaction of *one* orbital of benzene with the orbital of acetylene [1] , see figure 13.2.

As mentioned in the previous chapter, we want the energies of the HO (LU) of p2 in terms of the main contribution, that is the interaction between the HOs (LUs) of benzene

[1] $\langle\varphi_{\mathrm{A}}|\hat{h}|\varphi_{\mathrm{B,p2}}\rangle = \langle\varphi_{\mathrm{A}}|\hat{h}|\frac{\varphi_{\mathrm{B,left}}+\varphi_{\mathrm{B,right}}}{\sqrt{2}}\rangle = \frac{2}{\sqrt{2}}\langle\varphi_{\mathrm{A}}|\hat{h}|\varphi_{\mathrm{B}}\rangle = \sqrt{2}\beta$

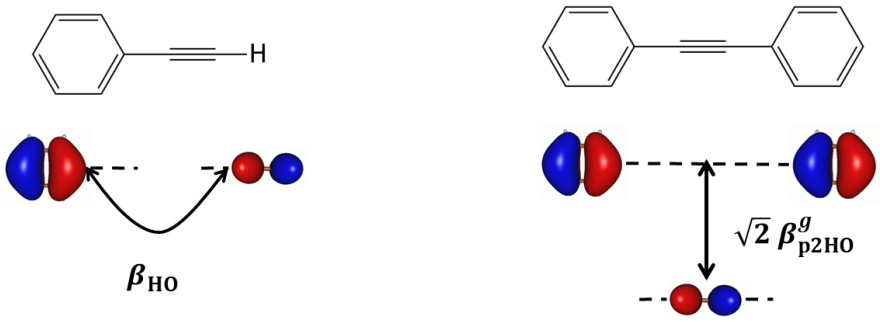

Figure 13.2: Normalization of the resonance integral in the interaction involving symmetrized orbitals with respect to the interaction between two orbitals. Example of the HO of benzene with the π-orbital of acetylene.

and acetylene (square in dashed line).

Yet, we do not want to approximate $\boldsymbol{H}^{\text{Huck}}_{\text{p2}}$ with a brute truncature. Instead, we apply the theory of effective Hamiltonians: the complete space describing the system is reduced to a subspace accounting for the main contribution(s), which will be optimized so that the effective Hamiltonian reproduces the same eigenvalues as the complete Hamiltonian [140].

In our case, this comes to considering that the interactions between the frontier orbitals (square in dashed lines) dominate, which thus constitutes a good zeroth-order Hamiltonian $\hat{H}^0$ for the effective Hamiltonian. The latter will be obtained eventually upon fitting the energies and resonance integrals (see below). This naturally discriminates the occupied and unoccupied systems. Under these conditions, the effective Hamiltonian for p2 reads

$$\boldsymbol{H}^{\text{eff}}_{\text{p2}} = \begin{pmatrix} \alpha^{\text{eff}}_{\text{B,LU}} & \beta^{\text{eff}}_{\text{p2,LU}} & & 0 \\ \beta^{\text{eff}}_{\text{p2,LU}} & \alpha_{\text{A,LU}} & & \\ & & \alpha_{\text{A,HO}} & \beta^{\text{eff}}_{\text{p2,HO}} \\ 0 & & \beta^{\text{eff}}_{\text{p2,HO}} & \alpha^{\text{eff}}_{\text{B,HO}} \end{pmatrix} \tag{13.2}$$

where we remove the symmetry labels g and u since there is no ambiguity.

Since all the contributing orbitals of acetylene are taken into account in our effective model, the frontier orbitals of acetylene will not be altered with respect to the original XH solutions. On the contrary, the energies of the frontier orbitals of benzene (and the resonance integral) have to be optimized to account for the contributions of all benzene orbitals in an effective manner.

Including the energies of the acetylene orbitals in the set of parameters to be optimized would, of course, give more flexibility to the model. Yet, doing so, the acetylene orbitals would change to account for contributions of benzene orbitals, for no good reason from a

chemical point of view.

Finally, $\boldsymbol{H}_{\mathrm{p2}}^{\mathrm{eff}}$ describes two independent systems, the occupied one (pink) and the unoccupied one (blue), under the form of two 2×2 symmetric matrices. For a 2×2 symmetric matrix, $\boldsymbol{M} = \begin{bmatrix} a_1 & b \\ b & a_2 \end{bmatrix}$, the eigenvalues read

$$\varepsilon_{\pm} = \frac{a_1 + a_2}{2} \pm \sqrt{\left(\frac{a_1 - a_2}{2}\right)^2 + b^2} \tag{13.3}$$

where $\varepsilon_- < \varepsilon_+$.

The energies of the HO (LU) of p2 have the form of ϵ_+ and (ϵ_-), respectively, consistently with the antibonding (bonding) interaction between the symmetrized HO (LU) for the pair of benzenes and the π- (π^*-) orbitals of acetylene, see figure 13.3.

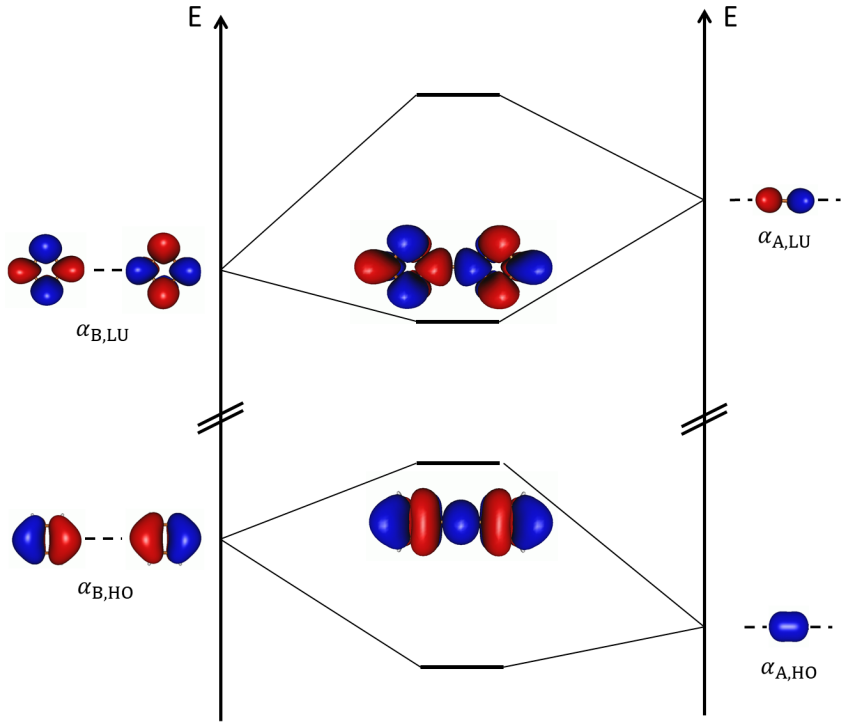

Figure 13.3: Interactions between the symmetrized FOs of the combination of two benzenes and the FOs of acetylene in p2.

Finally, the effective energies for the frontier orbitals read

$$\varepsilon^{\text{eff}}_{\text{p2,HO}} = \frac{\alpha^{\text{eff}}_{\text{B,HO}} + \alpha_{\text{A,HO}}}{2} + \sqrt{\left(\frac{\alpha^{\text{eff}}_{\text{B,HO}} - \alpha_{\text{A,HO}}}{2}\right)^2 + \left(\beta^{\text{eff}}_{\text{p2,HO}}\right)^2} \tag{13.4}$$

$$\varepsilon^{\text{eff}}_{\text{p2,LU}} = \frac{\alpha^{\text{eff}}_{\text{B,LU}} + \alpha_{\text{A,LU}}}{2} - \sqrt{\left(\frac{\alpha^{\text{eff}}_{\text{B,LU}} - \alpha_{\text{A,LU}}}{2}\right)^2 + \left(\beta^{\text{eff}}_{\text{p2,LU}}\right)^2} \tag{13.5}$$

where $\beta^{\text{eff}}_{\text{p2,LU}} = \sqrt{2}\beta^{\text{eff}}$.

The effective energies are analytical and will thus be used later on for the fit.

13.2 Generalization to *para*-PPEs

In the present paragraph, we expose how the previous results can be generalized to any *para*-PPE with n rings.

13.2.1 Fragment frontier orbital (FFO) decomposition

To do so, we divide the molecule into two fragments constituted of all benzenes (benzene fragment) and all acetylenes (acetylene fragment), respectively, see figure 13.4. We recall that we count two orbitals on each site (HO/LU for each benzene, π/π^* for each acetylene), and that the occupied and unoccupied systems will be treated separately.

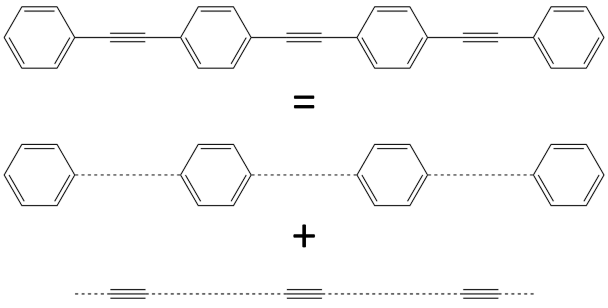

Figure 13.4: Decomposition of p4 into a benzene fragment and an acetylene fragment.

The energies of the FOs of any pn depend on the energies of the molecular orbitals of benzene (B) and acetylene (A), and on the interactions between the orbitals of an A-B pair of sites. From geometrical considerations, we assume here for simplicity that the energies of the molecular orbitals and the interactions between the pairs are conserved along a molecule (homogeneity) and from a *para*-PPE to another (transferability). Thus, the *para*-PPEs only differ by the value of n (number of rings) in this approach.

Considering this, we choose to describe the system upon relying on a first-neighbor approach, in which each site interacts with its neighbor through the same resonance integral β_{FO} (FO = HO, LU) [2]. The treatment of the interaction between both fragments is thus equivalent to the treatment of the interaction in a carbon polyene, see figure 13.5.

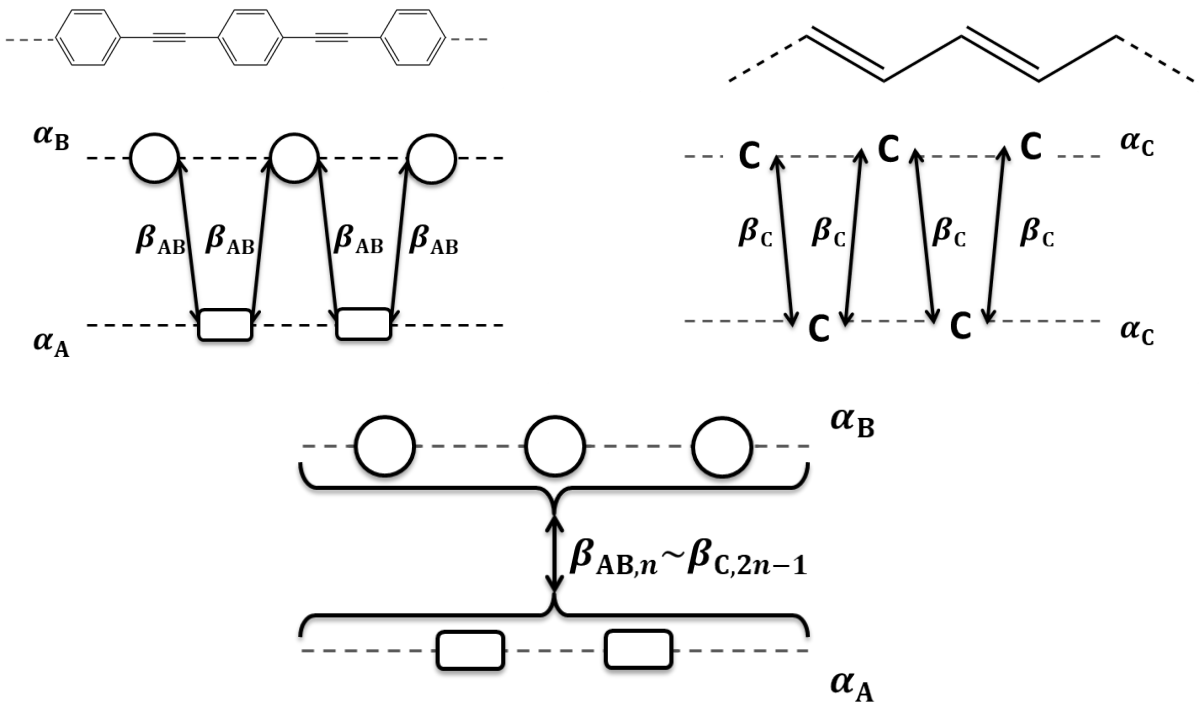

Figure 13.5: Interactions between the frontier orbitals in a *para*-PPE (left) and in a polyene (right) within the tight-binding approach.

The resulting resonance integral $\beta_{n,j}$ between the fragment orbitals leading to the j^{th} molecular orbital of an n-ring *para*-PPE is then related to the resonance integral β between two adjacent sites through a Coulson-type relation (see figure 13.5)

$$\beta_{n,j} = 2\cos\frac{j\pi}{2n}\beta = \gamma_{n,j}\beta \tag{13.6}$$

where $j \in [\![1; 2n-1]\!]$. $2n-1$ is the number of sites in the n-ring *para*-PPE, and thus the number of molecular orbitals for the occupied (unoccupied) system. This formula can be verified analytically with the Mathematica software [141] for instance.

The Hamiltonian (matrix) $\boldsymbol{H}_{n,FO}$, which will yield the frontier orbitals of *para*-PPEs, expressed in terms of the energies and interactions of the frontier orbitals (HO or LU, respectively) of benzene and acetylene is tridiagonal, much as the Hamiltonian describing polyenes

[2] Note that this β_{FO} is also the resonance integral between benzene and acetylene in phenylacetylene.

$$\boldsymbol{H}_{n,FO} = \begin{bmatrix} \alpha_{\mathrm{B},FO} & \beta_{FO} & & & & \\ \beta_{FO} & \alpha_{\mathrm{A},FO} & \beta_{FO} & & 0 & \\ & \ddots & \alpha_{\mathrm{B},FO} & \ddots & & \\ & & \ddots & \ddots & \ddots & \\ & & 0 & \ddots & \alpha_{\mathrm{A},FO} & \beta_{FO} \\ & & & & \beta_{FO} & \alpha_{\mathrm{B},FO} \end{bmatrix} . \tag{13.7}$$

It is important to note that this Hamiltonian is conceptually really different from the Hamiltonian $\boldsymbol{H}_{p2}$ previously introduced.

When defining the Hamiltonian $\boldsymbol{H}_{p2}$, in the previous section, we considered the combination of orbitals with respect to the inversion center. Now, in the Hamiltonian $\boldsymbol{H}_{n,FO}$, we list the sites in the order in which they appear in pn (B_1 A_2 B_3 A_4 $\cdots$), and report the corresponding FOs along with their first-neighbor interactions. Thus, the eigenvectors of $\boldsymbol{H}_{n,FO}$ correspond to linear combinations of benzene HOs (LUs) and acetylene π- (π^*-) orbitals. They are not the eigenvectors of the exact Hamiltonian but the energies (eigenvalues) of the two "model" FOs will be fitted to reproduce the energies of the two "target" FOs of pn (effective model).

The Hamiltonian $\boldsymbol{H}_{n,FO}$ is a square matrix of rank $2n-1$ corresponding to the $2n-1$ sites of an n-ring *para*-PPE. Its eigenvalues satisfy

$$\varepsilon^n_{0,FO} = \alpha_{\mathrm{B},FO} \tag{13.8}$$

$$\varepsilon^n_{\pm j,FO} = \frac{\alpha_{\mathrm{A},FO} + \alpha_{\mathrm{B},FO}}{2} \pm \sqrt{\left(\frac{\alpha_{\mathrm{A},FO} - \alpha_{\mathrm{B},FO}}{2}\right)^2 + \left(2\sin\frac{j\pi}{2n}\beta_{FO}\right)^2} \tag{13.9}$$

where $j \in [\![1; n-1]\!]$. The structure of the expression of $\varepsilon^n_{\pm j,FO}$ definitely reminds of the expressions of the eigenvalues of 2×2 symmetric matrices. This is due to the fact that the Hamiltonian $\boldsymbol{H}_{n,FO}$ can always be block-diagonalized into 2×2 blocks. Again, this can be verified analytically with Mathematica for example.

Strikingly enough, each of these energies depends on three Hückel-type parameters only: $\alpha_{\mathrm{A},FO}$, $\alpha_{\mathrm{B},FO}$, and β_{FO}. The latter are always the same, irrespectively of the number of rings n. The energies depend parametrically on n *via* the pre-factor in front of

β_{FO}. As a result, only six values of parameters are needed to calculate the HO–LU gap of any pn, for any n (with FO = HO or LU). The energies and parameters of equation 13.9 will become effective when performing the fit of the model to the target; this will be indicated by the exponent "eff".

The values of the sine pre-factor are reported in table 13.1.

n \ j	1	2	3	4	5	6
2	$\sqrt{2}$					
3	1	$\sqrt{3}$				
4	$\sqrt{2-\sqrt{2}}$	$\sqrt{2}$	$\sqrt{2+\sqrt{2}}$			
5	$\sqrt{\frac{3-\sqrt{5}}{2}}$	$\sqrt{\frac{5-\sqrt{5}}{2}}$	$\sqrt{\frac{3+\sqrt{5}}{2}}$	$\sqrt{\frac{5+\sqrt{5}}{2}}$		
6	$\sqrt{2-\sqrt{3}}$	1	$\sqrt{2}$	$\sqrt{3}$	$\sqrt{2+\sqrt{3}}$	

Table 13.1: Values of $2\sin\frac{j\pi}{2n}$ for $n \in [\![2;6]\!]$ and $j \in [\![1;n-1]\!]$. Radical expressions obtained with Mathematica.

13.2.2 Focus on the frontier orbitals

The HO (LU) results from a fully antibonding (bonding) interaction between all the pairs B-A of sites within the molecule (see figure 13.6), and is thus associated with the value $j = n - 1$.

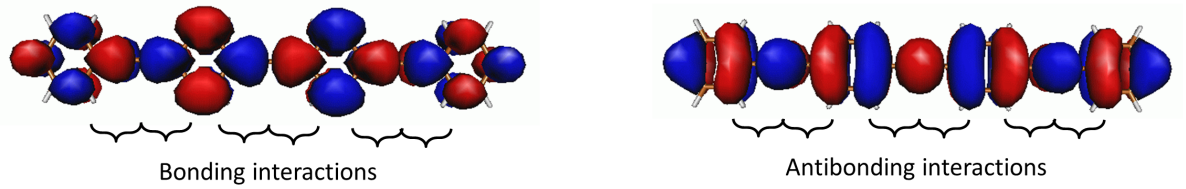

Figure 13.6: Interactions between the LUs (left) or the HOs (right) of benzene and acetylene in p4.

Consequently, the Coulson-type pre-factor in front of β_{FO} reads $2\sin\frac{(n-1)\pi}{2n} = 2\cos\frac{\pi}{2n}$, which leads to

$$|\gamma_{n,\mathrm{LU}}| = \gamma_{n,\mathrm{HO}} = 2\cos\frac{\pi}{2n} \tag{13.10}$$

owing to the following relationship

$$\cos\frac{(2n-1)\pi}{2n} = \cos\left(2\pi - \frac{(2n-1)\pi}{2n}\right) = -\cos\frac{\pi}{2n}\ . \tag{13.11}$$

The effective Hamiltonian can thus be generalized as

$$\boldsymbol{H}^{\text{eff}}_{\text{p}n,FO} = \begin{bmatrix} \alpha_{\text{A},FO} & \beta^{\text{eff}}_{n,FO} \\ \beta^{\text{eff}}_{n,FO} & \alpha^{\text{eff}}_{\text{B},FO} \end{bmatrix} \tag{13.12}$$

and the effective energies of the frontier orbitals satisfy

$$\begin{cases} \varepsilon^{\text{eff}}_{n,\text{HO}} = \dfrac{\alpha^{\text{eff}}_{B,HO} + \alpha_{A,HO}}{2} + \sqrt{\left(\dfrac{\alpha^{\text{eff}}_{B,HO} - \alpha_{A,HO}}{2}\right)^2 + \left(2\cos\dfrac{\pi}{2n}\beta^{\text{eff}}_{HO}\right)^2} \\ \varepsilon^{\text{eff}}_{n,\text{LU}} = \dfrac{\alpha^{\text{eff}}_{B,LU} + \alpha_{A,LU}}{2} - \sqrt{\left(\dfrac{\alpha^{\text{eff}}_{B,LU} - \alpha_{A,LU}}{2}\right)^2 + \left(2\cos\dfrac{\pi}{2n}\beta^{\text{eff}}_{LU}\right)^2} \end{cases} \tag{13.13}$$

where $\beta_{n,FO} = 2\cos\dfrac{\pi}{2n}\beta_{FO}$ and FO = HO or LU.

One may note that for p2, $\beta^{\text{eff}}_{2,FO} = 2\cos\dfrac{\pi}{4}\beta^{\text{eff}}_{FO} = \sqrt{2}\beta^{\text{eff}}_{FO}$, as we obtained from normalization reasons. We recall that the acetylene FOs do not require to be fitted in our model.

The effective values of the Hückel-type parameters are then fitted so that $\varepsilon^{\text{eff}}_{n,FO}$ reproduces $\varepsilon^{\text{exact}}_{n,FO}$ as much as possible (see below).

13.3 Validation

Questioning the validity of the FFO approximation is equivalent to questioning the physical meaning of the effective parameters. Thus, even if every secondary interactions are taken into account implicitly through the effective formalism, it is important to confirm that the main interaction we consider actually is predominant.

The values of the four effective parameters $\alpha^{\text{eff}}_{\text{B},FO}$ and β^{eff}_{FO} (FO = HO, LU) are fitted according to equation 13.13 for several values of n (further details are given below). Provided that the approximation is based on solid physical grounds, the effective Hamiltonian can be considered as the sum of the zeroth-order Hamiltonian (see equation 13.12 before optimizing the parameters) and a small perturbation. The values of the four effective parameters are thus expected to be close to original values, which are the values of the parameters $\alpha_{\text{B},FO}$ and β_{FO} (FO = HO, LU) in $\boldsymbol{H}^0$.

We evaluate numerically the consequences of the optimization of $\alpha_{\text{B},FO}$ and β_{FO}. The procedure is performed at oversymmetrized geometries close to the equilibrium geometries

of the ground state and the first excited state, to avoid any effect due to inhomogeneities in the molecules; note that these values will not be used further because, eventually, every parameter will depend on the nuclear coordinates.

The optimization is performed separately for the occupied and unoccupied systems. It consists in minimizing the root-mean-square deviation (RMSD) between the effective (model) energies $\varepsilon^{\text{eff}}_{n,FO}$, expressed as in equation 13.13, and the reference (target) energies $\varepsilon^{\text{exact}}_{n,FO}$, keeping the energies of the acetylene orbitals (see equation 13.14), in order to get optimal values of the effective parameters (FO = HO, LU).

The reference energies are obtained by direct calculations using the extended-Hückel method (Caesar 2.0 software). We chose this method because, in addition to the orbital energies, it provides the values of the integrals H_{ii}, H_{ij}, and S_{ij} for the fragment orbitals, that is the original values that are required to verify the validity of the model. Those quantities will also be used in the next chapter for the parametrization according to the nuclear modes.

$$\begin{cases} \sqrt{\frac{1}{6}\sum_{n=2}^{7}\left(\varepsilon^{\text{eff}}_{n,FO} - \varepsilon^{\text{exact}}_{n,FO}\right)^2} \\ \alpha_{A,FO} \text{ is unchanged} \end{cases} \tag{13.14}$$

where FO = HO or LU.

The procedure is performed over a sample composed of the chromophores p2 to p7 at an oversymmetrized geometry close to the equilibrium geometry of the ground state, see figure 13.7.

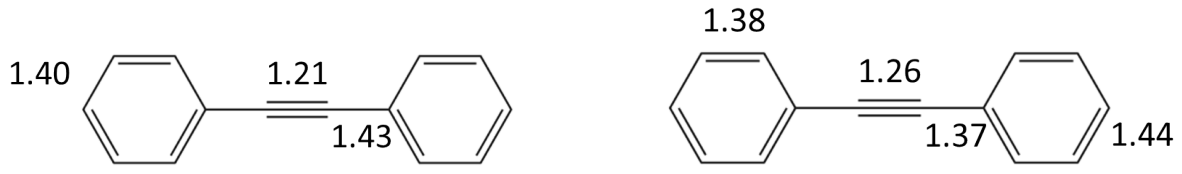

Figure 13.7: Geometrical characteristics of the oversymmetrized geometries considered for the validation. At the oversymmetrized $min\text{S}_0$ (left), benzenes are assimilated to regular hexagons with same bond lengths; at the oversymmetrized $min\text{S}_1$ (right), quinoidal bonds are shorter than the other bonds of the rings. In both cases, the planar angles of benzene are set to 120°. Bond lengths are given in Å.

This ensures that the original values for the energies or interactions among orbitals are equivalent from a *site* or pair of *sites* to another, both in a molecule and between the different molecules of the sample (p2 to p7).

As mentioned before, the value of each parameter is the same for any number of rings in the chromophore. We impose this equality by running the optimization simultaneously for all the molecules of the sample. The result of this optimization is presented in Table 13.2.

Finally, the original values of the parameters are extracted from extended-Hückel calculations that explicitly account for the overlap S_{ij} between two orbitals localized on sites i and j, respectively. On the contrary, this overlap is only taken into account implicitly in our model, through the optimization. In other words, the optimized parameters are expressed in an implicitly orthonormal basis whilst the original parameters are not.

Thus, the extended-Hückel basis must be orthonormalized prior to comparing the optimized effective values of the parameters to the original ones (to compare comparable quantities).

In the orthonormalized basis (Schmidt), the extended-Hückel matrix reads

$$\boldsymbol{H}_{\mathrm{XH}}^{\mathrm{ortho}} = \begin{bmatrix} \alpha_A & \dfrac{H_{BA} - \alpha_A S}{\sqrt{(1-S^2)}} \\ \dfrac{H_{BA} - \alpha_A S}{\sqrt{(1-S^2)}} & \dfrac{\alpha_B - 2H_{BA}S + \alpha_A S^2}{1-S^2} \end{bmatrix} . \tag{13.15}$$

The details of the derivation and discussion about the basis choice are provided in Appendix C. In addition, the closest $\boldsymbol{H}^{\mathrm{eff}}$ and $\boldsymbol{H}^0$, the smallest the perturbation, so we define the criterion for validating the main-interaction approximation by identification

$$\begin{cases} \beta^{\mathrm{eff}} \approx \dfrac{H_{AB} - \alpha_A S}{\sqrt{(1-S^2)}} \\ \alpha_B^{\mathrm{eff}} \approx \dfrac{\alpha_B - 2H_{AB}S + \alpha_A S^2}{1-S^2} \end{cases} . \tag{13.16}$$

The results at the minimum of the ground state are presented in table 13.2. The same order of magnitude between the optimized and original parameters proves the relevance of the FFO approximation.

The same analysis is carried out at an oversymmetrized geometry close to the equilibrium geometry of S_1 and leads to the same observations and conclusions, see table 13.3.

	HO		LU	
Model	Effective FFO	extended-Hückel	Effective FFO	extended-Hückel
α_A / eV	-13.53		-7.00	
α_B / eV	-12.95	-12.68	-8.37	-8.15
β / eV	-0.76	-0.60	-0.96	-1.36

Table 13.2: Comparison between the optimized values of the tight-binding parameters in the FFO model and the original values of the extended-Hückel parameters projected in an orthonormal basis set, at *min*S1.

	HO		LU	
Model	Effective FFO	extended-Hückel	Effective FFO	extended-Hückel
α_A / eV	-13.41		-7.61	
α_B / eV	-12.97	-12.51	-8.64	-8.38
β / eV	-0.91	-0.69	-0.99	-1.45

Table 13.3: Comparison between the optimized values of the tight-binding parameters in the FFO model and the original values of the extended-Hückel parameters projected in an orthonormal basis set, at *min*S1.

The main approximation of the FFO model is to consider that one FO of the chromophore comes from a single main interaction. Thus, the optimization implicitly accounts for secondary interactions between the orbitals of the benzene fragment and orbitals of the acetylene fragment. For the HO (LU) of pn, this concerns in particular all the interactions involving the non-HO (LU) orbitals of benzene. Basically the optimization of the energies of the FOs of benzene is equivalent to taking the three other orbitals on an average manner.

13.4 Extension to *meta*-PPEs

The idea of the last step (see figure 13.8) is to describe the first two excited states of *meta*-PPEs in terms of a coupling between the first excited state of each building block, along the line of excitonic models that are proposed in literature [60,142,143]. The energy of the electronic states depends on both the orbital energies and their occupations.

Thus, in a first step, we examine the coupling between the frontier orbitals, which will be reflected in the coupling between the electronic states. We examine the possibility of using the FFO formalism to describe the interaction between the frontier orbitals of

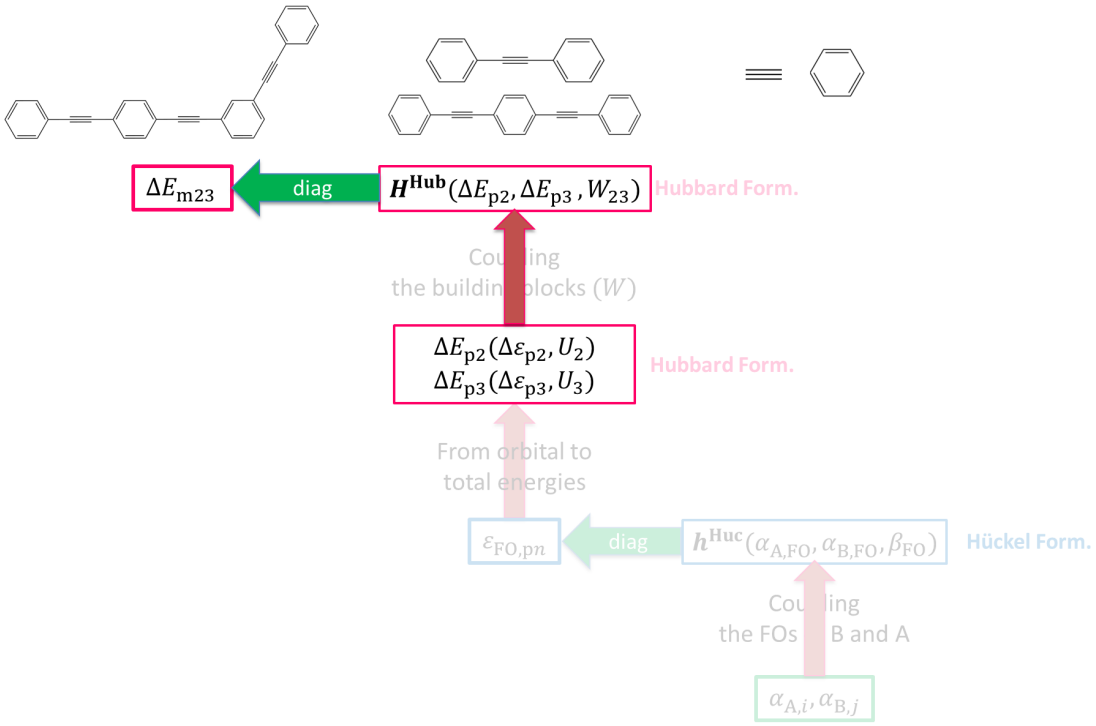

Figure 13.8: Structure of the vibronic model.

meta-PPEs.

13.4.1 Pseudo-fragments

The derivation is presented on m22.

As mentioned in Part IV we consider the building blocks of a *meta*-PPEs as pseudo-fragments. Since they share a common benzene, see figure 13.9, building blocks cannot be considered as proper fragments within the theory of fragment orbitals. Yet, their orbitals overlap and interact as any usual fragment orbitals, yielding the molecular orbitals of the *meta*-PPE.

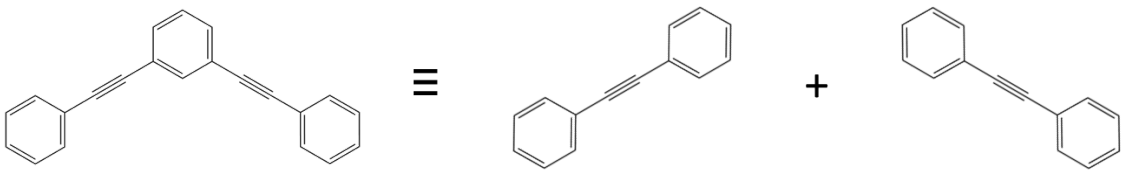

Figure 13.9: Pseudo-fragment decomposition of m22.

We recall the shapes of the near frontier orbitals of m22 in figure 13.10, along with the implication of the properties of the degenerate orbitals of benzene.

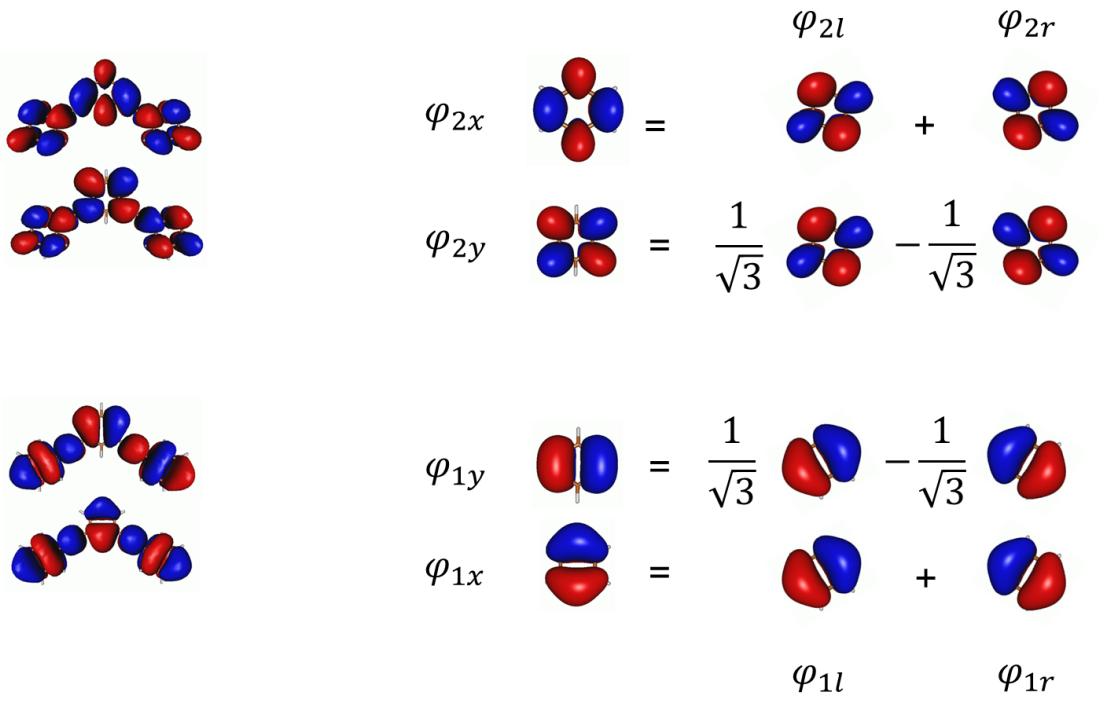

Figure 13.10: Near frontier orbitals of m22 by increasing energy from bottom to top (left), properties of the degenerate orbitals of benzene (right).

The superimposition of the pseudo-fragment orbitals yields new couplings between the orbitals of one building block and the orbitals of the other building block. In particular, the HO (LU) of benzene for the l.h.s. building block interacts with the π- (π^*-) orbital of acetylene for the r.h.s. building block, see figure 13.12. These two interactions will be termed *meta*-couplings.

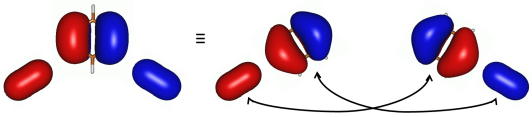

Figure 13.11: Illustration of the *meta*-couplings arising around the *meta*-junction. Example with the scheme of the HO around the common phenylene of m22.

We define the energies of interaction due to *meta*-couplings in terms of the energy of interaction due to the common *para*-couplings in an A–B pair, that is β_{FO}, see figure 13.12. The two superimposed orbitals (HOs or LUs, respectively) are identical except for the angle between the pseudo-fragments (about 120°), and thus form a non-orthogonal

basis of the space of the degenerate orbitals [3].

Consequently, the *meta*-coupling interaction is proportional to the common *para*-coupling interaction through the overlap between the non-orthogonal orbitals. We consider the ideal case of an angle of $\pi/3$ between the two building blocks, and thus between the two superimposed orbitals of benzene, see figure 13.12.

Hence the relation between the *meta*-coupling interaction β_{FO}^{meta} and the common *para*-coupling interaction β_{FO}

$$\beta_{FO}^{\text{meta}} = -\frac{1}{2}\beta_{FO} \tag{13.17}$$

with FO = HO or LU.

Thus, we write the matrices $\boldsymbol{H}_{n,m,FO}$ containing the frontier orbilals of a *meta*-PPE as the reunion of the Hückel-type matrices $\boldsymbol{H}_{n,FO}$ of the building blocks with extra *meta*-couplings. Considering the example of m22, that would be $\boldsymbol{H}_{2,FO}$ and $\boldsymbol{H}_{2,FO}$, see equation 13.19.

$$\boldsymbol{H}_{2,2,FO} = \left[\begin{array}{c|c} \boldsymbol{H}_{2,FO} & \text{couplings} \\ \hline \text{couplings} & \boldsymbol{H}_{2,FO} \end{array}\right] \tag{13.18}$$

$$= \left[\begin{array}{ccc|ccc} \alpha_{\text{B},FO} & \beta_{FO} & 0 & 0 & 0 & 0 \\ \beta_{FO} & \alpha_{\text{A},FO} & \beta_{FO} & -\frac{1}{2}\beta_{FO} & 0 & 0 \\ 0 & \beta_{FO} & \alpha_{\text{B},FO} & 0 & -\frac{1}{2}\beta_{FO} & 0 \\ \hline 0 & -\frac{1}{2}\beta_{FO} & 0 & \alpha_{\text{B},FO} & \beta_{FO} & 0 \\ 0 & 0 & -\frac{1}{2}\beta_{FO} & \beta_{FO} & \alpha_{\text{A},FO} & \beta_{FO} \\ 0 & 0 & 0 & 0 & \beta_{FO} & \alpha_{\text{B},FO} \end{array}\right] . \tag{13.19}$$

[3] In the orthonormal basis $(\varphi_{\text{x}}, \varphi_{\text{y}})$, the pseudo-fragment orbitals read

$$\begin{cases} \varphi_{\text{l}} = -\left\{\cos\left(-\frac{\pi}{3}\right)\varphi_{\text{x}} + \sin\left(-\frac{\pi}{3}\right)\varphi_{\text{y}}\right\} = -\frac{1}{2}\varphi_{\text{x}} + \frac{\sqrt{3}}{2}\varphi_{\text{y}} \\ \varphi_{\text{r}} = -\left\{\cos\left(\frac{\pi}{3}\right)\varphi_{\text{x}} + \sin\left(\frac{\pi}{3}\right)\varphi_{\text{y}}\right\} = -\frac{1}{2}\varphi_{\text{x}} - \frac{\sqrt{3}}{2}\varphi_{\text{y}} \end{cases}$$

Thus, $\langle\varphi_{\text{l}}|\varphi_{\text{r}}\rangle = -\frac{1}{2}$.

A drawback remains though. Since the left/right superimposed orbitals are not orthogonal, the overlap matrix of the basis must be considered while solving the eigenvalue problem, which thus does not reduces to the diagonalization of $\boldsymbol{H}_{2,2,FO}$ (see Appendix C).

To tackle this issue, we write the interaction Hamiltonian $\boldsymbol{H}^{\text{ortho}}_{2,2,FO}$ in the basis containing the orthogonalized FOs of benzene (that appear on the common phenylene in the near FOs of m22) instead of the left/right ones, see figure 13.13. The off-diagonal terms corresponding to the interaction of the π- (π^*-) orbital of acetylene with the orthogonalized HOs (LUs) of benzene can be obtained by expanding the orthogonalized orbitals in the basis of the left/orbitals, see figure 13.12.

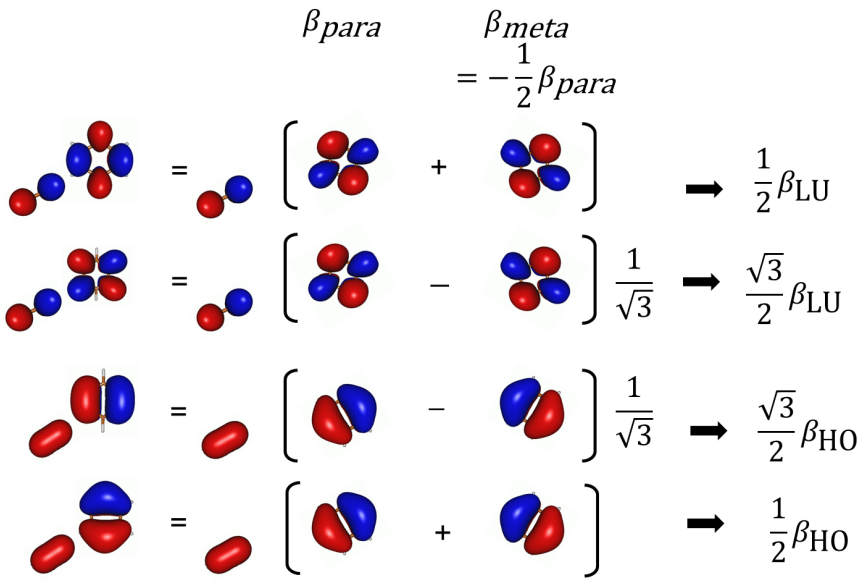

Figure 13.12: Interaction of the π^*-orbital of the acetylene of the l.h.s. building block with the superimposed LUs on the common phenylene (top); Interaction of the π-orbital of the acetylene of the l.h.s. building block with the superimposed HOs on the common phenylene (bottom).

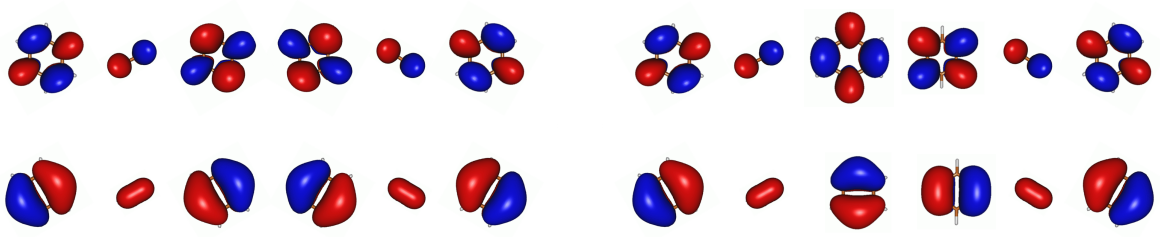

Figure 13.13: Bases of the orbitals over which are written $\boldsymbol{H}_{2,2,FO}$ (left) and $\boldsymbol{H}^{ortho}_{2,2,FO}$ (right). Bases with the left/right FOs of benzene are on the left, basis with orthogonal FOs of benzene are on the right.

$$\boldsymbol{H}^{\text{ortho}}_{2,2,FO} = \begin{bmatrix} \alpha_{\text{B},FO} & \beta_{FO} & 0 & 0 & 0 & 0 \\ \beta_{FO} & \alpha_{\text{A},FO} & \frac{1}{2}\beta_{FO} & \frac{\sqrt{3}}{2}\beta_{FO} & 0 & 0 \\ 0 & \frac{1}{2}\beta_{FO} & \alpha_{\text{B},FO} & 0 & \frac{1}{2}\beta_{FO} & 0 \\ 0 & \frac{\sqrt{3}}{2}\beta_{FO} & 0 & \alpha_{\text{B},FO} & -\frac{\sqrt{3}}{2}\beta_{FO} & 0 \\ 0 & 0 & \frac{1}{2}\beta_{FO} & -\frac{\sqrt{3}}{2}\beta_{FO} & \alpha_{\text{A},FO} & \beta_{FO} \\ 0 & 0 & 0 & 0 & \beta_{FO} & \alpha_{\text{B},FO} \end{bmatrix} \tag{13.20}$$

This can be generalized to any coupling between the n- and m-ring building blocks of mnm. The corresponding Hamiltonian $\boldsymbol{H}_{n,m,FO}$ reads

$$\boldsymbol{H}_{n,m,FO} = \left[\begin{array}{ccccc|ccccc} \alpha_{\text{B},FO} & \beta_{FO} & 0 & 0 & 0 & 0 & 0 & 0 & 0 & 0 \\ \beta_{FO} & \alpha_{\text{A},FO} & \ddots & 0 & 0 & 0 & 0 & 0 & 0 & 0 \\ 0 & \ddots & \ddots & \ddots & 0 & 0 & 0 & 0 & 0 & 0 \\ 0 & 0 & \ddots & \alpha_{\text{A},FO} & \frac{1}{2}\beta_{FO} & \frac{\sqrt{3}}{2}\beta_{FO} & 0 & 0 & 0 & 0 \\ 0 & 0 & 0 & \frac{1}{2}\beta_{FO} & \alpha_{\text{B},FO} & 0 & -\frac{1}{2}\beta_{FO} & 0 & 0 & 0 \\ \hline 0 & 0 & 0 & \frac{\sqrt{3}}{2}\beta_{FO} & 0 & \alpha_{\text{B},FO} & -\frac{\sqrt{3}}{2}\beta_{FO} & 0 & 0 & 0 \\ 0 & 0 & 0 & 0 & \frac{1}{2}\beta_{FO} & -\frac{\sqrt{3}}{2}\beta_{FO} & \alpha_{\text{A},FO} & \ddots & 0 & 0 \\ 0 & 0 & 0 & 0 & 0 & 0 & \ddots & \ddots & \ddots & 0 \\ 0 & 0 & 0 & 0 & 0 & 0 & 0 & \ddots & \alpha_{\text{A},FO} & \beta_{FO} \\ 0 & 0 & 0 & 0 & 0 & 0 & 0 & 0 & \beta_{FO} & \alpha_{\text{B},FO} \end{array}\right] \tag{13.21}$$

and its eigenvalues satisfy

$$\varepsilon^{n,m}_{0\pm,FO} = \alpha_{\text{B},FO} \tag{13.22}$$

$$\varepsilon^{n,m}_{\pm j,FO} = \frac{\alpha_{\text{A},FO} + \alpha_{\text{B},FO}}{2} \pm \sqrt{\left(\frac{\alpha_{\text{A},FO} - \alpha_{\text{B},FO}}{2}\right)^2 + \left(\gamma^{n,m}_j \beta_{FO}\right)^2} \tag{13.23}$$

where $j \in [\![1; n+m-2]\!]$. Once again, this can be verified with Mathematica for example.

The values of $\gamma^{n,m}_j$ are analytical and we report them in table 13.4.

(n,m) \ j	1	2	3	4	5	6
(2,2)	$\sqrt{\frac{3}{2}}$	$\sqrt{\frac{5}{2}}$				
(2,3)	$\sqrt{2-\frac{\sqrt{5}}{2}}$	$\sqrt{2}$	$\sqrt{2+\frac{\sqrt{5}}{2}}$			
(3,3)	$\frac{\sqrt{7-\sqrt{17}}}{2}$	$\frac{\sqrt{9-\sqrt{17}}}{2}$	$\frac{\sqrt{7+\sqrt{17}}}{2}$	$\frac{\sqrt{9+\sqrt{17}}}{2}$		
(3,4)	$\frac{1}{\sqrt{2}}$	1	$\sqrt{2}$	$\sqrt{3}$	$\sqrt{\frac{7}{2}}$	
(4,4)	$\frac{\sqrt{x_1^I}}{2}$ ≈ 0.66	$\frac{\sqrt{x_1^{II}}}{2}$ ≈ 0.83	$\frac{\sqrt{x_2^I}}{2}$ ≈ 1.33	$\frac{\sqrt{x_2^{II}}}{2}$ ≈ 1.50	$\frac{\sqrt{x_3^I}}{2}$ ≈ 1.82	$\frac{\sqrt{x_3^{II}}}{2}$ ≈ 1.89

Table 13.4: Values of $\gamma_j^{n,m}$ for $n, m \in [\![2;4]\!]$ and $j \in [\![1; n+m-2]\!]$. Formal expressions obtained with Mathematica.

x_k^I and x_k^{II} $(k = 1, 2, 3)$ are the roots of the following polynomials

$$P^I(x) = \prod_{k=1}^{3}(x - x_k^I) = x^3 - 22x^2 + 128x - 160$$
$$P^{II}(x) = \prod_{k=1}^{3}(x - x_k^{II}) = x^3 - 26x^2 + 192x - 352 \ .$$

13.4.2 Validation

To verify the validity of our proposition, the energies of the orbitals calculated using our model are compared to the energies obtained from direct XH calculations (consistently with the procedure applied for *para*-PPEs).

The effective parameters optimized over the sampling of *para*-PPEs (presented in table 13.2) are injected into the expressions for the energies of the orbitals of *meta*-PPEs (equations 13.23). The energies of the frontier orbitals are associated with the value $j = n + m - 2$, the ones of the second frontier orbitals are associated with the value $j = n + m - 3$.

The energies of the near frontier orbitals of m22, m23, m33, m34, and m44 are presented in table 13.5, for direct calculations and our model.

The energies of the HO–1 and LU+1 of m22, m33 and m44 are presented, yet we will not discuss them. Indeed, our point is to propose a model that would reproduce the transition energies to local excited states that correspond to transitions between (near) frontier orbitals. Yet, as mentioned in Part IV section 9.2 , the HO–1–LU+1 transition

model	FO	m22	m23	m33	m34	m44
XH calculation E_{XH}	LU+1	-9.09	-9.19	-9.41	-9.45	-9.54
	LU	-9.30	-9.48	-9.51	-9.58	-9.60
	HO	-12.05	-11.90	-11.87	-11.81	-11.79
	HO-1	-12.21	-12.13	-11.95	-11.91	-11.84
	HO–LU gap	2.74	2.42	2.36	2.23	2.19
	HO-1–LU+1 gap	3.12	2.95	2.54	2.46	2.29
FFO model E_{FFO}	LU+1	-9.04	-9.20	-9.42	-9.48	-9.56
	LU	-9.35	-9.51	-9.55	-9.60	-9.62
	HO	-12.00	-11.87	-11.83	-11.79	-11.77
	HO-1	-12.27	-12.13	-11.94	-11.89	-11.83
	HO–LU gap	2.66	2.36	2.28	2.19	2.15
	HO-1–LU+1 gap	3.22	2.92	2.52	2.41	2.27
$E_{FFO} - E_{XH}$	LU+1	0.04	-0.02	-0.02	-0.03	-0.01
	LU	-0.04	-0.03	-0.04	-0.02	-0.02
	HO	0.04	0.03	0.04	0.02	0.02
	HO-1	-0.05	0.01	0.01	0.02	0.01
	HO–LU gap	-0.09	-0.07	-0.08	-0.04	-0.04
	HO-1–LU+1 gap	0.10	-0.02	-0.03	-0.05	-0.02

Table 13.5: Energies of the near frontier orbitals in some *meta*-PPEs (in eV).

does not yield such local excited states in symmetrical *meta*-PPEs, for symmetry reasons (plus and minus delocalized states), see figure 13.14.

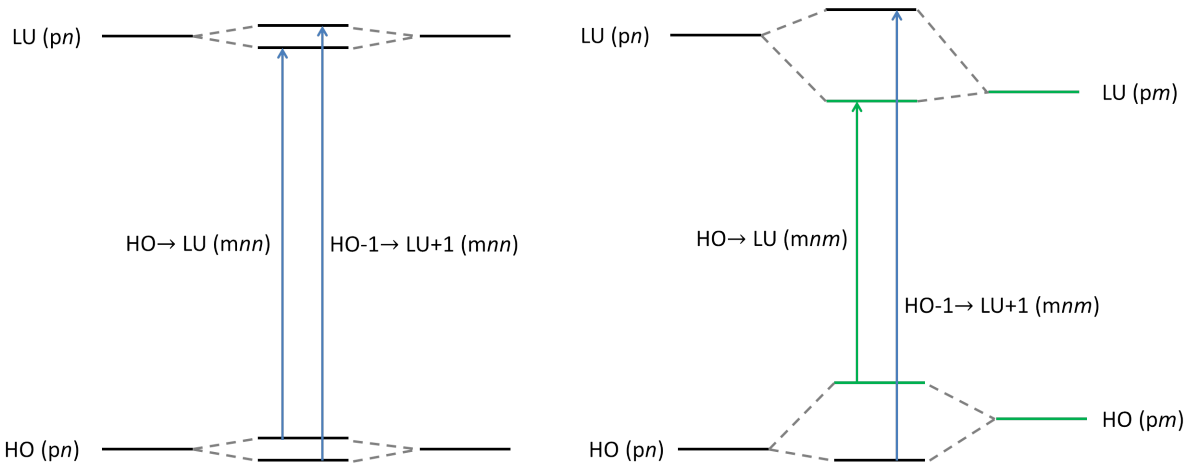

Figure 13.14: Illustration of the transitions betwen frontier and second frontier orbitals in symmetrical (left) or mixed (right) *meta*-PPEs.

The difference between the energies calculated with our model and the reference ones is within 0.01 eV and 0.04 eV in absolute value, which is decent considering the simplicity of the model. The energies for the occupied (vacant) system are systematically overestimated (underestimated) by a similar amount. This reflects the fact that our model overestimates

the interactions between the benzene and acetylene fragments, since the HO and HO–1 (LU and LU+1) result from an ideal fully antibonding (bonding) interaction among identical site orbitals.

The errors in the energies of occupied and unoccupied orbitals cumulate in the energy gaps, so our model underestimates the energy gaps by amounts within 0.02 and 0.09 eV. Again, this error is acceptable considering our level of approximation.

This confrontation confirms that our model accounts for the physics of *meta*-PPEs, and thus validates its relevance to express the energies of frontier orbitals of *meta*-PPEs.

We cannot go further, from a vibronic perspective, without considering the relationship between parameters along with their dependence with respect to the nuclear coordinates. Consequently, the values of the parameters presented in the present chapter will be further refined later on. In particular, the coupling between building blocks will be refined in the last step of the construction to be applied to electronic states and energies.

Chapter 14

Parametrization

One of the ultimate objectives of this project is to set up a strategy for building a quasi-diabatic vibronic model of the potential energy surfaces of PPEs, that is an expression of the electronic energy matrix in terms of nuclear modes. Within this perspective, we will see that one of the key-points is to determine the relative evolution of the TDDFT S_0-S_1 transition energies ΔE and the XH HO$-$LU energy gaps $\Delta\varepsilon$ for *para*-PPEs. This basically reduces to a mapping of the potential energy surface to an effective model. A similar strategy was already proposed considering an effective Frenkel Hamiltonian for a polymer constituted of a single type of monomer [144].

We are now interested in the variations of the (effective) parameters, namely how they are affected by the nuclear motions. Remembering that we are using a tight-binding formalism, it is decent to consider that the energy of a local orbital attached to a site will only depend on the deformation of this site, that is the length of the acetylene bond or various deformations of the benzene rings, see figure 14.1. Similarly, the resonance interaction between a benzene and an acetylene will only be affected by the distance between them.

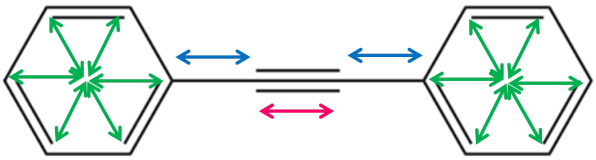

Figure 14.1: Local deformations of a PPE.

It must be noted that the relative torsions between adjacent benzenes should play a role by affecting the interactions between sites. In the present work, we focus on the

planar behavior of PPEs and ignore the influence of torsions. Yet, this contribution could be added later on. It should account for the fact that the torsions never disrupt totally the conjugation (due to the cylindric triple bonds) and could take the form of a periodic function.

14.1 Functional expression of ΔE

14.1.1 General empirical affine relation

We start by examining the relative variations of ΔE and $\Delta\varepsilon$ upon plotting them for various numbers of rings n and geometries (which will be defined later on), see figure 14.2. From this plot, we notice that ΔE and $\Delta\varepsilon$ are connected *via* a near-affine relation, which leads to the following empirical relation: $\Delta E \sim A\Delta\varepsilon + \Delta U$.

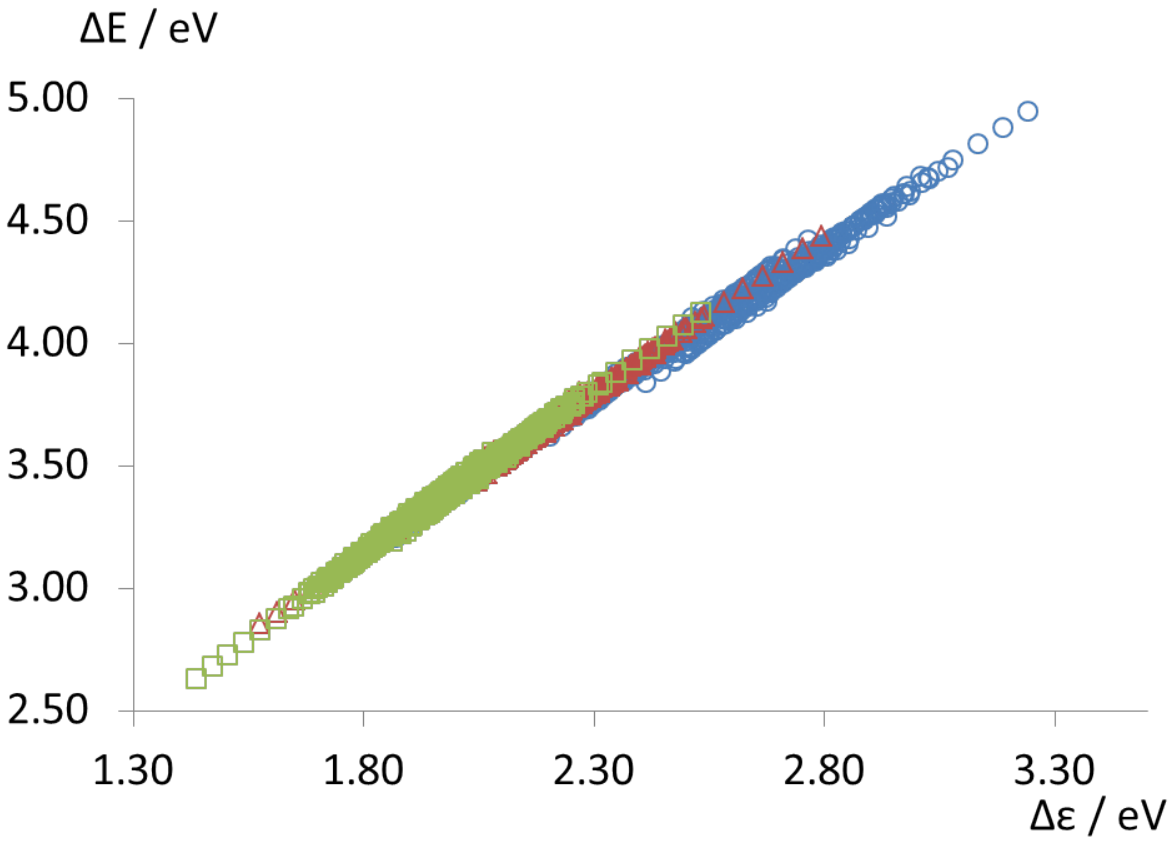

Figure 14.2: TDDFT $S_0 - S_1$ transition energies ΔE *vs.* XH HO − LU energy gaps $\Delta\varepsilon$ for various geometries of p2 (blue circles), p3 (red triangles), p4 (green squares). The linear regression for p2, with energies in eV, gives $y = 1.2450\ x + 0.9032$ with $R^2 = 0.9899$; for p3, $y = 1.2855$ x + 0.8391 with $R^2 = 0.9962$; for p4, $y = 1.3561\ x + 0.6953$ with $R^2 = 0.9964$.

It appears in the parameters of the linear regression that the amplification factor A

and the shift ΔU slightly change with the number of rings n. As a matter of fact, they may also depend on the coordinates $\boldsymbol{Q}$ and slightly change between two given geometries, see table 14.1.

$\boldsymbol{Q}$	vertex	p2		p3		p4	
		$A^{(2)}(\boldsymbol{Q})$	$\Delta U^{(2)}(\boldsymbol{Q})$	$A^{(3)}(\boldsymbol{Q})$	$\Delta U^{(3)}(\boldsymbol{Q})$	$A^{(4)}(\boldsymbol{Q})$	$\Delta U^{(4)}(\boldsymbol{Q})$
[100]	(000)	1.5139	0.1391	1.4074	0.5532	1.4687	0.4541
	(001)	1.5422	0.1700	1.4119	0.5896	1.4975	0.4371
	(010)	1.5023	0.1981	1.4003	0.5686	1.4799	0.4319
	(011)	1.5312	0.2261	1.4041	0.6027	1.5067	0.4227
[010]	(000)	1.3544	0.5957	1.4128	0.5405	1.4654	0.4609
	(001)	1.3702	0.6223	1.4403	0.5282	1.4795	0.4728
	(100)	1.3448	0.6019	1.4071	0.5540	1.4700	0.4511
	(101)	1.3616	0.6242	1.4334	0.5452	1.4829	0.4652
[001]	(000)	1.0654	1.4234	1.1819	1.0883	1.2399	0.9488
	(010)	1.0707	1.3589	1.1875	1.0486	1.2487	0.8992
	(100)	1.0555	1.3942	1.1819	1.0660	1.2451	0.9244
	(110)	1.0623	1.3269	1.1874	1.0279	1.2528	0.8778

Table 14.1: Values of the amplification factor $A^{(n)}(\boldsymbol{Q})$ and the shift $\Delta U^{(n)}(\boldsymbol{Q})$ along the different nuclear coordinates $\boldsymbol{Q}$ and passing by different vertices for p2, p3, and p4. All the determination coefficients R^2 involved are equal to 1.0000.

Considering this, we propose the following expression

$$\Delta E^{(n)}(\boldsymbol{Q}) = A^{(n)}(\boldsymbol{Q})\Delta\varepsilon^{(n)}(\boldsymbol{Q}) + \Delta U^{(n)}(\boldsymbol{Q}) \tag{14.1}$$

where $\boldsymbol{Q} = (Q^k)$ are linear variations of the nuclear coordinates with respect to the equilibrium geometry of S_0 ($\boldsymbol{Q}_0 = \boldsymbol{0}$).

This expression is actually a mere recasting and remains general until further constraints are applied on $A^{(n)}(\boldsymbol{Q})$ and $\Delta U^{(n)}(\boldsymbol{Q})$.

It is important to note that $\Delta U^{(n)}$ is different from the on-site repulsion U of the Hubbard model. In the Hubbard model, no repulsion between the electrons is accounted for before U is introduced, which is not the case in the XH energies of orbitals. In the XH methods, electronic repulsion is implicitly considered through the inital parametrization of the method. Then, $\Delta U^{(n)}$ would be a correction to the electronic repulsion, adapted to each species we consider.

14.1.2 Simplifications

First, both ΔE and $\Delta\varepsilon$ vary almost linearly along each coordinate, see figure 14.3.

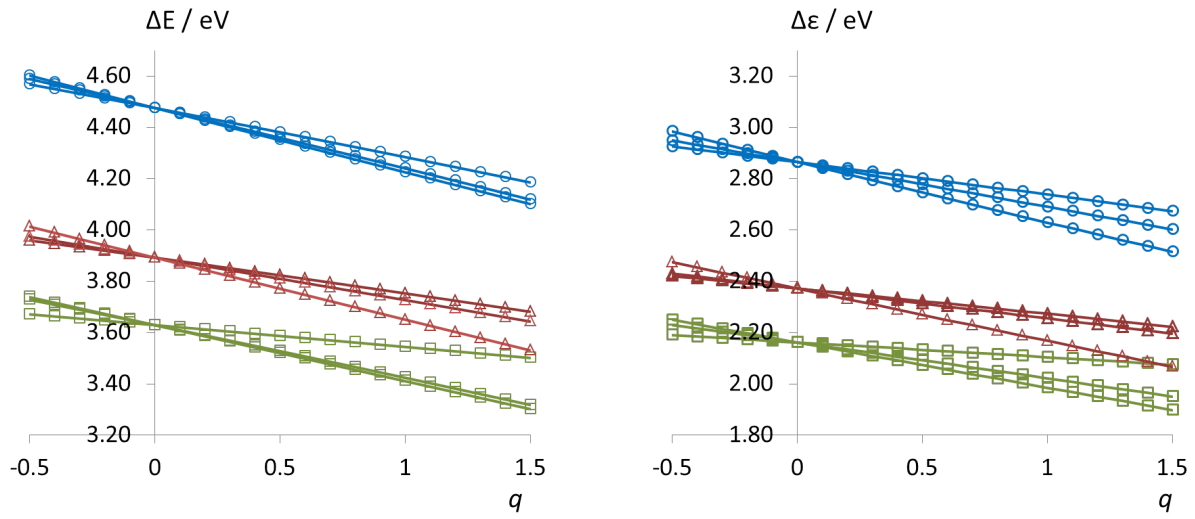

Figure 14.3: TDDFT $S_0 - S_1$ transition energies ΔE (left) and XH HO − LU energy gaps $\Delta\varepsilon$ (right) as functions of the nuclear modes $\boldsymbol{Q}$ for p2 (blue circles), p3 (red triangles), p4 (green squares). Here are presented the interpolations passing by the equilibrium geometry of S_0. All the corresponding determination coefficients are greater than 0.9998.

Relying on this, we assume that ΔE, $\Delta\varepsilon$, and ΔU are all multidimensional affine functions of $\boldsymbol{Q}$

$$\begin{cases} \Delta\varepsilon^{(n)}(\boldsymbol{Q}) = \Delta\varepsilon_0^{(n)} + \sum_k a_k^{(n)} Q^k \\ \Delta U^{(n)}(\boldsymbol{Q}) = \Delta U_0^{(n)} + \sum_k b_k^{(n)} Q^k \\ \Delta E^{(n)}(\boldsymbol{Q}) = \Delta E_0^{(n)} + \sum_k c_k^{(n)} Q^k \end{cases} \tag{14.2}$$

where $\Delta\varepsilon_0 = \Delta\varepsilon(\mathbf{0})$, $\Delta U_0 = \Delta U(\mathbf{0})$, and $\Delta E_0 = \Delta E(\mathbf{0})$.

This allows to determine $a_k^{(n)}$ and $c_k^{(n)}$. Then A must be constant with respect to $\boldsymbol{Q}$. If not, ΔE would vary to second order at least with respect to $\boldsymbol{Q}$. In addition, as ΔE and $\Delta\varepsilon$, ΔU must be a multidimensional affine function of $\boldsymbol{Q}$ and may depend on n. This leads to the following relations at zeroth and first orders

$$\Delta E_0^{(n)} = A^{(n)} \Delta\varepsilon_0^{(n)} + \Delta U_0^{(n)} \tag{14.3}$$

$$c_k^{(n)} = A^{(n)} a_k^{(n)} + b_k^{(n)} \ . \tag{14.4}$$

Second, A and ΔU_0 do not vary with n. Indeed, the behavior of $\Delta E_0^{(n)}$ with respect to $\Delta\varepsilon_0^{(n)}$ reveals an affine relationship, see figure 14.4. Plots were performed for an extended (p2 to p7) and a reduced (p2 to p4) sample, which leads to $A \sim 1.2$ and $\Delta U_0 \sim 1.0$ eV.

To the best of our knowledge, literature rarely reports studies involving more-than-four-ring *para*-PPEs or *meta*-PPEs composed of such building blocks. Thus, we will

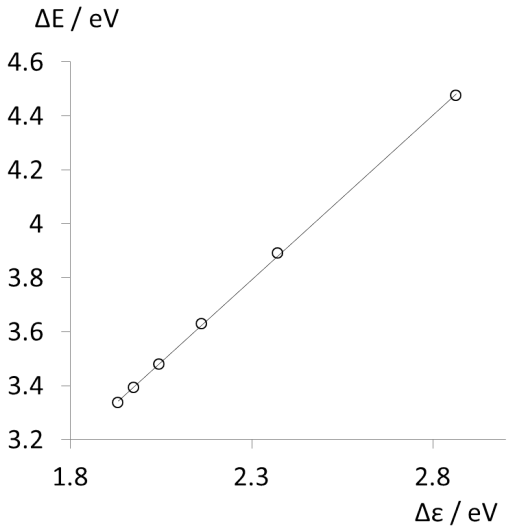

Figure 14.4: TDDFT $S_0 - S_1$ transition energies ΔE *vs.* XH HO $-$ LU energy gaps $\Delta\varepsilon$ at the equilibrium geometries of p2 to p7. The linear regression on the full sample gives $y = 1.2198\ x + 0.9877$ (for energies in eV) with $R^2 = 0.9998$; the linear regression on the reduced sample (p2, p3, p4) gives $y = 1.2013\ x + 1.0364$ with $R^2 = 0.9998$.

use the values fitted on the reduced sample in the following, that is $A = 1.2013$ and $\Delta U_0 = 1.0364$ eV.

Consequently, equation 14.4 becomes

$$c_k^{(n)} = A a_k^{(n)} + b_k^{(n)} \tag{14.5}$$

and $b_k^{(n)}$ is fully determined by $a_k^{(n)}$ and $c_k^{(n)}$ (which can be evaluated from the variation of $\Delta\varepsilon^{(n)}$ and $\Delta E^{(n)}$ with respect to Q^k since A is now known).

Those two simplifications arise from the relative behavior of the energy differences along the deformations Q^k. No further simplification can be obtained unless specific dependences or relationships involving n can be found.

Expressing ΔE as a functional of $\Delta\varepsilon$, it comes

$$\Delta E\left[\Delta\varepsilon, \boldsymbol{Q}; n\right] = \Delta E^{(n)}(\boldsymbol{Q}) \tag{14.6}$$

$$= A\Delta\varepsilon + \Delta U_0 + \sum_k b_k^{(n)} Q^k \tag{14.7}$$

where $\Delta\varepsilon = \Delta\varepsilon^{(n)}(\boldsymbol{Q})$ shows that ΔE as a function of $\Delta\varepsilon$ is almost affine (as observed on figure 14.2) because the typical contribution of $b_k^{(n)} Q^k$ stays small compared to typical variations of ΔE with $\Delta\varepsilon$.

14.2 Determination of the first-order parameters

14.2.1 Nuclear coordinates

For each PPE of the sample, we define a reduced set of three local nuclear coordinates that connect the equilibrium geometries of S_0 and S_1. Those are the stretching of the acetylene bonds (Q^1), the stretching of the internal bonds between benzene and acetylene (Q^2), and the global deformation of the rings (Q^3), see figure 14.5.

We associate these coordinates with the edges of a cube connecting the equilibrium geometries of S_0 and S_1.

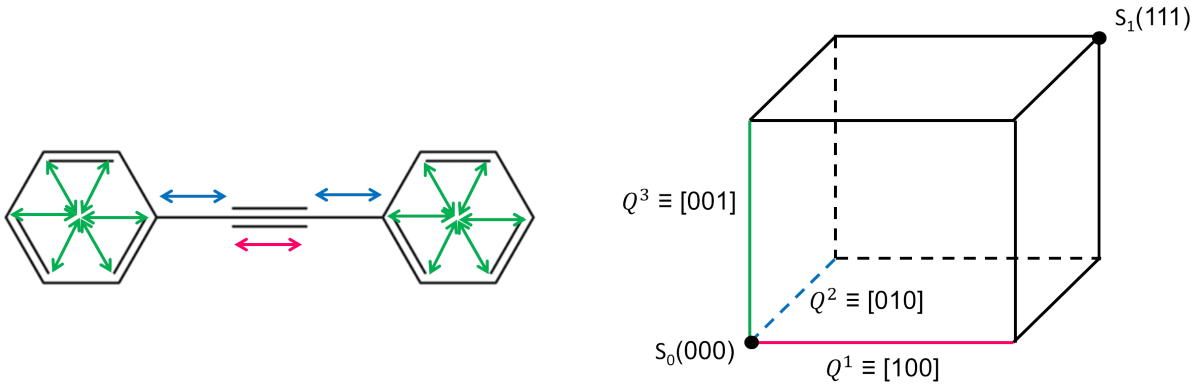

Figure 14.5: Representation of the nuclear coordinates as the egdes of a cube.

We recall that the equilibrium geometries of S_1 are not homogeneous from a *para*-PPE to another (see table 14.2), so the coordinates $\boldsymbol{Q}$ actually depends parametrically on n. For each mode, we normalize the difference of Q^k between $min S_0$ and $min S_1$ to 1 in order to be able to compare the displacements in the different *para*-PPEs.

n	mean $d_{\text{C-Ph}}$	$\sigma(d_{\text{C-Ph}})$	mean d_{CC}	$\sigma(d_{\text{CC}})$	mean d_{quin}	$\sigma(d_{\text{quin}})$
2	1.374	0*	1.255	0*	1.377	0*
3	1.391	0.008	1.233	0*	1.374	0.009
4	1.399	0.013	1.229	0.008	1.378	0.008
5	1.404	0.013	1.223	0.007	1.377	0.008
6	1.408	0.013	1.223	0.007	1.379	0.007
7	1.410	0.012	1.219	0.006	1.379	0.007
all n	1.404	0.015	1.227	0.011	1.377	0.008

Table 14.2: Lengths and standard deviations (in Å) of the characteristic bonds of *para*-PPEs in their first excited state. * indicates a standard deviation that is zero for symmetry reasons.

Scans are performed along each edge (12), ascending face diagonal (6), and the ascending space diagonal of the cube for p2, p3, and p4 to generate test sets that will be

used for the fitting (next paragraph). The so-called ascending diagonals correspond to increments of +1 along two coordinates of $\boldsymbol{Q}$, for example we will consider the diagonal from (000) to (011) (denoted [011]) but not the diagonal from (001) to (010) (denoted [01-1]).

We performed linear interpolations along each edge and ascending face diagonal, with a normalized step value of 0.1 for $||\boldsymbol{Q}|| \in [-0.5; 1.5]$, that is 21 geometries along each direction. Along the space diagonal, the interpolation runs for $||\boldsymbol{Q}|| \in [-1; 2]$ that is 31 geometries. Overall, we generated 409 geometries for each test set associated with $n = 2, 3, 4$. Among a test set, all the vertices are represented four times (three edges, one ascending face diagonal), except $min\mathrm{S}_0$ and $min\mathrm{S}_1$ which are represented seven times (three edges, three face diagonals, the space diagonal). Since the coordinates are scaled to unity along the shift between the S_0 and S_1 minima, the values of the expansion coefficients introduced further can be compared directly.

Variations of $\Delta\varepsilon^{(n)}(\boldsymbol{Q})$ with respect to $\boldsymbol{Q}$ are linear (the values of the coefficient of determination R^2 lie between 0.9999 and 1.0000) along the edges of the cube and the [110] diagonal, which correspond to a concerted motion along the coordinates Q^1 (streching of the acetylene bonds) and Q^2 (stretching of the internal bonds). They are almost linear in a few cases, in particular along the diagonal associated with concerted motions involving the benzene modes, see table 14.3.

diagonal	going through	n	R^2
[101]	$min\mathrm{S}_0$	2	0.9996
[101]	$min\mathrm{S}_1$	2	0.9995
[011]	$min\mathrm{S}_0$	3	0.9998
[011]	$min\mathrm{S}_1$	3	0.9997
[111]	$min\mathrm{S}_0$ and $min\mathrm{S}_1$	2	0.9993
[111]	$min\mathrm{S}_0$ and $min\mathrm{S}_1$	3	0.9996

Table 14.3: Values of the coefficients of determination R^2 of $\Delta\varepsilon^{(n)}(\boldsymbol{Q})$ along some diagonals of the cube for $n = 2, 3$.

Variations of $\Delta E^{(n)}(\boldsymbol{Q})$ along the same directions are almost linear too (R^2 lies within 0.9997 and 1.0000). For both $\Delta\varepsilon^{(n)}(\boldsymbol{Q})$ and $\Delta E^{(n)}(\boldsymbol{Q})$, deviations from linearity are slightly larger along diagonal cuts where Q^3 (localized on benzene) varies together with either Q^1, Q^2, or both. They reflect a small "coupling" between Q^3 and the other two

coordinates.

From the determination coefficients, we can consider that the behavior of $\Delta E^{(n)}(\boldsymbol{Q})$ and $\Delta\varepsilon^{(n)}(\boldsymbol{Q})$ is linear with respect to each Q^k, which allows to neglect quadratic terms quite safely. Yet, this does not prevent from a multilinear behavior.

14.2.2 Multilinear parameters

The contributions of the coupled nuclear modes can be accounted for using the following multilinear expansions

$$\begin{aligned}\Delta\varepsilon^{(n)}(\boldsymbol{Q}) &= \Delta\varepsilon_0^{(n)} + a_1^{(n)}Q^1 + a_2^{(n)}Q^2 + a_3^{(n)}Q^3 \\ &\quad + a_{12}^{(n)}Q^1Q^2 + a_{13}^{(n)}Q^1Q^3 + a_{23}^{(n)}Q^2Q^3 + a_{123}^{(n)}Q^1Q^2Q^3 \qquad (14.8)\\ \Delta E^{(n)}(\boldsymbol{Q}) &= \Delta E_0^{(n)} + c_1^{(n)}Q^1 + c_2^{(n)}Q^2 + c_3^{(n)}Q^3 \\ &\quad + c_{12}^{(n)}Q^1Q^2 + c_{13}^{(n)}Q^1Q^3 + c_{23}^{(n)}Q^2Q^3 + c_{123}^{(n)}Q^1Q^2Q^3 \qquad (14.9)\end{aligned}$$

Applying an eight-point formula to the eight parameters of equations 14.8 and 14.9 with the eight vertices of the cube provides exact values for the expansion parameters (slopes are simple differences between the energies at two different vertices). The so-called vertex parameters are summarized in table 14.4.

Let us now verify that the values of the parameters allow to reproduce reasonably the values of $\Delta\varepsilon^{(n)}(\boldsymbol{Q})$ and $\Delta E^{(n)}(\boldsymbol{Q})$ for other geometries.

First, we inject the values of the expansion parameters into equations 14.8 and 14.9, and evaluate the values of $\Delta\varepsilon^{(n)}(\boldsymbol{Q})$ and $\Delta E^{(n)}(\boldsymbol{Q})$ thus calculated and compare them to the exact ones for the three test sets of 409 geometries. Proceeding this way, we obtain small values of the RMSD (see table 14.5), which confirms that overall our energetic description is relevant.

Second, we re-optimize the expansion parameters over the test sets (409 points for each pn). The values of the re-fitted parameters are very close to the values of the vertex parameters (see table 14.4), so the latter can be used in the framework of our model. This is confirmed by the values of the RMSD (see table 14.5).

In addition, in both cases, the values of the multilinear parameters are small compared to the linear ones (at least by one order of magnitude). The largest multilinear coefficients are $a_{13}^{(2)}$ and $a_{23}^{(3)}$, or $c_{13}^{(2)}$ and $c_{23}^{(3)}$, in agreement with the deviations from linearity reflected in the values of R^2 (table 14.3). This confirms that the linear contribution dominates

	Vertex param.			Re-fitted param.		
	$n=2$	$n=3$	$n=4$	$n=2$	$n=3$	$n=4$
$\Delta\varepsilon_0^{(n)}$	2.8646	2.3724	2.1621	2.8640	2.3721	2.1616
$a_1^{(n)}$	-0.1264	-0.0989	-0.0580	-0.1256	-0.0983	-0.0573
$a_2^{(n)}$	-0.1737	-0.1170	-0.1401	-0.1727	-0.1166	-0.1393
$a_3^{(n)}$	-0.2352	-0.2043	-0.1762	-0.2349	-0.2039	-0.1756
$a_{12}^{(n)}$	0.0015	0.0004	-0.0001	-0.0002	-0.0005	-0.0012
$a_{13}^{(n)}$	0.0123	0.0020	0.0031	0.0118	0.0014	0.0024
$a_{23}^{(n)}$	0.0050	0.0081	0.0020	0.0044	0.0077	0.0011
$a_{123}^{(n)}$	-0.0005	-0.0001	0.0001	0.0011	0.0010	0.0014
$\Delta E_0^{(n)}$	4.4748	3.8924	3.6295	4.4737	3.8913	3.6282
$c_1^{(n)}$	-0.1913	-0.1392	-0.0851	-0.1887	-0.1377	-0.0837
$c_2^{(n)}$	-0.2354	-0.1653	-0.2053	-0.2324	-0.1641	-0.2034
$c_3^{(n)}$	-0.2507	-0.2415	-0.2184	-0.2485	-0.2403	-0.2170
$c_{12}^{(n)}$	0.0037	0.0013	-0.0008	-0.0001	-0.0006	-0.0031
$c_{13}^{(n)}$	0.0154	0.0024	0.0029	0.0128	0.0009	0.0015
$c_{23}^{(n)}$	0.0042	0.0085	0.0009	0.0013	0.0073	-0.0012
$c_{123}^{(n)}$	-0.0009	-0.0002	0.0004	0.0020	0.0015	0.0025

Table 14.4: Values of the coefficients of the multilinear expansions of $\Delta\varepsilon^{(n)}(\boldsymbol{Q})$ and $\Delta E^{(n)}(\boldsymbol{Q})$ calculated from the vertices of the cube (left) or fitted from the 409-point samples (right).

	From vertex param.			From re-fitted param.		
	$n=2$	$n=3$	$n=4$	$n=2$	$n=3$	$n=4$
RMSD $\Delta\varepsilon^{(n)}$	0.0013	0.0007	0.0008	0.0010	0.0004	0.0005
RMSD $\Delta E^{(n)}$	0.0029	0.0009	0.0004	0.0017	0.0008	0.0011

Table 14.5: RMSD (in eV) for $\Delta\varepsilon$ and ΔE in p2, p3, p4 obtained with vertices parameters or re-fitted parameters.

in the behavior of $\Delta\varepsilon$ and ΔE with respect to Q^1, Q^2, and Q^3, as assumed above. We recall that the values of the linear and multilinear coefficients can be compared because all displacements were normalized to one.

14.2.3 Purely linear parameters

Since the multilinear contribution is small compared to the linear one, we neglect it, and thus almost divide the number of expansion parameters by two.

Let us now determine the values of the first-order parameters, $a_k^{(n)}$, $b_k^{(n)}$, and $c_k^{(n)}$.

To do so, we consider the linear expansions of $\Delta\varepsilon^{(n)}$, $\Delta E^{(n)}$, and $\Delta U^{(n)}$ with respect

to the nuclear coordinates

$$\Delta\varepsilon^{(n)}(\boldsymbol{Q}) = \Delta\varepsilon_0^{(n)} + a_1^{(n)}Q^1 + a_2^{(n)}Q^2 + a_3^{(n)}Q^3 \tag{14.10}$$

$$\Delta E^{(n)}(\boldsymbol{Q}) = \Delta E_0^{(n)} + c_1^{(n)}Q^1 + c_2^{(n)}Q^2 + c_3^{(n)}Q^3 \tag{14.11}$$

$$\Delta U^{(n)}(\boldsymbol{Q}) = \Delta U_0 + b_1^{(n)}Q^1 + b_2^{(n)}Q^2 + b_3^{(n)}Q^3 \tag{14.12}$$

For each value of n, the four parameters of the linear expansion of $\Delta\varepsilon^{(n)}(\boldsymbol{Q})$ and $\Delta E^{(n)}(\boldsymbol{Q})$ can be determined by a fit over equations 14.10 and 14.11, respectively. The fit is performed using the energies at the geometries corresponding to the eight vertices of the cube, that is $Q^1, Q^2, Q^3 = 0$ or 1. The results are summarized in table 14.6.

	$n=2$	$n=3$	$n=4$
$\Delta\varepsilon_0^{(n)}$	2.8600	2.3698	2.1608
$a_1^{(n)}$	-0.1196	-0.0977	-0.0564
$a_2^{(n)}$	-0.1706	-0.1128	-0.1391
$a_3^{(n)}$	-0.2267	-0.1993	-0.1737
$\Delta E_0^{(n)}$	4.4702	3.8894	3.6286
$c_1^{(n)}$	-0.1820	-0.1374	-0.0839
$c_2^{(n)}$	-0.2317	-0.1604	-0.2051
$c_3^{(n)}$	-0.2411	-0.2361	-0.2164
exact $\Delta\varepsilon_0^{(n)}$	2.8646	2.3724	2.1621
exact $\Delta E_0^{(n)}$	4.4758	3.8924	3.6295

Table 14.6: Values of the coefficients of the linear expansions of $\Delta\varepsilon^{(n)}(\boldsymbol{Q})$ and $\Delta E^{(n)}(\boldsymbol{Q})$; Values of $\Delta\varepsilon_0^{(n)}$ and $\Delta E_0^{(n)}$ from direct XH calculations (two bottom lines).

Injecting these values of the linear coefficients into equations 14.10 and 14.11, respectively, one can evaluate $\Delta\varepsilon^{(n)}$ and $\Delta E^{(n)}$ for each geometry $\boldsymbol{Q}$. We term these values "model values" for both quantities. The difference between the model and the exact values lies within 0.003 eV for both $\Delta\varepsilon_0^{(n)}(\boldsymbol{Q})$ and $\Delta E^{(n)}(\boldsymbol{Q})_0$, which is a more than acceptable error.

As for the multilinear coefficients in the previous paragraph, the transferability of the linear coefficients determined from the data at the eight vertices of the cube can also be assessed by two procedures. First, we compare the model values to the exact ones; the RMSD are 0.007, 0.004, and 0.002 eV, for both $\Delta\varepsilon^{(n)}(\boldsymbol{Q})$ and $\Delta E^{(n)}(\boldsymbol{Q})$. Then, a further re-fitting is performed over the test sets, which does not improve the quality of the description.

The $b_k^{(n)}$ coefficients can now be obtain directly using equation 14.5, the values of the linear coefficients in table 14.6 and $A = 1.2013$ (previously defined), see table 14.7.

	$n=2$	$n=3$	$n=4$
$b_1^{(n)}$	-0.0383	-0.0200	-0.0162
$b_2^{(n)}$	-0.0267	-0.0250	-0.0380
$b_3^{(n)}$	0.0312	0.0033	-0.0078

Table 14.7: Values of the $b_k^{(n)}$ coefficients from equation 14.5.

Using these values of $b_k^{(n)}$, we can now generate model values of ΔE at two levels.

The first one ensures the validity of the linear expression of $\Delta U^{(n)}$. To do so, we inject the exact (calculated) values of $\Delta\varepsilon$ along with the fitted values of $b_k^{(n)}$ into equation 14.7. The values of ΔE calculated this way are compared to the exact ones using the RMSD, see table 14.9.

The $b_k^{(n)}$ parameters can also be re-optimized over each test set, using either calculated (exact) or model values for $\Delta\varepsilon$, which only slightly improves the description: RMSD = 0.003, 0.004, and 0.003 eV when using calculated values of $\Delta\varepsilon$, and 0.007, 0.006, 0.003 eV when using model values. The re-fitted parameters $b_k^{(n)}$ are summarized in table 14.8.

	with calculated values of $\Delta\varepsilon$			with model values of $\Delta\varepsilon$		
	$n=2$	$n=3$	$n=4$	$n=2$	$n=3$	$n=4$
$b_1^{(n)}$	-0.0392	-0.0177	-0.0177	-0.0383	-0.0171	-0.0174
$b_2^{(n)}$	-0.0275	-0.0227	-0.0395	-0.0265	-0.0222	-0.0391
$b_3^{(n)}$	0.0303	0.0056	-0.0093	0.0312	0.0063	-0.0089

Table 14.8: Values of the $b_k^{(n)}$ coefficients from different optimizations.

		$n=2$	$n=3$	$n=4$
From calculated $b_k^{(n)}$		0.003	0.006	0.0004
From re-fitted $b_k^{(n)}$	model $\Delta\varepsilon$	0.007	0.006	0.003
	exact $\Delta\varepsilon$	0.003	0.004	0.003

Table 14.9: RMSD (in eV) for ΔE in p2, p3, p4 for different sets of $b_k^{(n)}$ and $\Delta\varepsilon$; exact values of $\Delta\varepsilon$ were obtained with XH calculations.

Both the values of $b_k^{(n)}$ and the RMSD of ΔE are similar whether the fitting is performed using exact or model values of $\Delta\varepsilon$. Considering the RMSD of ΔE, we also note

that using fitted values of $b_k^{(n)}$ instead of the calculated ones does not improve much the description of ΔE. This proves the self-consistency of our model so far.

At the second level, we prove that we are able to reproduce decently the reference values of $\Delta E^{(n)}$ using only the values of the linear parameters and, of course, the geometry. This is done by considering the following equation

$$\Delta E_{\text{lin}}^{(n)}(\boldsymbol{Q}) = A\left\{\Delta\varepsilon_0^{(n)} + \sum_{k=1}^{3} a_k^{(n)} Q^k\right\} + \Delta U_0 + \sum_{k=1}^{3} b_k^{(n)} Q^k \ . \tag{14.13}$$

We recall that the values of A and ΔU_0 were determined above. This is rigourously equivalent to injecting model values of $\Delta\varepsilon$ into equation 14.7.
Doing so for the 409 geometries of each test set gives a RMSD for ΔE of 0.007, 0.008, and 0.004 eV for n =2, 3, and 4, respectively. This is the same order of magnitude as for the first level, so both descriptions are of similar quality. The difference between $\Delta E_{\text{lin}}^{(n)}$ and exact values of $\Delta E^{(n)}$ lies within 0.04 eV on the space diagonal, 0.01 eV elsewhere. This again validates the global relevance and self-consistency of our model.

Equation 14.13 also allows the simultaneous optimization of all the linear parameters including A and ΔU_0 (see table 14.10). The RMSD for ΔE thus obtained are 0.007, 0.004, and 0.002 eV for p2, p3, and p4, respectively. Then, adding these two degrees of freedom to the optimization does not improve the quality of the description significantly. Consistently, the values of the parameters do not vary much with respect to tables 14.7 and 14.8.

	$n=2$	$n=3$	$n=4$
$\Delta\varepsilon_0$	2.8596	2.3739	2.1596
$a_1^{(n)}$	-0.1187	-0.0988	-0.0557
$a_2^{(n)}$	-0.1696	-0.1139	-0.1383
$a_3^{(n)}$	-0.2258	-0.2004	-0.1728
$b_1^{(n)}$	-0.0389	-0.0168	-0.0166
$b_2^{(n)}$	-0.0271	-0.0217	-0.0311
$b_3^{(n)}$	0.0310	0.0069	-0.0078
A		1.2050	
ΔU_0		1.0263	

Table 14.10: Effective values of the linear coefficients for a simultaneous optimization.

14.3 Parametrization of the FFO model

14.3.1 General framework

With equation 14.13, we express the transition energy $\Delta E_{\text{lin}}^{(n)}$ in terms of the nuclear modes $\boldsymbol{Q}$, the linear parameters A and ΔU_0 previously determined and $\Delta\varepsilon_0^{(n)}$. This expression exclusively comes from graphic considerations and does not invoke any specific formalism except for the linear expansion.

In particular, instead of linearly expanding the energy gap $\Delta\varepsilon$ in equation 14.7, one can use its effective expression in terms of the Hückel-type parameters, that is equation 13.13. Considering this, the dependence of $\Delta\varepsilon$ with the nuclear coordinates is now indirect through the Hückel-type parameters.

Thus, we investigate in the present part the feasability of using such an expression for ΔE, which could be resumed as follows

$$\Delta E_{\text{FFO}}^{(n)}(\boldsymbol{Q}) = A'\Delta\varepsilon_{\text{FFO}}^{(n)} + \Delta U_0' + \sum_{k=1}^{3} b_k'^{(n)} Q^k \tag{14.14}$$

where

$$\Delta\varepsilon_{\text{FFO}}^{(n)} = \varepsilon_{\text{LU},n}^{\text{FFO}} - \varepsilon_{\text{HO},n}^{\text{FFO}} \tag{14.15}$$

$$= \frac{(\alpha_{\text{B,LU}}^{\text{FFO},(n)} - \alpha_{\text{B,HO}}^{\text{FFO},(n)}) + (\alpha_{\text{A,LU}}^{\text{FFO},(n)} - \alpha_{\text{A,HO}}^{\text{FFO},(n)})}{2}$$

$$- \sqrt{\left(\frac{\alpha_{\text{B,LU}}^{\text{FFO},(n)} - \alpha_{\text{A,LU}}^{\text{FFO},(n)}}{2}\right)^2 + \left(2\cos\frac{\pi}{2n}\beta_{\text{LU}}^{\text{FFO},(n)}\right)^2} \tag{14.16}$$

$$- \sqrt{\left(\frac{\alpha_{\text{B,HO}}^{\text{FFO},(n)} - \alpha_{\text{A,HO}}^{\text{FFO},(n)}}{2}\right)^2 + \left(2\cos\frac{\pi}{2n}\beta_{\text{HO}}^{\text{FFO},(n)}\right)^2}. \tag{14.17}$$

The evolution $\alpha_{\text{A},FO}$ (FO = HO,LU) with the length of the acetylene bond d_{CC} of the molecule of acetylene is almost linear, see figure 14.6. This also stands for the evolution of β_{FO} with the internal distance $d_{\text{C-Ph}}$ in phenylacetylene and for the evolution of $\alpha_{\text{B},FO}$ with the length of the quinoidal bond d_{quin} of the molecule of benzene. Consequently, we assume that the Hückel-type parameters linearly depend on the local nuclear modes Q^k ($k = 1, 2, 3$) in p2, p3, p4.

$$\begin{cases} \alpha_{\text{A},FO}^{\text{FFO},(n)}(Q^1) = \alpha_{\text{A},FO}^{0,(n)} + d_{FO}^{(n)} Q^1 \\ \beta_{FO}^{\text{FFO},(n)}(Q^2) = \beta_{FO}^{0,(n)} + e_{FO}^{(n)} Q^2 \\ \alpha_{\text{B},FO}^{\text{FFO},(n)}(Q^3) = \alpha_{\text{B},FO}^{0,(n)} + f_{FO}^{(n)} Q^3 \end{cases} \tag{14.18}$$

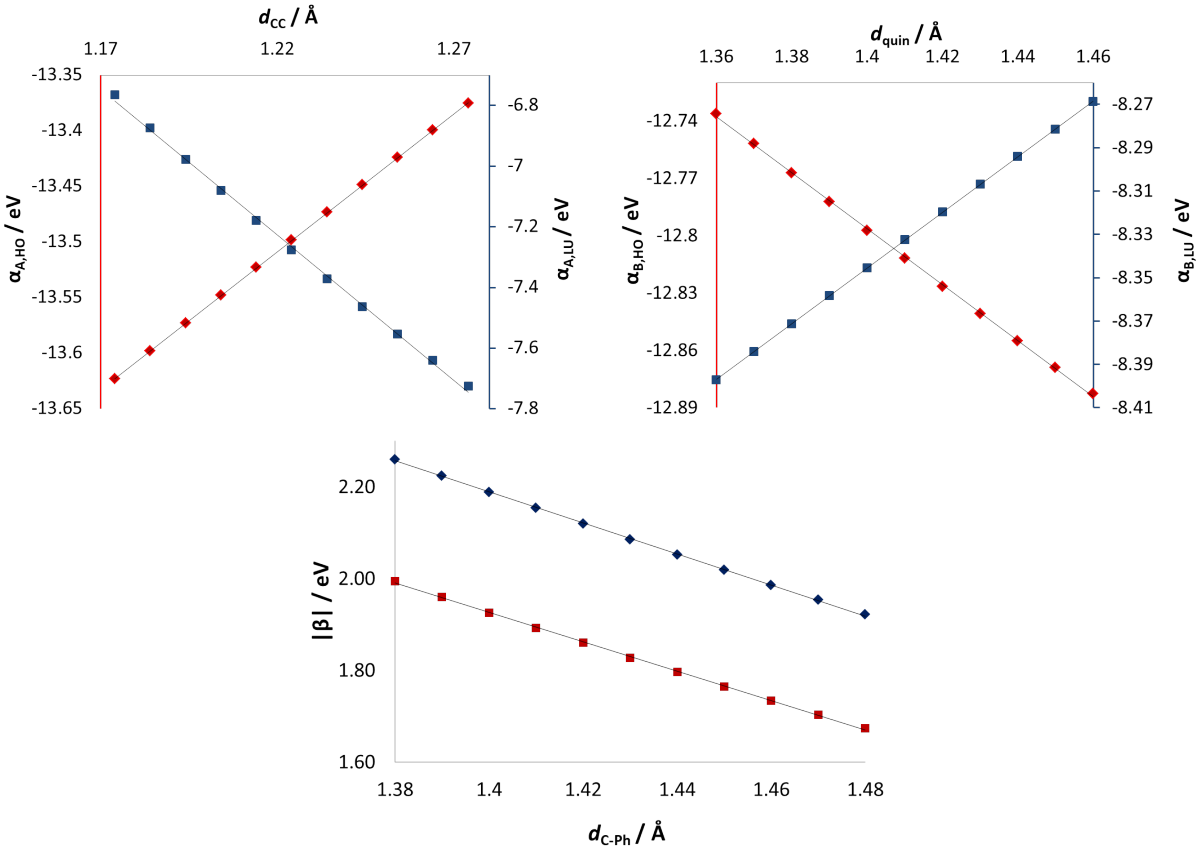

Figure 14.6: Evolution of the Hückel-type parameters with local coordinates: $\alpha_{A,FO}$ (FO = HO,LU) with d_{CC} in acetylene (left), $\alpha_{B,FO}$ with d_{quin} of benzene (right), and β_{FO} with $d_{C\text{-}Ph}$ in phenylacetylene (bottom). Data relative to the HO are represented in red, data relative to the LU are represented in blue. The determination coefficients are $R^2 = 1.0000$, $R^2 = 0.9987$, $R^2 = 0.9996$, $R^2 = 0.9997$, $R^2 = 0.9997$ and $R^2 = 1.0000$ for $\alpha_{A,FO}$, β_{FO}, and $\alpha_{B,FO}$ with FO = HO,LU, respectively.

Several remarks must be made at this point.

We allow the linear coefficients in the Hückel-type parameters to depend parametrically on n to compensate for the diffences in the equilibrium geometries of p2, p3, and p4 (see paragraph 14.2.1). If we considered oversymmetrized (and thus homogeneus) and equivalent equilibrium geometries for the three structures, we would expect d_{FO}, e_{FO}, and f_{FO} to be independent of n.

Along the same line, the origins $\alpha^{0,(n)}_{A,FO}$, $\beta^{0,(n)}_{FO}$, and $\alpha^{0,(n)}_{B,FO}$ have the meaning of effective values at the equilibrium geometries of the ground state. In the ideal case of equivalent equilibrium geometries for p2, p3, and p4, they are expected to be independant of n too.

Then, contrarily to the procedure used in section 13.3, the effective values of the Hückel-type parameters will not be optimized directly but indirectly through the linear expansion coefficients $d^{(n)}_{FO}$, $e^{(n)}_{FO}$, $f^{(n)}_{FO}$, $\alpha^{0,(n)}_{A,FO}$, $\beta^{0,(n)}_{FO}$, and $\alpha^{0,(n)}_{B,FO}$, which is the object of the present paragraph.

In the following, we consider the "original" value of the Hückel parameter for the frontier orbitals of acetylene at the relaxed ground states (see section 13.3). Since the length of the acetylene bonds is the same in p2, p3, and p4 (see chapter 6), we consider the same value of this parameter for the three structures, that is

$$\alpha_{\mathrm{A},FO}^{0,(n)} = \alpha_{\mathrm{A},FO}^{0} \tag{14.19}$$

where FO = HO, LU.

Along the same line, we impose that the effective values of $\beta_{FO}^{0,(n)}$ and $\alpha_{\mathrm{B},FO}^{0,(n)}$ are the same for p2, p3, and p4. Rigourously, this is an approximation since a deviation of the corresponding local nuclear coordinates was observed in their relaxed structures, yet the deviation is small enough ($\sigma \approx 0.001$ Å) to be neglected, at least in a first stage.

$$\beta_{FO}^{0,(n)} = \beta_{FO}^{0,\mathrm{eff}} \tag{14.20}$$

$$\alpha_{\mathrm{B},FO}^{0,(n)} = \alpha_{\mathrm{B},FO}^{0,\mathrm{eff}} \tag{14.21}$$

where FO = HO, LU.

14.3.2 Linear Hückel-type parameters

In a first stage, we optimize the linear coefficients of the Hückel-type parameters in order to minimize the RMSD of $\Delta\varepsilon$, using constraint 13.14.

As for in section 14.2, we start by optimizing the values of $\beta_{FO}^{0,\mathrm{eff}}$, $\alpha_{\mathrm{B},FO}^{0,\mathrm{eff}}$, $d_{FO}^{(n)}$, $e_{FO}^{(n)}$, and $f_{FO}^{(n)}$ (for FO = HO, LU and $n = 2, 3, 4$) over the geometries of the eight vertices of the cube. Without further constraint, this leads to the results summarized in table 14.11.

$\alpha_{\mathrm{A},FO}^{0,(n)}$ is supposed to be exact, and the evolution of $\alpha_{\mathrm{A},FO}^{\mathrm{FFO},(n)}$ depends only on the length of the acetylene bond. Then we can also use the exact mean slope of $\alpha_{\mathrm{A},FO}^{\mathrm{FFO},(n)}$ along the edges [100] to determine the values of $d_{FO}^{(n)}$. These values along with the corresponding re-optimization are summarized in table 14.12.

In the first case (no extra constraint), the values of the RMSD stay small (less than 0.005 eV), which makes the description of $\Delta\varepsilon$ satisfying. On the contrary, using the exact values of $d_{FO}^{(n)}$ reduces dramatically the quality of the description (most of the RMSD values are above 0.010 eV), despite the physical ground of the constraint. This may be due to the fact that the values of $\beta_{FO}^{0,\mathrm{eff}}$ and $\alpha_{\mathrm{B},FO}^{0,\mathrm{eff}}$ at each vertex are effective and thus do

	HO			LU		
	$n=2$	$n=3$	$n=4$	$n=2$	$n=3$	$n=4$
α_{A}^{0}		-13.53			-7.14	
$\beta_{FO}^{0,\mathrm{eff}}$		-0.75			-0.95	
$\alpha_{\mathrm{B},FO}^{0,\mathrm{eff}}$		-12.89			-8.38	
$d_{FO}^{\mathrm{eff},(n)}$	0.11	0.13	0.05	-0.28	-0.13	-0.12
$e_{FO}^{\mathrm{eff},(n)}$	0.07	0.03	0.05	0.06	0.04	0.04
$f_{FO}^{\mathrm{eff},(n)}$	0.10	0.10	0.10	-0.23	-0.20	-0.18
RMSD $\Delta\varepsilon$ / eV	0.001	0.004	0.002	0.001	0.003	0.002

Table 14.11: Effective values of the linear coefficients of the Hückel-type parameters using the eight vertices of the cube.

	HO			LU		
	$n=2$	$n=3$	$n=4$	$n=2$	$n=3$	$n=4$
α_{A}^{0}		-13.53			-7.14	
$\beta_{FO}^{0,\mathrm{eff}}$		-0.75			-0.94	
$\alpha_{\mathrm{B},FO}^{0,\mathrm{eff}}$		-12.88			-8.44	
$d_{FO}^{(n)}$	0.04	0.05	0.02	-0.08	-0.04	-0.04
$e_{FO}^{\mathrm{eff},(n)}$	0.07	0.03	0.04	0.06	0.04	0.04
$f_{FO}^{\mathrm{eff},(n)}$	0.10	0.10	0.09	-0.23	-0.19	-0.17
RMSD $\Delta\varepsilon$ / eV	0.012	0.017	0.006	0.030	0.016	0.013

Table 14.12: Effective values of the linear coefficients of the Hückel-type parameters using the eight vertices of the cube and exact values of $d_{FO}^{(n)}$.

not behave as simply as we would expect (this depends on the evolution of the implicit interactions) with respect to the local coordinates. In particular, their evolution may be multilinear, and constraining the linearity requires to give more flexibility to the function *via* $\alpha_{\mathrm{B},FO}^{0,\mathrm{eff}}$.

Using the first set of parameters (table 14.11) for the 409-point test sets gives small values for the RMSD of $\Delta\varepsilon$: 0.002/0.005, 0.005/0.005, and 0.004/0.004 eV for the HO/LU of p2, p3, and p4 respectively. Re-fitting over the whole test set does not improve the global description.

The values of $\Delta\varepsilon$ obtained using the Hückel-type parameters optimized over the eight vertices are associated to the values of A and $\Delta U(\boldsymbol{Q})$ presented in table 14.10 to calculate ΔE. Since the two sets of parameters are obtained from different methods, such an evaluation is purely indicative. Yet, it gives decent values of RMSD for ΔE (0.007, 0.016, and 0.010 eV for p2, p3, and p4, respectively).

Re-fitting simultaneously the values of A', $\Delta U'_0$, $b_k^{\prime(n)}$, $d_{FO}^{\mathrm{eff},(n)}$, $e_{FO}^{\mathrm{eff},(n)}$, $f_{FO}^{\mathrm{eff},(n)}$ over each test sets slightly improves the description. The values are summarized in table 14.13.

	HO			LU		
	$n=2$	$n=3$	$n=4$	$n=2$	$n=3$	$n=4$
α_{A}^{0}		-13.53			-7.14	
$\beta_{FO}^{0,\mathrm{eff}}$		-0.75			-0.95	
$\alpha_{\mathrm{B},FO}^{0,\mathrm{eff}}$		-12.89			-8.37	
$d_{FO}^{\mathrm{eff},(n)}$	0.11	0.13	0.05	-0.27	-0.13	-0.12
$e_{FO}^{\mathrm{eff},(n)}$	0.07	0.03	0.05	0.06	0.04	0.04
$f_{FO}^{\mathrm{eff},(n)}$	0.10	0.10	0.10	-0.23	-0.20	-0.18

	$n=2$	$n=3$	$n=4$
A'		1.1997	
$\Delta U'_0$		1.0398	
$b_1^{(n)}$	-0.0391	-0.0179	-0.0177
$b_2^{(n)}$	-0.0275	-0.0226	-0.0398
$b_3^{(n)}$	0.0306	0.0053	-0.0095
RMSD / eV	0.006	0.014	0.010

Table 14.13: Re-fitted linear parameters from the optimization over the 409-point test sets, with ΔE values as targets.

The values of the RMSD for ΔE lie between 0.006 and 0.014 eV, which is acceptable even though some improvements could be made. Yet, it is quite engouraging while considering the level of approximations involved at each step of the evaluation of ΔE. Thus, we proved the validity of our decomposition of ΔE for *para*-PPEs, and the possibility of providing a simple expression in terms of local nuclear coordinates.

Chapter 15

Conclusions and future prospects

Chapter 13 introduces the FFO (frontier fragment orbitals) model along with effective expression for the energies of the frontier orbitals of PPEs. Those expressions rely on: (i) a first neighbor approach between the frontier orbitals of two different sites, that is benzene and acetylene; (ii) the dominant character of the frontier orbitals of the constitutive sites in the final frontier orbitals; (iii) a weak coupling between the frontier orbitals of the pseudo-fragments (for *meta*-PPEs). The order of magnitude of the effective Hückel-type parameters is similar as the one of the reference (extended-Hückel) parameters for both *para*- and *meta*-PPEs. This legitimates assumptions (i) and (ii), though refinements are welcome.

In addition, we reasonably reproduced the energies of the frontier and second frontier orbitals of *meta*-PPEs, despite our rough approximation of the coupling. This confirms assumption (iii) and suggests that the evaluation of the actual overlap between the pseudo-fragment orbitals should improve our results for *meta*-PPEs.

These results confirm the relevance of an effective description of the energy of the HO–LU gap of both *para*- and *meta*-PPE in terms of the frontier orbitals of benzene and acetylene, which is an important result. Though, the effective values of the parameters obtained in chapter 13 correspond to a static description of PPEs, and will thus not be kept for the final vibronic model, they should be adapted to any nuclear coordinate.

We start to address this point in chapter 14, by investigating the possibility of parametrizing the energy (of the frontier orbitals and electronic states) of *para*-PPEs in several ways, in particular with respect to local nuclear coordinates.

Those involve the stretching of the acetylene bond, the stretching of the internal bond between benzene and acetylene, and the collective deformation of benzene from the ground-state equilibrium geometry to the first excited state one. We proved that both the orbital and electronic energies are related through an affine relationship and that each can be considered as linearly dependent with respect to the nuclear coordinates.

Due to the inhomogeneity of the coordinates both in a *para*-PPE and between two different ones, deviations are introduced in the indirect optimization of the Hückel-type parameters. Consequently, this work only represents a proof of principle of the validity of our description, since we are able to reproduce the reference values of the electronic energies within 0.05 eV, which is quite decent in any case.

The effects of the inhomogeneity of the coordinates in a *para*-PPE can be evaluated considering cubes involving oversymmetrized equilibrium geometries of S_0 and S_1. The bond lengths of those may differ from one *para*-PPE to another. Considering oversymmetrized geometries with equal bond lengths for all *para*-PPEs, we can evaluate the effect of inhomogeneity between *para*-PPEs. Most importantly, this will allow to proceed to the parametrization without any bias due to inhomogeneity.

The final prospect hereby is to study the transferability of this decomposition to *meta*-PPEs, and thus to consider the coupling between pseudo-fragments (which we started to investigate form a static perspective) along with its geometry dependence.

Part VI

General conclusions and prospects

15.1 Conclusions

The present thesis has focused on PPEs both as a study system on their own and as a support for the construction of a novel type of vibronic model for similar hierarchical π-conjugated macromolecules. The study of PPEs aimed to rationalize the unidirectional excitation transfer that occurs after light absorption, whilst the vibronic model is to provide functional expressions of the electronic energies in terms of nuclear coordinates.

We validated TDDFT as a quantitative method for the description of the electronic structure of PPEs. TDDFT was then used to characterize *para*- and *meta*-PPEs at the relaxed geometries of their first electronic states from geometric, energetic, orbital, and vibrational perspectives. In the case of *para*-PPEs, the vibrationally resolved electronic absorption spectra were also computed and the main contributions were assigned.

In *para*-PPEs from 2- to 7-rings, we showed that the lengths of three types of bonds (acetylene, quinoidal, and internal), and vibrational frequencies are typical of the electronic states (S_0 or S_1). The S_0–S_1 transition energy, along with the energy gap between the frontier orbitals are typical of the number of rings. The shape of the frontier orbitals is preserved for any number of rings, and reveals the dominant involvement of the frontier orbitals of benzene and acetylene.

The characterization of some *meta*-PPEs regarding the properties mentioned above proves that each one of the first excited states is localized on a given building block delimited by (and including) *meta*-substituted phenylene(s). In particular, we insist on the fact that the excited states mainly result from a single excitation between the frontier (or second frontier) orbitals of the species, which are localized on the building blocks. This conclusion comes from the fact that the building blocks of *meta*-PPEs present characteristics that are highly similar to the ones of the corresponding *para*-PPEs, and are almost additive in a *meta*-PPE. The selective localization of the excited states, and the shape of the frontier orbitals inevidence a strong hierarchy in the intramolecular interactions governing the behaviour of PPEs.

The PES of the smallest symmetric (2,2)-*meta*-PPE was explored along particular nuclear motions, allowing to identify several conical intersections that are energetically accessible. Doing so, we also identified components of their branching spaces. In par-

ticular, we confirmed the role of the stretching of the acetylene bonds in the excitation transfer, which was already suggested in the literature. This exploration also highlighted the importance of the stretching of the quinoidal bonds on the common phenylene, which had not been reported yet.

The localization of the excited states on the building blocks allows to rationalize the lifting of degeneracy at the conical intersections in terms of coupled, local diabatic states. This interpretation echoes the assumption of a *shishiodoshi* cascade mediating the energy transfer in large *meta*-PPEs [42] and is confirmed by the exploration of the PES of the mixed (2,3)-*meta*-PPE. In this prototypical species, tightly avoided crossings are identified between S_1 and S_2 that, at the relaxed ground-state geometry, localized on the 3- and 2-ring building blocks, respectively.

A strategy for building a novel vibronic model based on the energies of PPEs has been proposed. Relying on the hierarchy of couplings governing the local interactions in PPEs, this model was constructed step by step following a multiscale approach, see figure 15.1. Each one of the steps consists in the description of an interaction due to either a coupling between orbitals (or electronic states) or electronic repulsion. Since the photochemistry of the PPEs is governed by the π-system, tight-binding formalisms are adapted to describe each step of the model.

An effective Hückel-type Hamiltonian has been proposed that provides effective expressions for the energies of the frontier orbitals of *para*-PPEs from effective Hückel-type parameters related to the frontier orbitals of benzene and acetylene, and their coupling (FFO model). The effective values for the Hückel-type parameters and orbital energies were obtained by an optimization procedure running over a sample of *para*-PPEs.

This formalism has been extended to *meta*-PPEs. The effective expressions for the energy in *meta*-PPEs along with the effective energies of *para*-PPEs allow to reproduce the HO–LU gap within 0.05 eV, which confirms that our effective Hamiltonian describes the essential physics of both *para*- and *meta*-PPEs.

Then, we considered the evolution of the energy along the in-plane nuclear coordinates that are known to be involved in the excitation transfer in PPEs. Those are localized respectively on benzene, acetylene, and between both. We proved that the S_0–S_1 transi-

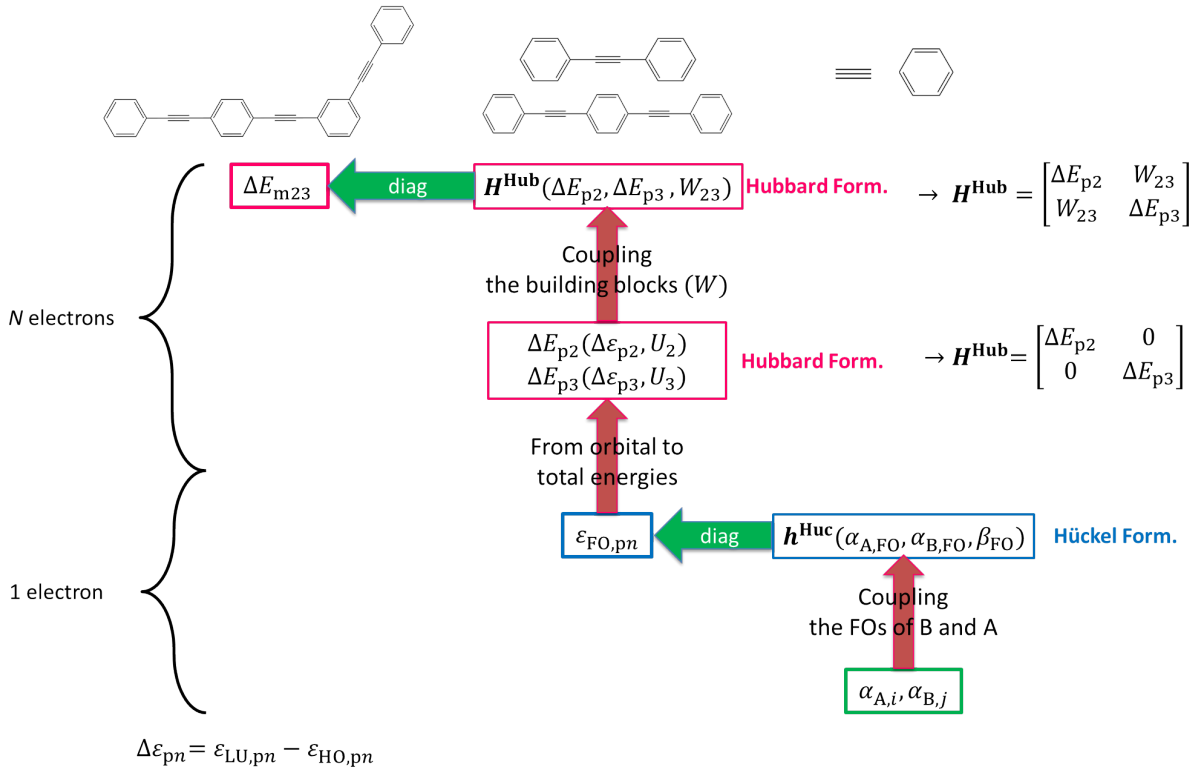

Figure 15.1: Structure of the vibronic model. Decomposition of the transition energy. FO = HO or LU.

tion energies (TDDFT calculations), the HO–LU gap energies and effective Hückel-type parameters depend almost linearly on those local coordinates. In addition, we presented a linear mapping between the S_0–S_1 transition energies and the HO–LU orbital gap energies in *para*-PPEs.

This mapping involves an offset that can be interpreted as a correction to the correlation energy, and which depends on both the number of rings of the PPE and the nuclear motion considered, and a constant slope.

Following the multiscale approach, the mapping equation was combined with the effective expression of the energy gap of the FFO model, thus allowing to express the S_0–S_1 transition energy as a simple function of the local nuclear coordinates only. With this expression, we reproduced the transition energy of the three smallest *para*-PPEs at various geometries within 0.05 eV, thus validating the overall procedure.

15.2 Future prospects

The static study of PPEs shall be completed by the identification of conical intersections in the non-symmetrical *meta*-PPE m23 and the characterization of exact branching

spaces. This will provide the most efficient directions of relaxation of the system once the electronic transfer occurs. To do so, we could use automated procedures that follow the derivatives of the energy along the nuclear coordinates. This task is still in progress, and has not been fully completed for technical reasons.

The final vibronic model also is still under construction. In particular, the linear parameters for the *para*-PPEs have to be determined exactly using samples of oversymmetrized geometries to avoid any bias, then exprapolated to varied geometries, and the parametrization of the model has to be carried out for all sorts of *meta*-PPEs. The determination of exact linear expansion parameters for the *para*-PPEs is not expected to be an issue, but has to handled carefully.

The parametrization of the model for *meta*-PPEs requires to describe the dependence of the coupling between the building blocks in terms of the collective motion of the *meta*-phenylene. One of the main difficulties of this parametrization will come from the fact that the deformation of the *meta*-phenylene not only affects the coupling but may also alter the energies of the two building blocks, with a magnitude that is still to be determined.

Once the general vibronic model is set up, it will be expected to be able to be used to perfom quantum dynamics using energies obtained at the TDDFT level, which is still out of reach for larger PPEs if no such transferable procedure is used.

Appendix A

Validity of TDDFT for studying PPEs

Article reprint:

Vibronic properties of para-polyphenylene ethynylenes: TD-DFT insights, by Emmeline Kim-Lien Ho, Thibaud Etienne, and Benjamin Lasorne, published in the Journal of Chemical Physics, 146, 164303 (2017).

THE JOURNAL OF CHEMICAL PHYSICS **146**, 164303 (2017)

Vibronic properties of *para*-polyphenylene ethynylenes: TD-DFT insights

Emmeline Kim-Lien Ho, Thibaud Etienne, and Benjamin Lasorne
Institut Charles Gerhardt, UMR 5253 CNRS, Université de Montpellier, Place Eugène Bataillon, Montpellier, France

(Received 17 February 2017; accepted 9 April 2017; published online 25 April 2017)

The first singlet excited states of a series of *para*-polyphenylene ethynylenes (PPEs) are investigated using time-dependent density functional theory (TD-DFT). Vibronic absorption spectra are calculated and show excellent agreement with the experiments, thus validating the adequacy of TD-DFT for such systems. The vibronic structure is assigned to the excitation of a few typical stretching and bending modes. The significant discrepancy between the simulated vertical-transition energies and the experimental absorption maxima in PPEs is underlined and explained. The evolution of the spectroscopic properties and of the electronic structure with the chain length is discussed and characterized. *Published by AIP Publishing.* [http://dx.doi.org/10.1063/1.4981802]

I. INTRODUCTION

Dendrimers based on phenylene ethynylene have drawn much attention during the last two decades because of their remarkable properties in terms of light harvesting and energy transfer.[1–4] Their highly branched structure consists of linear building blocks of *para*-polyphenylene ethynylenes (linear PPEs) linked to each other through *meta*-substitutions on phenylene nodes. Particular arrangements stand out as molecular realizations of Cayley trees,[5] in which all the building blocks present the same number of rings, and the extended dendrimers, in which the number of rings increases from the periphery to the core.

A well-known example of extended dendrimer is the so-called nanostar. Both experimental[2–4,6–9] and theoretical[10–13] studies showed that the first three UV absorption bands correspond to bright excited electronic states that are localized on linear building blocks of increasing length. The energy of each excited state is related to the number of rings of the building block on which it is localized: the larger the number of rings, the smaller the energy of the excited state. Sequences of building blocks with a different number of rings linked together thus lead to an energy gradient. As a consequence, the peripheral shorter blocks get the initial excitation, which is then transferred unidirectionally toward the core of the nanostar in a sequential way.[11,14–16] In addition, the absorption spectrum of the nanostar is almost the simple sum of the absorption spectra of linear PPEs because their optical properties are barely affected by *meta*-substitution.[17] Thus, describing quantitatively the electronic structure of linear PPEs is essential in order to understand the energy transfer through the nanostar and eventually design new molecules in which this transfer could be optimized.

The present work is a computational study of the S_0–S_1 absorption process in the 2- to 7-ring linear PPEs. The most popular electronic-structure method able to deal with the excited states of such large molecules is time-dependent density functional theory (TD-DFT). Yet, different conclusions were published about the ability of TD-DFT to describe PPEs correctly.[18,19] Here we show that TD-DFT, along with an adequate level of theory, is perfectly able to describe the S_1 states of linear PPEs. However, calculated vertical-transition energies must not be compared to experimental absorption maxima at low temperature.

Assessing the validity of a computational method upon comparing the calculated vertical-transition energy to the experimental absorption maximum is a common practice. However, one should keep in mind that this approximation may badly fail in some cases.[19–21] Ethylene is a well-known example for which the vertical-transition energy should not be compared to the absorption maximum.[20,21] In such a situation, a safer comparison can be made between the calculated vibronic spectrum and the experimental absorption spectrum. This is the case for linear PPEs whereby the experimental absorption maximum at low temperature happens to be the 0–0 transition.[2–4,6,8] TD-DFT calculations provide calculated vertical-transition energies that are quite different from the experimental absorption maxima for PPEs but the simulated vibronic spectra are in excellent agreement with the experimental ones. The latest point thus assesses the validity of TD-DFT for such systems.

Vibronic spectra are also useful theoretical tools for assigning the vibrational structure of an experimental absorption band. Here, three types of vibrational modes are involved in the S_0–S_1 absorption process, the most important one being the stretching of the acetylene bond, as already pointed out in other studies.[15,19]

In addition, we present an analysis in terms of natural transition orbitals (NTOs)[22] performed on the 2- to 7-ring PPEs. Such an analysis is based on a unitary transformation of the transition-density matrix produced by the excited-state calculation. It is often used to condensate the physical information related to the electronic transition into one (sometimes two) couple(s) of orbitals, which provides straightforward insights into the nature of the transition. The transition may then be pictured as a *hole* (occupied NTO) and a *particle* (virtual NTO) wavefunction. Here, we show that the S_0–S_1 absorption is clearly dominated by a single bonding-to-antibonding

transition and that the extent of border effects depends on the number of rings.

II. COMPUTATIONAL DETAILS

All the calculations were performed with the Gaussian 09 package[23] (revision D01) using DFT (ground states) and TD-DFT (exited states) calculations at the CAM-B3LYP/6-31+G* level of theory. This combination of range-separated hybrid (RSH) functional and diffuse-containing basis set has already been used to simulate the vibronic spectrum of diphenylacetylene (2-ring PPE) in good agreement with experiments.[19] This level of theory is assumed to be adequate for describing extensively delocalized electronic states. Geometries were optimized and minima were characterized with frequency calculations for all members of the PPE series (from two to seven rings) both in S_0 and S_1. The S_0 and S_1 normal modes were used to calculate Franck-Condon factors and thus simulate vibronic absorption spectra with the method implemented in Gaussian 09.[24] NTOs were produced with the NancyEX software,[25] which post-processes TD-DFT calculations obtained with Gaussian 09.

III. RESULTS AND DISCUSSIONS

A. Electronic *vs.* vibronic spectra

In Ref. 18, vertical-transition energies are provided for the 2- and 3-ring linear PPEs. These and the energies at the absorption maxima[17] are off by about 0.3–0.4 eV. It was concluded that TD-DFT with the CAM-B3LYP/6-311G* level of theory was unable to describe correctly the excited states of PPEs. Surprisingly, the conclusion was the same for other high-level multireference methods. However, in Ref. 19, TD-DFT with the CAM-B3LYP/6-31+G* level of theory was used to calculate the absorption spectrum of the 2-ring PPE, matching successfully the experimental one. The basis sets used in Refs. 18 and 19 are different but lead to almost identical results (see Table S1 of the supplementary material). TD-DFT with the CAM-B3LYP functional thus seems valid for such systems. We show below the reason for this apparent paradox.

The vertical-transition energies of the 2-, 3-, and 4-ring PPEs calculated with the CAM-B3LYP/6-31+G* level of theory are given in Table I. Our calculations and those reported in Refs. 18 and 19 produce equivalent values for the vertical-transition energies and, indeed, these quantities are substantially different from the experimental energies at the absorption maxima; see Table I. A vivid illustration of this

TABLE I. E_0: 0–0 transition energies; E_a: adiabatic-transition energies (without vibrational contribution, i.e., well to well); E_v: vertical-transition energies. All values are given in eV for the 2-, 3-, and 4-ring PPEs. TD-DFT calculations were performed at the CAM-B3LYP/6-31+G* level of theory. Experimental data at 77 K are courtesy of Kleiman, see also Ref. 17.

	2-ring			3-ring			4-ring		
	E_0	E_a	E_v	E_0	E_a	E_v	E_0	E_a	E_v
Expt.	4.09			3.56			3.32		
TD-DFT	4.05	4.14	4.48	3.54	3.62	3.89	3.29	3.37	3.63

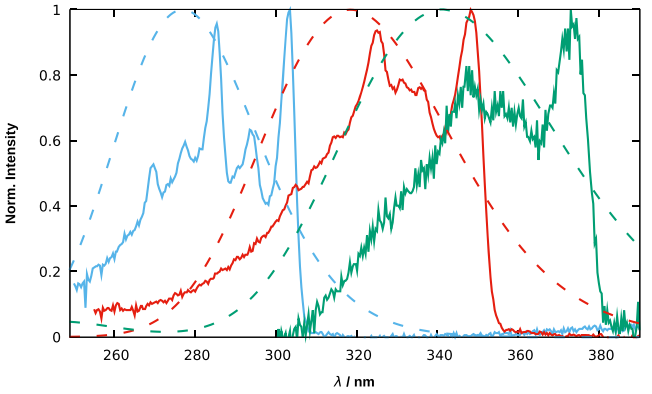

FIG. 1. Experimental (full lines) and simulated (dashed lines) absorption spectra for the 2- (blue), 3- (red), and 4-ring (green) PPEs. The calculated spectra presented here are purely electronic, i.e., obtained upon convoluting vertical-transition energies at the ground-state equilibrium geometries with a Gaussian band shape. Experimental data at 77 K are courtesy of Kleiman, see also Ref. 17.

discrepancy is shown in Figure 1 where the experimental spectra are compared to the UV-visible electronic spectra obtained with the standard procedure available in GaussView for post-processing TD-DFT results calculated with, e.g., Gaussian 09.[23]

In fact, the absorption spectrum provided in Ref. 19 is a so-called vibronic spectrum, simulated using the procedure based on Franck-Condon factors[24] implemented in Gaussian 09.[23] This type of calculation requires the Hessians at both minima in S_0 and S_1. It uses explicitly the geometrical shift vector between both equilibrium structures and the Duschinsky rotation matrix that accounts for the variation of the vibrational normal modes between these points. In contrast, the spectra shown in Figure 1 are vibrationless electronic spectra obtained upon mere convolution of the vertical-transition energy calculated at the ground-state equilibrium geometry with a Gaussian band shape. We thus calculated the vibronic absorption spectra of the 2-, 3-, and 4-ring PPEs with the CAM-B3LYP/6-31+G* level of theory. These are shown in Figure 2. We now observe almost perfect agreement with the experimental ones. This

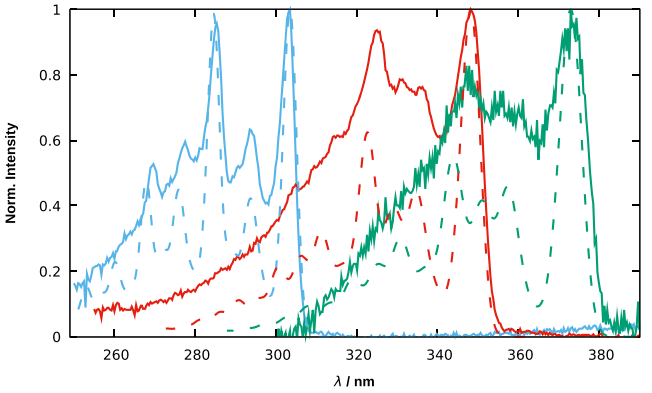

FIG. 2. Experimental (full lines) and simulated (dashed lines) absorption spectra for the 2- (blue), 3- (red), and 4-ring (green) PPEs. Vibronic spectra were calculated using a Gaussian broadening with a half-width at half-maximum (HWHM) of 200 cm^{-1} and blue-shifted by about 2-3 nm to fit the experimental 0–0 absorption maxima on the figure (homogeneous shift applied in the energy domain and data further converted to the wavelength domain). Experimental data at 77 K are courtesy of Kleiman.

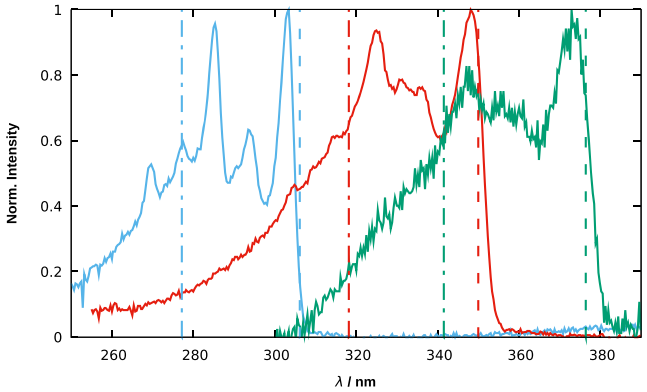

FIG. 3. Absorption spectra of the 2- (blue), 3- (red), and 4-ring (green) PPEs. Experimental data at 77 K (full lines) are courtesy of Kleiman. The energies of vertical transitions, E_v (dashed-dotted lines), and 0–0 transitions, E_0 (dashed lines), were computed at the CAM-B3LYP/6-31+G* level of theory.

unequivocally proves the validity of TD-DFT to describe the excited states of linear PPEs.

Assessing the validity of a computational method upon comparing calculated vertical-transition energies to experimental energies at the absorption maxima is a common procedure. Despite the fact that the absorption process is hardly vertical,[19–21] this approximation of the absorption maximum (AAM) is fair as long as the difference between both values does not exceed 0.1 eV (≈800 cm^{-1}), which is the expected order of magnitude of the accuracy of (high-level) excited-state quantum chemistry methods. Some of the factors influencing the validity of the AAM were previously discussed by one of the authors of this paper.[21] In any case, it is essential to keep in mind that the AAM is only an approximation and one that may badly fail under some circumstances. As a rule of thumb, for molecules such as a linear PPE presenting an absorption spectrum with a non-trivial shape and vibrational structure, the adequacy of a computational method should not be assessed from the vertical-transition energy only. When frequency calculations are tractable for both ground and excited states, simulating the vibronic spectrum is a much safer option.

In particular, TD-DFT was thought unable to describe PPEs correctly in Ref. 18 because the AAM was used referring to experimental spectra at 77 K. The latter are highly nonsymmetrical (see Figure 2) and the absorption maxima happen to correspond to 0–0 transition energies, i.e., vibrationless band origins.[2–4,6,8] In other words, vertical-transition energies were compared to 0–0 transition energies. Such quantities are expected to be quite different (except in situations where the equilibrium geometries of both electronic states are similar, which is not the case here). For the 2-, 3-, and 4-ring PPEs,

TABLE II. Energies of the secondary absorption maxima in eV (one quantum in the main vibrational progression involving the acetylene stretching mode). E_{exp} comes from the experimental spectrum, and E_{sim} from the vibronic spectrum simulated using the results of TD-DFT frequency calculations (CAM-B3LYP/6-31+G*). Experimental data at 77 K are courtesy of Kleiman.

	2-ring	3-ring	4-ring
E_{exp}	4.34	3.81	3.57
E_{sim}	4.32	3.83	3.58

the discrepancy lies within a range of about 0.35–0.40 eV for TD-DFT calculations (see Table I and Figure 3). In contrast, the calculated 0–0 transition energies are in excellent agreement with experimental data (E_0: difference lower than 0.04 eV; see Table I). Note that this still holds for the adiabatic-transition energies, for which zero-point energies are not taken into account (E_a: difference lower than 0.06 eV; see Table I). It thus happens that most of the computational methods tested in Ref. 18 are actually better than originally expected, including TD-DFT.

Yet, Ref. 18 addresses a crucial point for studying the excitation transfer in PPE dendrimers. Even though *meta*-substitution does not affect the optical properties of the linear building blocks (which allows one to consider that the first transition energies of the (2,3)-ring *meta*-substituted PPE are almost equal to those of the 2- and 3-ring linear PPEs), it may induce the appearance of charge-transfer states between linear units. If so, it is correct to point out that TD-DFT may not be the most adequate treatment for such states. However, charge-transfer states are not optically active (dark states) and are not directly responsible for the excitation transfer in *meta*-substituted PPEs. In contrast, the excited states that are optically active (bright states) are expected to dominate this process and TD-DFT thus seems adequate for computing them.

Now, let us note that the AAM may be adapted upon comparing the calculated vertical-transition energy to the second-most-intense band of the experimental spectrum (see Table II for the 2-, 3-, and 4-ring PPEs). The second band corresponds to one quantum in the main vibrational progression (see below). The calculated energies then remain only 0.1 eV greater than the experimental ones on average, right within the acceptable limit. As pointed out in Ref. 20, another and safer option is to compare the vertical-transition energy to the average-transition energy of the transition. In the 2-ring PPE, for example, the former is equal to 4.48 eV and the latter to 4.49 eV. In addition, for PPEs, the relative intensities of the two absorption maxima are swapped when rising the

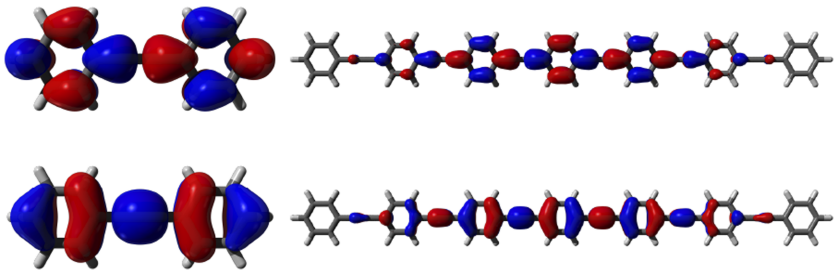

FIG. 4. First couple of NTOs for PPEs with two rings (left) and seven rings (right). For each couple, the occupied (virtual) NTO is at the bottom (top).

temperature,[17] which means that the AAM becomes valid at room temperature. More generally, rising the experimental temperature may help for this smoothes the vibrational structure and causes the experimental spectrum to be more symmetrical; the AAM may then be applied with better results but vibrational information is then lost. This effect can be simulated upon increasing the convolution width (see Fig. S2 of the supplementary material).

Finally, in order to get more detailed insight into the nature of the first excited states of linear PPEs, we analyzed the NTOs corresponding to the S_0–S_1 transition for each of the 2- to 7-ring PPEs. The first couple of NTOs is plotted in Figure 4 for the 2- and 7-ring PPEs. Their relative weights are reported in Table S3 of the supplementary material together with those of the 3- to 6-ring PPEs. Figure S4 of the supplementary material depicts the first NTO couples for the 3- to 6-ring PPEs. In every case, we see that the transition is of bonding-to-antibonding nature, essentially between frontier orbitals. Figure 4 and Figure S4 of the supplementary material show that when the number of rings increases, the external rings of the molecular system are less and less involved in the first electronic transition. One also sees in Table S3 of the supplementary material that the composition of the electronic transition, in terms of number of pairs of molecular orbitals or in terms of NTO couples, increases from one to two when the number of rings grows (considering relative weights greater than ten percent). Accordingly, the relative weight of the second couple of NTOs increases with the size of the system, but no more than two NTO couples are necessary to describe the transition. For each linear PPE, the frontier MOs are very similar to the first couple of NTOs, as proved by the similar values of the relative weights in both pictures. Figure S5 of the supplementary material depicts the second couple of NTOs with significant weights (for the 4- to 7-ring PPEs). One can notice that the correction provided by the second couple of NTOs consists of a transfer of the most important location of the transition from the central ring(s) to the ring(s) between the center and the extremities of the PPEs.

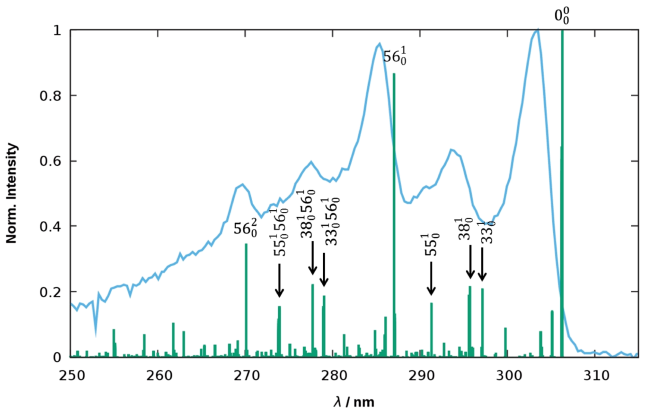

FIG. 5. Experimental absorption spectrum at 77 K (blue) and simulated absorption stick spectrum (green) of the 2-ring PPE.

B. Vibrational assignment

A vibronic treatment also proves to be a useful tool for rationalizing experimental spectra upon providing the assignment of the peaks and the identification of the corresponding photoactive modes. Figure 5 confronts the simulated stick spectrum with the experimental spectrum recorded at 77 K for the 2-ring PPE in order to assign the vibrational structure of the electronic transition. As aforementioned, the simulated spectrum agrees nicely with the experimental one with respect to the position of the peaks (the simulated 0–0 transition wavelength is only 3 nm greater than the experimental maximum) and their relative intensities.

The vibrational structure of the experimental spectrum at 77 K is characterized by five main bands involving four vibrational modes (see Figure 6). The maximum-absorption band at 303 nm is the 0–0 transition (ω_{0-0} = 33 003 cm^{-1}). From our analysis, the 293 nm band (1126 cm^{-1} *vs.* 0–0) is assigned to overlapping transitions with one quantum in either of the bending modes 33 and 38; the 290 nm shoulder (1479 cm^{-1} *vs.* 0–0) and the 285 nm band (2084 cm^{-1} *vs.* 0–0) correspond to one quantum in the stretching modes 55 and 56, respectively. The band and shoulder between 276 nm

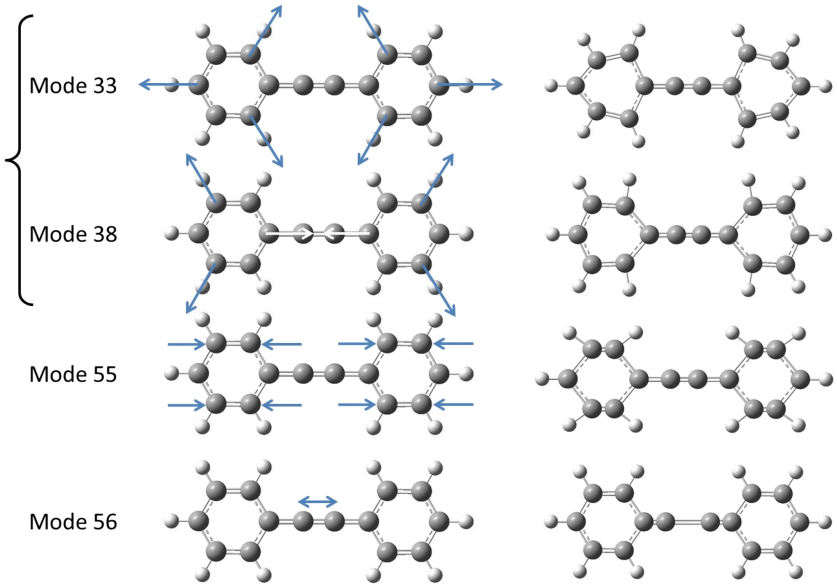

FIG. 6. Photoactive vibrational modes of the 2-ring PPE.

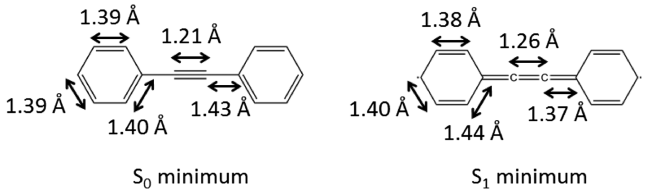

FIG. 7. Characteristic lengths at the S_0 (left) and S_1 (right) minima.

(3229 cm^{-1} *vs.* 0–0) and 273 nm (3627 cm^{-1} *vs.* 0–0) are overtones between mode 56 on the one hand and modes 33, 38, and 55 on the other hand; finally the 269 nm band (4171 cm^{-1} *vs.* 0–0) is due to two quanta in mode 56.

Modes 33 and 38 are centrosymmetric combinations of the triangular bending mode of benzene, different with respect to the relative orientations of the triangles in the dimer. In mode 33 the triangles head toward the extremities of the molecule; in mode 38 they head toward the center, altering the bonding scheme between the four central carbons. Mode 55 is a symmetric stretching of the quinoidal carbons of the two rings while mode 56 is the stretching of the acetylene bond.

The intensity of each band increases with the magnitude of the displacement along the corresponding mode. This agrees with the optimized geometries in the S_0 and S_1 states (see Figure 7) that mainly differ by the bonding scheme on the four central carbons (bond alternated in the S_0 minimum and of cumulene type in the S_1 minimum) and the length between the quinoidal carbons (shorter distance for the S_1 minimum). Those four photoactive modes thus reflect how the 2-ring PPE relaxes its geometry after the S_0–S_1 vertical absorption.

Figure 8 shows the normalized vibronic spectra of the PPEs from two to seven rings; for clarity, the spectra are presented with the same origin taken at the 0–0 transition energy. As the number of rings grows, the shape, relative energies, and relative intensities of the bands are essentially preserved, confirming that the bonding schemes of both states and the photoactive vibrational modes are similar for all members in the series.

On the other hand, at the 0–0 band origin (absorption maximum), the energy decreases and the absolute intensity increases by an order of magnitude from the shorter to the longer PPE (see Table S2 of the supplementary material).

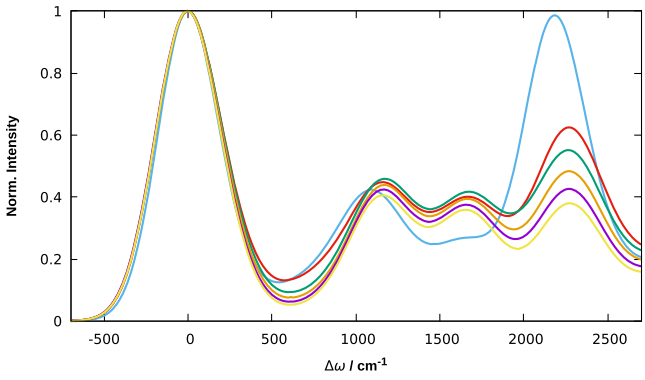

FIG. 8. (Normalized) simulated absorption spectra shifted to the 0–0 transition energy for the 2- (blue), 3- (red), 4- (green), 5- (orange), 6- (purple), and 7-ring (yellow) PPEs.

This behavior is in agreement with extending the conjugation through the system.[26,27] Note that simulations of the whole vibronic absorption spectra for the PPEs from two to seven rings were performed with the same convolution width (HWHM = 200 cm^{-1}) and can be found in Fig. S3 of the supplementary material.

The bands of simulated spectra for the 3- to 7-ring PPEs are assigned to centrosymmetric combinations of vibrational modes already identified for the 2-ring PPE: $\Delta\omega$ = 1000-1200 cm^{-1} triangular bending modes, $\Delta\omega$ = 1600-1800 cm^{-1} quinoidal stretching modes, $\Delta\omega$ = 2200-2300 cm^{-1} acetylene stretching modes, with $\Delta\omega = \omega - \omega_{0-0}$. As the chain grows, the emergence of new modes causes enlargement of the bands for two reasons: (i) increasing the number of rings increases the number of combinations allowed for each type of bending and stretching modes (e.g., there are as many acetylene stretching modes as acetylene bonds and a certain number of combinations are centrosymmetric); (ii) increasing the chain length also increases its flexibility and thus the importance of anharmonic low-frequency modes (such as torsions), which will induce a broad background that cannot be accounted for by our harmonic simulations. Such modes will generate conformational disorder when the temperature increases and may modify the interactions between PPEs and their environment in dendrimers.

In summary, linear PPEs are characterized by only three types of vibrational modes defining the very particular structure and shape of their absorption spectra for the S_0–S_1 transition. All the geometrical parameters of the ground (respectively, excited) states are unchanged with the number of rings, leading to tight (≈200 cm^{-1}) wavenumber domains that are characteristic of each type of photoactive vibrations.

IV. CONCLUSIONS

Calculations of vertical-transition energies and vibronic absorption spectra were performed for the 2- to 7-ring linear PPEs and compared to experimental spectra for the three shorter ones. The calculated spectra present the same shapes and vibrational structures as the experimental ones and perfectly match the experimental 0–0 transition energies. The good agreement of our calculated spectra with the experimental ones proves that TD-DFT along with an RSH functional (CAM-B3LYP) is a reliable approach for describing the optical properties of linear PPEs. Confronting vibronic spectra with vertical-transition energies, we showed that applying the common approximation of the absorption maximum to PPEs may lead to wrong conclusions regarding the validity of computational methods. Other procedures for assessing the adequacy of a computational method using experimental spectra were discussed.

The simulated stick vibronic spectra were calculated and used to assign the main bands of the experimental spectra. Three types of vibrations were identified as photoactive for all members of the series: the triangular bending and quinoidal stretching modes of each benzene ring and the stretching mode of each acetylene bond. Those vibrational modes are consistent with the geometrical deformations occurring between the S_0 and S_1 minima. Comparison of the vibronic spectra for

different numbers of rings shows that the geometrical properties at the S_0 and S_1 minima, the respective electronic structure of each state, and the type of vibrations excited by the electronic transition are essentially the same in all members of the series of linear PPEs.

The NTO analysis provided a clear picture of the transition nature and showed that it simply consists of a bonding-to-antibonding population transfer, essentially between frontier orbitals. Such an analysis also revealed that when the size of the system increases, border effects for the electron redistribution become more significant. This observation was consistent between the Kohn-Sham orbitals and NTO analyses.

The present work provides a basis for investigating the optoelectronic properties of *meta*-substituted PPEs. TD-DFT was shown to be valid for describing the first bright state of each linear PPE. Yet, as pointed out in Ref. 18, *meta*-substitution potentially induces the appearance of dark charge-transfer states between two linear units, which may no longer be correctly handled unless a more sophisticated strategy is considered.

SUPPLEMENTARY MATERIAL

See supplementary material for further information about the calculations, as well as the Cartesian coordinates of the S_0 and S_1 minima of the 2-, 3-, and 4-ring PPEs.

ACKNOWLEDGMENTS

We warmly thank V. D. Kleiman for kindly providing the experimental data shown here.

[1]Z. Xu and J. S. Moore, Acta Polym. **45**, 83 (1994).
[2]M. R. Shortreed, S. F. Swallen, Z.-Y. Shi, W. Tan, Z. Xu, C. Devadoss, J. S. Moore, and R. Kopelman, J. Phys. Chem. B **101**, 6318 (1997).
[3]R. Kopelman, M. Shortreed, Z.-Y. Shi, W. Tan, Z. Xu, J. S. Moore, A. Bar-Haim, and J. Klafter, Phys. Rev. Lett. **78**, 1239 (1997).
[4]S. F. Swallen, R. Kopelman, J. S. Moore, and C. Devadoss, J. Mol. Struct. **485**, 585 (1999).
[5]S. M. Risser, D. N. Beratan, and J. N. Onuchic, J. Phys. Chem. **97**, 4523 (1993).
[6]C. Devadoss, P. Bharathi, and J. S. Moore, J. Am. Chem. Soc. **118**, 9635 (1996).
[7]S. Tretiak, V. Chernyak, and S. Mukamel, J. Phys. Chem. B **102**, 3310 (1998).
[8]V. D. Kleiman, J. S. Melinger, and D. McMorrow, J. Phys. Chem. B **105**, 5595 (2001).
[9]A. Tortschanoff, A. Piryatinski, and S. Mukamel, J. Lumin. **94**, 569 (2001).
[10]K. Harigaya, Chem. Phys. Lett. **300**, 33 (1999).
[11]M. Nakano, M. Takahata, H. Fujita, S. Kiribayashi, and K. Yamaguchi, Chem. Phys. Lett. **323**, 249 (2000).
[12]T. Minami, S. Tretiak, V. Chernyak, and S. Mukamel, J. Lumin. **87-89**, 115 (2000).
[13]C. Wu, S. V. Malinin, S. Tretiak, and V. Y. Chernyak, Nat. Phys. **2**, 631 (2006).
[14]S. Fernandez-Alberti, V. D. Kleiman, S. Tretiak, and A. E. Roitberg, J. Phys. Chem. A **113**, 7535 (2009).
[15]S. Fernandez-Alberti, V. D. Kleiman, S. Tretiak, and A. E. Roitberg, J. Phys. Chem. Lett. **1**, 2699 (2010).
[16]S. Fernandez-Alberti, A. E. Roitberg, V. D. Kleiman, T. Nelson, and S. Tretiak, J. Chem. Phys. **137**, 22A526 (2012).
[17]J. L. Palma, E. Atas, L. Hardison, T. B. Marder, J. C. Collings, A. Beeby, J. S. Melinger, J. L. Krause, V. D. Kleiman, and A. E. Roitberg, J. Phys. Chem. C **114**, 20702 (2010).
[18]J. Huang, L. Du, D. Hu, and Z. Lan, J. Comput. Chem. **36**, 151 (2015).
[19]C. Adamo and D. Jacquemin, Chem. Soc. Rev. **42**, 845 (2013).
[20]E. R. Davidson and A. A. Jarzcki, Chem. Phys. Lett. **285**, 155 (1998).
[21]B. Lasorne, J. Jornet-Somoza, H.-D. Meyer, D. Lauvergnat, M. A. Robb, and F. Gatti, Spectrochim. Acta, Part A **119**, 52 (2014).
[22]T. Etienne, J. Chem. Phys. **142**, 244103 (2015).
[23]M. J. Frisch, G. W. Trucks, H. B. Schlegel, G. E. Scuseria, M. A. Robb, J. R. Cheeseman, G. Scalmani, V. Barone, B. Mennucci, G. A. Petersson, H. Nakatsuji, M. Caricato, X. Li, H. P. Hratchian, A. F. Izmaylov, J. Bloino, G. Zheng, J. L. Sonnenberg, M. Hada, M. Ehara, K. Toyota, R. Fukuda, J. Hasegawa, M. Ishida, T. Nakajima, Y. Honda, O. Kitao, H. Nakai, T. Vreven, J. A. Montgomery, Jr., J. E. Peralta, F. Ogliaro, M. Bearpark, J. J. Heyd, E. Brothers, K. N. Kudin, V. N. Staroverov, R. Kobayashi, J. Normand, K. Raghavachari, A. Rendell, J. C. Burant, S. S. Iyengar, J. Tomasi, M. Cossi, N. Rega, J. M. Millam, M. Klene, J. E. Knox, J. B. Cross, V. Bakken, C. Adamo, J. Jaramillo, R. Gomperts, R. E. Stratmann, O. Yazyev, A. J. Austin, R. Cammi, C. Pomelli, J. W. Ochterski, R. L. Martin, K. Morokuma, V. G. Zakrzewski, G. A. Voth, P. Salvador, J. J. Dannenberg, S. Dapprich, A. D. Daniels, O. Farkas, J. B. Foresman, J. V. Ortiz, J. Cioslowski, and D. J. Fox, GAUSSIAN 09, Revision D.01, Gaussian, Inc., Wallingford, CT, 2009.
[24]F. Santoro, A. Lami, R. Improta, J. Bloino, and V. Barone, J. Chem. Phys. **128**, 224311 (2008).
[25]See http://sourceforge.net/projects/nancyex/ for Nancy_EX 2.0 Software Suite, 2015.
[26]C. A. Coulson, Proc. R. Soc. A **164**, 383 (1938).
[27]C. A. Coulson, Proc. R. Soc. A **169**, 413 (1939).

Appendix B

Linear response theory

The conceptual bases for this chapter can be found in reference [103]

B.1 The time-dependent problem

We consider a physical system described by the Hamiltonian $\hat{H}_0$. Its eigenvalues and eigenvectors are denoted E_n and φ_n, respectively, and the corresponding eigenstates are stationary provided that $\hat{H}_0$ does not depend on time.

At time $t = 0$, the system undergoes a perturbation turning the total Hamiltonian into

$$\hat{H}(t) = \hat{H}_0 + \lambda \hat{W}(t) \tag{B.1}$$

where λ is a real parameter, satisfying $\lambda \ll 1$, and $\hat{W}(t)$ represents the action of the time-dependent perturbation on the system, of similar amplitude as $\hat{H}_0$.

Continuity considerations impose that at time $t = 0$ when the perturbation is applied, the system is in the same state as for $t < 0$, that is a stationary eigenstate φ_i of $\hat{H}_0$. Since the eigenstates of the two Hamiltonians $\hat{H}(t)$ and $\hat{H}_0$ are different, the system starts evolving as soon as it is perturbed, namely transitions occur from the initial stationary state φ_i to other ones. At time $t > 0$, the system is in the state $|\Psi(t)\rangle$, a wavepacket solution of the time-dependent Schrödinger equation, which can be expanded over the complete basis of the stationary eigenstates.

$$\mathrm{i}\hbar\frac{d}{dt}|\Psi(t)\rangle = \left[\hat{H}_0 + \lambda\hat{W}(t)\right]|\Psi(t)\rangle \tag{B.2}$$

$$|\Psi(t)\rangle = \sum_f \tilde{C}_f(t)|\varphi_f\rangle \tag{B.3}$$

$$\forall f, \tilde{C}_f(t) = e^{-\mathrm{i}E_f t/\hbar}c_f(t) \tag{B.4}$$

Equation B.4 constitutes an interaction representation: the expansion coefficients are conveniently factorized into a time-dependent part $c_f(t)$ due to the time-dependent perturbation and a phase factor $e^{-\mathrm{i}E_f t/\hbar}$ due to the time-independent Hamiltonian $\hat{H}_0$. If the time-dependent perturbation is actually small before $\hat{H}_0$, the factor $c_f(t)$ will evolve far much slowly than the phase factor. In the limit of a vanishing time-dependent perturbation, the expansion coefficient is constant up to the phase factor and the system stays in its initial state.

$$\lim_{\lambda\to 0}\tilde{C}_f(t) = e^{-\mathrm{i}E_f t/\hbar}c_f \tag{B.5}$$

The probability for a system, initially in the state $|\Psi(t=0)\rangle = |\varphi_i\rangle$ to undergo a transition to the state $|\varphi_f\rangle$ is given by

$$P_{if}(t) = |\langle\varphi_f|\Psi(t)\rangle|^2 = |c_f(t)|^2 \tag{B.6}$$

and the elements $W_{nk}(t)$ of the perturbation matrix in the basis of the stationary states read

$$W_{nk}(t) = \langle\varphi_n|\hat{W}(t)|\varphi_k\rangle \tag{B.7}$$

Finally, introducing equations B.3 and B.4 into the time-independent Schrödinger equation B.2 and projecting over the stationary state $|\varphi_n\rangle$, we obtain

$$\mathrm{i}\hbar\frac{d}{dt}c_n(t) = \lambda\sum_k e^{\mathrm{i}\Delta\omega_{nk}t}W_{nk}(t)c_k(t) \tag{B.8}$$

where $\Delta\omega_{nk} = \dfrac{E_n - E_k}{\hbar}$ is the Bohr angular frequency related to the levels E_n and E_k.

The group of equations B.8 for all values of n is a system of coupled differential equations of first order with respect to time, the coupling being exclusively due to the perturbation $\lambda\hat{W}(t)$.

B.2 First-order resolution

The system of equations B.8 is perfectly equivalent to the time-dependent Schrödinger equation B.2, and we are generally not able to get to its exact solutions $c_n(t)$. Provided that $\lambda \ll 1$, expanding the solutions $c_n(t)$ in powers of λ is a decent approximation.

$$c_n(t) = c_n^{(0)}(t) + \lambda c_n^{(1)}(t) + \lambda^2 c_n^{(2)}(t) + \cdots \tag{B.9}$$

This expansion reflects how the system reacts to the perturbation and, thus, is also called response theory. The complete expansion is exact. The 0^{th} order corresponds to the unperturbed time-dependent system, the 1^{st} order to a linear response to the perturbation, and so on.

Using this expansion in the time-dependent Schrödinger equation, we have at the 0^{th} order:

$$\mathrm{i}\hbar \frac{d}{dt} c_n^{(0)}(t) = 0 \tag{B.10}$$

that is that $c_n^{(0)}(t)$ is a constant of time. This also implies that for $\lambda = 0$, the unperturbed system is described by a time-dependent Schrödinger equation and the static Hamiltonian $\hat{H}_0$. The coefficient $c_n(t)$ for the unperturbed system is also a time constant and the eigenstate $|\Psi(t)\rangle$ at time t is identical to the initial stationary state $|\varphi_i\rangle$ up to a phase (determined by initial continuity conditions, *i.e.*, boundary conditions).

$$c_n^{(0)}(t) = \delta_{ni} \tag{B.11}$$

$$c_n(t)|_{\lambda=0} = c_n(t = 0^-) = \delta_{ni} \tag{B.12}$$

$$|\Psi(t)\rangle = e^{-\mathrm{i}\omega_i t}|\varphi_i\rangle \tag{B.13}$$

For the 1^{st} order, it comes:

$$\mathrm{i}\hbar \frac{d}{dt} c_n^{(1)}(t) = \sum_k e^{\mathrm{i}\Delta\omega_{nk}t} W_{nk}(t) c_k^{(0)}(t) \tag{B.14}$$

which simplifies considering equation B.11 into:

$$\mathrm{i}\hbar \frac{d}{dt} c_n^{(1)}(t) = e^{\mathrm{i}\Delta\omega_{ni}t} W_{ni}(t) \tag{B.15}$$

using the previous boundary condition, this integrates as

$$c_n^{(1)}(t) = \frac{1}{\mathrm{i}\hbar}\int_0^t dt' e^{\mathrm{i}\Delta\omega_{ni}t'} W_{ni}(t') \tag{B.16}$$

Finally the probability to find the system in the state $|\varphi_f\rangle$ at time t, after a transition from the state $|\varphi_i\rangle$ (the states are supposed to be different) due to the perturbation $\lambda\hat{W}$ reads

$$P_{if}(t) = \lambda^2 |c_n^{(1)}(t)|^2 = \frac{\lambda^2}{\hbar^2}\left|\int_0^t dt' e^{\mathrm{i}\Delta\omega_{nf}t'} W_{nf}(t')\right|^2 \tag{B.17}$$

The $c_n(t)$ are called linear response coefficients and are the quantities that define the wavefunction at time t, and so the transitions that occured between the stationary states of the unpertubed system. In the particular case where the initial state is the ground-state φ_0, the perturbation can only generate transitions to the excited states (those that are accessible according to transition selection rules, which are governed by the values of the perturbation matrix elements).

In particular, linear response theory for TDDFT takes an external electric field times the electric dipole moment of the molecular system as the perturbation, and the resolution corresponds to the specific case of a sinusoidal perturbation. Electronic selection rules are determined by the values of the transition dipole between electronic states.

B.3 Sinusoidal perturbation and linear response theory

We consider the transitions from the ground-state $|\varphi_0\rangle$ to the excited states $|\varphi_n\rangle, n > 0$. Let us write the perturbation under a sinusoidal form

$$\hat{W}(t) = \hat{W}\cos(\omega t) \tag{B.18}$$

where $\hat{W}$ is a time-independent observable the magnitude of which is small before the one of $\hat{H}_0$, ω is a constant angular frequency.

The elements $W_{n0}(t)$ of the perturbation matrix inducing a transition from φ_0 to φ_n then read

$$W_{n0}(t) = W_{n0}\cos(\omega t) = \frac{W_{n0}}{2}\left(e^{\mathrm{i}\omega t} + e^{-\mathrm{i}\omega t}\right) \tag{B.19}$$

where W_{n0} is a complex time-independent number. Inserting this into equation B.16 gives the expression of the coefficient $c_n^{(1)}(t)$.

$$c_n^{(1)}(t) = \frac{W_{n0}}{2\hbar}\left[\frac{1 - e^{\mathrm{i}(\Delta\omega_n + \omega)t}}{\Delta\omega_n + \omega} + \frac{1 - e^{\mathrm{i}(\Delta\omega_n - \omega)t}}{\Delta\omega_n - \omega}\right] \tag{B.20}$$

where $\Delta\omega_n = \Delta\omega_{n0} = \dfrac{E_n - E_0}{\hbar}$

Within linear response theory, the latter usually is recast as

$$c_n^{(1)}(t) = X_n(\omega)\left[e^{\mathrm{i}(\Delta\omega_n + \omega)t} - 1\right] + X_n(-\omega)\left[e^{-\mathrm{i}(\omega - \Delta\omega_n)t} - 1\right] \tag{B.21}$$

where $X_n(\omega) = -\dfrac{W_{n0}}{2\hbar(\omega + \Delta\omega_n)}$.

For convenience, we now use a matrix form to describe the problem. The frequency-dependent linear response coefficients $X_n(\omega)$ and $X_n^*(\omega)$ are gathered into a linear response column vector such as

$$\begin{bmatrix} X_1(-\omega) \\ \vdots \\ X_n(-\omega) \\ \vdots \\ X_1^*(\omega) \\ \vdots \\ X_n^*(\omega) \\ \vdots \end{bmatrix} = \begin{bmatrix} \boldsymbol{X}(-\omega) \\ \boldsymbol{X}^*(\omega) \end{bmatrix} \tag{B.22}$$

Considering the definition of the frequency-dependent coefficients $X_n(-\omega)$ (excitations) and $X_n^*(\omega)$, it appears that the linear response vector is solution of the linear response equation B.23.

$$\left(\underbrace{\begin{bmatrix} \boldsymbol{A} & \boldsymbol{B} \\ \boldsymbol{B}^* & \boldsymbol{A}^* \end{bmatrix}}_{\boldsymbol{E}^{[2]}} - \omega \begin{bmatrix} \mathbf{1} & \mathbf{0} \\ \mathbf{0} & -\mathbf{1} \end{bmatrix}\right) \begin{bmatrix} \boldsymbol{X}(-\omega) \\ \boldsymbol{X}^*(\omega) \end{bmatrix} = -\underbrace{\begin{bmatrix} \boldsymbol{\mathcal{V}} \\ \boldsymbol{\mathcal{V}}^* \end{bmatrix}}_{\boldsymbol{\mathcal{V}}^{[1]}} \tag{B.23}$$

where $\boldsymbol{\mathcal{V}}_j = \dfrac{W_{j0}}{2\hbar}$, $\boldsymbol{A}_{ij} = \delta_{ij}\omega_j$, $\boldsymbol{B}_{ij} = 0$.

We usually call $\boldsymbol{E}^{[2]}$ the energy Hessian matrix and $\boldsymbol{\mathcal{V}}^{[1]}$ the gradient property vector. This represents a system of non-linear coupled equations which are to be solved iteratively.

The excitation energies previously defined are obtained by solving the generalized diagonalization problem associated to the linear response equation.

$$\begin{bmatrix} \boldsymbol{A} & \boldsymbol{B} \\ \boldsymbol{B}^* & \boldsymbol{A}^* \end{bmatrix} \boldsymbol{\Lambda}(\omega) = \omega \begin{bmatrix} \mathbf{1} & \mathbf{0} \\ \mathbf{0} & -\mathbf{1} \end{bmatrix} \boldsymbol{\Lambda}(\omega) \tag{B.24}$$

The positive-valued solutions correspond to absorption while the negative-valued solutions correspond to emission.

In the exact theory, which requires the exact wavefunction, the Hessian is diagonal and the excitation energies are exact. This is not true anymore while using approximate wavefunctions.

The probability for the transition from φ_0 to an excited states φ_n then reads

$$P_{n0}(t,\omega) = \frac{|W_{n0}|^2}{4\hbar^2} \left| \frac{1 - e^{\mathrm{i}(\Delta\omega_n + \omega)t}}{\Delta\omega_n + \omega} + \frac{1 - e^{\mathrm{i}(\Delta\omega_n - \omega)t}}{\Delta\omega_n - \omega} \right|^2 \tag{B.25}$$

For a fixed time t, the probability is now only a function of the pulsation ω. In particular, the probability diverges for $\omega \to \Delta\omega_n$ and $\omega \to -\Delta\omega_n$. These are resonances that formally correspond to the absorption from the ground state and the emission from the excited state respectively. The corresponding transitions can only happen for a nonzero coupling W_{n0}. While nonzero, the amplitude of this coupling also gives an indication of the intensity of the transition through the oscillator strength.

$$f_n = 2\omega_{n0}|W_{n0}|^2 \tag{B.26}$$

Divergence of $P_{n0}(t,\omega)$ and $c_n^{(1)}(t)$ can be avoided introducing a damping parameter to the linear response coefficients.[1]

Even though sinusoidal functions are a specific case for the resolution, they are actually of great use in physics, since all time-resolved signals can be decomposed spectrally in terms of sinusoids[2]. In particular, electromagnetic fields are usually handled through this formalism.

[1] In damped response theory, the perturbation reads $\hat{W}(t) = \hat{W}e^{\mathrm{i}\gamma}\cos(\omega t)$ were $1/\gamma$ can be interpreted as the lifetime of the perturbation.

[2] discrete decomposition in Fourier series for periodic signals or continuous Fourier transform for non-periodic ones.

Appendix C

Schmidt orthogonalization

In the simplest case of phenylacetylene, the matrices $\boldsymbol{H}_{\text{eff}}$ (effective FFO model) and $\boldsymbol{H}_{\text{XH}}$ (extended Hückel model) read, respectively,

$$\boldsymbol{H}_{\text{eff}} = \begin{bmatrix} \alpha_{\text{A}} & \beta^* \\ \beta^* & \alpha_{\text{B}}^* \end{bmatrix} \tag{C.1}$$

$$\boldsymbol{H}_{\text{XH}} = \begin{bmatrix} \langle\varphi_{\text{A}}|\hat{H}_{\text{XH}}|\varphi_{\text{A}}\rangle & \langle\varphi_{\text{A}}|\hat{H}_{\text{XH}}|\varphi_{\text{B}}\rangle \\ \langle\varphi_{\text{B}}|\hat{H}_{\text{XH}}|\varphi_{\text{A}}\rangle & \langle\varphi_{\text{B}}|\hat{H}_{\text{XH}}|\varphi_{\text{B}}\rangle \end{bmatrix} = \begin{bmatrix} \alpha_{\text{A}} & H_{\text{AB}} \\ H_{\text{AB}} & \alpha_{\text{B}} \end{bmatrix} \tag{C.2}$$

where φ_{A} and φ_{B} are the orbitals of the benzene and acetylene fragments respectively, over which is developed the extended-Hückel model. We showed above that all the following developments are valid for any length of the n-ring chromophore.

Since the extended-Hückel basis (φ_{A}, φ_{B}) is non-orthogonal, the overlap matrix $\boldsymbol{S}$ is defined as

$$\boldsymbol{S} = \begin{bmatrix} \langle\varphi_{\text{A}}|\varphi_{\text{A}}\rangle & \langle\varphi_{\text{A}}|\varphi_{\text{B}}\rangle \\ \langle\varphi_{\text{B}}|\varphi_{\text{A}}\rangle & \langle\varphi_{\text{B}}|\varphi_{\text{B}}\rangle \end{bmatrix} = \begin{bmatrix} 1 & S \\ S & 1 \end{bmatrix} . \tag{C.3}$$

We look for a unitary transformation from $\boldsymbol{H}_{\text{XH}}$ to $\boldsymbol{H}_{\text{XH}}^{\text{L}}$ where $\boldsymbol{H}_{\text{XH}}^{\text{L}}$ is a Hermitian matrix involving the energy α_{A} of the fragment orbital of acetylene (same form as $\boldsymbol{H}_{\text{eff}}$)

$$\boldsymbol{H}_{\text{XH}}^{\text{L}} = \begin{bmatrix} \alpha_{\text{A}} & x \\ x & y \end{bmatrix} \tag{C.4}$$

where x and y depend on α_{A}, α_{B}, H_{AB} and S.

Let (φ_1^0,ε_1) and (φ_2^0,ε_2) be two couples of solutions of an eigenvalue problem related to the extended-Hückel operator $\hat{H}_{\text{XH}}$. Then (φ_1^0,φ_2^0) is an orthonormal basis allowing to

define the eigenvalue matrix $\boldsymbol{\varepsilon}$

$$\boldsymbol{\varepsilon} = \begin{bmatrix} \langle\varphi_1^0|\hat{H}_{\mathrm{XH}}|\varphi_1^0\rangle & \langle\varphi_1^0|\hat{H}_{\mathrm{XH}}|\varphi_2^0\rangle \\ \langle\varphi_2^0|\hat{H}_{\mathrm{XH}}|\varphi_1^0\rangle & \langle\varphi_2^0|\hat{H}_{\mathrm{XH}}|\varphi_2^0\rangle \end{bmatrix} = \begin{bmatrix} \varepsilon_1 & 0 \\ 0 & \varepsilon_2 \end{bmatrix} . \tag{C.5}$$

In the non-orthogonal basis (φ_{A},φ_{B}), the eigenfunctions φ_1^0 and φ_2^0 read

$$\begin{cases} \varphi_1^0 = c_{1,\mathrm{A}}\varphi_{\mathrm{A}} + c_{1,\mathrm{B}}\varphi_{\mathrm{B}} \\ \varphi_2^0 = c_{2,\mathrm{A}}\varphi_{\mathrm{A}} + c_{2,\mathrm{B}}\varphi_{\mathrm{B}} \end{cases} \tag{C.6}$$

leading to the coefficient matrix $\boldsymbol{c}$

$$\boldsymbol{c} = \begin{bmatrix} c_{1,\mathrm{A}} & c_{2,\mathrm{A}} \\ c_{1,\mathrm{B}} & c_{2,\mathrm{B}} \end{bmatrix} . \tag{C.7}$$

The extended-Hückel matrix satisfies a generalized eigenvalue problem

$$\boldsymbol{H}_{\mathrm{XH}}\boldsymbol{c} = \boldsymbol{S}\boldsymbol{c}\boldsymbol{\varepsilon} \tag{C.8}$$

which is equivalent to the eigenvalue problem

$$\left(\boldsymbol{S}^{-1}\boldsymbol{H}_{\mathrm{XH}}\right)\boldsymbol{c} = \boldsymbol{c}\boldsymbol{\varepsilon} . \tag{C.9}$$

Since $\boldsymbol{S}$ and so $\boldsymbol{S}^{-1}$ are positive definite, $\boldsymbol{S}^{-1}$ can be decomposed as

$$\boldsymbol{S}^{-1} = \boldsymbol{L}\boldsymbol{L}^{\dagger} \tag{C.10}$$

where $\boldsymbol{L}$ is an invertible matrix. Then Eq. C.9 becomes

$$\begin{aligned} &\boldsymbol{L}\boldsymbol{L}^{\dagger}\boldsymbol{H}_{\mathrm{XH}}\boldsymbol{L}\boldsymbol{L}^{-1}\boldsymbol{c} = \boldsymbol{c}\boldsymbol{\varepsilon} \\ \Leftrightarrow\ &\boldsymbol{L}^{\dagger}\boldsymbol{H}_{\mathrm{XH}}\boldsymbol{L}\left(\boldsymbol{L}^{-1}\boldsymbol{c}\right) = \left(\boldsymbol{L}^{-1}\boldsymbol{c}\right)\boldsymbol{\varepsilon} \end{aligned}$$

and the new eigenvalue problem reads

$$\boldsymbol{H}_{\mathrm{XH}}^{\mathrm{L}}\boldsymbol{C} = \boldsymbol{C}\boldsymbol{\varepsilon} \tag{C.11}$$

$$\text{where} \begin{cases} \boldsymbol{H}_{\mathrm{XH}}^{\mathrm{L}} = \boldsymbol{L}^{\dagger}\boldsymbol{H}_{\mathrm{XH}}\boldsymbol{L} \\ \boldsymbol{C} = \boldsymbol{L}^{-1}\boldsymbol{c} \end{cases} . \tag{C.12}$$

The matrix $\boldsymbol{H}_{\mathrm{XH}}^{\mathrm{L}}$ in the new base is Hermitian by construction, and $\boldsymbol{L}$ appears to be the passage matrix from the non-orthogonal basis (φ_{A},φ_{B}) to a new basis that we want to be

orthogonal. The last condition, which is that φ_{A} is common to both the non-orthogonal and the orthogonalized basis set, imposes that $\boldsymbol{L}$ is up-triangular. To satisfy all the aforeconditions, a Gram-Schmidt orthonormalization procedure is used.

The vectors ψ_1^{GS} and ψ_2^{GS} built from the Gram-Schmidt orthogonalization read

$$\begin{cases} \psi_1^{\mathrm{GS}} = \varphi_{\mathrm{A}} \\ \psi_2^{\mathrm{GS}} = \dfrac{-S\varphi_{\mathrm{A}} + \varphi_{\mathrm{B}}}{\sqrt{1-S^2}} \end{cases} \tag{C.13}$$

leading to the orthogonalization matrix $\boldsymbol{L}^{\mathrm{GS}}$ and its adjoint matrix $\left(\boldsymbol{L}^{\mathrm{GS}}\right)^{\dagger}$

$$\boldsymbol{L}^{\mathrm{GS}} = \begin{bmatrix} 1 & -\dfrac{S}{\sqrt{(1-S^2)}} \\ 0 & \dfrac{1}{\sqrt{(1-S^2)}} \end{bmatrix} \tag{C.14}$$

$$\left(\boldsymbol{L}^{\mathrm{GS}}\right)^{\dagger} = \begin{bmatrix} 1 & 0 \\ -\dfrac{S}{\sqrt{(1-S^2)}} & \dfrac{1}{\sqrt{(1-S^2)}} \end{bmatrix} . \tag{C.15}$$

Then, the extended-Hückel matrix in the orthogonalized basis set reads

$$\boldsymbol{H}_{\mathrm{XH}}^{\mathrm{L}} = \boldsymbol{H}_{\mathrm{XH}}^{\mathrm{GS}} = \left(\boldsymbol{L}^{\mathrm{GS}}\right)^{\dagger} \boldsymbol{H}_{\mathrm{XH}} \boldsymbol{L}^{\mathrm{GS}} \tag{C.16}$$

$$\boldsymbol{H}_{\mathrm{XH}}^{\mathrm{L}} = \begin{bmatrix} \alpha_{\mathrm{A}} & \dfrac{H_{\mathrm{AB}} - \alpha_{\mathrm{A}} S}{\sqrt{(1-S^2)}} \\ \dfrac{H_{\mathrm{AB}} - \alpha_{\mathrm{A}} S}{\sqrt{(1-S^2)}} & \dfrac{\alpha_{\mathrm{B}} - 2H_{\mathrm{AB}} S + \alpha_{\mathrm{A}} S^2}{1-S^2} \end{bmatrix} . \tag{C.17}$$

Appendix D

Résumé substantiel

D.1 Contexte

Les semi-conducteurs organiques sont des matérieux photo et electroactifs capables de transporter un flux d'énergie *via* leur système π. Ils peuvent aussi être utilisés pour la production et la conduction d'un courant électrique généré par l'absorption de lumière (ou à l'inverse, la conduction puis restitution d'énergie par émission de lumière) [1–7]. Ces composés sont conçus comme la nouvelle génération des composés électroniques et optoélectroniques appliqués aux domaines de la photovoltaïque, de l'électroluminescence et de la photosynthèse artificielle: cellules solaires organiques [7], transistors organiques [8], diodes à émission de lumière organiques (OLEDs) [9], et antennes biomimétiques collectrices de lumière [10–14]. C'est dans ce contexte que le prix Nobel de Chimie a été attribué en 2000 à la découverte au développement de polymères conducteurs [15–18].

Ainsi, il est crucial de comprendre les mécanismes impliqués dans le transfert d'énergie dans de tels composés. La nanostar est un système de choix pour cela, dans lequel le transfert d'énergie est à la fois particulièrement efficace (rendement d'environ 98%) et rapide (quelques picosecondes) [19, 20].

La nanostar est un dendrimère macromoléculaire de polyphénylène éthynylène (PPE) terminé par un pérylène, synthétisée pour la première fois par l'équipe de J. S. Moore en 1994 [21] pour imiter la photosynthèse naturelle.

Les PPEs sont des molécules organiques π-conjuguées complexes mais hiérarchisées qui présentent un grand potentiel en tant que composés organiques nanomoléculaires pour

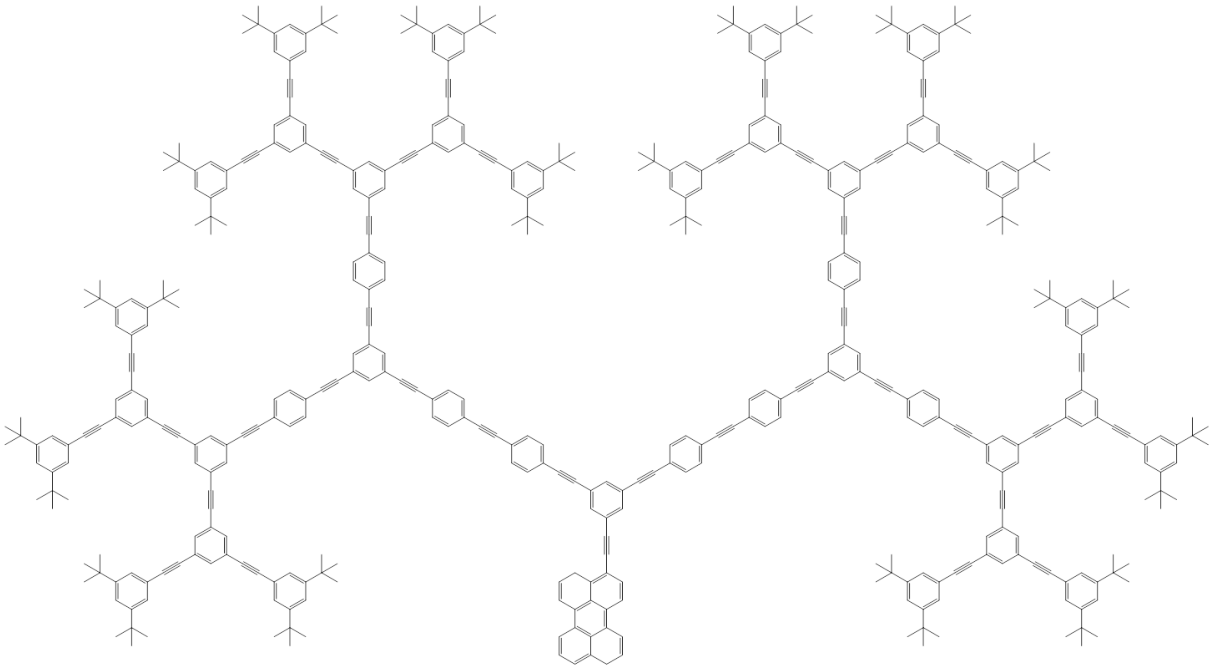

Figure D.1: The "nanostar".

des applications optoélectroniques [8, 13]. Parmi les PPEs, ceux présentant une structure dendritiques peuvent être classés en deux catégories, compacts et étendus. Dans les deux cas, le dendrimère est une antenne collectrice de lumière rendue particulièrement efficace grâce à sa structure ramifiée semblable à un arbre, le rendant capable de collecter des photons au niveau de différents points périphériques.

Les dendrimères compacts sont constitués de briques *para* de même longueur, donc l'entropie y est responsable d'une partie des transferts d'énergie [11, 23–26]. A l'inverse, les dendrimères étendus (comme la nanostar) sont constitués de briques de longueur croissante à partir de la périphérie, ce qui engendre un gradient d'énergie à l'origine d'un transfert d'énergie efficace [19, 27, 28].

Dans cette thèse, nous nous intéressons au transfert d'énergie au sein de PPE photo-excités, en cherchant à le mettre en lien avec les propriétés de leurs unités constitutives, afin de comprendre et rationaliser les mécanismes mis en jeu, puis de le simuler.

Quantités d'efforts ont été fait au cours des 30 dernières années pour comprendre les mécanismes gouvernant le comportement des PPEs aux niveaux moléculaire et microscopique. Pour autant, identifier les relations structure/propriété dans des macromolécules tout en considérant ces mêmes relations au sein de leurs entités constitutives soulève des problèmes à la fois théoriques et expérimentaux [29].

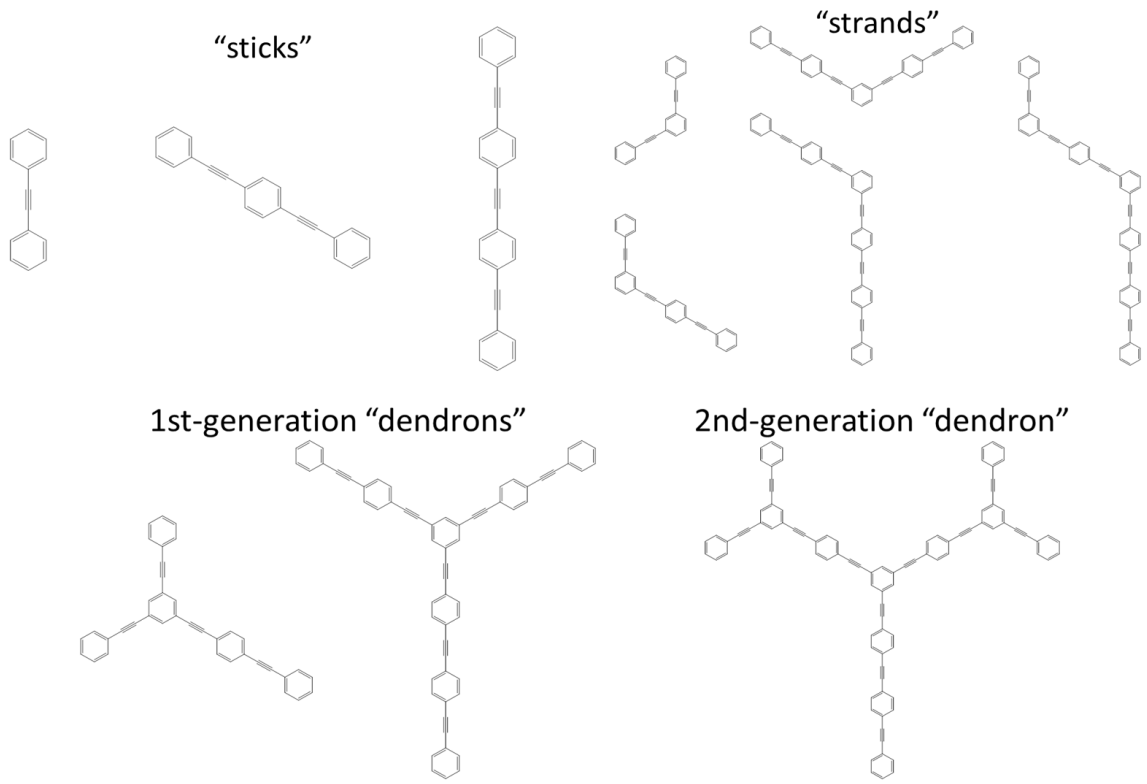

Figure D.2: Various PPEs.

Ce genre de description nécessite de prendre en compte correctement des effets divers, agissant à des échelles de longueur, de temps et d'énergie différentes, ce qui n'est pas simple à première vue.

Les premières informations sur la structure électronique de PPE sont venues d'expériences de spectroscopie des états stationnaires [27, 30]. Les auteurs ont alors mis en évidence l'additivité du spectre d'absorption de la nanostar ainsi que les contributions dominantes, dues à des transitions $\pi \rightarrow \pi^*$ entre états excités localisés sur des "sticks". Ces éléments ont ensuite été confirmés par des études aussi bien expérimentales [20, 28, 31–33] que théoriques [34–42] sur d'autres *meta*-PPEs. Une description quantitative de la relation entre les structures électronique et géométrique est nécessaire, en particulier pour rationaliser la rupture partielle de la conjugaison π au niveau des jonctions *meta* [34, 43–45].

D'un point de vue dynamique, le transfert d'énergie dans la nanostar est un transfert ultrarapide et unidirectionel d'excitation se produisant *via* une cascade de conversions internes entre des "sticks" de longueur croissante [19,27,30,41,42,48–53]. Les chromophores en périphérie absorbent la lumière à haute énergie et transfèrent ensuite l'excitation au chromophore adjacent en suivant le gradient d'énergie induit par la différence de longueur

des chromophores (effet *shishiodoshi*) [42]. Pour le moment, il est admis que ce mécanisme idéal implique des intersections coniques qui n'ont pas encore pu être caractérisées.

Des calculs approchés (dynamique mixte quantique-classique sur des surfaces d'énergie potentielle semi-empiriques) ont montré que le transfert est médié vibroniquement le long de modes de vibrations des C≡C dans le plan [42, 48, 49, 51–53]. Une étude plus complète recquiert d'avoir accès à l'évolution des populations entre les états électroniques impliqués et des cohérences en fonction du temps. De telles informations nécessitent d'effectuer des simulations à plus haut niveau et des expériences de spectroscopie ultra-rapide.

D.2 Travail effectué

Dans cette thèse, nous nous sommes intéressé à des PPE à la fois en tant que molécules à étudier et supports pour la construction d'un nouveau modèle vibronique. L'étude des PPE visait à permettre la rationalisation du processus de transfert d'excitation unidirectionnel suivant l'absorption lumineuse, tandis que modèle vibronique avait pour but de fournir une expression fonctionnelle de l'énergie électronique en fonction des coordonnées nucléaires (en d'autres termes de fournir une représentation de la surface d'énergie potentielle).

Nous avons commencé par vérifier la validité de la méthode utilisée pour la description de la structure électronique des PPEs, à savoir la TDDFT (CAM-B3LYP/6-31+G*) [63]. Par cette vérification, nous avons levé un désaccord posé dans la littérature au cours des dernières années [118, 130]. La TDDFT a ensuite été utilisée pour caractériser des *para* et *meta*-PPE aux géométries d'équilibre de divers états électroniques, des points de vue géométrique, énergétique, orbitalaire et vibrationnel. Pour les *para*-PPEs, le spectre d'absorption électronique résolu vibrationnellement a été simulé et les principales contributions vibrationnelles ont été attribuées.

Nous avons montré que l'état électronique (S_0 ou S_1) des *para*-PPE (de deux à sept cycles) pouvait être caractérisé par certaines longueurs de liaison (acetylene, quinoidal, internes) ou par les fréquences de vibration associées à des modes particuliers. De même, l'énergie de transition S_0-S_1, ainsi que le gap entre orbitales frontières, permettent quant à eux de discriminer des *para*-PPE de longueurs différentes. La forme des orbitales frontières

est similaire quelle que soit la longueur du *para*-PPE et laisse clairement apparaitre la forme des orbitales frontières du benzene et de l'acetylene.

La caractérisation des *meta*-PPE vis-à-vis des propriétés mentionnées ci-dessus a prouvé que chacun des premiers états excités était localisé sur un "stick" particulier, l'énergie de l'état excité augmentant à mesure que la longueur de chaine diminue. Nous avons particulièrement insisté sur le fait que chaque état excité résulte majoritairement d'une mono-excitation entre une paires d'orbitales frontières (ou HO-1/LU+1 etc), elles-mêmes localisées sur des "sticks". La localisation des états excités dans les *meta*-PPE ainsi que la forme des orbitales frontières dans les *para* témoignent d'une forte hiérarchie entre les interactions gouvernant les propriétés photochimiques des PPE.

La surface d'énergie potentielle du (2,2)-*meta*-PPE a été explorée le long de modes nucléaires particuliers, ce qui nous a permis d'identifier plusieurs intersections coniques accessibles en terme d'énergie. De fait, les modes en question sont donc des composantes de l'espace de branchement. Nous avons ainsi confirmé le rôle, déjà mentionné dans la littérature, de l'élongation des liaisons acetylène dans le transfert d'excitation. Nous avons également mis en évidence l'importance de l'élongation des liaisons quinoidales sur le phénylène coquin, ce qui n'avait pas encore rapporté.

L'interprétation que nous avons proposée de la levée de dégénérescence à l'intersection conique en termes d'états diabatiques localisés sur les sticks fait écho au mécanisme de transfert par cascade *shishiodoshi* présenté dans la littérature. Nous avons également pu confirmer cette hypothèse par l'identification dans le (2,3)-*meta*-PPE de croisements faiblements évités entre S_1 et S_2, états localisés au minimum de l'état fondamental.

Nous avons proposé une stratégie visant à construire un nouveau modèle vibronique pour l'énergie de PPE. En s'appuyant sur la hiérarchie gouvernant les interactions dans les PPE, nous avons construit le modèle étape par étape en suivant une approche multi-échelle. Chaque étape correspond à la description d'une interaction due soit à un couplage (entre orbitales ou états électroniques) soit à la répulsion électronique. La photochimie des PPE étant gouvernée par le système π, les formalismes de type tight-binding sont adaptés à la description de chaque étape.

Nous avons donc proposé un Hamiltonien effectif de type Hückel permettant d'exprimer

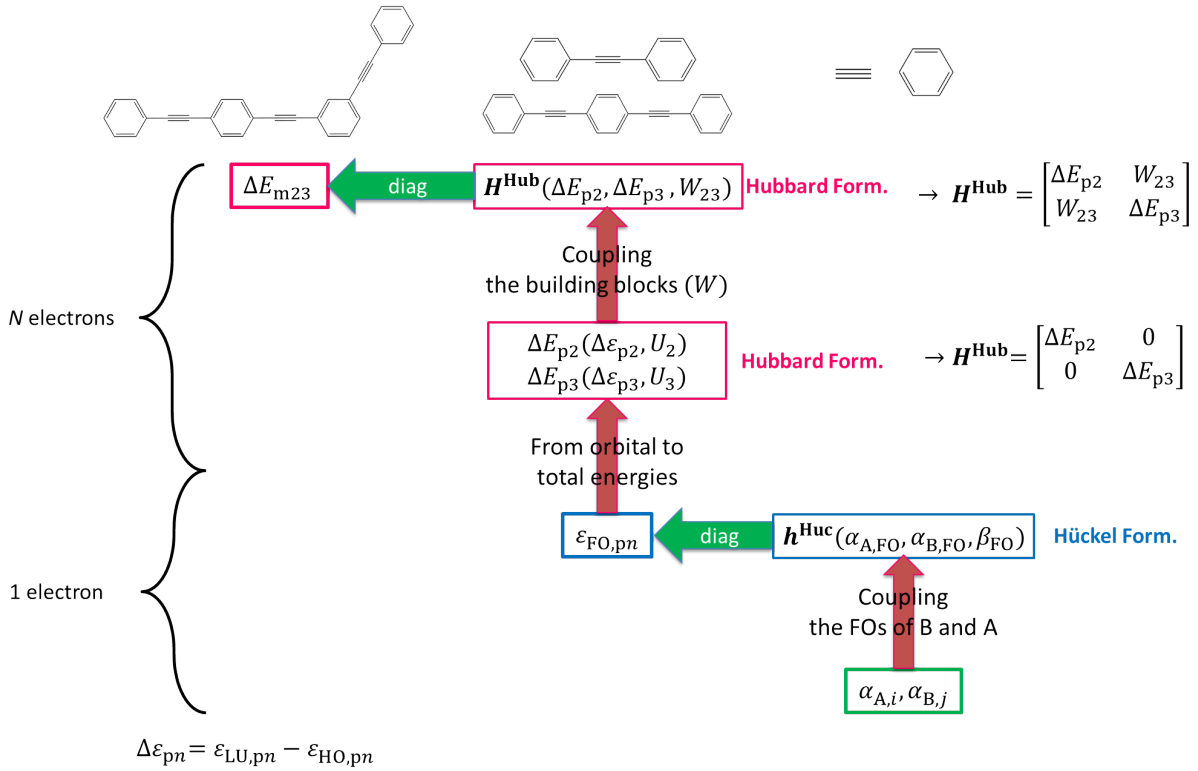

Figure D.3: Structure of the vibronic model. Decomposition of the transition energy. FO = HO or LU.

les énergies des orbitales frontières des *para*-PPEs en fonction de paramètres effectifs décrivant les orbitales frontières du benzène, de l'acétylène, et leur interaction (modèle FFO). Les valeurs effectives de ces paramètres de type Hückel et des énergies des orbitales frontières ont été optimisées en considérant plusieurs *para*-PPEs.

Ce formalisme a été étendu aux *meta*-PPE, permettant de reproduire un gap HO-LU de référence (calcul Hückel étendu) à 0.05 eV près. De tels résultats sont particulièrement encourageants considérant le niveau d'approximations utilisées dans l'élaboration du modèle.

Nous avons également vérifié la possibilité de décrire l'évolution des paramètres du modèle et des énergies des orbitales frontières comme des fonctions linéaires des coordonnées locales précédemment identifiées, avec succès. Un travail de mapping a été effectué entre les énergies de transitions entre états électroniques et les énergies de transition entre orbitales frontières dans divers PPE. Ce mapping a permis d'établir empiriquement une relation affine entre ces deux grandeurs. La combinaison du mapping et de l'expression fonctionnelle des orbitales frontières nous a permis d'aboutir à une expression pour l'énergie de transition électronique en fonction d'un nombre réduit de coordonnées nucléaires locales.

Glossary

BB building block

CIS configuration interaction singles

Coin conical intersection

DFT density functional theory

FC Franck-Condon

FO frontier orbital

HF Hartree-Fock

HT Herzberg-Teller

KS Kohn-Sham

LDA local density approximation

LCAO linear combination of atomic orbitals

MO molecular orbitals

NAC non-adiabatic coupling

PES potential energy surface

PPE polyphenylene ethynylene

RMSD root-mean-square deviation

TDA Tamm-Dancoff approximation

TDDFT time-dependent density functional theory

CTMM Team "Chimie Théorique, Méthodologies, Modélisation" in the Institut Charles Gerhardt de Montpellier

XH extended-Hückel

Bibliography

[1] O. A. Matthews, A. N. Shipway, and J. F. Stoddart, "Dendrimers-Branching out from curiosities into new technologies," *Progress in Polymer Science*, vol. 23, pp. 1–56, Jan. 1998.

[2] F. Charra, V. Agranovič, and NATO Advanced Research Workshop on Organic Nanophotonics, *Organic nanophotonics*. Dordrecht: Kluwer Academic Publishers, 2003. OCLC: 905504331.

[3] A. Credi, "Introducing the Research Front on Photoactive and Electroactive Dendrimers," *Aust. J. Chem.*, vol. 64, pp. 127–128, Mar. 2011.

[4] V. Balzani, "Dendrimers: Order, Complexity, Functions," *Aust. J. Chem.*, vol. 64, pp. 129–130, Mar. 2011.

[5] P. Ceroni and M. Venturi, "Photoactive and Electroactive Dendrimers: Future Trends and Applications," *Aust. J. Chem.*, vol. 64, pp. 131–146, Mar. 2011.

[6] E. Abbasi, S. F. Aval, A. Akbarzadeh, M. Milani, H. T. Nasrabadi, S. W. Joo, Y. Hanifehpour, K. Nejati-Koshki, and R. Pashaei-Asl, "Dendrimers: synthesis, applications, and properties," *Nanoscale Research Letters*, vol. 9, p. 247, May 2014.

[7] X. Zhang, Y. Zeng, T. Yu, J. Chen, G. Yang, and Y. Li, "Advances in Photofunctional Dendrimers for Solar Energy Conversion," *The Journal of Physical Chemistry Letters*, vol. 5, pp. 2340–2350, July 2014.

[8] T. Oyamada, G. Shao, H. Uchiuzou, H. Nakanotani, A. Orita, J. Otera, M. Yahiro, and C. Adachi, "Optical and Electrical Properties of Bis(4-(phenylethynyl)phenyl)ethynes and Their Application to Organic Field-Effect Transistors," *Japanese Journal of Applied Physics*, vol. 45, pp. L1331–L1333, Dec. 2006.

[9] J. Cornil, D. Beljonne, J.-P. Calbert, and J.-L. Brédas, "Interchain Interactions in Organic pi-Conjugated Materials: Impact on Electronic Structure, Optical Response, and Charge Transport," *Adv. Mater.*, vol. 13, no. 14, pp. 1053–1067, 2001.

[10] S. Mukamel, "Photochemistry: Trees to trap photons," *Nature*, vol. 388, no. 6641, pp. 425–427, 1997.

[11] A. Bar-Haim and J. Klafter, "Dendrimers as light harvesting antennae," *Journal of Luminescence*, vol. 76, pp. 197–200, 1998.

[12] D. Gust, T. A. Moore, and A. L. Moore, "Mimicking Photosynthetic Solar Energy Transduction," *Accounts of Chemical Research*, vol. 34, pp. 40–48, Jan. 2001.

[13] R. Ziessel, G. Ulrich, A. Haefele, and A. Harriman, "An Artificial Light-Harvesting Array Constructed from Multiple Bodipy Dyes," *Journal of the American Chemical Society*, vol. 135, pp. 11330–11344, July 2013.

[14] Z. Chen, E. M. Grumstrup, A. T. Gilligan, J. M. Papanikolas, and K. S. Schanze, "Light-Harvesting Polymers: Ultrafast Energy Transfer in Polystyrene-Based Arrays of pi-Conjugated Chromophores," *J. Phys. Chem. B*, vol. 118, pp. 372–378, Jan. 2014.

[15] C. K. Chiang, C. R. Fincher, Y. W. Park, A. J. Heeger, H. Shirakawa, E. J. Louis, S. C. Gau, and A. G. MacDiarmid, "Electrical Conductivity in Doped Polyacetylene," *Phys. Rev. Lett.*, vol. 39, pp. 1098–1101, Oct. 1977.

[16] H. Shirakawa, E. J. Louis, A. G. MacDiarmid, C. K. Chiang, and A. J. Heeger, "Synthesis of electrically conducting organic polymers: halogen derivatives of polyacetylene, (CH)x," *J. Chem. Soc., Chem. Commun.*, vol. 0, pp. 578–580, Jan. 1977.

[17] C. K. Chiang, M. A. Druy, S. C. Gau, A. J. Heeger, E. J. Louis, A. G. MacDiarmid, Y. W. Park, and H. Shirakawa, "Synthesis of highly conducting films of derivatives of polyacetylene, (CH)x," *J. Am. Chem. Soc.*, vol. 100, pp. 1013–1015, Feb. 1978.

[18] C. K. Chiang, Y. W. Park, A. J. Heeger, H. Shirakawa, E. J. Louis, and A. G. MacDiarmid, "Conducting polymers: Halogen doped polyacetylene," *The Journal of Chemical Physics*, vol. 69, pp. 5098–5104, Dec. 1978.

[19] C. Devadoss, P. Bharathi, and J. S. Moore, "Energy transfer in dendritic macromolecules: molecular size effects and the role of an energy gradient," *Journal of the American Chemical Society*, vol. 118, no. 40, pp. 9635–9644, 1996.

[20] J. S. Melinger, Y. Pan, V. D. Kleiman, Z. Peng, B. L. Davis, D. McMorrow, and M. Lu, "Optical and Photophysical Properties of Light-Harvesting Phenylacetylene Monodendrons Based on Unsymmetrical Branching," *J. Am. Chem. Soc.*, vol. 124, pp. 12002–12012, Oct. 2002.

[21] Z. Xu and J. S. Moore, "Design and synthesis of a convergent and directional molecular antenna," *Acta Polymerica*, vol. 45, no. 2, pp. 83–87, 1994.

[22] P. Reineker, A. Engelmann, and V. I. Yudson, "Excitons in dendrimers: optical absorption and energy transport," *Journal of Luminescence*, vol. 94, pp. 203–206, Dec. 2001.

[23] A. Bar-Haim and J. Klafter, "Geometric versus energetic competition in light harvesting by dendrimers," *The Journal of Physical Chemistry B*, vol. 102, no. 10, pp. 1662–1664, 1998.

[24] P. Reineker, A. Engelmann, and V. I. Yudson, "Energy Transfer and Optical Properties of Dendrimers," *Nonlinear Optics*, vol. 29, no. 10-12, pp. 671–678, 2002.

[25] D.-J. Heijs, V. A. Malyshev, and J. Knoester, "Trapping time statistics and efficiency of transport of optical excitations in dendrimers," *The Journal of Chemical Physics*, vol. 121, no. 10, p. 4884, 2004.

[26] S.-i. Koda, "A theoretical investigation of symmetry-origin unidirectional energy gradient in light-harvesting dendrimers," *The Journal of Chemical Physics*, vol. 144, p. 114101, Mar. 2016.

[27] M. R. Shortreed, S. F. Swallen, Z.-Y. Shi, W. Tan, Z. Xu, C. Devadoss, J. S. Moore, and R. Kopelman, "Directed energy transfer funnels in dendrimeric antenna supermolecules," *The Journal of Physical Chemistry B*, vol. 101, no. 33, pp. 6318–6322, 1997.

[28] S. F. Swallen, R. Kopelman, J. S. Moore, and C. Devadoss, "Dendrimer photoantenna supermolecules: energetic funnels, exciton hopping and correlated excimer formation," *Journal of molecular structure*, vol. 485, pp. 585–597, 1999.

[29] T. Nelson, S. Fernandez-Alberti, A. E. Roitberg, and S. Tretiak, "Electronic Delocalization, Vibrational Dynamics, and Energy Transfer in Organic Chromophores," *J. Phys. Chem. Lett.*, vol. 8, pp. 3020–3031, July 2017.

[30] R. Kopelman, M. Shortreed, Z.-Y. Shi, W. Tan, Z. Xu, J. S. Moore, A. Bar-Haim, and J. Klafter, "Spectroscopic evidence for excitonic localization in fractal antenna supermolecules," *Physical review letters*, vol. 78, no. 7, p. 1239, 1997.

[31] S. M. Risser, D. N. Beratan, and J. N. Onuchic, "Electronic coupling in starburst dendrimers: connectivity, disorder, and finite size effects in macromolecular bethe lattices," *The Journal of Physical Chemistry*, vol. 97, no. 17, pp. 4523–4527, 1993.

[32] A. Bar-Haim, J. Klafter, and R. Kopelman, "Dendrimers as controlled artificial energy antennae," *Journal of the American Chemical Society*, vol. 119, no. 26, pp. 6197–6198, 1997.

[33] V. D. Kleiman, J. S. Melinger, and D. McMorrow, "Ultrafast Dynamics of Electronic Excitations in a Light-Harvesting Phenylacetylene Dendrimer," *The Journal of Physical Chemistry B*, vol. 105, pp. 5595–5598, June 2001.

[34] S. Tretiak, V. Chernyak, and S. Mukamel, "Localized electronic excitations in phenylacetylene dendrimers," *The Journal of Physical Chemistry B*, vol. 102, no. 18, pp. 3310–3315, 1998.

[35] K. Harigaya, "Optical excitations in fractal antenna supermolecules with conjugated electrons: extended dendrimers," *Chemical Physics Letters*, vol. 300, pp. 33–36, Jan. 1999.

[36] K. Harigaya, "Coupled exciton model with off-diagonal disorder for optical excitations in extended dendrimers," *Physical Chemistry Chemical Physics*, vol. 1, no. 7, pp. 1687–1689, 1999.

[37] E. Y. Poliakov, V. Chernyak, S. Tretiak, and S. Mukamel, "Exciton-scaling and optical excitations of self-similar phenylacetylene dendrimers," *The Journal of Chemical Physics*, vol. 110, no. 16, p. 8161, 1999.

[38] T. Minami, S. Tretiak, V. Chernyak, and S. Mukamel, "Frenkel-exciton Hamiltonian for dendrimeric nanostar," *Journal of Luminescence*, vol. 87–89, pp. 115–118, 2000.

[39] J. C. Kirkwood, C. Scheurer, V. Chernyak, and S. Mukamel, "Simulations of energy funneling and time- and frequency-gated fluorescence in dendrimers," *The Journal of Chemical Physics*, vol. 114, no. 5, p. 2419, 2001.

[40] C. Wu, S. V. Malinin, S. Tretiak, and V. Y. Chernyak, "Exciton scattering and localization in branched dendrimeric structures," *Nature Physics*, vol. 2, pp. 631–635, Sept. 2006.

[41] J. L. Palma, E. Atas, L. Hardison, T. B. Marder, J. C. Collings, A. Beeby, J. S. Melinger, J. L. Krause, V. D. Kleiman, and A. E. Roitberg, "Electronic Spectra of the Nanostar Dendrimer: Theory and Experiment †," *The Journal of Physical Chemistry C*, vol. 114, pp. 20702–20712, Dec. 2010.

[42] S. Fernandez-Alberti, A. E. Roitberg, V. D. Kleiman, T. Nelson, and S. Tretiak, "Shishiodoshi unidirectional energy transfer mechanism in phenylene ethynylene dendrimers," *The Journal of Chemical Physics*, vol. 137, no. 22, p. 22A526, 2012.

[43] K. M. Gaab, A. L. Thompson, J. Xu, T. J. Martínez, and C. J. Bardeen, "Meta-Conjugation and Excited-State Coupling in Phenylacetylene Dendrimers," *Journal of the American Chemical Society*, vol. 125, pp. 9288–9289, Aug. 2003.

[44] A. L. Thompson, K. M. Gaab, J. Xu, C. J. Bardeen, and T. J. Martínez, "Variable Electronic Coupling in Phenylacetylene Dendrimers: The Role of Förster, Dexter, and Charge-Transfer Interactions," *The Journal of Physical Chemistry A*, vol. 108, pp. 671–682, Jan. 2004.

[45] Q. Chu and Y. Pang, "Vibronic structures in the electronic spectra of oligo(phenylene ethynylene): effect of m-phenylene to the optical properties of poly(m-phenylene ethynylene)," *Spectrochimica Acta Part A: Molecular and Biomolecular Spectroscopy*, vol. 60, pp. 1459–1467, June 2004.

[46] J. Huang, L. Du, J. Wang, and Z. Lan, "Photoinduced Excited-State Energy-Transfer Dynamics of a Nitrogen-Cored Symmetric Dendrimer: From the Perspective of the Jahn–Teller Effect," *The Journal of Physical Chemistry C*, vol. 119, pp. 7578–7589, Apr. 2015.

[47] S. S. K. Raavi, P. Docampo, C. Wehrenfennig, M. J. P. Alcocer, G. Sadoughi, L. M. Herz, H. J. Snaith, and A. Petrozza, "Impact of Molecular Charge-Transfer States on Photocurrent Generation in Solid State Dye-Sensitized Solar Cells Employing Low-Band-Gap Dyes," *The Journal of Physical Chemistry C*, vol. 118, pp. 16825–16830, July 2014.

[48] S. Fernandez-Alberti, V. D. Kleiman, S. Tretiak, and A. E. Roitberg, "Nonadiabatic Molecular Dynamics Simulations of the Energy Transfer between Building Blocks in a Phenylene Ethynylene Dendrimer †," *The Journal of Physical Chemistry A*, vol. 113, pp. 7535–7542, July 2009.

[49] S. Fernandez-Alberti, V. D. Kleiman, S. Tretiak, and A. E. Roitberg, "Unidirectional Energy Transfer in Conjugated Molecules: The Crucial Role of High-Frequency C≡C Bonds," *The Journal of Physical Chemistry Letters*, vol. 1, pp. 2699–2704, Sept. 2010.

[50] T. Nelson, S. Fernandez-Alberti, A. E. Roitberg, and S. Tretiak, "Nonadiabatic Excited-State Molecular Dynamics: Modeling Photophysics in Organic Conjugated Materials," *Accounts of Chemical Research*, vol. 47, pp. 1155–1164, Apr. 2014.

[51] J. F. Galindo, E. Atas, A. Altan, D. G. Kuroda, S. Fernandez-Alberti, S. Tretiak, A. E. Roitberg, and V. D. Kleiman, "Dynamics of Energy Transfer in a Conjugated Dendrimer Driven by Ultrafast Localization of Excitations," *Journal of the American Chemical Society*, vol. 137, pp. 11637–11644, Sept. 2015.

[52] J. F. Galindo, S. Fernandez-Alberti, and A. E. Roitberg, "Electronic Excited State Specific IR Spectra for Phenylene Ethynylene Dendrimer Building Blocks," *The Journal of Physical Chemistry C*, vol. 117, pp. 26517–26528, Dec. 2013.

[53] D. Ondarse-Alvarez, S. Kömürlü, A. E. Roitberg, G. Pierdominici-Sottile, S. Tretiak, S. Fernandez-Alberti, and V. D. Kleiman, "Ultrafast electronic energy relaxation in

a conjugated dendrimer leading to inter-branch energy redistribution," *Phys. Chem. Chem. Phys.*, vol. 18, pp. 25080–25089, Sept. 2016.

[54] A. Tortschanoff, A. Piryatinski, and S. Mukamel, "Femtosecond pump–probe spectroscopy of the dendrimeric nanostar," *Journal of luminescence*, vol. 94, pp. 569–573, 2001.

[55] A. Tortschanoff and S. Mukamel, "Pump−Probe Simulation Study of the Two-Exciton Manifold of Dendrimers †," *The Journal of Physical Chemistry A*, vol. 106, pp. 7521–7529, Aug. 2002.

[56] G. D. Scholes and G. Rumbles, "Excitons in nanoscale systems," *Nature Materials*, vol. 5, pp. 683–696, Sept. 2006.

[57] W. Ortiz, B. P. Krueger, V. D. Kleiman, J. L. Krause, and A. E. Roitberg, "Energy Transfer in the Nanostar: The Role of Coulombic Coupling and Dynamics," *The Journal of Physical Chemistry B*, vol. 109, pp. 11512–11519, June 2005.

[58] L. T. Liu, D. Yaron, M. I. Sluch, and M. A. Berg, "Modeling the Effects of Torsional Disorder on the Spectra of Poly- and Oligo-(p -phenyleneethynylenes) †," *The Journal of Physical Chemistry B*, vol. 110, pp. 18844–18852, Sept. 2006.

[59] R. Magyar, S. Tretiak, Y. Gao, H.-L. Wang, and A. Shreve, "A joint theoretical and experimental study of phenylene–acetylene molecular wires," *Chemical Physics Letters*, vol. 401, pp. 149–156, Jan. 2005.

[60] R. Binder, J. Wahl, S. Römer, and I. Burghardt, "Coherent exciton transport driven by torsional dynamics: a quantum dynamical study of phenylene-vinylene type conjugated systems," *Faraday Discuss.*, vol. 163, pp. 205–222, July 2013.

[61] T. Nelson, S. Fernandez-Alberti, A. E. Roitberg, and S. Tretiak, "Conformational disorder in energy transfer: beyond Förster theory," *Phys. Chem. Chem. Phys.*, vol. 15, pp. 9245–9256, May 2013.

[62] M. J. Frisch, G. W. Trucks, H. B. Schlegel, G. E. Scuseria, M. A. Robb, J. R. Cheeseman, G. Scalmani, V. Barone, B. Mennucci, G. A. Petersson, H. Nakatsuji, M. Caricato, X. Li, H. P. Hratchian, A. F. Izmaylov, J. Bloino, G. Zheng, J. L. Sonnenberg, M. Hada, M. Ehara, K. Toyota, R. Fukuda, J. Hasegawa, M. Ishida,

T. Nakajima, Y. Honda, O. Kitao, H. Nakai, T. Vreven, J. A. Montgomery, Jr., J. E. Peralta, F. Ogliaro, M. Bearpark, J. J. Heyd, E. Brothers, K. N. Kudin, V. N. Staroverov, R. Kobayashi, J. Normand, K. Raghavachari, A. Rendell, J. C. Burant, S. S. Iyengar, J. Tomasi, M. Cossi, N. Rega, J. M. Millam, M. Klene, J. E. Knox, J. B. Cross, V. Bakken, C. Adamo, J. Jaramillo, R. Gomperts, R. E. Stratmann, O. Yazyev, A. J. Austin, R. Cammi, C. Pomelli, J. W. Ochterski, R. L. Martin, K. Morokuma, V. G. Zakrzewski, G. A. Voth, P. Salvador, J. J. Dannenberg, S. Dapprich, A. D. Daniels, . Farkas, J. B. Foresman, J. V. Ortiz, J. Cioslowski, and D. J. Fox, "Gaussian∼09 Revision E.01," Gaussian Inc. Wallingford CT 2009.

[63] E. K.-L. Ho, T. Etienne, and B. Lasorne, "Vibronic properties of para-polyphenylene ethynylenes: TD-DFT insights," *The Journal of Chemical Physics*, vol. 146, p. 164303, Apr. 2017.

[64] A. Szabo and O. Neil S., *Modern Quantum Chemistry an Introduction to Advanced Electronic Structure Theory*. 1982.

[65] A. Perveaux, *Study of photo induce process by quantum chemistry and quantum dynamics methods*. PhD thesis, 2015. Thèse de doctorat dirigée par Lauvergnat, David Chimie Paris Saclay 2015.

[66] B. Gonon, *Simulations quantiques non-adiabatiques d'un photo-interrupteur moléculaire vers un dialogue expérience-théorie*. PhD thesis, 2017.

[67] F. Gatti, B. Lasorne, H.-D. Meyer, and A. Nauts, *Applications of Quantum Dynamics in Chemistry*. Lecture Notes in Chemistry, Springer International Publishing, 2017.

[68] D. J. Tannor, *Introduction to Quantum Mechanics*. University Science Books, Jan. 2007. Google-Books-ID: t7m08j3Wi9YC.

[69] L. S. Cederbaum, *BORN–OPPENHEIMER APPROXIMATION AND BEYOND*, pp. 3–40.

[70] M. Desouter, Y. Justum, and X. Chapuisat, *Introduction à la Théorie Quantique Concepts Pratiques et Applications.* Ellipses, 2017.

[71] O. E. Alon and L. S. Cederbaum, "Hellmann-Feynman theorem at degeneracies," *Phys. Rev. B*, vol. 68, p. 033105, July 2003.

[72] I. Prigogine and S. A. Rice, *Advances in Chemical Physics*. John Wiley & Sons, Sept. 2009. Google-Books-ID: l0dUT6kfuLsC.

[73] W. Domcke, D. Yarkony, and H. Köppel, *Conical Intersections: Electronic Structure, Dynamics & Spectroscopy*. World Scientific, 2004.

[74] W. Domcke, D. R. Yarkony, and H. Köppel, *Conical Intersections: Theory, Computation and Experiment*. World Scientific, 2011. Google-Books-ID: Fc1bN093a4wC.

[75] R. A. Marcus, "On the Theory of Oxidation-Reduction Reactions Involving Electron Transfer. I," *The Journal of Chemical Physics*, vol. 24, pp. 966–978, May 1956.

[76] R. A. Marcus, "Electron transfer reactions in chemistry. Theory and experiment," *Rev. Mod. Phys.*, vol. 65, pp. 599–610, July 1993.

[77] A. D. Walsh, "466. The electronic orbitals, shapes, and spectra of polyatomic molecules. Part I. AH2 molecules," *J. Chem. Soc.*, vol. 0, pp. 2260–2266, Jan. 1953.

[78] A. D. Walsh, "467. The electronic orbitals, shapes, and spectra of polyatomic molecules. Part II. Non-hydride AB2 and BAC molecules," *J. Chem. Soc.*, vol. 0, pp. 2266–2288, Jan. 1953.

[79] A. D. Walsh, "468. The electronic orbitals, shapes, and spectra of polyatomic molecules. Part III. HAB and HAAH molecules," *J. Chem. Soc.*, vol. 0, pp. 2288–2296, Jan. 1953.

[80] A. D. Walsh, "469. The electronic orbitals, shapes, and spectra of polyatomic molecules. Part IV. Tetratomic hydride molecules, AH3," *J. Chem. Soc.*, vol. 0, pp. 2296–2301, Jan. 1953.

[81] A. D. Walsh, "470. The electronic orbitals, shapes, and spectra of polyatomic molecules. Part V. Tetratomic, non-hydride molecules, AB3," *J. Chem. Soc.*, vol. 0, pp. 2301–2306, Jan. 1953.

[82] A. D. Walsh, "471. The electronic orbitals, shapes, and spectra of polyatomic molecules. Part VI. H2ab molecules," *J. Chem. Soc.*, vol. 0, pp. 2306–2317, Jan. 1953.

[83] A. D. Walsh, "472. The electronic orbitals, shapes, and spectra of polyatomic molecules. Part VII. A note on the near-ultra-violet spectrum of acetaldehyde," *J. Chem. Soc.*, vol. 0, pp. 2318–2320, Jan. 1953.

[84] A. D. Walsh, "473. The electronic orbitals, shapes, and spectra of polyatomic molecules. Part VIII. Pentatomic molecules: CH3i," *J. Chem. Soc.*, vol. 0, pp. 2321–2324, Jan. 1953.

[85] A. D. Walsh, "474. The electronic orbitals, shapes, and spectra of polyatomic molecules. Part IX. Hexatomic molecules: ethylene," *J. Chem. Soc.*, vol. 0, pp. 2325–2329, Jan. 1953.

[86] A. D. Walsh, "475. The electronic orbitals, shapes, and spectra of polyatomic molecules. Part X. A note on the spectrum of benzene," *J. Chem. Soc.*, vol. 0, pp. 2330–2331, Jan. 1953.

[87] C. S. Miller and M. Ellison, "Walsh Diagrams: Molecular Orbital and Structure Computational Chemistry Exercise for Physical Chemistry," *J. Chem. Educ.*, vol. 92, pp. 1040–1043, June 2015.

[88] S. Matsika and D. R. Yarkony, "Accidental conical intersections of three states of the same symmetry. I. Location and relevance," *The Journal of Chemical Physics*, vol. 117, pp. 6907–6910, Sept. 2002.

[89] M. S. Schuurman and D. R. Yarkony, "On the Characterization of Three-State Conical Intersections Using a Group Homomorphism Approach: The Two-State Degeneracy Spaces," *J. Phys. Chem. B*, vol. 110, pp. 19031–19039, Sept. 2006.

[90] M. Assmann, G. A. Worth, and L. González, "9d nonadiabatic quantum dynamics through a four-state conical intersection: Investigating the homolysis of the O–O bond in anthracene-9,10-endoperoxide," *The Journal of Chemical Physics*, vol. 137, p. 22A524, Aug. 2012.

[91] R. Hoffmann and R. B. Woodward, "Orbital Symmetries and endo-exo Relationships in Concerted Cycloaddition Reactions," *J. Am. Chem. Soc.*, vol. 87, pp. 4388–4389, Oct. 1965.

[92] R. Hoffmann and R. B. Woodward, "Orbital Symmetries and Orientational Effects in a Sigmatropic Reaction," *J. Am. Chem. Soc.*, vol. 87, pp. 4389–4390, Oct. 1965.

[93] R. Hoffmann and R. B. Woodward, "Selection Rules for Concerted Cycloaddition Reactions," *J. Am. Chem. Soc.*, vol. 87, pp. 2046–2048, May 1965.

[94] R. B. Woodward and R. Hoffmann, "Selection Rules for Sigmatropic Reactions," *J. Am. Chem. Soc.*, vol. 87, pp. 2511–2513, June 1965.

[95] R. B. Woodward and R. Hoffmann, "Stereochemistry of Electrocyclic Reactions," *J. Am. Chem. Soc.*, vol. 87, pp. 395–397, Jan. 1965.

[96] T. A. Nguyên, *Introduction à la chimie moléculaire*. Ellipses, 1994. Google-Books-ID: lP9rAAAACAAJ.

[97] P. Hiberty and N. T. Anh, *Introduction à la chimie quantique*. Editions Ecole Polytechnique, 2008. Google-Books-ID: rxn5m7w_mgsC.

[98] R. G. Parr and W. Yang, *Density-Functional Theory of Atoms and Molecules*. Oxford University Press, 1989.

[99] C. J. Cramer, *Essentials of Computaional Chemistry, Theories and Models*. John Wiley & Sons, Ltd, 2nd ed., 2006.

[100] D. S. Sholl and J. A. Steckel, *Density Functional Theory A practical introduction*. John Wiley & Sons, 2009.

[101] P. Hohenberg and W. Kohn, "Inhomogeneous Electron Gas," *Phys. Rev.*, vol. 136, pp. B864–B871, Nov. 1964.

[102] W. Kohn and L. J. Sham, "Self-Consistent Equations Including Exchange and Correlation Effects," *Phys. Rev.*, vol. 140, pp. A1133–A1138, Nov. 1965.

[103] C. Cohen-Tannoudji, D. Bernard, and F. Laloë, *Mécanique quantique Tome II*. No. 16 in Enseignement des sciences, Hermann, 1986.

[104] M. A. L. Marques, C. Ullrich, F. Nogueira, A. Rubio, K. Burke, and E. K. U. Gross, eds., *Time-Dependent Density Functional Theory*. Lecture Notes in Physics, Berlin Heidelberg: Springer-Verlag, 2006.

[105] C. A. Ullrich, *Time-Dependent Density-Functional Theory: Concepts and Applications*. Oxford Graduate Texts, Oxford, New York: Oxford University Press, Dec. 2011.

[106] E. Rebolini, *Range-separated density-functional theory for molecular excitation energies*. Theses, Université Pierre et Marie Curie - Paris VI, June 2014.

[107] E. Fromager, "Excited states in density-functional theory: time-dependent and time-independent approaches, https://quantique.u-strasbg.fr/."

[108] E. Runge and E. K. U. Gross, "Density-Functional Theory for Time-Dependent Systems," *Phys. Rev. Lett.*, vol. 52, pp. 997–1000, Mar. 1984.

[109] M. E. Casida, "Time-dependent density-functional response theory for molecules," in *Recent Advances in Density Functional Methods, Part I*, vol. 9, p. 155, Singapore, World Scientific, 1995.

[110] S. Hirata and M. Head-Gordon, "Time-dependent density functional theory within the Tamm-Dancoff approximation," *CHEM. PHYS. LETT., Chemical physics letters*, vol. 314, pp. 291–299, Dec. 1999.

[111] A. D. Becke, "Density-functional exchange-energy approximation with correct asymptotic behavior," *Phys. Rev. A*, vol. 38, pp. 3098–3100, Sept. 1988.

[112] J. P. Perdew, J. A. Chevary, S. H. Vosko, K. A. Jackson, M. R. Pederson, D. J. Singh, and C. Fiolhais, "Atoms, molecules, solids, and surfaces: Applications of the generalized gradient approximation for exchange and correlation," *Phys. Rev. B*, vol. 46, pp. 6671–6687, Sept. 1992.

[113] J. P. Perdew, K. Burke, and M. Ernzerhof, "Generalized Gradient Approximation Made Simple," *Phys. Rev. Lett.*, vol. 77, pp. 3865–3868, Oct. 1996.

[114] A. D. Becke, "Density-functional thermochemistry iii. the role of exact exchange," *The Journal of Chemical Physics*, vol. 98, pp. 5648–5652, Apr. 1993.

[115] C. Lee, W. Yang, and R. G. Parr, "Development of the Colle-Salvetti correlation-energy formula into a functional of the electron density," *Phys. Rev. B*, vol. 37, p. 785, Jan. 1988.

[116] Y. Tawada, T. Tsuneda, S. Yanagisawa, T. Yanai, and K. Hirao, "A long-range-corrected time-dependent density functional theory," *The Journal of Chemical Physics*, vol. 120, pp. 8425–8433, Apr. 2004.

[117] T. Yanai, D. P. Tew, and N. C. Handy, "A new hybrid exchange–correlation functional using the Coulomb-attenuating method (CAM-B3lyp)," *Chemical Physics Letters*, vol. 393, pp. 51–57, July 2004.

[118] C. Adamo and D. Jacquemin, "The calculations of excited-state properties with Time-Dependent Density Functional Theory," *Chemical Society Reviews*, vol. 42, no. 3, pp. 845–856, 2013.

[119] D. Jacquemin, B. Mennucci, and C. Adamo, "Excited-state calculations with TD-DFT: from benchmarks to simulations in complex environments," *Physical Chemistry Chemical Physics*, vol. 13, pp. 16987–16998, Sept. 2011.

[120] V. Barone, J. Bloino, and M. Biczysko, "Vibrationally-resolved electronic spectra in GAUSSIAN 09," *September*, vol. 2, p. 2009, 2009.

[121] F. Santoro, A. Lami, R. Improta, J. Bloino, and V. Barone, "Effective method for the computation of optical spectra of large molecules at finite temperature including the Duschinsky and Herzberg-Teller effect: the Qx band of porphyrin as a case study," *J Chem Phys*, vol. 128, p. 224311, June 2008.

[122] C. Eckart, "Some Studies Concerning Rotating Axes and Polyatomic Molecules," *Phys. Rev.*, vol. 47, pp. 552–558, Apr. 1935.

[123] A. Sayvetz, "The Kinetic Energy of Polyatomic Molecules," *The Journal of Chemical Physics*, vol. 7, pp. 383–389, June 1939.

[124] Y. Jean and F. Volatron, *Structure électronique des molécules. Tome 2, géométrie, réactivité et méthode de Hückel*. 1994.

[125] E. Canadell, M.-L. Doublet, and C. Iung, *Orbital Approach to the Electronic Structure of Solids*. Oxford, New York: Oxford University Press, Jan. 2012.

[126] K. Jug, "Theoretical basis and design of the PPP model Hamiltonian," *Int. J. Quantum Chem.*, vol. 37, pp. 403–414, Apr. 1990.

[127] E. Hückel, "Quantentheoretische Beiträge zum Benzolproblem," *Z. Physik*, vol. 70, pp. 204–286, Mar. 1931.

[128] R. Hoffmann, "An extended hückel theory. i hydrocarbons," *The Journal of Chemical Physics*, vol. 39, pp. 1397–1412, Sept. 1963.

[129] M. Wolfsberg and L. Helmholz, "The spectra and electronic structure of the tetrahedral ions mno4-, cro4-, and clo4-," *The Journal of Chemical Physics*, vol. 20, pp. 837–843, May 1952.

[130] J. Huang, L. Du, D. Hu, and Z. Lan, "Theoretical analysis of excited states and energy transfer mechanism in conjugated dendrimers," *Journal of Computational Chemistry*, vol. 36, pp. 151–163, Jan. 2015.

[131] E. R. Davidson and A. A. Jarzęcki, "Zero point corrections to vertical excitation energies," *Chemical Physics Letters*, vol. 285, pp. 155–159, Mar. 1998.

[132] B. Lasorne, J. Jornet-Somoza, H.-D. Meyer, D. Lauvergnat, M. A. Robb, and F. Gatti, "Vertical transition energies vs. absorption maxima: Illustration with the UV absorption spectrum of ethylene," *Spectrochimica Acta Part A: Molecular and Biomolecular Spectroscopy*, vol. 119, pp. 52–58, Feb. 2014.

[133] P. Software, "Caesar, 2.0."

[134] T. Tada, D. Nozaki, M. Kondo, and K. Yoshizawa, "Molecular Orbital Interactions in the Nanostar Dendrimer," *The Journal of Physical Chemistry B*, vol. 107, pp. 14204–14210, Dec. 2003.

[135] M. Head-Gordon, A. M. Grana, D. Maurice, and C. A. White, "Analysis of Electronic Transitions as the Difference of Electron Attachment and Detachment Densities," *J. Phys. Chem.*, vol. 99, pp. 14261–14270, Sept. 1995.

[136] A. Dreuw and M. Head-Gordon, "Single-Reference ab Initio Methods for the Calculation of Excited States of Large Molecules," *Chem. Rev.*, vol. 105, pp. 4009–4037, Nov. 2005.

[137] T. Etienne, "Theoretical insights into the topology of molecular excitons from single-reference excited states calculation methods," in *Excitons* (S. Pyshkin, ed.), ch. 3, Rijeka: InTech, 2018.

[138] B. Gonon, A. Perveaux, F. Gatti, D. Lauvergnat, and B. Lasorne, "On the applicability of a wavefunction-free, energy-based procedure for generating first-order non-adiabatic couplings around conical intersections," *The Journal of Chemical Physics*, vol. 147, p. 114114, Sept. 2017.

[139] M. Krämer, U. H. F. Bunz, and A. Dreuw, "Comprehensive Look at the Photochemistry of Tolane," *J. Phys. Chem. A*, vol. 121, pp. 946–953, Feb. 2017.

[140] Brandow B. H., "Formal theory of effective pi-electron hamiltonians," *International Journal of Quantum Chemistry*, vol. 15, pp. 207–242, Oct. 2004.

[141] W. R. Inc., "Mathematica, Version 11.3." Champaign, IL, 2018.

[142] M. Takahata, M. Nakano, H. Fujita, and K. Yamaguchi, "Mechanism of exciton migration of dendritic molecular aggregate: a master equation approach including weak exciton–phonon coupling," *Chemical physics letters*, vol. 363, no. 5, pp. 422–428, 2002.

[143] H. Li, S. V. Malinin, S. Tretiak, and V. Y. Chernyak, "Effective tight-binding models for excitons in branched conjugated molecules," *The Journal of Chemical Physics*, vol. 139, p. 064109, Aug. 2013.

[144] R. Binder, S. Römer, J. Wahl, and I. Burghardt, "An analytic mapping of oligomer potential energy surfaces to an effective Frenkel model," *The Journal of Chemical Physics*, vol. 141, p. 014101, July 2014.

Résumé

Cette thèse s'intéresse à la rationalisation du mécanisme de transfert d'excitation dans des polyphénylènes éthynylènes (PPE). Une étude statique approfondie a été réalisée en utilisant la TDDFT, permettant de confirmer la localisation des états excités de méta-PPE sur des fragments para, ainsi que la hiérarchie des interactions régissant les propriétés photochimiques des PPE. Des intersections coniques ont été identifiées, de même que les principales composantes de l'espace de branchement. Leur étude a soutenu l'hypothèse d'un transfert d'énergie par conversion interne entre états excités localisés sur des fragments para.

D'autre part, nous avons proposé un modèle vibronique multiéchelles pour l'énergie des états électroniques. En particulier, nous avons exprimé les énergies des orbitales frontières de PPE en fonction des énergies des orbitales frontières du benzène et de l'acetylène via un Hamiltonien effectif de type Hückel. Un travail de mapping et d'optimisation nous a permis d'aboutir à une expression pour l'énergie de transition électronique en fonction d'un nombre réduit de coordonnées nucléaires locales.

Abstract

The present work is focused on the rationalization of the excitation transfer mechanism in polyphenylene ethynylenes (PPEs). A static study was performed using TDDFT, allowing to confirm both the localization of the excited states of meta-PPEs on para building blocks and the hierarchy in the interactions governing the photochemical properties of PPEs. Conical intersections were identified, along with few components of their branching spaces. Studying those supported the assumption of an energy transfer proceeding through internal conversion between excited states localized on different building blocks.

In addition, we proposed a multiscale vibronic model for the energy of the eletronic states. In particular, we expressed the energies of the frontier orbitals of PPEs in terms of the energies of the frontier orbitals of benzene and acetylene, using an effective Hückel-type Hamiltonian. Perfoming different optimizations, we achieved to propose an expression for the energy of the electronic transition in terms of a reduced number of local nuclear coordinates.